

ABSTRACT

Title of dissertation:

QUANTUM SIMULATION OF
INTERACTING SPIN MODELS
WITH TRAPPED IONS

Kazi Rajibul Islam, Doctor of Philosophy, 2012

Dissertation directed by:

Professor Christopher Monroe
Joint Quantum Institute,
University of Maryland Department of Physics and
National Institute of Standards and Technology

The quantum simulation of complex many body systems holds promise for understanding the origin of emergent properties of strongly correlated systems, such as high- T_c superconductors and spin liquids. Cold atomic systems provide an almost ideal platform for quantum simulation due to their excellent quantum coherence, initialization and readout properties, and their ability to support several forms of interactions. In this thesis, I present experiments on the quantum simulation of long range Ising models in the presence of transverse magnetic fields with a chain of up to sixteen ultracold $^{171}\text{Yb}^+$ ions trapped in a linear radiofrequency Paul trap. Two hyperfine levels in each of the $^{171}\text{Yb}^+$ ions serve as the spin-1/2 systems. We detect the spin states of the individual ions by observing state-dependent fluorescence with single site resolution, and can directly measure any possible spin correlation function. The spin-spin interactions are engineered by applying dipole forces from precisely tuned lasers whose beatnotes induce stimulated Raman transitions that

couple virtually to collective phonon modes of the ion motion. The Ising couplings are controlled, both in sign and strength with respect to the effective transverse field, and adiabatically manipulated to study various aspects of this spin model, such as the emergence of a quantum phase transition in the ground state and spin frustration due to competing antiferromagnetic interactions. Spin frustration often gives rise to a massive degeneracy in the ground state, which can lead to entanglement in the spin system. We detect and characterize this frustration induced entanglement in a system of three spins, demonstrating the first direct experimental connection between frustration and entanglement. With larger numbers of spins we also vary the range of the antiferromagnetic couplings through appropriate laser tunings and observe that longer range interactions reduce the excitation energy and thereby frustrate the ground state order. This system can potentially be scaled up to study a wide range of fully connected spin networks with a few dozens of spins, where the underlying theory becomes intractable on a classical computer.

Quantum Simulation of Interacting Spin Models
with Trapped Ions

by

Kazi Rajibul Islam

Dissertation submitted to the Faculty of the Graduate School of the
University of Maryland, College Park in partial fulfillment
of the requirements for the degree of
Doctor of Philosophy
2012

Advisory Committee:

Professor Christopher Monroe, Chair/Advisor
Professor Steve Rolston
Dr. Ian Spielman
Professor Christopher Jarzynski
Professor Dianne O'Leary

© Copyright by
Kazi Rajibul Islam
2012

To my parents

Acknowledgments

First of all, I thank my advisor Prof. Chris Monroe for giving me the opportunity to work on this project. Instead of writing a long essay on his amazing capabilities as a physicist, and as an advisor, I would just say that he is very close to the ideal advisor I could have hoped for. I appreciate his constant encouragement to engage in fruitful conversations with other people, particularly the theorists, and the independence that he gave me to pursue my experimental ideas.

Research in experimental physics is surely a group effort, and this is so true in our group. I have been fortunate to work with a pool of great postdocs and fellow graduate and undergraduate students. Ming-Shien Chang, Kihwan Kim, Emily Edwards and Wes Campbell were all very gifted postdocs, and I learned a lot from them. Thanks to you all. I enjoyed lots of stimulating physics conversations with Wes Campbell over the years. I wish him all the best for his new position as a faculty member at UCLA. It was fun to work with the fellow graduate students, Simcha Korenblit, Jake Smith and Crystal Senko; and the undergrads, Andrew Chew, Aaron Lee, who decided that he loved this experiment too much to leave, and is continuing as a grad student, and most recently with the new undergrad in the team Geoffrey Ji.

It was a privilege working with smart theorists like Luming Duan and his students Guin-Dar Lin and Zhexuan Gong, Jim Freericks and his postdoc Joseph Wang, Howard Carmichael and his student Changsuk Noh, and Dvir Kafri. David Huse and Rajdeep Sensarma taught me many aspects of the quantum Ising model.

Thanks to all of you.

I enjoyed interacting with the other members of the group immensely, though I did not directly work with them. Thanks to Taeyoung Choi, Susan Clark, Charles Conover, Shantanu Debnath, Brian Fields, Ilka Geisel, Dave Hayes, David Hucul, Volkan Inlek, Kale Johnson, Kenny Lee, Le Luo, Andrew Manning, Dzmitry Matsukevich, Peter Maunz, Jonathan Mizrahi, Steve Olmschenk, Qudsia Quraishi and Jon Sterk.

A special thanks to Crystal, Wes and Emily for going over my thesis manuscripts and suggesting important corrections.

I thank all my thesis committee members (Steve Rolston, Ian Spielman, Chris Jarzynski, Dianne O'Leary, and of course Chris Monroe) for their support in scheduling the defense talk, and accommodating my delays. Thanks to Victor Galitski for serving on my PhD candidacy committee two and a half years back.

The Joint Quantum Institute provided an excellent environment for research, and I learned a lot from almost all the members in the basement and on the second floor of the CSS building during our random interactions. Thanks to all of you. Thanks to all the staff members of JQI for helping me with non-academic tasks most efficiently, and always in a timely manner.

I thank all the funding agents for making my graduate student life smoother. In particular, the DARPA Optical Lattice Emulator program has been a wonderful experience for the last five years. I thoroughly enjoyed many intellectually invigorating discussions in all the OLE meetings.

My friends were a constant source of support over all these years. Fortunately,

they are too numerous to name here.

Last but not the least, my family members were always there whenever I needed them. I am eternally grateful to all of you.

Table of Contents

List of Tables	viii
List of Figures	ix
List of Abbreviations	xi
1 Introduction	1
2 Trapped Ions as a Platform for Quantum Simulation	8
2.1 Overview	8
2.2 Ion Trapping	8
2.2.1 Trapping $^{171}\text{Yb}^+$ in our Paul trap	15
2.3 Manipulation of $^{171}\text{Yb}^+$ spin and motional states	18
2.3.1 Hyperfine states	18
2.3.2 Doppler cooling	20
2.3.3 Detection of the spin states	22
2.3.4 State initialization by optical pumping	26
2.3.5 Coherent manipulation of the spin states	27
2.3.6 Raman sideband cooling	45
2.4 Vibrational normal modes of trapped ions	46
2.5 Simulating the quantum Ising model	53
2.5.1 Ising interactions	54
2.5.2 Adiabatic quantum simulation	66
2.6 Experimental Apparatus	68
2.6.1 Ti:Sapphire laser	68
2.6.2 Generating 369.5 nm light by frequency doubling	78
2.6.3 369.5 nm optics schematics	78
2.6.4 Mode-locked 355 nm laser	81
2.6.5 Optical set up for the Raman transitions	91
2.7 Quantum simulation recipe for experimentalists	97
2.8 Troubleshooting with $^{174}\text{Yb}^+$	107
3 Simulation of the ferromagnetic quantum Ising model	109
3.1 Overview	109
3.2 Symmetries of the Hamiltonian	111
3.3 Low energy eigenstates at $T=0$	112
3.3.1 States near $B/J = 0$	112
3.3.2 States near $B/J \rightarrow \infty$	117
3.3.3 Quantum phase transition at $B = J$	118
3.4 Experiment: onset of a quantum phase transition	121
3.4.1 Engineering the ferromagnetic Ising couplings	121
3.4.2 Experimental protocol and order parameters of the transition	124
3.4.3 Results	127

3.4.4	Sources of error in the quantum simulation	130
3.5	Scaling up the simulation to $N = 16$ with 355 nm mode locked laser .	139
4	Three frustrated Ising spins on a triangle	142
4.1	Overview	142
4.2	Frustrated quantum Ising model	145
4.2.1	States near $B/J = 0$	145
4.2.2	Preparing the entangled state in adiabatic quantum simulation	147
4.3	Frustration and entanglement	148
4.4	Experimental methods	151
4.5	Experimental Results	154
4.6	Summary and outlook	160
5	Frustrated magnetic ordering with tunable range antiferromagnetic couplings	161
5.1	Overview	161
5.2	Some features of the long range antiferromagnetic quantum Ising model	163
5.2.1	Ground and low energy eigenstates	163
5.2.2	Frustration and the range of the interactions	166
5.3	Experimental simulation of the model	169
5.3.1	Tuning the range of Ising interactions	171
5.3.2	Experimental protocol and the order parameters	174
5.4	Results of the quantum simulation	177
5.4.1	Onset of antiferromagnetic correlations in quantum simulation for $N = 10$ and $N = 16$ spins	177
5.4.2	Frustration of the AFM order with increasing range of inter- actions	180
5.5	Discussions and conclusion	184
6	Outlook	185
6.1	Scaling up the system - large numbers of equally spaced ions in a Paul trap	185
6.2	Creating an arbitrary lattice geometry	187
6.3	Other interesting spin physics	188
A	Quantum trajectory calculations	190
B	Detection of spin states	192
C	Relevant Frequencies for $^{171}\text{Yb}^+$ and $^{174}\text{Yb}^+$	194
	Bibliography	195

List of Tables

2.1	Phases of various pulses used in quantum simulation.	107
3.1	Symmetries of the eigenstates	119
5.1	Experimental parameters used to generate long range Ising model with variable range	174
C.1	Frequency lock points for various lasers	194

List of Figures

2.1	Schematics of the three layer linear Paul trap	13
2.2	Ionization beam and oven geometry	17
2.3	$^{171}\text{Yb}^+$ level diagram	19
2.4	Detection of the spin states	23
2.5	Fluorescence histograms of the spin states	25
2.6	Optical pumping to the $ \downarrow_z\rangle$ state	26
2.7	Two photon stimulated Raman transition in a Λ -system	28
2.8	Adiabatic elimination of the excited state	32
2.9	Resonant hyperfine (Carrier) Rabi oscillations in $^{171}\text{Yb}^+$ spin states .	41
2.10	Ramsey interferometry in a $^{171}\text{Yb}^+$ ion	42
2.11	Carrier and sideband transitions	44
2.12	Raman sideband cooling	46
2.13	Image of ten bright $^{171}\text{Yb}^+$ ions in a linear configuration	47
2.14	Axial and transverse vibrational modes of trapped ions	49
2.15	Transverse mode eigenvectors for $N = 10$ ions	51
2.16	Nineteen ions in a zig-zag configuration	52
2.17	Mølmer-Sørensen transition in a system of two spins	55
2.18	Ising couplings for various Mølmer-Sørensen detuning	63
2.19	Ising oscillations between spin states	64
2.20	Experimental sequence in a quantum simulation	66
2.21	Schematics of the MBR-110 Ti:Sapphire laser	70
2.22	MBR modes	71
2.23	MBR-110 Ti:Sapphire laser	77
2.24	Schematics of the 369.5 nm beams	79
2.25	Schematics of a two photon Raman transition using a mode-locked laser	83
2.26	Radio frequency comb-teeth used in the two photon Raman transitions	84
2.27	Drift in the repetition rate of the 355 nm mode-locked laser	86
2.28	Schematics of the repetition rate lock	87
2.29	The role of the Phase locked loop in the repetition rate stabilization scheme	90
2.30	Raman transition set up	93
2.31	The Clebsh-Gordan coefficients relevant for the two photon hyperfine Raman transition	96
3.1	Energy spectrum of the ferromagnetic transverse Ising model for $N = 2$ spins	113
3.2	Ground state degeneracy splitting by the transverse field	116
3.3	A few low energy eigenstates of Eq. (3.1) for $N = 5$ spins	120
3.4	Raman spectrum of vibrational modes and Ising coupling profile for $N = 9$ spins	123
3.5	Binder cumulant and magnetization for the adiabatic theory	126

3.6	Emergence of the ferromagnetic spin order	128
3.7	Onset of a quantum phase transition- sharpening of the crossover curves with increasing system size.	129
3.8	Suppression in the ferromagnetic fidelity with increasing system size .	131
3.9	Spontaneous emission from the Raman beams	133
3.10	Detection with a PMT – overlapping photon count histograms	136
3.11	Suppression in the GHZ coherence with increasing system size	137
3.12	Quantum simulation of the ferromagnetic Ising model with $N = 16$ spins	140
4.1	Three frustrated Ising spins on a triangle	143
4.2	Increased sensitivity to quantum fluctuations in presence of frustration	146
4.3	Energy diagram for $J_1 \neq J_2$	153
4.4	Population of spin states with ferromagnetic and antiferromagnetic Ising couplings	155
4.5	Entanglement generation through the quantum simulation	157
4.6	Entanglement from the frustration	158
5.1	Energy of creating spin excitations in the long range antiferromagnetic Ising model	165
5.2	Dependence of the spectrum of Hamiltonian (5.1) on frustration	167
5.3	Ising coupling profile and fit to a power law	170
5.4	Dependence of the range of Ising interactions on the Mølmer-Sørensen detuning and the bandwidth of vibrational modes	172
5.5	Onset of the antiferromagnetic ordering with 10 spins	178
5.6	Antiferromagnetic spin ordering with 16 spins	179
5.7	CCD image of $N = 10$ antiferromagnetically ordered spins	181
5.8	Frustration of antiferromagnetic spin ordering with increasing range of interactions	182
5.9	Plausible decoherence in our quantum simulation	183

List of Abbreviations

AFM	Antiferromagnetic
AOM	Acousto Optic Modulator
bsb	Blue sideband
CCD	Charged Coupled Device
COM	Center of Mass
CW	Continuous Wave (lasers)
DC	Direct Current (here used to refer to static voltages)
DMRG	Density Matrix Renormalization Group
EOM	Electro Optic Modulator
FM	Ferromagnetic
GHZ	Greenberg-Horne-Zeilinger (entanglement)
ICCD	Intensified Charged Coupled Device
PMT	Photo Multiplier Tube
QPT	Quantum Phase Transition
RF	Radio frequency
rsb	Red sideband
RWA	Rotating Wave Approximation
Yb	Ytterbium

Chapter 1

Introduction

A quantum system can be in a superposition of several possible states at the same time, a feature distinctly different from the classical superposition [1]. This bizarre property results in many counter-intuitive phenomena, such as non-local correlations or entanglement between different parts of a quantum system, leading to the famous Einstein-Podolsky-Rosen paradox [2]. Quantum superposition presents an outstanding challenge in computing, as we have to keep track of an exponentially large number of coefficients to describe the time evolution of a quantum system. As an example, a system consisting of N two level objects (referred to as the qubits, or spins) is represented by a wavefunction $|\Psi\rangle$, which can be written as,

$$|\Psi\rangle = \sum_{s_1=\{\uparrow,\downarrow\}} \dots \sum_{s_N=\{\uparrow,\downarrow\}} a_{s_1,s_2,\dots,s_N} |s_1, s_2, \dots s_N\rangle. \quad (1.1)$$

Here $|s_1, s_2, \dots, s_N\rangle$ is the state where the first spin is in state s_1 (either \uparrow , or \downarrow) and so on. A full specification of the wavefunction requires 2^N of the amplitudes a_{s_1,s_2,\dots,s_N} . A classical system, on the other hand, requires only N coefficients to describe the probability of an outcome. Conventional computers used for computing today are composed of classical bits, and hence require resources exponentially large in N to faithfully simulate the properties of an arbitrary N – qubit quantum system.

In his 1981 seminal lecture on ‘Simulating Physics with Computers’ [3], Feyn-

man suggested using quantum logic gates to simulate the behavior of a quantum system. He envisioned the idea of a quantum computer that will “*do exactly the same as nature.*” In 1996, Lloyd showed that quantum computers can be programmed to simulate any local quantum system [4]. Although building a full scale universal quantum simulator or a quantum computer [5] with error correcting codes [6] is a distant dream as of now, experimental efforts to use a controlled quantum system for manipulating specific quantum information are underway. These systems include trapped ions [7, 8, 9, 10], neutral atoms in optical lattices [11, 12], resonator coupled superconducting qubit arrays [13, 14], electron spins in quantum dots and nitrogen vacancy centers in ultra-pure diamond crystals [15, 14], and photons [16, 17, 18, 19].

A quantum simulator based on Feynman’s original idea may be called a digital quantum simulator [20], where the desired Hamiltonian, H is constructed from piecewise application of local Hamiltonians, $H = \sum_{i=1}^l H_i$, following the Trotter expansion,

$$e^{-iHt} \approx (e^{-iH_1 t/n} e^{-iH_2 t/n} \dots e^{-iH_l t/n})^n. \quad (1.2)$$

The error in simulating the Hamiltonian can be kept under a given value by properly choosing the number of steps, n . Another class of quantum simulators, known as analog simulators, continuously follow the Hamiltonian evolution of a physically different but mathematically equivalent system [21]. Analog quantum simulators are restricted to simulating a few classes of Hamiltonians, but they prove to be very useful to study some non-trivial many body physics so far.

Understanding the physics of many body emergent phenomena is one of the

main areas of research in modern physics. Despite many minimalistic models [22, 23, 24] to understand the behavior of the strongly correlated systems [25, 26], such as high temperature superconductors [27], heavy fermion materials [28], colossal magneto-resistance materials [29], frustrated spin liquids [30], and quasi-low dimensional materials [31], the mechanism behind some of the exotic properties remains mostly unknown. Numerical techniques such as quantum Monte Carlo [32] and density matrix renormalization group (DMRG) [33] provide valuable insights into the many body physics of a quantum system, but they do not work very well when the underlying model involves frustration [34] and long range interactions [35]. A quantum simulator takes a bottom-up approach, where the behavior of a quantum system under a well understood Hamiltonian is experimentally studied, and complexities are added piece by piece. The search is for the minimal interactions between the fundamental building blocks required to explain the many body emergent properties of the macroscopic system.

Cold atomic systems provide a nearly ideal platform for quantum simulation, due to their long coherence time, near perfect initialization and detection fidelities and ability to support many classes of interactions. In recent years, a number of cold atom experiments, with both neutral atoms and ions, have simulated and studied interesting many-body physics, such as transition from superfluid to Mott insulator in Bosonic systems [36, 37, 38], quantum phase transitions between spin phases or quantum magnetism [39, 40, 41, 42, 43, 44], Bardeen-Cooper-Schrieffer (BCS) pairing [45] and BEC-BCS crossover physics [46], investigation of quantum criticality [47, 48, 49], synthetic gauge fields to simulate quantum Hall physics and

topological insulators [50], quantum simulation of relativistic dynamics [51, 52], and long range spin models involving spin frustration [43, 53]. Cold atom systems offer some distinct advantages over the condensed matter systems, some of which are,

- Cold atom systems show remarkable tunability, and often can access a much larger parameter range than the condensed matter systems. As we shall discuss in this thesis, the effective spin interactions in a simulated spin model can be changed in sign, magnitude, and range by changing the frequency of a laser beam [54]. In solid state systems, the sign of the magnetic interactions cannot be changed, and altering the strength of the couplings by a modest amount may require application of large hydrostatic pressures [55]. Another example is the control of interactions in a cold atomic system provided by Feshbach resonances [56, 57].
- Cold atomic systems have a very low level of defects compared to the solid state systems. For example, the extreme low entropy in a spin-polarized Mott insulator state allows the study of quantum magnetism [40]. Defects can be controllably added to study the physics of disordered systems such as Anderson localization [58, 59, 60].
- They have ultra-low densities compared to the solid state systems. Typical spacing between the neighboring trapped ions or optical lattice sites is of the order of a micron, much larger than the typical electronic spacing of a few Angstroms in solid state materials. This allows optical imaging of individual components, and direct observations of spin ordering in quantum magnetism [43, 61].
- The time scale of the dynamics in a cold atom system is longer and more experi-

mentally accessible than their solid state counterpart.

Trapped ions have been in the forefront of quantum information processing since experimental investigation began [62], demonstrating universal quantum gates [63, 64, 65, 66], and quantum teleportation [67, 68, 69, 70]. The long coherence time of trapped ion systems, and the easy access to long range tunable interactions [71, 54] make them an outstanding choice to simulate long range spin models that demonstrate quantum phase transitions [47] and spin frustrations [72]. In this work, we simulate a long range quantum Ising model with a chain of up to sixteen $^{171}\text{Yb}^+$ ions in a radio-frequency trap. Two hyperfine states of each $^{171}\text{Yb}^+$ ion constitute an effective spin- $\frac{1}{2}$ system. The collective vibrational modes of the trapped ions, excited off-resonantly with stimulated Raman transitions by precisely tuned laser fields, act as an ‘information bus’, and mediate the two body spin interactions [71]. An effective transverse external field, simulated by stimulated Raman transitions between the spin levels, introduces quantum fluctuations in the system. We study the ground state properties and excitations in the system by preparing the spins in an eigenstate of a trivial Hamiltonian and tuning it to the more complicated one to be simulated, following the adiabatic quantum simulation protocol [73].

With our quantum simulator we investigate various non-trivial many body physics, such as a quantum phase transition between magnetic phases [41], spin frustration leading to entanglement [43], and the observation of spin ordering in a system of sixteen spins (two qubits), the largest number of spins used to process quantum information in a linear trap to this date. The present work serves as a

benchmark for quantum simulation with larger systems, where the underlying theory becomes intractable with conventional computers.

This thesis is divided into the following chapters.

- The second chapter gives the necessary theoretical and experimental background on quantum simulation with trapped ions. This includes a brief discussion on the collective vibrational motion of a chain of $^{171}\text{Yb}^+$ ions in a radio-frequency Paul trap, that are used to generate the spin interactions. We derive the effective Ising Hamiltonian starting from the basic interactions of the ions with the Raman laser field. Control over the Ising couplings, and the quantum simulation protocol are discussed. In the experimental section, we discuss the hardware used in the set up, in particular the lasers that drive the stimulated Raman transitions. Section 2.7 is devoted to discussing the experimental procedure step by step.
- The third chapter discusses and presents some results on the quantum simulation of the ferromagnetic Ising model. We observe the onset of ferromagnetic spin ordering in a system of up to sixteen spins. As the effective external field is tuned with respect to the Ising interactions, the system undergoes a crossover from the paramagnetic to the ferromagnetic phases. The sharpness of this crossover increases with the system size, consistent with the expected quantum phase transition in the thermodynamic limit.
- We simulate the long range antiferromagnetic quantum Ising model in the fourth and the fifth chapters with up to sixteen spins. The long range interactions in the trapped ion system gives rise to a fully connected spin network. The interactions

can be suitably tailored to simulate a higher dimensional lattice geometry, in this one dimensional chain of ions. In chapter 4, we simulate a frustrated spin network with three spins interacting antiferromagnetically on the corners of a triangle, and study the many body ground state. Frustration leads to a large degeneracy, with six of the eight ($= 2^3$) basis spin states belonging to the ground state manifold. We detect and characterize the entanglement coming out of this frustration induced degeneracy, and contrast it to the entanglement coming out of the symmetries in the Hamiltonian (section 3.2). The amount of frustration in the long range antiferromagnetic Ising model is controlled by varying the range of the antiferromagnetic couplings. We compare the spin order for various degrees of frustration in chapter 5.

- The sixth chapter gives an outlook for future directions.

Chapter 2

Trapped Ions as a Platform for Quantum Simulation

2.1 Overview

This chapter gives a brief overview of the theoretical and experimental tools needed in our quantum simulation experiment with trapped $^{171}\text{Yb}^+$ ions. I briefly describe the working principle of an ion trap, without going into too much detail. Two hyperfine states of the $^{171}\text{Yb}^+$ ions are used as the pseudo spin- $\frac{1}{2}$ states, which are manipulated by various standard atomic physics techniques, such as Doppler cooling, optical pumping, stimulated Raman transitions, and Raman sideband cooling. We give a short introduction to each of these topics. Finally we describe some of our experimental apparatus in detail, particularly focusing on the lasers used to drive the stimulated Raman transitions.

2.2 Ion Trapping

A charged particle cannot be trapped in space by electrostatic forces alone, as pointed out by Samuel Earnshaw [74] in 1842. This is due to the fact that, an electrostatic potential $V(X, Y, Z)$ has to satisfy the constraint $\nabla^2 V(X, Y, Z) = 0$ (The Laplace equation, $\nabla^2 \equiv \frac{\partial^2}{\partial X^2} + \frac{\partial^2}{\partial Y^2} + \frac{\partial^2}{\partial Z^2}$) everywhere in the free space, and the properties of the Laplace equation prevents its solution to admit any local extremum.

Ion traps work by applying either an oscillating electric field (Paul traps [75]), or a static magnetic field (Penning traps [76]) in conjunction with static electric fields to create an extremum in the effective time averaged potential. We use a radio frequency Paul trap for our quantum simulation experiments.

An electrostatic potential created by applying static voltages on metallic electrodes cannot create a potential extremum in space, but by properly choosing the boundary conditions, it is possible to create a potential saddle. As an example, the general form of a quadrupole potential is,

$$V(X, Y, Z) = \alpha X^2 + \beta Y^2 + \gamma Z^2. \quad (2.1)$$

The Laplace equation puts the constraint $\alpha + \beta + \gamma = 0$, which admits the solution $\alpha = -2, \beta = 1, \gamma = 1$ for some specific boundary conditions. The potential has a saddle point at $(X = 0, Y = 0, Z = 0)$, *i.e.*, $V(X, Y, Z)$ is confining along the Y and the Z directions, but anti-confining along the X direction for a positive charge.

On top of the electrostatic field, we superpose a spatially inhomogeneous oscillating electric field, the time average of which will generate an effective confining potential. Let's consider the motion of a charged particle in an oscillating field [77] alone. The force equation is,

$$m\ddot{X} = F_X(t) = eE_0(X) \cos \Omega_{rf}t. \quad (2.2)$$

Here we assume that the oscillating electric field with frequency Ω_{rf} and amplitude

$E_0(X)$ couples to the X component only, e and m are the charge and the mass of the particle respectively. If $E_0(X) = E_0$ is a homogeneous field, the average force $\langle F_X(t) \rangle_t = 0$, since $\langle \cos \Omega_{rf} t \rangle_t = 0$, and the solution to Eq. (2.2) is,

$$X(t) = -\frac{eE_0}{m\Omega_{rf}^2} \cos \Omega_{rf} t + X_0. \quad (2.3)$$

Here $X_0 = \langle X(t) \rangle_t$ is an integration constant and represents the time averaged position of the charged particle, and we have assumed that at $t = 0$ the particle was at rest, *i.e.*, $\dot{X}(t = 0) = 0$. Here $\langle \dots \rangle_t$ denotes averaging over a time long compared to the time period of the oscillating field. Hence, under a homogeneous oscillating electric field, a charge particle does not experience any confining potential, and oscillates with the driving field. The oscillation of the charged particle at the frequency of the driving field is known as the micromotion.

Now, we add a small inhomogeneity in the driving field amplitude $E_0(X)$, maintaining its value at $X = X_0$, and expand it about $X = X_0$,

$$E_0(X) = E_0(X_0) + \left. \frac{\partial E_0(X)}{\partial X} \right|_{X=X_0} (X - X_0). \quad (2.4)$$

Let $\zeta(t) \equiv X(t) - X_0$ be the displacement of the charged particle about the mean position (we assume that the mean position of the charged particle is unchanged with this added inhomogeneity. For a detailed discussion see ref [77]).

From Eq. (2.2), the time averaged value of the force is,

$$\begin{aligned}
F_X(t) &= eE_0(X) \cos \Omega_{rf} t \\
&= e \left(E_0(X_0) + \frac{\partial E_0(X)}{\partial X} \Big|_{X=X_0} \zeta(t) \right) \cos \Omega_{rf} t \\
&= eE_0(X_0) \cos \Omega_{rf} t - \frac{e^2}{m\Omega_{rf}^2} E_0(X_0) \frac{\partial E_0(X)}{\partial X} \Big|_{X=X_0} (\cos \Omega_{rf} t)^2. \quad (2.5)
\end{aligned}$$

Here we have approximated $\zeta(t)$ by the displacement of the charge particle in a homogeneous field (Eq. (2.3)) in the last line. The time average of this force is,

$$\begin{aligned}
\bar{F}(X_0) \equiv \langle F_X(t) \rangle_t &= -\frac{e^2}{2m\Omega_{rf}^2} E_0(X_0) \frac{\partial E_0(X)}{\partial X} \Big|_{X=X_0} \\
&= -\frac{e^2}{4m\Omega_{rf}^2} \frac{\partial}{\partial X_0} E_0^2(X_0) \\
&= -e \frac{\partial}{\partial X_0} \left[\frac{e}{4m\Omega_{rf}^2} E_0^2(X_0) \right]. \quad (2.6)
\end{aligned}$$

We identify the quantity inside the square bracket in the last line of Eq. (2.6) as a pseudo-potential, known as the ponderomotive potential,

$$\Psi_{pond}(X_0) \equiv \frac{e}{4m\Omega_{rf}^2} E_0^2(X_0), \quad (2.7)$$

and the time averaged force in Eq. (2.6) is known as the ponderomotive force. Note that the force is independent of the sign of the charge, and hence the same ponderomotive potential can trap both a positive and a negative charge. It can be shown that the kinetic energy in the micromotion of the charged particle is $E_{kinetic} = e\Psi_{pond}(X_0)$. This kinetic energy vanishes for $E_0(X_0) = 0$, *i.e.*, where the

amplitude of the oscillating field vanishes. The region of $E_0(X_0) = 0$ is referred to as a ‘radio-frequency null’. Depending on the geometry of the trap, the radio-frequency null may be a point, a collection of discrete points, or a line. In a quantum information experiment, the static potentials are adjusted so that the equilibrium positions of the ions lie on a radio-frequency null to minimize the micromotion [78], which may couple to the vibrational modes of the ion chain, and result in quantum decoherence by heating up the modes.

A more rigorous analysis of the motion of a charged particle in an ion trap involves solving the Mathieu equation, discussed in Ref. [75]. The ponderomotive potential overcomes the deconfining potential due to static electric fields along the X -direction in our example, and the superposition of the static and the ponderomotive potentials result in a three dimensional confinement of the charged particle. The effective potential takes the form,

$$V(X, Y, Z) = \frac{1}{2}m(\omega_X^2 X^2 + \omega_Y^2 Y^2 + \omega_Z^2 Z^2), \quad (2.8)$$

where $(\omega_X, \omega_Y, \omega_Z)$ are called the secular frequencies along the three trap axes.

While constructing an ion trap for an experiment, the desired trapping potential is simulated with commercially available softwares, such as the 3-D Charged Particle Optics Program (CPO-3D) produced by CPO Ltd. The software solves the Laplace equation for a set of boundary conditions, given in terms of voltages on the electrodes. Ref. [70] gives a detailed instruction on how to use CPO-3D for electrostatics simulations.

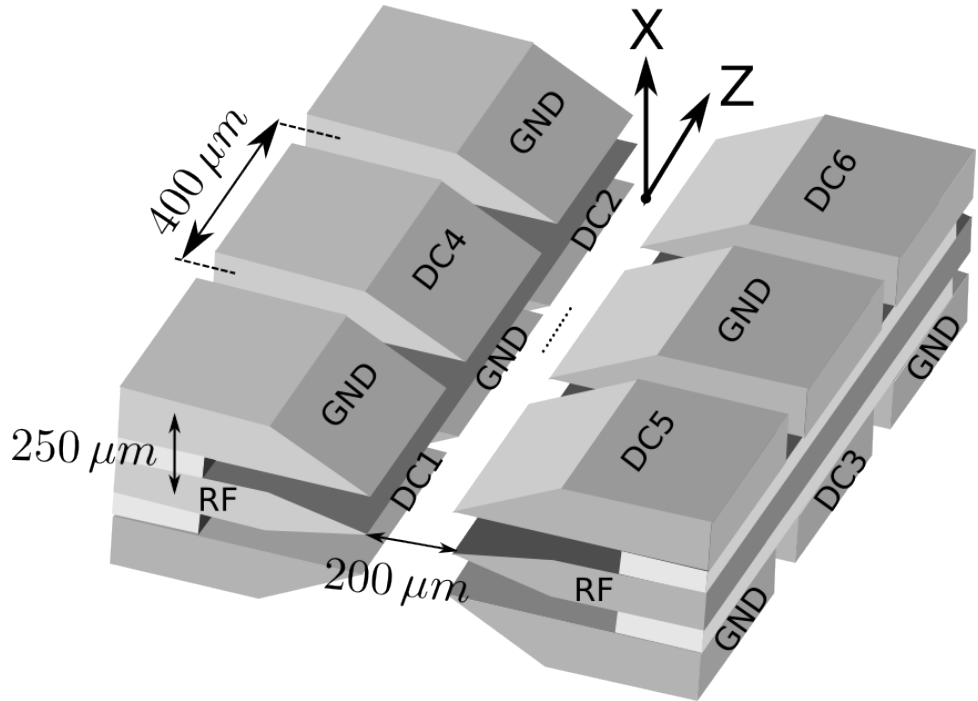


Figure 2.1: Schematics of the three layer linear Paul trap: A linear chain of $^{171}\text{Yb}^+$ ions are confined in a three layer radio-frequency (Paul) trap. The electrodes are gold-coated on alumina substrates. The top and the bottom sets of electrodes are approximately $250\ \mu\text{m}$ thick, and carry static voltages (DC), and the middle ones are approximately $125\ \mu\text{m}$, and carry a radio frequency (rf) voltage at a frequency of $\Omega_{rf}/2\pi = 38.6\ \text{MHz}$. The ions (shown in dots) form a linear crystal along the Z -axis of the trap. The electrodes labeled GND are grounded.

Fig 2.1 shows a schematic of the radio-frequency trap used to trap Ytterbium ions (Yb^+) in our experiment. The top and the bottom electrodes carrying static voltages of up to a hundred volts are segmented into three zones each. A radio-frequency signal at about 38.6 MHz is coupled to the middle electrodes through a helical resonator (transformer) [79], with a resonance around 38.6 MHz and a Q-factor of about 200. The input power to the helical resonator is approximately 27 dBm, or 500 mW. This generates a radio-frequency voltage of about 200-300 Volts, leading to secular frequencies of $\omega_X \approx \omega_Y \approx 2\pi \times 5$ MHz. The three layer trap is housed in a vacuum chamber with a pressure of $< 10^{-11}$ Torr (reading *EO3* on a SenTorr vacuum gauge).

The static voltages DC1 through DC6 (along with the radio frequency) in fig 2.1 control the trapping potential. The static voltages are provided by an 8 channel high precision HV module from the Iseg Spezialelektronik GmbH company. Linear combinations of the static voltages are used to manipulate the position of the ions and properties of the trapping potential, such as

- The end average voltage $V_{end} = (V_1 + V_2 + V_5 + V_6)/4$ and the central average $V_{central} = (V_3 + V_4)/2$ control the overall strength of the trapping potential, where V_i is the static voltage applied on the electrodes labeled DC*i* ($i = 1, 2, \dots, 6$). The ratio of these two voltages also controls the principal axes of the trap along the transverse directions. Principle axes are the Cartesian coordinate axes X and Y such as the trapping potential does not involve any term coupling both the coordinates, *i.e.*, the coefficient $\alpha_{XY} = 0$ in the

generalized form of a quadratic potential, $V(X, Y) = \alpha_{XX}X^2 + \alpha_{XY}XY + \alpha_{YY}Y^2$.

- The Z -push voltage $V_Z = [(V_1 + V_5) - (V_2 + V_6)]/2$ controls the ions position along the Z -axis. The displacement of the ion for a given change in the Z -push voltage depends on V_{end} as well. For example, a change of 3 Volts in V_Z results in a single ion displacement of about 20 μm when the end average voltage $V_{end} = 10$ Volts.
- The end vertical difference $V_{\Delta end-vert} = [(V_1 + V_2) - (V_5 + V_6)]/2$ and the central difference $V_{\Delta central} = V_3 - V_4$ are used to minimize the radio frequency micromotion of the ions [78].

2.2.1 Trapping $^{171}\text{Yb}^+$ in our Paul trap

The vacuum chamber housing the trap contains two ovens made of stainless steel hypodermic needles (in a Titanium holder) packed with neutral Ytterbium metal, one with naturally abundant Yb, dominated by ^{174}Yb (30%), and the other with isotopically enriched ^{171}Yb ($\approx 90\%$ isotope purity). Ytterbium ions ($^{171}\text{Yb}^+$) are loaded into our linear Paul trap from the isotopically enriched oven by photoionization. A current of 2.4-2.8 Ampere is sent through the oven, and the Joule heating produced by the current sublimates Yb atoms into a directional spray. Neutral Yb is ionized into $^{171}\text{Yb}^+$ in two steps.

- Exciting an electron from the 1S_0 level to the 1P_1 level of the neutral Yb.

- Ionizing that electron by supplying 1P_1 -energy continuum or more. Another radiation at 369.5 nm or 355 nm ionizes the atom into a $^{171}\text{Yb}^+$ ion.

The first step is done by a 1 mW laser beam of 398.911 nm radiation from a semiconductor diode laser (Toptica DL-100). This beam is focused cylindrically with beam waists ($1/e^2$ radius in intensity) of $\sim 100 \mu\text{m}$ in the horizontal direction and $\sim 50 \mu\text{m}$ in the vertical direction. The second step can be performed by any light with a wavelength under 394.1 nm. We use about 1 mW of 369.5 nm light beam focused into a cylindrical spot with waists $100 \mu\text{m} \times 50 \mu\text{m}$ to ionize. It takes about half a minute to trap a single ion after the oven warms up (a couple of minutes after the current source is turned on). The 369.5 nm light is generated by frequency doubling 739 nm light (generated by a Ti:Sapphire laser or a semiconductor diode laser with a tapered amplifier system) by an LBO crystal in a cavity (WaveTrain, made by Spectra-Physics). The loading process can be expedited greatly with a brief pulse (under a second) of 355 nm light (about 1 W light focused into $100 \mu\text{m} \times 7 \mu\text{m}$, this beam is also used for stimulated Raman transitions) providing the ionizing energy.

- **Isotope selectivity** - The oven used for loading $^{171}\text{Yb}^+$ contains 90% pure 171 -isotope. The remaining is mostly $^{174}\text{Yb}^+$ isotope, 1% other isotopes of Yb and other impurities. The isotope shift between the $^{171}\text{Yb}^+$ and $^{174}\text{Yb}^+$ in the $^1S_0 - ^1P_1$ transition frequency is about 800 MHz [80], more than the power broadened transition width (about 200 MHz, found empirically). We send the ionization beams approximately perpendicular to the direction of the atomic spray from the oven (Fig. 2.2), thus eliminating first order Doppler broadening. Empirically, we load $^{171}\text{Yb}^+$

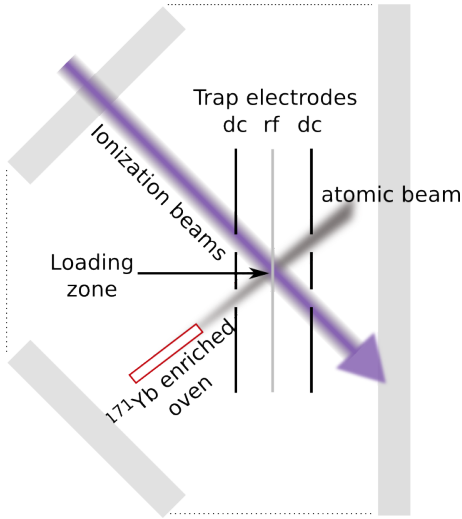


Figure 2.2: Ionization beam and oven geometry: The ionization beam is sent nearly perpendicular to the atomic beam jet sprayed from the $^{171}\text{Yb}^+$ enriched (90% isotopically pure) oven. This nearly eliminates the Doppler broadening of the $^1S_0 - ^1P_1$ transition line. The gray rectangles denote the vacuum chamber windows. This figure is not to scale.

with more than 98% success rate. While loading $^{171}\text{Yb}^+$ ions we shine the loading region with the Doppler cooling beam and the 935 nm repump (along with the two loading beams), and look for a fluorescence signal on a charged coupled device (CCD) imager. The integration time of the CCD is set to about 200 ms. A wrong isotope of Ytterbium or another atomic species does not fluoresce from the Doppler cooling beam, and appears as a dark spot in the ion chain. We experimentally find that a lower radio frequency and static voltage on the trap electrodes make the trapping easier. An additional cooling beam, called the protection beam, which is detuned from the $^2S_{1/2} \rightarrow ^2P_{1/2}$ resonance by 600 MHz is also kept on during the loading process. When we use 369.5 nm beam for the second step in the ionization, the ions load one by one, but with the 355 nm beam, multiple ions load at the same time.

- **Melting of the ion crystal and re-capturing** - One of the most important problems of dealing with a long chain of ions is collisions with background gases present in the vacuum chamber, which result in melting of the crystal. The rate of the background collisions increase with increasing system size, and is typically one melting event per five minutes on an average for a chain of 10 ions (this is approximate, we did not investigate the statistics of these collision events). Once the ion chain melts, we try to re-capture them by turning on the Doppler cooling and the protection beam, and lowering the trap depth. The radio frequency power going into the trap is lowered by about 11 dB (from 26 dBm to 15 dBm), and the average static voltage (End average DC) is reduced to about 4 Volts. These settings are empirically found. In our quantum simulation experiments, we monitor the Doppler cooling fluorescence from the ions on a PMT to check for melting. If the re-crystallization process is initiated soon enough after the melting occurs, all or most of the ions come back into the crystalline structure with a decent probability (works > 50% of the time).

2.3 Manipulation of $^{171}\text{Yb}^+$ spin and motional states

2.3.1 Hyperfine states

$^{171}\text{Yb}^+$ has a spin- $\frac{1}{2}$ nucleus, resulting in hyperfine structure in the electronic ground state. Figure 2.3 shows the fine structure levels with their hyperfine sublevels in $^{171}\text{Yb}^+$. The two hyperfine states of $^2S_{1/2}|F = 1, m_F = 0\rangle$ and $^2S_{1/2}|F = 0, m_F = 0\rangle$ form an effective spin- $\frac{1}{2}$ system, identified as $|\uparrow_z\rangle$ and $|\downarrow_z\rangle$ respectively. Here

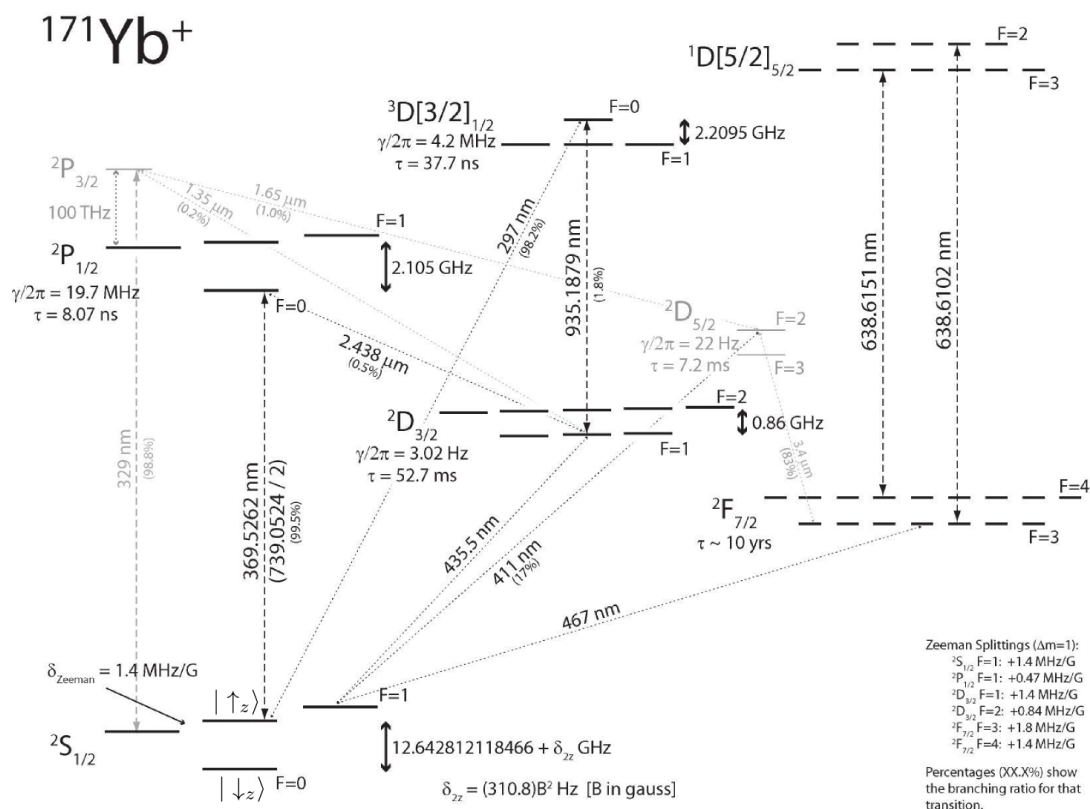


Figure 2.3: $^{171}\text{Yb}^+$ level diagram

$\hbar\sqrt{F(F+1)}$ is the total angular momentum of the atom, and $\hbar m_F$ is its projection along the quantization axis, in our experiments defined by the externally applied magnetic field of $B_Y \approx 5$ G, where $\hbar = h/2\pi$, h being the Planck's constant. *This magnetic field is not to be confused with any effective magnetic field in the spin models that we want to simulate with this system.* As we shall discuss later, we simulate the effective transverse field (B) in the quantum Ising model by laser induced stimulated Raman transitions. The spin states are not sensitive to the Zeeman shift in the leading order of the applied magnetic field B_Y , making them useful in precision atomic clocks [81]. The hyperfine frequency splitting between them is $\omega_{hf}/2\pi = 12\,642\,812\,118.5$ Hz + $B_Y^2 \times 310.8$ (Hz/G²) [82].

2.3.2 Doppler cooling

The $^{171}\text{Yb}^+$ ions are Doppler cooled on the $^2S_{1/2}-^2P_{1/2}$ line, with a Gaussian beam at a wavelength $\lambda = 369.521525$ nm, red detuned from the resonance by about 25 MHz. Each time an atom absorbs a photon, it acquires an $\hbar k$ recoil momentum from the radiation field, where \vec{k} is the momentum vector of the cooling light. When an atom moves opposite to the direction of beam propagation, *i.e.*, towards the light source, the frequency of the light as observed from the atom's rest frame is up-shifted from its laboratory frame frequency, due to the Doppler effect. Since the beam is red detuned from the $^2S_{1/2}-^2P_{1/2}$ resonance, the up-shifted frequency is closer to atomic resonance, and the atom absorbs more photons. On the other hand, when the atom moves away from the source, it sees a down-shifted frequency of the cooling beam,

and absorbs less. Thus on an average, the atom experiences more momentum kick (and more radiation pressure) while moving opposite to the beam propagation than while moving along the beam propagation direction. Thus the atom slows down, on average, by absorbing photons from the radiation field. Once in the excited state, the atom emits the photon back to the field via spontaneous emission, but this photon is emitted in a random direction with zero average momentum, and the average momentum transferred to the atom from the field vanishes. Thus the beam slows down the atom. For trapped ions, the confinement is achieved by electrical voltages, and thus Doppler cooling works provided the cooling beam couples to motion along all the principle axes.

In order to cool both the spin states ($|\uparrow_z\rangle$ and $|\downarrow_z\rangle$), we frequency modulate the Doppler cooling beam at 7.37 GHz by using an Electro Optic Modulator (EOM). The second sideband ($\approx 1\%$ of the carrier strength) generated by this EOM at 14.74 GHz couples the $^2S_{1/2}|F = 0, m_F = 0\rangle$ state (or the spin $|\downarrow_z\rangle$ state) to $^2P_{1/2}|F = 1, m_F = 0\rangle$ state. Thus both the spin states scatter from the Doppler cooling beam. The optical power in the cooling beam used is approximately 25 μW focused to a spot size of approximately $100 \mu\text{m} \times 10 \mu\text{m}$ at the ion , and we cool the ions for about 3 ms.

To efficiently cool the ion, we use an additional laser at 935.2 nm (Toptica DL-100) sent through an EOM driven at 3.07 GHz to re-pump the $^2D_{3/2}$ levels that $^2P_{1/2}$ states leak into with a probability of about 0.005 [70]. This laser pumps the atom to the $^3D[3/2]_{1/2}$ state, from which it returns promptly to the $^2S_{1/2}$ states [83], without mixing between the $|\uparrow_z\rangle$ and the $|\downarrow_z\rangle$ states, as the transition $^3D[3/2]_{1/2}|F =$

$|0, m_F = 0\rangle \rightarrow |\downarrow_z\rangle$ is forbidden. The 935 nm laser beam has about 20 mW power, and is not focused tightly (with about a few hundred microns Gaussian beam waist at the ion location) to make the alignment process easier. We frequency stabilize this laser by feeding back to the grating in the laser cavity and the diode current, using a slow software lock that compares the frequency of this laser measured by a wavemeter (WS Ultimate Precision by High Finesse GmbH) and a set frequency (320.56922 THz). This software lock is technically easier than implementing other cavity based locks, such as a Pound-Drever-Hall lock [84], and empirically found to be sufficient for the current application.

The atom may also leak into the long lived low lying $^2F_{7/2}$ states with a lifetime of about 10 yrs, presumably in a non-radiative process involving collisions with the background atoms in the vacuum chamber [85, 86], at a rate of approximately one every couple of hours for a single atom. A laser at 638.6 nm is scanned between the two transitions near the wavelengths of 638.6151 nm ($^2F_{7/2}|F = 4\rangle \rightarrow ^1D[5/2]_{5/2}|F = 3\rangle$) and 638.6102 nm ($^2F_{7/2}|F = 3\rangle \rightarrow ^1D[5/2]_{5/2}|F = 2\rangle$) (Fig. 2.3), again by using the wavemeter frequency lock.

2.3.3 Detection of the spin states

The spin states are detected by a spin dependent fluorescent technique. The spin $|\uparrow_z\rangle$ state is excited with a 369.53 nm beam, on resonance with the $^2S_{1/2}|F = 1, m_F = 0\rangle \leftrightarrow ^2P_{1/2}|F = 0, m_F = 0\rangle$ transition. Once excited to the $^2P_{1/2}|F = 0, m_F = 0\rangle$ state, the ion spontaneously decays to one of the three $^2S_{1/2}|F = 1, m_F =$

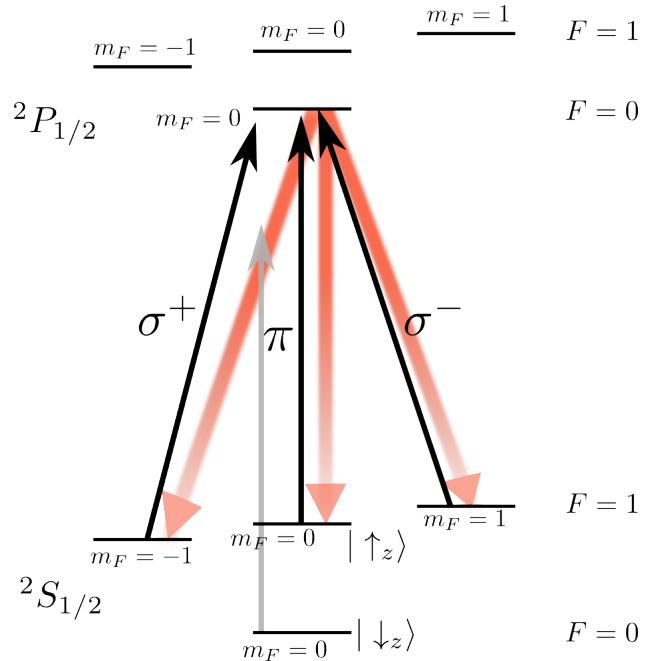


Figure 2.4: Detection of the spin states: A near resonant laser beam at 369.5 nm couples the $|\uparrow_z\rangle$ state to the $^2P_{1/2}|F=0, m_F=0\rangle$ state, which can fluoresce back into the $|\uparrow_z\rangle$ state, or to the Zeeman states $^2S_{1/2}|F=1, m_F=\pm 1\rangle$, but not to the spin $|\downarrow_z\rangle$ state. The detection beam has all the polarization components (π, σ^+, σ^-) and hence the Zeeman states are excited back to the $^2P_{1/2}|F=0, m_F=0\rangle$ state, and the atom can fluoresce again. This light appears off-resonant to the $|\downarrow_z\rangle$ state by 12.6 GHz, and hence hardly scatters from the $|\downarrow_z\rangle$ state. We collect the fluorescence by a diffraction limited optics on a PMT (Fig. 2.5) or a CCD imager. Here the solid black arrows represent stimulated absorption of the detection laser beam by the ion, and the red fuzzy lines show the spontaneous emission channels. The gray arrow shows the same detection light as appears to the $|\downarrow_z\rangle$ state (the dark state).

$|0, \pm 1\rangle$ states after about 10 ns [87]. Since ${}^2P_{1/2}|F = 0, m_F = 0\rangle \leftrightarrow {}^2S_{1/2}|F = 0, m_F = 0\rangle$ transition is forbidden by having a zero matrix element of the dipole moment operator between these two states, this forms a cycling transition, and spin state $|\uparrow_z\rangle$ (and the Zeeman states) appears as a ‘bright’ state. Figure 2.4 shows the spontaneous channels used in the detection. We collect the fluorescence with diffraction limited optics (NA=0.25) on a photomultiplier tube (PMT) or a CCD imager. The overall imaging magnification is about 130, and the set up is similar to that explained in Ref. [88]. The number of emitted photons from a bright ion in a given time interval is distributed according to a Poisson distribution. We collect about 10 photons on average with the PMT, when the detection beam is on for 800 μs .

The same beam appears off-resonant to the spin state $|\downarrow_z\rangle$, by about 12.643 GHz, and hence does not excite this state. Spin $|\downarrow_z\rangle$ appears as a ‘dark’ state on the PMT or the CCD imager.

To repump from all the Zeeman states of ${}^2S_{1/2}$ manifold, the detection beam contains all the three polarizations (π, σ^+, σ^-) w.r.t. the external magnetic field of about 5 G, required to define the quantization axis and to avoid coherent population trapping [89].

The two spin states may get mixed up if the ${}^2P_{1/2}|F = 1, m_F = 0, \pm 1\rangle$ states are populated, as they couple to both the spin states. The detection beam is 2.105 GHz detuned from the ${}^2S_{1/2}|F = 1, m_F = 0\rangle \leftrightarrow {}^2P_{1/2}|F = 1, m_F = 0, \pm 1\rangle$ states, and the probability of off-resonantly populating the states is $\approx 10^{-5}$. This off-resonant excitation alters the emitted photon histogram only slightly [90, 91]. We

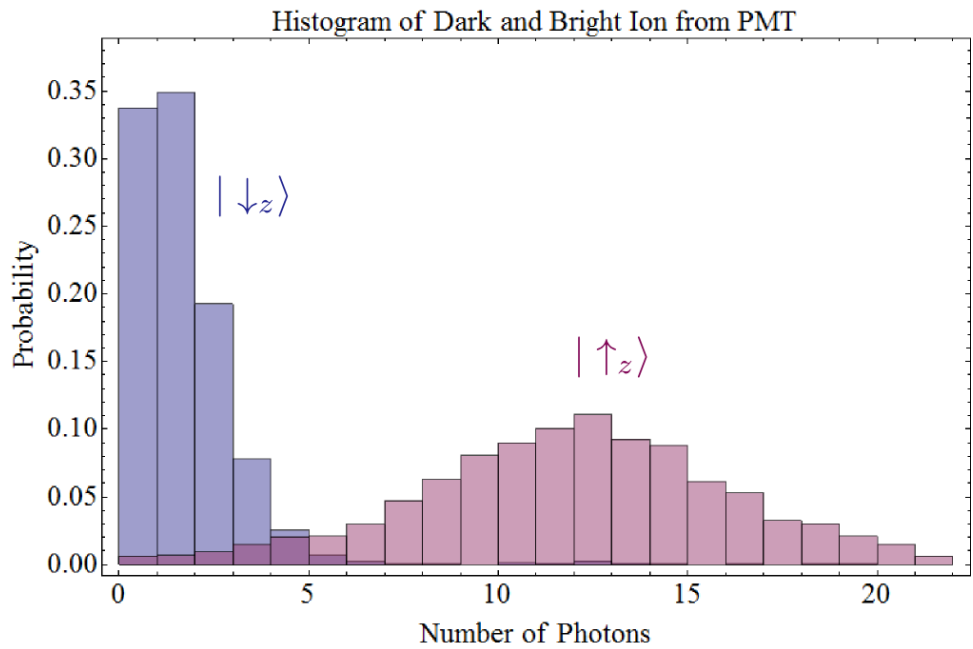


Figure 2.5: **Fluorescence histograms of the spin states:** A single $^{171}\text{Yb}^+$ ion is excited by a laser beam which is nearly on resonance with the $^2S_{1/2}|F = 1, m_F = 0\rangle \leftrightarrow ^2P_{1/2}|F = 0, m_F = 0\rangle$ transition. we collect the fluorescence of the ion on a photomultiplier tube (PMT) for $800 \mu\text{s}$. A histogram of the photon counts is shown for the bright state ($|\uparrow_z\rangle$) in red. The spin state $|\downarrow_z\rangle$ appears dark (blue histogram), as the detection laser beam is off-resonant to the $^2S_{1/2}|F = 0, m_F = 0\rangle \leftrightarrow ^2P_{1/2}|F = 0, m_F = 0\rangle$ transition. Here we prepared the dark state by optical pumping, and the bright state by applying a carrier Raman π pulse.

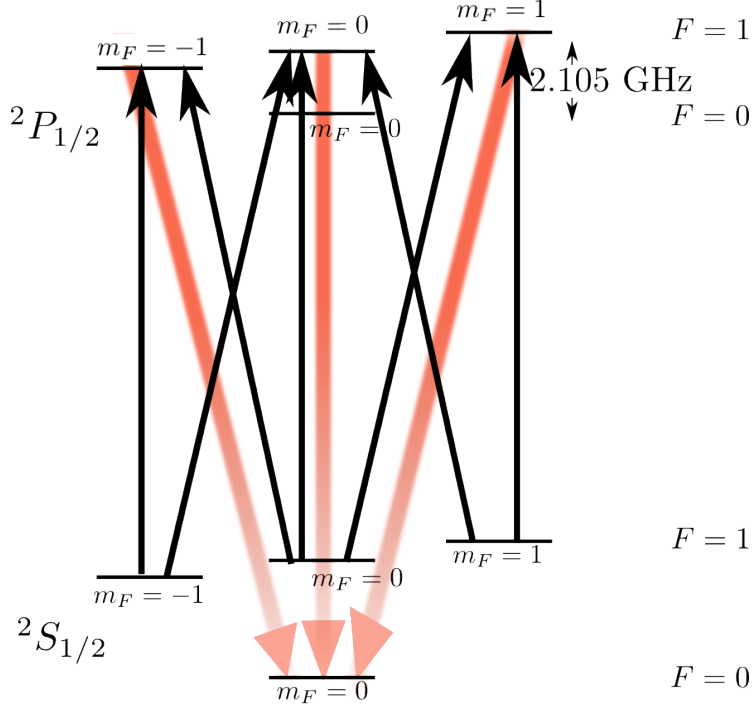


Figure 2.6: Optical pumping to the $|\downarrow_z\rangle$ state: A laser beam resonant with the $^2S_{1/2}|F=1,m_F=0\rangle \rightarrow ^2P_{1/2}|F=0,m_F=0\rangle$ (the line used for detecting the spin states, Fig. 2.4) is frequency modulated by a 2.105 GHz EOM. The first order sideband couples the $|\uparrow_z\rangle$ state to the $^2P_{1/2}|F=1,m_F=0,\pm 1\rangle$ states, that can spontaneously decay to the $|\downarrow_z\rangle$ state. The ion gets trapped in this state. Here the solid black lines represent stimulated absorption of the detection laser beam by the ion, and the red fuzzy lines show the spontaneous emission channels. We have only shown the stimulated absorption and spontaneous emission channels responsible for trapping the system in the dark state, and not shown any decay into the bright states.

get a spin detection fidelity of $\approx 98.5\%$ by a PMT, and about 93% by a CCD imager. The reduced fidelity with the CCD imager is primarily due to the presence of electronic noise on the CCD [91].

2.3.4 State initialization by optical pumping

The spin state of an ion is initialized in the $|\downarrow_z\rangle$ state by an incoherent optical pumping technique. For this, we frequency modulate the beam on resonance with

the $^2S_{1/2}|F = 1, m_F = 0\rangle \leftrightarrow ^2P_{1/2}|F = 0, m_F = 0\rangle$ transition by 2.105 GHz using an EOM. The first order sideband generated by the EOM couples the $^2S_{1/2}|F = 1, m_F = 0\rangle$ state to the $^2P_{1/2}|F = 1, m_F = 0, \pm 1\rangle$ states, which can decay into the spin $|\downarrow_z\rangle$ state (Fig. 2.6). Once the atom is in the $|\downarrow_z\rangle$ state, the optical beam is off-resonant from the $^2P_{1/2}$ states by 12.643 GHz, and hence hardly scatters, and gets trapped in that state. The probability of trapping into this dark state increases with number of scattering events, and eventually almost all the population is transferred to the spin $|\downarrow_z\rangle$ state. In our set up, the optical pumping efficiency is more than 99% for a 3 μs optical pumping time.

2.3.5 Coherent manipulation of the spin states

Once the pure state $|\downarrow_z\rangle$ is prepared using spontaneous emission induced optical pumping, it can be coherently manipulated either with microwave magnetic fields or with two photon laser induced stimulated Raman coupling. Microwave radiation couples to the magnetic dipole moment matrix element between two states, and induces coherent Rabi oscillations between them. While microwave radiation has been used to perform quantum information experiments in $^{171}\text{Yb}^+$, it is not ideal for quantum simulation of spin models, as the spin interactions are mediated by the phonon modes, and the microwave field does not have sufficient momentum to excite the vibrational modes of an ion chain.

We use stimulated Raman transition induced by optical fields for coherent manipulation of spins. The laser field couples the spin states to an excited state

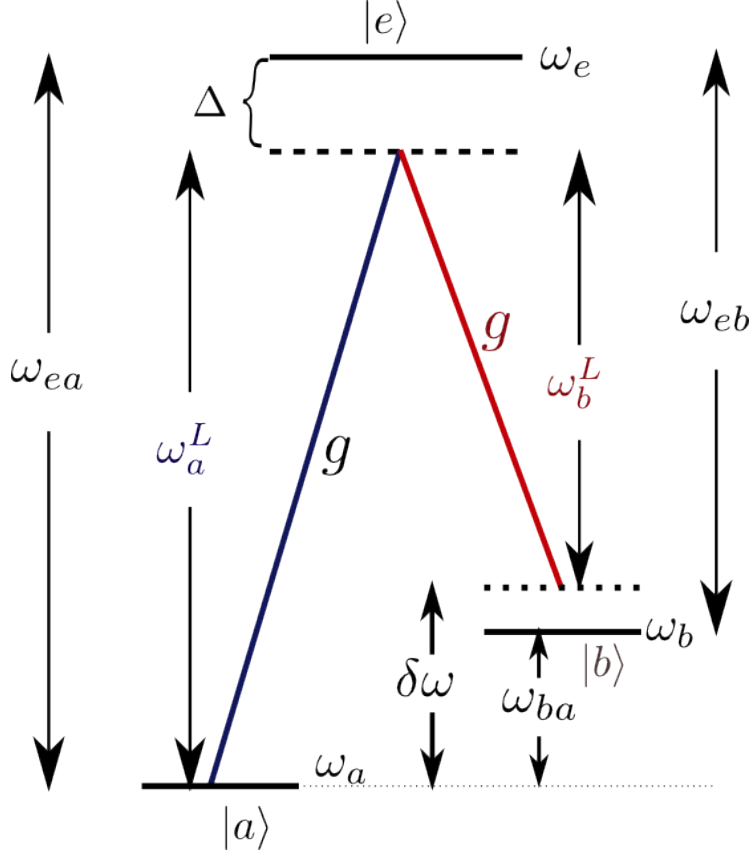


Figure 2.7: Two photon stimulated Raman transition in a Λ -system: Two laser beams with frequencies ω_a^L and ω_b^L off-resonantly couple the low lying energy states $|a\rangle$ and $|b\rangle$ to the excited state $|e\rangle$, with single photon Rabi frequencies g (defined in the text). If the system initially is in one of the states $|a\rangle$ or $|b\rangle$, and the detuning Δ from the excited state is much larger than the Rabi frequency g , this system can be approximated as a two level system, with coherent Rabi flopping between the states $|a\rangle$ and $|b\rangle$ at a rate $\Omega = g^*g/2\Delta$.

(${}^2P_{1/2}$ states). In order to understand the physics of two photon stimulated Raman transition, let's consider a Λ -system, shown in Fig. 2.7. The low lying energy states $|a\rangle$ and $|b\rangle$ with energies $\hbar\omega_a$ and $\hbar\omega_b$ respectively are coupled to the excited state $|e\rangle$ via the two continuous wave (CW) laser fields at frequencies ω_a^L and ω_b^L , that are detuned from the excited states by a frequency Δ .

We define,

$$\omega_{ea} \equiv \omega_e - \omega_a \quad (2.9a)$$

$$\omega_{eb} \equiv \omega_e - \omega_b \quad (2.9b)$$

$$\omega_{ba} \equiv \omega_b - \omega_a \quad (2.9c)$$

From Fig. 2.7, we get the relation between the frequencies,

$$\omega_{ea} - \omega_a^L = \Delta \quad (2.10a)$$

$$\omega_{ea} - \omega_b^L = \Delta + \delta\omega \quad (2.10b)$$

$$\omega_{eb} - \omega_a^L = \Delta - \omega_{ba} \quad (2.10c)$$

$$\omega_{eb} - \omega_b^L = \Delta + \delta\omega - \omega_{ba}. \quad (2.10d)$$

In the absence of the coupling fields, the atomic Hamiltonian ($\hbar = 1$) is,

$$H_0 = \omega_a |a\rangle\langle a| + \omega_b |b\rangle\langle b| + \omega_e |e\rangle\langle e|. \quad (2.11)$$

Let us assume that the wavefunction at time t ,

$$\psi(t) = C_a(t)|a\rangle + C_b(t)|b\rangle + C_e(t)|e\rangle. \quad (2.12)$$

Schrödinger's equation $i\frac{\partial\psi}{\partial t} = H_0\psi$ gives us,

$$C_\alpha(t) = C_\alpha(0)e^{-i\omega_\alpha t} \quad (\alpha = a, b, e) \quad (2.13)$$

where the coefficients $C_\alpha(0)$ are integration constants obtained from the initial conditions. The interaction Hamiltonian between the laser field and the atom is [92],

$$\begin{aligned} H_I &= -\mu \cdot E(t) \\ &= -\left[\mu_{ae}|a\rangle\langle e| + \mu_{ea}|e\rangle\langle a| + \mu_{be}|b\rangle\langle e| \right. \\ &\quad \left. + \mu_{eb}|e\rangle\langle b| \right] \mathcal{E}_0 \left[\cos(\omega_a^L t) + \cos(\omega_b^L t) \right]. \end{aligned} \quad (2.14)$$

Here $E(t)$ is the total electric field. Both the laser fields are assumed to have the same electric field amplitude, \mathcal{E}_0 . We ignore the spatially varying term (kX) and the off-set in the phases of the electric fields for now, and treat the problem in one dimension. Here μ is the dipole moment of the atom, with the matrix elements,

$$\mu_{ae} = \langle a | \mu | e \rangle \quad (2.15a)$$

$$\mu_{be} = \langle b | \mu | e \rangle \quad (2.15b)$$

$$\mu_{ea} = \mu_{ae}^* = \langle e | \mu | a \rangle \quad (2.15c)$$

$$\mu_{eb} = \mu_{be}^* = \langle e | \mu | b \rangle. \quad (2.15d)$$

We get the relations connecting $C_a(t)$, $C_b(t)$ and $C_e(t)$ in Eq. (2.12) by equating the coefficients of $|\alpha\rangle$ ($\alpha = a, b, e$) on both sides of the Schrödinger's equation,

$i\frac{\partial\psi(t)}{\partial t} = (H_0 + H_I)\psi(t)$ to each other,

$$i\dot{C}_a(t) = \omega_a C_a(t) - g C_e(t) \left[\cos(\omega_a^L t) + \cos(\omega_b^L t + \phi) \right] \quad (2.16a)$$

$$i\dot{C}_b(t) = \omega_b C_b(t) - g C_e(t) \left[\cos(\omega_a^L t) + \cos(\omega_b^L t + \phi) \right] \quad (2.16b)$$

$$i\dot{C}_e(t) = \omega_e C_e(t) - g^* \left[C_a(t) + C_b(t) \right] \left[\cos(\omega_a^L t) + \cos(\omega_b^L t + \phi) \right], \quad (2.16c)$$

where the single photon Rabi frequency, $g = \mu_{ae}\mathcal{E}_0 = \mu_{be}\mathcal{E}_0$, assuming $\mu_{ae} = \mu_{be}$. We want to see how the interaction Hamiltonian modifies Eqs. (2.13). Thus, we define the slowly varying amplitudes $\tilde{C}_a(t)$, $\tilde{C}_b(t)$ and $\tilde{C}_e(t)$ through the equations

$$C_\alpha(t) \equiv \tilde{C}_\alpha(t) e^{-i\omega_\alpha t} \quad (\alpha = a, b, e). \quad (2.17)$$

Note that for $H_I = 0$, $\tilde{C}_\alpha(t) = C_\alpha(0)$ ($\alpha = a, b, e$).

We use Eqs. (2.17) in Eqs. (2.16), expand the cosine terms to get the relations between $\tilde{C}_a(t)$, $\tilde{C}_b(t)$ and $\tilde{C}_e(t)$,

$$i\dot{\tilde{C}}_a(t) = \frac{g}{2} \tilde{C}_e(t) e^{-i\omega_{ea}t} \left[e^{i\omega_a^L t} + e^{-i\omega_a^L t} + e^{i\omega_b^L t} + e^{-i\omega_b^L t} \right] \quad (2.18a)$$

$$i\dot{\tilde{C}}_b(t) = \frac{g}{2} \tilde{C}_e(t) e^{-i\omega_{eb}t} \left[e^{i\omega_a^L t} + e^{-i\omega_a^L t} + e^{i\omega_b^L t} + e^{-i\omega_b^L t} \right] \quad (2.18b)$$

$$i\dot{\tilde{C}}_e(t) = \frac{g^*}{2} \left[\tilde{C}_a(t) e^{i\omega_{ea}t} + \tilde{C}_b(t) e^{i\omega_{eb}t} \right] \left[e^{i\omega_a^L t} + e^{-i\omega_a^L t} + e^{i\omega_b^L t} + e^{-i\omega_b^L t} \right]. \quad (2.18c)$$

Next, we make a rotating wave approximation (RWA), where we ignore fast oscillating terms in the exponentials, by neglecting exponents that involve a sum of two large (optical) frequencies. Using Eqs. (2.10) in Eqs. (2.18), we get, after

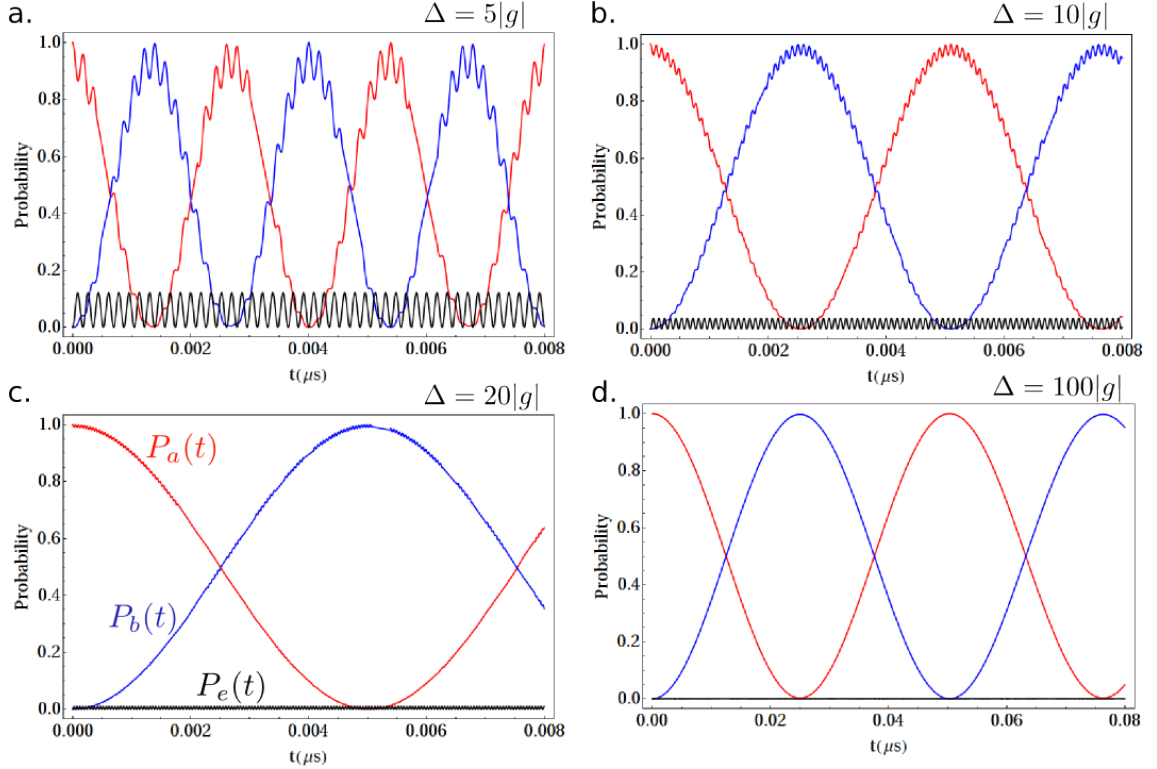


Figure 2.8: Adiabatic elimination of the excited state: Solution of Eqs. (2.19) for **a.** $\Delta = 5|g|$, **b.** $\Delta = 10|g|$, **c.** $\Delta = 20|g|$ **d.** $\Delta = 100|g|$. The red curve shows the probability that the system will be in state $|a\rangle$ at time t , $P_a(t) = |\tilde{C}_a(t)|^2 = |C_a(t)|^2$, similarly the blue and the black curves show $P_b(t)$ and $P_e(t)$. The curves are obtained by numerically solving the differential equations (Eqs. (2.19)) by Wolfram Mathematica, with the initial conditions $\tilde{C}_a(0) = 1, \tilde{C}_b(0) = 0, \tilde{C}_e(0) = 0$. The frequency splitting ω_{ba} between the states $|a\rangle$ and $|b\rangle$ is assumed to be very small compared to g and Δ . As the detuning Δ is increased compared to the single photon Rabi frequency g , the three level Λ -system behaves more like a two level system, composed of the low lying states $|a\rangle$ and $|b\rangle$.

RWA,

$$i\dot{\tilde{C}}_a(t) = \frac{g}{2}\tilde{C}_e(t) [e^{-i\Delta t} + e^{-i(\Delta+\delta\omega)t}] \quad (2.19a)$$

$$i\dot{\tilde{C}}_b(t) = \frac{g}{2}\tilde{C}_e(t) [e^{-i(\Delta-\omega_{ba})t} + e^{-i(\Delta-\omega_{ba}+\delta\omega)t}] \quad (2.19b)$$

$$i\dot{\tilde{C}}_e(t) = \frac{g^*}{2} [\tilde{C}_a(t) [e^{i\Delta t} + e^{i(\Delta+\delta\omega)t}] + \tilde{C}_b(t) [e^{i(\Delta-\omega_{ba})t} + e^{i(\Delta-\omega_{ba}+\delta\omega)t}]] \quad (2.19c)$$

These coupled differential equations can be numerically solved on a computer.

Fig 2.8 shows the time evolution of the co-efficients $|\tilde{C}_\alpha(t)|^2$ ($\alpha = a, b, e$) for four different ratios of $\Delta/|g|$ (we set $\omega_{ba} = \delta\omega = 0$ in this calculations), with the initial conditions, $\tilde{C}_a(0) = 1, \tilde{C}_b(0) = 0, \tilde{C}_e(0) = 0$.

- **Adiabatic elimination of the excited state** - Since the states $|a\rangle$ and $|b\rangle$ are not connected directly by a field, we expect the coefficients $\tilde{C}_a(t)$ and $\tilde{C}_b(t)$ to vary much more slowly compared to the exponentials in Eq. (2.19c) ($\Delta \gg |g|$).

Thus we integrate Eq. (2.19c), keeping $\tilde{C}_a(t)$ and $\tilde{C}_b(t)$ constant,

$$\begin{aligned}
\tilde{C}_e(t) &\approx -\frac{i}{2}g^* \left[\tilde{C}_a(t) \left[\int_0^t e^{i\Delta t} dt + \int_0^t e^{i(\Delta+\delta\omega)t} dt \right] \right. \\
&\quad \left. + \tilde{C}_b(t) \left[\int_0^t e^{i(\Delta-\omega_{ba})t} dt + \int_0^t e^{i(\Delta-\omega_{ba}+\delta\omega)t} dt \right] \right] \\
&= -\frac{i}{2}g^* \left[\tilde{C}_a(t) \left[\frac{e^{i\Delta t} - 1}{\Delta} + \frac{e^{i(\Delta+\delta\omega)t} - 1}{\Delta + \delta\omega} \right] \right. \\
&\quad \left. + \tilde{C}_b(t) \left[\frac{e^{i(\Delta-\omega_{ba})t} - 1}{\Delta - \omega_{ba}} + \frac{e^{i(\Delta-\omega_{ba}+\delta\omega)t} - 1}{\Delta - \omega_{ba} + \delta\omega} \right] \right] \\
&\approx -\frac{g^*}{2\Delta} \left[\tilde{C}_a(t) \left[e^{i\Delta t} + e^{i(\Delta+\delta\omega)t} - 2 \right] \right. \\
&\quad \left. + \tilde{C}_b(t) \left[e^{i(\Delta-\omega_{ba})t} + e^{i(\Delta-\omega_{ba}+\delta\omega)t} - 2 \right] \right]. \tag{2.20}
\end{aligned}$$

In the last line, we have approximated all the denominators by Δ , as $\Delta \gg \omega_{ba}, \delta\omega$.

Using Eq. (2.20) in Eq. (2.19a), we get,

$$\begin{aligned}
\dot{\tilde{C}}_a(t) &= i \frac{|g|^2}{4\Delta} \left[e^{-i\Delta t} + e^{-i(\Delta+\delta\omega)t} \right] \left[\tilde{C}_a(t) \left[e^{i\Delta t} + e^{i(\Delta+\delta\omega)t} - 2 \right] \right. \\
&\quad \left. + \tilde{C}_b(t) \left[e^{i(\Delta-\omega_{ba})t} + e^{i(\Delta-\omega_{ba}+\delta\omega)t} - 2 \right] \right] \\
&= i \frac{|g|^2}{4\Delta} \left[\tilde{C}_a(t) \left[2 + e^{i\delta\omega t} + e^{-i\delta\omega t} - 2e^{-i\Delta t} - 2e^{-i(\Delta+\delta\omega)t} \right] \right. \\
&\quad \left. + \tilde{C}_b(t) \left[2e^{-i\omega_{ba}t} + e^{-i(\omega_{ba}-\delta\omega)t} + e^{-i(\omega_{ba}+\delta\omega)t} - 2e^{-i\Delta t} - 2e^{-i(\Delta+\delta\omega)t} \right] \right] \\
&\approx i \frac{|g|^2}{4\Delta} \left[\tilde{C}_a(t) \left[2 + e^{i\delta\omega t} + e^{-i\delta\omega t} \right] \right. \\
&\quad \left. + \tilde{C}_b(t) \left[2e^{-i\omega_{ba}t} + e^{-i(\omega_{ba}-\delta\omega)t} + e^{-i(\omega_{ba}+\delta\omega)t} \right] \right], \tag{2.21}
\end{aligned}$$

where we have thrown out the fast oscillating terms $e^{-i\Delta t}$ and $e^{-i(\Delta+\delta\omega)t}$, as they average out to zero over a time period of oscillations of the other terms. Eq. (2.21) involves only the two states $|a\rangle$ and $|b\rangle$ and looks similar to Eq. (2.16a). We can further apply RWA to Eq. (2.21), and ignore terms that are oscillating at ω_{ba} and $\delta\omega$. This is a good approximation for the hyperfine transition between the $^{171}\text{Yb}^+$ $|\uparrow_z\rangle$ and $|\downarrow_z\rangle$ states, as $\omega_{ba} = \omega_{hf} \approx \delta\omega = 2\pi \times 12.6$ GHz, and $|g|^2/2\Delta \approx 2\pi \times 1$ MHz. Thus Eq. (2.21) becomes,

$$\dot{\tilde{C}}_a(t) \approx i \frac{|g|^2}{2\Delta} \tilde{C}_a(t) + i \frac{1}{2} \frac{|g|^2}{2\Delta} \tilde{C}_b(t) e^{-i(\omega_{ba}-\delta\omega)t}. \quad (2.22)$$

Similarly the coefficient for $|b\rangle$ obeys the equation,

$$\dot{\tilde{C}}_b(t) \approx i \frac{|g|^2}{2\Delta} \tilde{C}_b(t) + i \frac{1}{2} \frac{|g|^2}{2\Delta} \tilde{C}_a(t) e^{i(\omega_{ba}-\delta\omega)t}. \quad (2.23)$$

Eqs. (2.22) and (2.23) describe the dynamics of the two level system composed of the states $|a\rangle$ and $|b\rangle$ under the effective Hamiltonian,

$$\begin{aligned} H_{eff} &= -\frac{|g|^2}{2\Delta} |a\rangle\langle a| - \frac{|g|^2}{2\Delta} |b\rangle\langle b| - \frac{|g|^2}{4\Delta} e^{-i(\Delta\mathbf{k}\cdot\mathbf{r} + [\omega_{ba}-\delta\omega]t - \phi)} |a\rangle\langle b| \\ &\quad - \frac{|g|^2}{4\Delta} e^{i(\Delta\mathbf{k}\cdot\mathbf{r} + [\omega_{ba}-\delta\omega]t - \phi)} |b\rangle\langle a| \\ &= -\frac{|g|^2}{2\Delta} \mathbb{I} - \frac{\Omega}{2} e^{-i(\Delta\mathbf{k}\cdot\mathbf{r} + [\omega_{ba}-\delta\omega]t - \phi)} \sigma^- - \frac{\Omega}{2} e^{i(\Delta\mathbf{k}\cdot\mathbf{r} + [\omega_{ba}-\delta\omega]t - \phi)} \sigma^+. \end{aligned} \quad (2.24)$$

Now, we have inserted the spatial dependence and an offset phase ϕ in the phases. Here, $\Delta\mathbf{k}$ is the difference in momenta of the laser beams, and \mathbf{r} is the atom's

position vector. $\sigma^+ = |b\rangle\langle a|$ and $\sigma^- = |a\rangle\langle b|$ are the atomic raising and lowering operators.

In the last line of Eq. (2.24), we identify the two photon A.C. Stark shift of each of the states $|a\rangle$ and $|b\rangle$ as $-|g|^2/2\Delta$ ($-|g|^2/4\Delta$ from each of the beams), and the two photon Rabi oscillation strength as $\Omega = |g|^2/2\Delta$. For lasers with unequal intensities, and hence unequal single photon Rabi frequencies g_1 and g_2 , the two photon Rabi frequency $\Omega = \frac{g_1^* g_2}{4\Delta} + \frac{g_1 g_2^*}{4\Delta}$.

- **The differential A.C. Stark shift** - The A.C. Stark shift Eq. (2.24) is negative as the detuning is negative in Fig. 2.7 (we use Δ to denote the absolute value here.) Note that the differential A.C. Stark shift between the states $|a\rangle$ and $|b\rangle$ cancels to the leading order in $1/\Delta$. This is due to approximating all the denominators in the second sub-equation of Eq. (2.20) as Δ . The leading non-zero order in the differential A.C. Stark shift between the two states can be found by treating the beams separately. The two photon A.C. Stark shift on state $|\alpha\rangle$ ($\alpha = a, b$) measures the strength of $|\alpha\rangle \rightarrow |e\rangle \rightarrow |\alpha\rangle$ transition, where the intermediate state $|e\rangle$ is only virtually excited, since $\Delta \gg |g|$. The A.C. Stark shift experienced by the state $|a\rangle$ from the beam with frequency ω_a^L is $\Omega_a = -|g|^2/4\Delta$, and the A.C. Stark shift experienced by the state $|b\rangle$ from the same beam is $\Omega_b = -|g|^2/4(\Delta - \omega_{ba})$.

The differential A.C. Stark shift

$$\begin{aligned}
\Omega_{AC} &= \Omega_b - \Omega_a \\
&= -\frac{|g|^2}{4(\Delta - \omega_{ba})} + \frac{|g|^2}{4\Delta} \\
&= -\frac{|g|^2}{4\Delta} \left[\frac{1}{1 - \omega_{ba}/\Delta} - 1 \right] \\
&= -\frac{|g|^2}{2\Delta} \left[\left(1 + \frac{\omega_{ba}}{\Delta} - 1 \right) \right] \\
&= -\omega_{ba} \frac{|g|^2}{4} \frac{1}{\Delta^2}.
\end{aligned} \tag{2.25}$$

Note that

- $\Omega_{AC} < 0$, i.e., the states $|a\rangle$ and $|b\rangle$ get closer together while interacting with the beams.
- $\Omega_{AC} \propto |g|^2 \propto I$, where I is the intensity of the beam.
- $\Omega_{AC} \propto \frac{1}{\Delta^2}$, while the two photon Rabi frequency $\Omega \propto \frac{1}{\Delta}$. Thus the ratio of the differential A.C. Stark shift to the Rabi frequency can be reduced by increasing the detuning Δ .
- The two photon differential A.C. Stark shift, Ω_{AC} is independent of the sign of the detuning Δ , as $\Omega_{AC} \propto \frac{1}{\Delta^2}$. As an example, we can show that for $\omega_a^L > \omega_{ea}$ (Fig. 2.7), the differential A.C. Stark shift $\Omega_{AC} = \frac{|g|^2}{\Delta + \omega_{ba}} - \frac{|g|^2}{\Delta} < 0$, same as when $\omega_a^L < \omega_{ea}$. *Thus, the differential A.C. Stark shift from different levels do not cancel each other.*

The differential A.C. Stark shift can be nulled by going to a rotating frame

at frequency Ω_{AC} , which means that we adjust the beat-note frequency of the two lasers to account for the shift in the $|a\rangle \leftrightarrow |b\rangle$ resonance due to the Stark shift.

- **Hyperfine carrier transition** - In our experiment, the states $|a\rangle$ and $|b\rangle$ refer to the spin states $|\downarrow_z\rangle$ and $|\uparrow_z\rangle$ respectively, and hence $\omega_{ba} = \omega_{hf}$ is the hyperfine splitting. (we assume that we have already accounted for the differential A.C. Stark shift in defining ω_{hf}). For the resonant (or near resonant) hyperfine transition, the motional state of the ion is unchanged. Thus $\Delta\mathbf{k}\cdot\mathbf{r}$ in the phase in Eq. (2.24) is a constant *c*-number, and can be absorbed in ϕ . Setting $dw = \omega_{hf} + \delta_{carr}$, we get the effective Hamiltonian for the spin flip, or the carrier transition,

$$H_{carr} = -\frac{\Omega}{2} (\sigma^+ e^{-i(\delta_{carr}t+\phi)} + \sigma^- e^{i(\delta_{carr}t+\phi)}) , \quad [\text{Carrier}] \quad (2.26)$$

For $\delta_{carr} = 0$, Eq. (2.26) generates the resonant carrier transition between the spin states, at a Rabi rate of Ω . The phase ϕ sets the ‘axis of rotation’ of the spin vector.

$$\begin{aligned} H_{carr} &= -\frac{\Omega}{2} (\sigma^+ e^{-i\phi} + \sigma^- e^{i\phi}) \\ &= -\frac{\Omega}{2} \left(\frac{1}{2}[\sigma_x + i\sigma_y]e^{-i\phi} + \frac{1}{2}[\sigma_x - i\sigma_y]e^{i\phi} \right) \\ &= -\frac{\Omega}{2} \left(\sigma_x \left[\frac{e^{i\phi} + e^{-i\phi}}{2} \right] - i\sigma_y \left[\frac{e^{i\phi} - e^{-i\phi}}{2} \right] \right) \\ &= -\frac{\Omega}{2} (\sigma_x \cos \phi + \sigma_y \sin \phi) \\ &= -\frac{\Omega}{2} \sigma_\phi, \end{aligned} \quad (2.27)$$

where $\sigma_\phi \equiv \cos \phi \ \sigma_x + \sin \phi \ \sigma_y$. Thus the effective Hamiltonian is $-\frac{\Omega}{2} \sigma_x$ for $\phi = 0$

and $-\frac{\Omega}{2}\sigma_y$ for $\phi = \pi/2$. The unitary evolution operator of this Hamiltonian acts on the spin state $|\downarrow_z\rangle$ according to

$$\begin{aligned}
U(t)|\downarrow_z\rangle &= e^{-iH_{car}t}|\downarrow_z\rangle \\
&= e^{i\frac{\Omega t}{2}\sigma_\phi}|\downarrow_z\rangle \\
&= \left(\cos\frac{\Omega t}{2}\mathbb{I} + i\sin\frac{\Omega t}{2}\sigma_\phi\right)|\downarrow_z\rangle \\
&= \cos\frac{\Omega t}{2}|\downarrow_z\rangle + ie^{i\phi}\sin\frac{\Omega t}{2}|\uparrow_z\rangle.
\end{aligned} \tag{2.28}$$

The spin state precesses between $|\downarrow_z\rangle$ and $|\uparrow_z\rangle$ at a rate $\Omega/2$, with a phase ϕ . Note that the population precesses at a rate of Ω , as the probability of detecting $|\uparrow_z\rangle$ at time t is $P_{\uparrow_z}(t) = \sin^2\Omega t/2 = (1 - \sin\Omega t)/2$.

- **The Bloch Sphere** - The state of a two level system can be represented as a vector, called the Bloch vector moving on the surface of a sphere, known as the Bloch sphere. Two angles (θ, ϕ) completely specify a general state $|\psi(\theta, \phi)\rangle = \cos\frac{\theta}{2}|\downarrow_z\rangle + ie^{i\phi}\sin\frac{\theta}{2}|\uparrow_z\rangle$ of the two level system. The action of the unitary operator $U(t)$ on the Bloch vector is specified in terms of the rotation operator $R(\theta, \phi) = e^{-i\frac{\theta}{2}\sigma_\phi} = \cos\frac{\theta}{2}\mathbb{I} - i\sin\frac{\theta}{2}\sigma_\phi$. For a resonant carrier transition $\theta(t) = \Omega t$.

- **$\pi/2$ pulse** - A resonant Raman carrier transition of duration $\tau_{\pi/2}$ is known as a $\pi/2$ pulse if

$$\begin{aligned}
\theta(\tau_{\pi/2}) &= \pi/2 \\
\Rightarrow \tau_{\pi/2} &= \frac{\pi}{2\Omega}.
\end{aligned} \tag{2.29}$$

Under a $\pi/2$ pulse, the state $|\downarrow_z\rangle$ transforms to $|\downarrow_z\rangle - ie^{i\phi}|\uparrow_z\rangle$, and the state $|\uparrow_z\rangle$ transforms to $|\uparrow_z\rangle - ie^{i\phi}|\downarrow_z\rangle$.

- **π pulse** - A Raman carrier pulse of duration $\tau_\pi = \pi/\Omega$ is known as a π pulse. It flips the spin states, $|\downarrow_z\rangle \rightarrow -ie^{i\phi}|\uparrow_z\rangle$, $|\uparrow_z\rangle \rightarrow -ie^{i\phi}|\downarrow_z\rangle$.

- **Effective magnetic field** - From Eq. (2.28), we see that a Bloch vector precesses about the axis set by the Bloch vector angle ϕ under a resonant carrier transition. Thus the resonant transition simulates an effective magnetic field, and the phase ϕ sets the direction of it. In our experiment, we control the carrier Rabi frequency Ω (by varying the intensity or $|g|^2$) to control the magnitude of this effective field.

In our trapped $^{171}\text{Yb}^+$ system, the spin states $|\uparrow_z\rangle$ and $|\downarrow_z\rangle$ are coupled through the excited $^2P_{1/2}$ and $^2P_{3/2}$ states. We create the beat-note at $\delta\omega = \omega_{hf}$ by sending a CW laser beam through an electro optic modulator (EOM) that generates frequency modulated sidebands near ω_{hf} . Another way is to use the frequency comb generated by a mode-locked laser. We describe the operation of the mode-locked laser used in our experiment in section 2.6.4. Typical order of magnitude for the single photon Rabi frequency, $g/2\pi$ in our experiment is 1 GHz, and the detuning $\Delta/2\pi$ from the excited $^2P_{1/2}$ states range from 2.7 THz to 33 THz for two different lasers used. Fig 2.9 shows Rabi oscillation between the two spin states.

- **Ramsey interferometry** - The coherence time of the spin states is estimated by a standard Ramsey interferometric technique. A single spin is first prepared in the optically pumped state $|\downarrow_z\rangle$. Then a $\pi/2$ pulse is applied with a phase ϕ , either by a microwave or by the stimulated carrier Raman transition

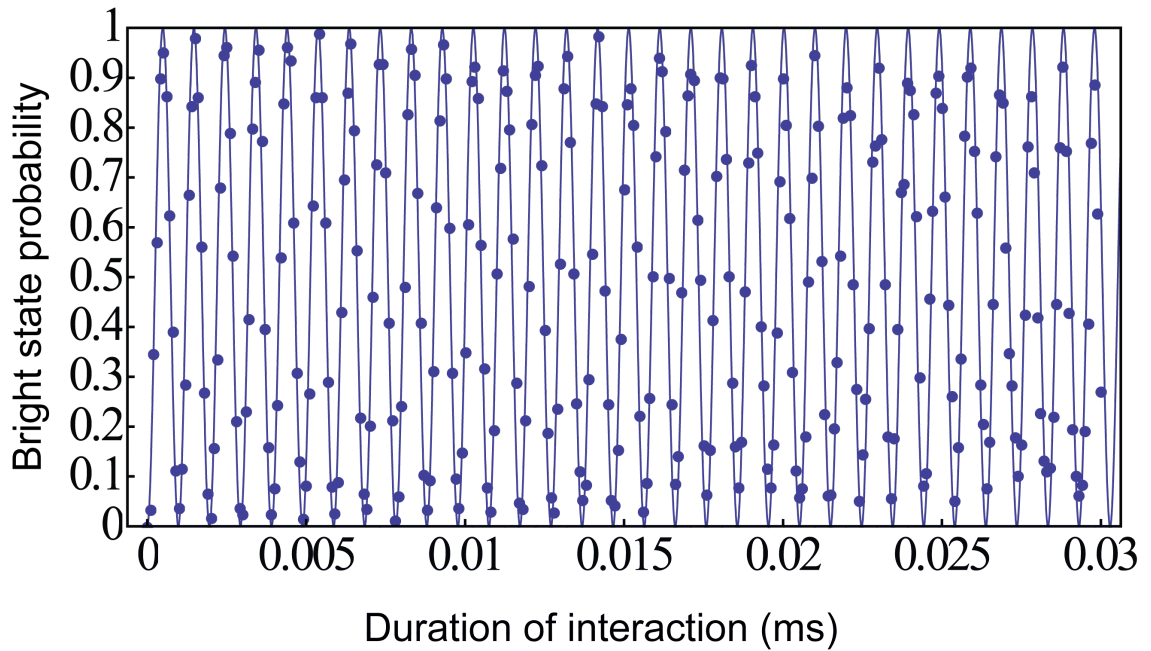


Figure 2.9: Resonant hyperfine (Carrier) Rabi oscillations in $^{171}\text{Yb}^+$ spin states: Two level Rabi oscillation between the spin $|\uparrow_z\rangle$ and $|\downarrow_z\rangle$ states of a single spin induced by two photon stimulated Raman transition from 355 nm laser light. The blue curve is a sinusoidal fit to the data (blue points), and its frequency is about $2\pi \times 1$ MHz. The spin is first prepared in the optically pumped $|\downarrow_z\rangle$ state. Each point is an average over about 200 experimental points.

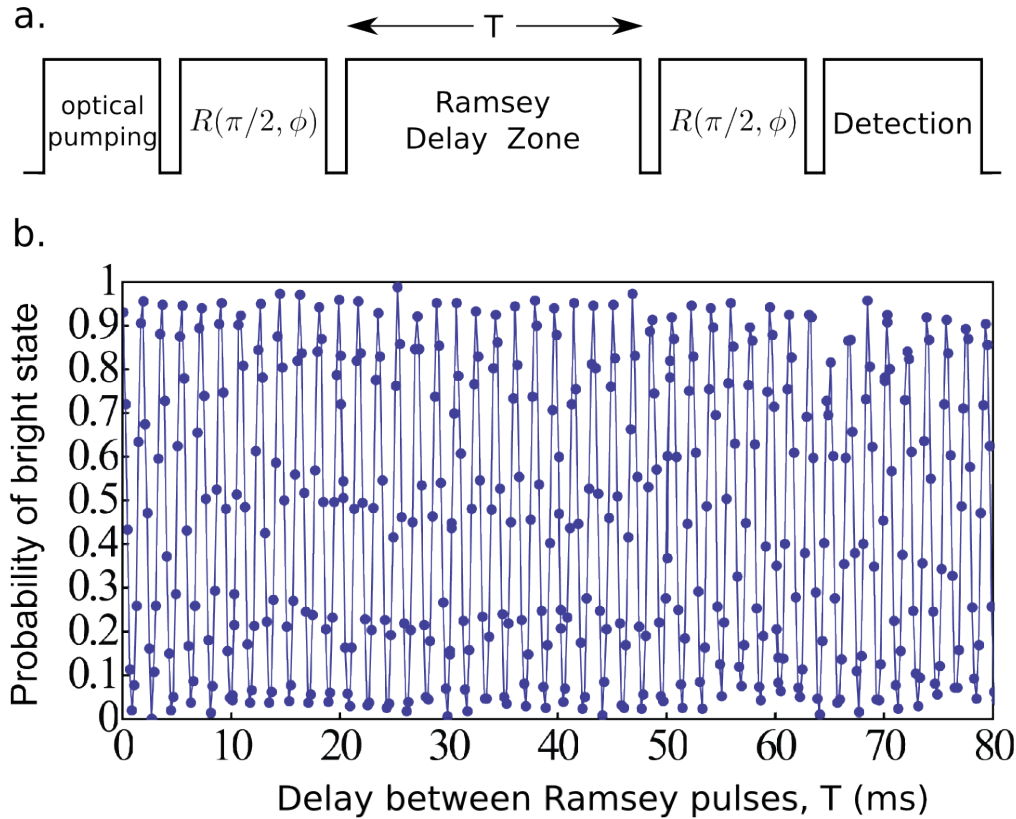


Figure 2.10: **Ramsey interferometry in a $^{171}\text{Yb}^+$ ion:** The oscillation in the probability of the spin states at the frequency difference between the oscillator driving the $\pi/2$ pulses and the atomic transition frequency denotes the coherence present in the spin states or the qubits. The $\pi/2$ pulses are provided by microwave radiation from a microwave horn antenna at 12.642819 GHz. The dots are data, and the solid line is a sinusoid fit with an exponential decay in amplitude. The decoherence time is estimated to be more than 800 ms from this data.

at frequency ω_{osc} , followed by a delay. Finally another $\pi/2$ pulse is applied from the same oscillator, and at the same phase, and the spin state is detected. This method compares the two clocks, namely the hyperfine splitting of the ion, and the oscillator used to drive the $\pi/2$ pulses. As the duration of the delay is scanned, a fringe is obtained in the observed probability of the bright state ($|\uparrow_z\rangle$) at frequency $|\omega_{osc} - \omega_{hf}|$, where ω_{hf} is the hyperfine frequency. Fig 2.10 shows the experimental sequence and a typical Ramsey fringe data in the experiment.

- **Coupling to the motional states** - The carrier transition flips the spin from $|\downarrow_z, n\rangle$ to the $|\uparrow_z, n\rangle$ state (n represents the number of vibrational quanta in a given mode), and does not change the phonon excitations in the system. To excite the vibrational mode at frequency ω_X along with the spin flip (we assume that the Raman beat-note momentum $\Delta\mathbf{k}$ is along the X -direction), we set the detuning $\delta\omega$ in Eq. (2.24) to $\delta\omega = \omega_{hf} + \omega_X + \delta$. We assume that the temperature of the ion is cold enough so that the motion can be expressed in terms of the vibrational mode phonon annihilation (\hat{a}) and the creation (\hat{a}^\dagger) operators, and the position coordinate $X(t)$ can be written as,

$$\hat{X}(t) = X_0 \left(\hat{a} e^{-i\omega_X t} + \hat{a}^\dagger e^{i\omega_X t} \right). \quad (2.30)$$

$X_0 = \sqrt{\frac{\hbar}{2m\omega_X}}$ is the characteristic length scale of the motional mode.

Thus the effective Hamiltonian of Eq. (2.24), ignoring the constant A.C. Stark

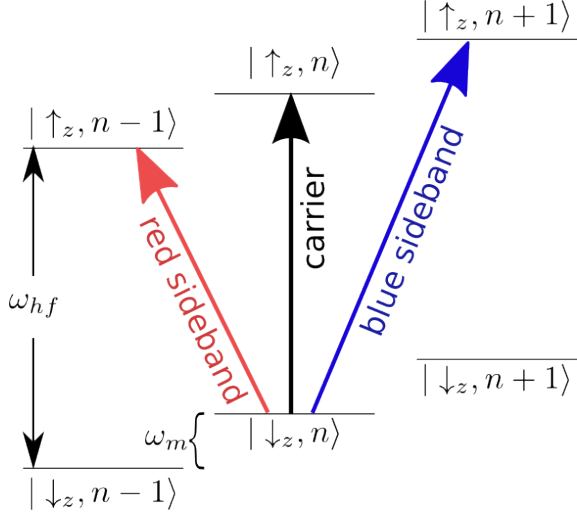


Figure 2.11: **Carrier and sideband transitions:** The harmonic oscillator energy ladder with the spin states (not to scale). A carrier transition induces coherent oscillation between the spin states without any change in the motional state, a blue sideband transition is higher in energy than a carrier transition, and involves the $|\downarrow_z, n\rangle \leftrightarrow |\uparrow_z, n+1\rangle$ transition. The red sideband transition is lower in energy than the carrier, and induces coherent oscillation between $|\downarrow_z, n\rangle \leftrightarrow |\uparrow_z, n-1\rangle$.

shift becomes,

$$\begin{aligned}
H_{bsb} &= -\frac{\Omega}{2}e^{-i(\Delta\mathbf{k}\cdot\mathbf{r} + [\omega_{ba} - \delta\omega]t - \phi)}\sigma^- - \frac{\Omega}{2}e^{i(\Delta\mathbf{k}\cdot\mathbf{r} + [\omega_{ba} - \delta\omega]t - \phi)}\sigma^+ \\
&= -\frac{\Omega}{2}e^{-i(\Delta k X_0 [ae^{-i\omega_X t} + a^\dagger e^{i\omega_X t}] - [\omega_X + \delta]t - \phi)}\sigma^- \\
&\quad - \frac{\Omega}{2}e^{i(\Delta k X_0 [ae^{-i\omega_X t} + a^\dagger e^{i\omega_X t}] - [\omega_X + \delta]t - \phi)}\sigma^+ \\
&\approx -\frac{\Omega}{2} [1 - i\eta[ae^{-i\omega_X t} + a^\dagger e^{i\omega_X t}]] e^{i[(\omega_X + \delta)t + \phi]} \sigma^- \\
&\quad - \frac{\Omega}{2} [1 + i\eta[ae^{-i\omega_X t} + a^\dagger e^{i\omega_X t}]] e^{-i[(\omega_X + \delta)t + \phi]} \sigma^+ \\
&\approx i\frac{\eta\Omega}{2} [a\sigma^- e^{i(\delta t + \phi)} - a^\dagger\sigma^+ e^{-i(\delta t + \phi)}], \quad [\text{blue side band}] \quad (2.31)
\end{aligned}$$

where we have expanded the exponential up to first order in the dimensionless

Lamb-Dicke parameter $\eta \equiv \Delta k X_0 \ll 1$ in the third line*, and used the RWA to throw away terms rotating at or near ω_X in the last line. H_{bsb} makes the transition $|\downarrow_z, n\rangle \leftrightarrow |\uparrow_z, n+1\rangle$, which is higher in energy than the carrier transition. For $\delta = 0$, this results in a resonant stimulated Raman blue sideband transition.

Similarly, if we set the beat-note between the lasers $\delta\omega = \omega_{hf} - \omega_X - \delta$, we get a stimulated Raman red sideband transition, with the effective Hamiltonian,

$$H_{rsb} = i \frac{\eta\Omega}{2} [a^\dagger \sigma^- e^{-i(\delta t - \phi)} - a \sigma^+ e^{i(\delta t - \phi)}], \quad [\text{red side band}] \quad (2.32)$$

We see that the transition strength between the states $|\downarrow_z, n-1\rangle$ and $|\uparrow_z, n\rangle$ is $\eta\Omega\sqrt{n}$, where the factor of \sqrt{n} is contributed by the creation operator ($\hat{a}^\dagger|n-1\rangle = \sqrt{n}|n\rangle$). Fig 2.11 illustrates the carrier, red sideband and the blue sideband processes.

2.3.6 Raman sideband cooling

Doppler cooling brings the average phonon occupation to $\bar{n} = \frac{\Gamma}{2\omega_m}$, where Γ is the natural linewidth of the cooling transition. The ions can be further cooled by mapping the motional degree of freedom to the spins, and then removing the spin entropy from the system by the optical pumping technique, described previously.

Fig 2.12 describes the Raman cooling scheme. Let us assume that a single ion is in the Fock state $|\downarrow_z, n\rangle$. We apply a red sideband π pulse, which annihilates a

*More rigorously, the exponential can be expanded if $\langle \Delta k X \rangle$ is small. This is equivalent to the Lamb-Dicke approximation $\eta\sqrt{n+1} \ll 1$. In our system $\eta \approx 0.06$ and average phonon occupation is < 3 after the Doppler cooling, and < 0.1 after side band cooling (the X -vibrational mode). Thus the Lamb-Dicke approximation holds good.

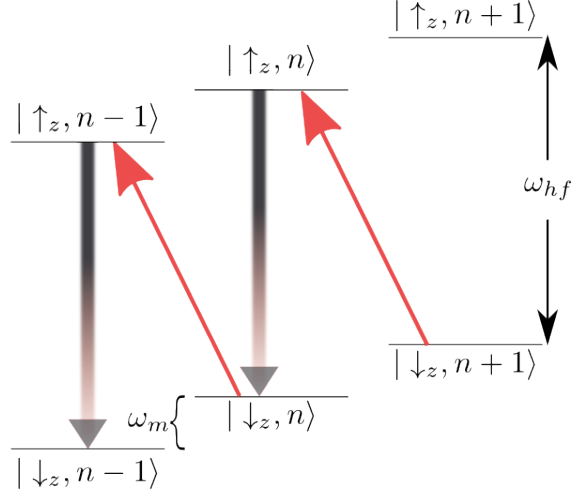


Figure 2.12: **Raman sideband cooling:** The spin system is initialized in the optical pumped state, *i.e.*, in the spin state $|\downarrow_z, n\rangle$, where n denotes the motional state of a vibrational mode with frequency ω_m . A red sideband π pulse (solid red arrow) transfers the spin to the $|\uparrow_z, n - 1\rangle$ state, and annihilates a phonon. This is followed by an optical pumping pulse (gray fuzzy line), which flips the spin back to the $|\downarrow_z\rangle$ state. This process is repeated, and the system rolls down the harmonic oscillator ladder, until it reaches $n = 0$.

phonon, while flipping the spin, *i.e.*, it takes the system to the state $|\uparrow_z, n - 1\rangle$.

We then optically pump the spin to $|\downarrow_z, n - 1\rangle$ state without changing the motional state, and thus extract a quantum of vibration from the system. This process can be repeated to reach the motional ground state. Since the strength of the sideband Rabi frequency depends on the motional state, the duration of the π pulse has to be adjusted accordingly. In our set up, we apply about 30 pulses to cool the COM mode to near zero point motion.

2.4 Vibrational normal modes of trapped ions

The confining potential created by the static and ponderomotive electric forces try to bring the ions closer together at the trap center. The Coulomb repulsion

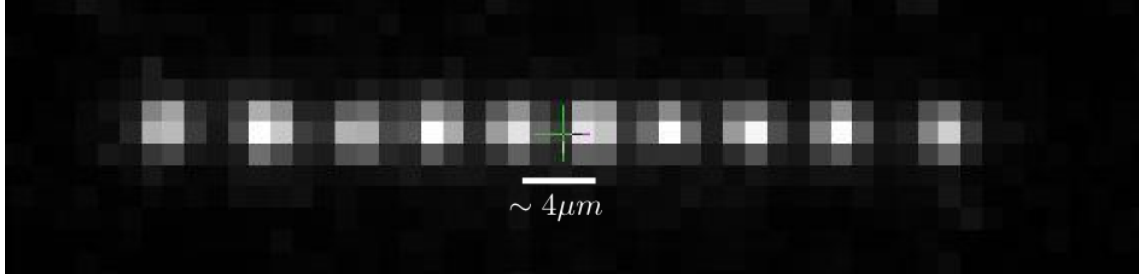


Figure 2.13: Image of ten bright $^{171}\text{Yb}^+$ ions in a linear configuration: Fluorescence light of ten $^{171}\text{Yb}^+$ ions, induced by the Doppler cooling beam, is captured by the imaging optics, and the signal is integrated for about 200 ms on a CCD camera. The ions form a linear configuration due to the high anisotropy in the trapping potential. The plus sign in the middle of the chain is a cursor used on the camera interface.

between the ions tend to push them away from each other. A compromise between the attractive and the repulsive components is reached when the ions are at a certain distance apart from each other, and they form a Coulomb crystal. In order to avoid micromotion, we make the trap anisotropic with $\omega_X \approx \omega_Y \gg \omega_Z$, so that the ions form a linear crystal along the Z -axis, and lie on the radio-frequency null in the trap.

Figure 2.13 shows a crystal of ten $^{171}\text{Yb}^+$ ions held in a linear configuration. The spacing between the ions in a crystal depend on the axial confinement strength (characterized by the secular frequency, ω_Z) and the number of ions, and varies between 2 and 5 microns for the range of trap settings used in our experiments.

A small perturbation from the equilibrium positions of the ions makes them oscillate about the equilibrium. In general the ions oscillate in complicated patterns, but any oscillation of the system (with small amplitudes) can be Fourier decomposed into collective vibrational modes, known as the normal modes of vibration [93]. For

a system of N ions, there are N normal modes along each of the three dimensions.

The nature of the axial and the transverse normal modes are very different in a Coulomb crystal.

- **Axial Normal modes** - The axial normal modes are lower in frequency compared to the transverse modes, due to the anisotropy in the trapping potential required to keep the ions in a linear configuration. The lowest mode is the center of mass (COM) mode, at a frequency of ω_Z independent of the number of ions N . All the ions move back and forth uniformly in this mode, with an eigenvector component of $1/\sqrt{N}$ for all the ions. The COM mode has the longest spatial wavelength. The next mode is the ‘breathing’ mode, with a frequency of $\sqrt{3}\omega_Z$ independent of the number of ions, N . The frequencies of the axial normal modes increase monotonically with decreasing wavelength.

- **Transverse Normal modes** - The transverse normal modes are higher in frequency due to stronger confinement along the transverse direction, and bunched closer together compared to the axial modes. Contrary to the axial vibrational motion, the transverse COM modes (at frequencies ω_X and ω_Y for all N) have the highest frequencies among all the modes along that specific transverse direction. In our trap, the X -modes are slightly higher in frequency than the Y -modes, and the splitting between the X and Y -COM modes depends on the axial confinement. For a stronger axial confinement, the X and Y -COM modes are separated more. The next lower frequency mode is the ‘tilt’ mode, where the two halves of the chain oscillate with opposite phases, and the amplitude of vibration increases away from

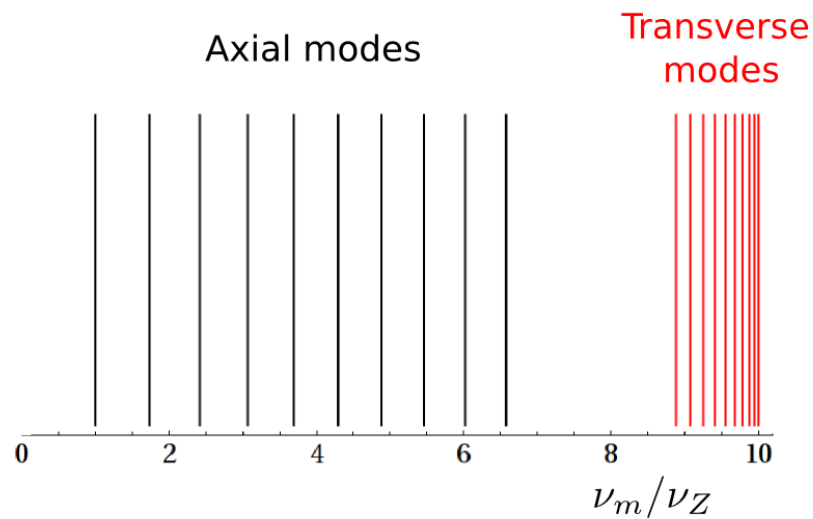


Figure 2.14: Axial and transverse vibrational modes of trapped ions: Frequencies of the Axial and the transverse modes (along the X -direction) of $N = 10$ trapped ions, for a trap anisotropy of $\beta_X = 10$. Each solid line represents a normal mode at frequency ν_m . The horizontal axis shows the ratio of the mode frequencies to the axial COM frequency. The Axial modes (black) are almost equispaced, but the transverse modes (red) are not. They are closely bunched together at the high frequencies. The axial COM mode is the *lowest* in frequency of all the axial modes, while the transverse COM mode is the highest in frequency of all the transverse modes.

the center of the chain. This mode occurs at a frequency of

$$\omega_{tilt} = \sqrt{\omega_X^2 - \omega_Z^2} \quad (2.33)$$

for all N . For an odd system size, the center ion does not take part in this mode. As we shall discuss later, the spin interactions in our simulated Ising Hamiltonian are mediated by the phonons [71], and the center spin does not interact with any other spin if only the tilt mode is used to generate the interactions in a system with odd number of ions. The frequencies of the transverse normal modes decrease monotonically with decreasing wavelength, and hence the transverse modes show anomalous dispersion.

As seen from Eq. (2.33), the splitting between the COM and the tilt modes is dependent on the axial confinement. In general the bandwidth of the transverse modes increases with increasing axial confinement. Fig 2.14 compares the axial and the X -transverse modes for an anisotropy $\beta_X = 10$. While the neighboring axial modes maintain an almost fixed separation in frequency, the transverse modes are bunched together, especially at the higher frequencies. Figure 2.15 shows the eigenvectors of the transverse normal modes for a system of 10 ions.

- **Transition to a zig-zag configuration** - As the anisotropy in the trapping potential, defined by the dimensionless parameters, $\beta_X = \frac{\omega_X}{\omega_Z}$ and $\beta_Y = \frac{\omega_Y}{\omega_Z}$ is decreased, by increasing the axial confinement strength keeping the transverse confinement fixed, the ions come closer to each other, and the bandwidth of the transverse vibrational modes increases.

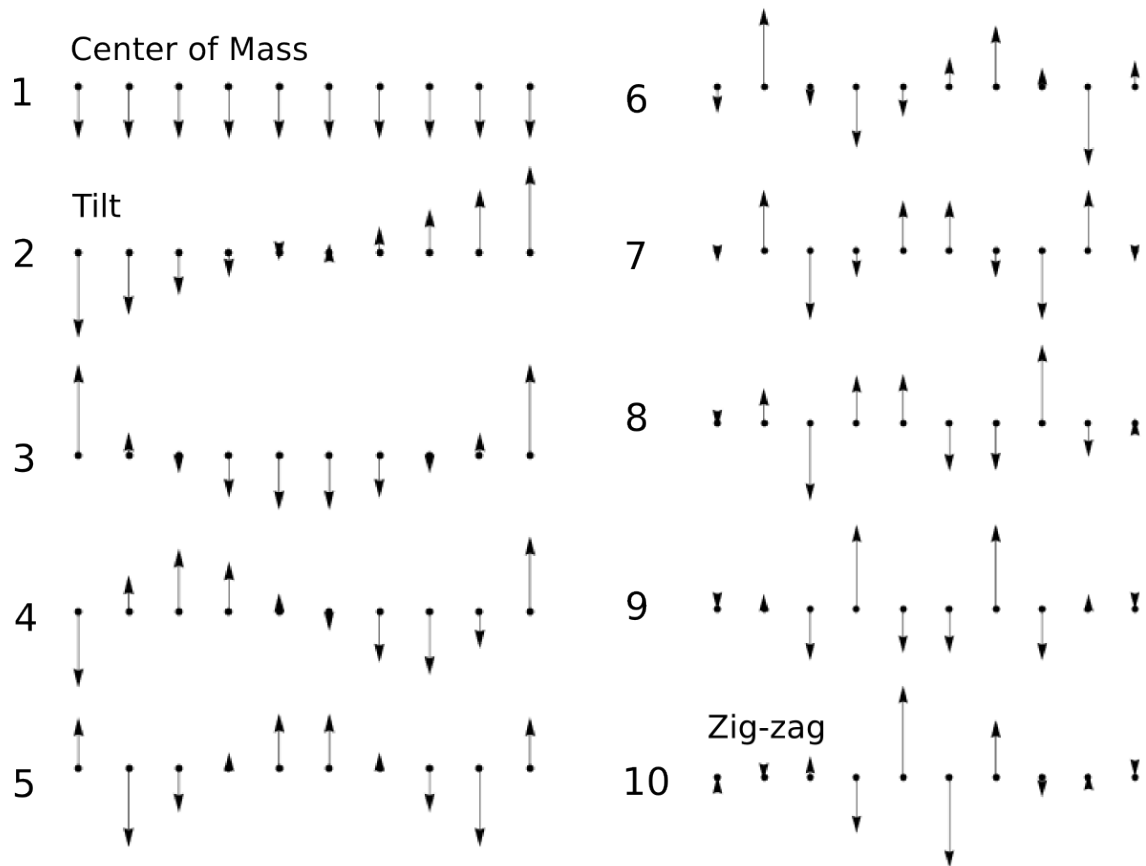


Figure 2.15: **Transverse mode eigenvectors for $N = 10$ ions:** The dots represent the equilibrium position of the ions, and the arrows represent the eigenvector components for the mode (enumerated on the left). The simulated Ising coupling between spins i and j depend on the product of the eigenvector components of the normal mode(s) excited to generate the spin interactions, according to Eq. (2.53).

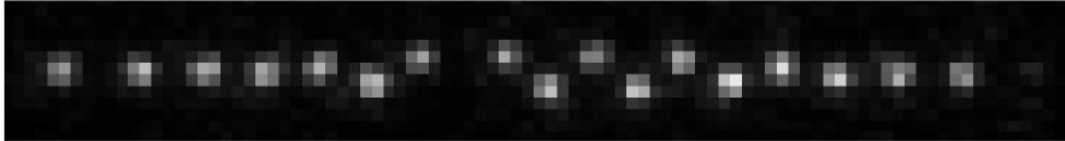


Figure 2.16: Nineteen ions in a zig-zag configuration: The ion chain undergoes a structural phase transition from a linear configuration to a zig-zag configuration at a certain trap anisotropy. The central region of the chain undergoes this transition before the outer region. The 8th ion from the left is either another isotope of Yb⁺ or another species, and hence it does not fluoresce from the cooling and detection beams. The low fluoresce count from the rightmost ion is due to the finite aperture size of a pinhole used in the imaging system. This configuration of the ions is equal in energy to its spatially reflected (about the Z -axis of the chain) configuration. These two configurations are referred to as the ‘zig’ and the ‘zag’ configurations.

Eventually, the frequency of the smallest wavelength mode, the zig-zag vibrational mode reaches zero and the ion chain undergoes a structural phase transition to a zig-zag configuration [94, 95]. This structural phase transition occurs at approximately $\beta_{X,Y} = \frac{\omega_{X,Y}}{\omega_Z} = 0.73N^{0.86}$, as found numerically [96]. For a large system ($N \gg 1$), the transition point can be found analytically [95] as $\beta_{X,Y} = \frac{\omega_{X,Y}}{\omega_Z} = 0.77\frac{N}{\sqrt{\log N}}$. Ions near the center of the chain are closely packed together compared to the ions near the edge, and these central ions break into the zig-zag configuration before the others. In our trap the Y vibrational modes are slightly lower in frequencies than the respective X vibrational modes, and hence the zig-zag transition occurs in the Y -direction first, as the axial confinement strength is tuned keeping the transverse frequencies the same. For slightly tighter confinement along the axial direction, the X zig-zag mode reaches zero frequency as well, as the ions form a helix in the $X - Y$ plain. The zig-zag vibrational mode must not be

confused with the zig-zag configuration, the former is a pattern of vibration where the equilibrium positions of the ions are still on a one dimensional chain, while in the latter the equilibrium position of the ions form a zig-zag configuration resulting in an entirely new set of vibrational modes.

In the zig-zag phase, there are two degenerate configurations for the ions, the ‘zig’ and the ‘zag’ configurations forming a double well potential. This opens up the possibility of observing many interesting physical phenomena, such as simulating non-linear lattice models, the defect formation while traversing a phase transition (Kibble-Zurek mechanism [97, 98]), and coherent tunneling between the two wells in the double well potential [99].

2.5 Simulating the quantum Ising model

In this work, we simulate the quantum Ising model, with the Hamiltonian,

$$H = \sum_{i=1}^N \sum_{j=1}^{i-1} J_{i,j} \sigma_x^i \sigma_x^j + B \sum_{i=1}^N \sigma_y^i, \quad (2.34)$$

where $J_{i,j}$ is the Ising coupling between the spins i and j ($i, j = 1, 2, \dots, N$), B is an effective transverse magnetic field, and σ_α 's are the spin- $\frac{1}{2}$ Pauli matrices ($\alpha = x, y, z$). As described previously, a resonant carrier transition between the spin states $|\uparrow_z\rangle$ and $|\downarrow_z\rangle$ with a phase $\phi = \pi/2$ in Eq. (2.26) acts as an effective transverse magnetic field. In this section we describe the simulation of the Ising interactions.

2.5.1 Ising interactions

The ising interactions are simulated by following Mølmer-Sørensen scheme [71], where we apply Raman laser beams to excite the vibrational modes off-resonantly. Figure 2.17 shows the schematics of a Mølmer-Sørensen transition, in the case of two spins interacting through a single vibrational mode at frequency $\omega_m = 2\pi\nu_m$. Two laser beat-notes are applied, with their frequencies symmetrically detuned from the carrier. We shall call these beat-notes **bsb** and **rsb**, tuned near a blue sideband transition and a red sideband transition with frequencies $\nu_{hf} \pm \mu$ respectively. We also define the Mølmer-Sørensen detuning $\delta \equiv \mu - \nu_m$.

Let's focus on the spin state $|\downarrow_z\downarrow_z, n\rangle$. If it absorbs a **rsb** photon, it may get off-resonantly excited to the state $|\uparrow_z\downarrow_z, n-1\rangle$ or $|\downarrow_z\uparrow_z, n-1\rangle$ with equal probabilities. Since the frequencies of the **rsb** and the **bsb** add up to $2\nu_{hf}$, it may make a transition to the $|\uparrow_z\uparrow_z, n\rangle$ by absorbing a **bsb** photon. If the Mølmer-Sørensen detuning δ is kept larger than the sideband Rabi frequency $\eta\Omega\sqrt{n}$, the intermediate single spin excited states can be adiabatically eliminated, and the amplitude of the $|\downarrow_z\downarrow_z, n\rangle \rightarrow |\uparrow_z\uparrow_z, n\rangle$ transition is

$$\begin{aligned}\Omega_{|\downarrow_z\downarrow_z, n\rangle \rightarrow |\uparrow_z\uparrow_z, n\rangle, \text{path 1}} &= \frac{\Omega_{|\downarrow_z\downarrow_z, n\rangle \rightarrow |\uparrow_z\downarrow_z, n-1\rangle} \Omega_{|\uparrow_z\downarrow_z, n-1\rangle \rightarrow |\uparrow_z\uparrow_z, n\rangle}}{-4\delta} \\ &= \frac{(\eta\Omega\sqrt{n})(\eta\Omega\sqrt{n})}{-4\delta} \\ &= -n \frac{(\eta\Omega)^2}{4\delta}. \end{aligned} \tag{2.35}$$

Here the minus sign denotes that the Raman beat-note is tuned red to the red

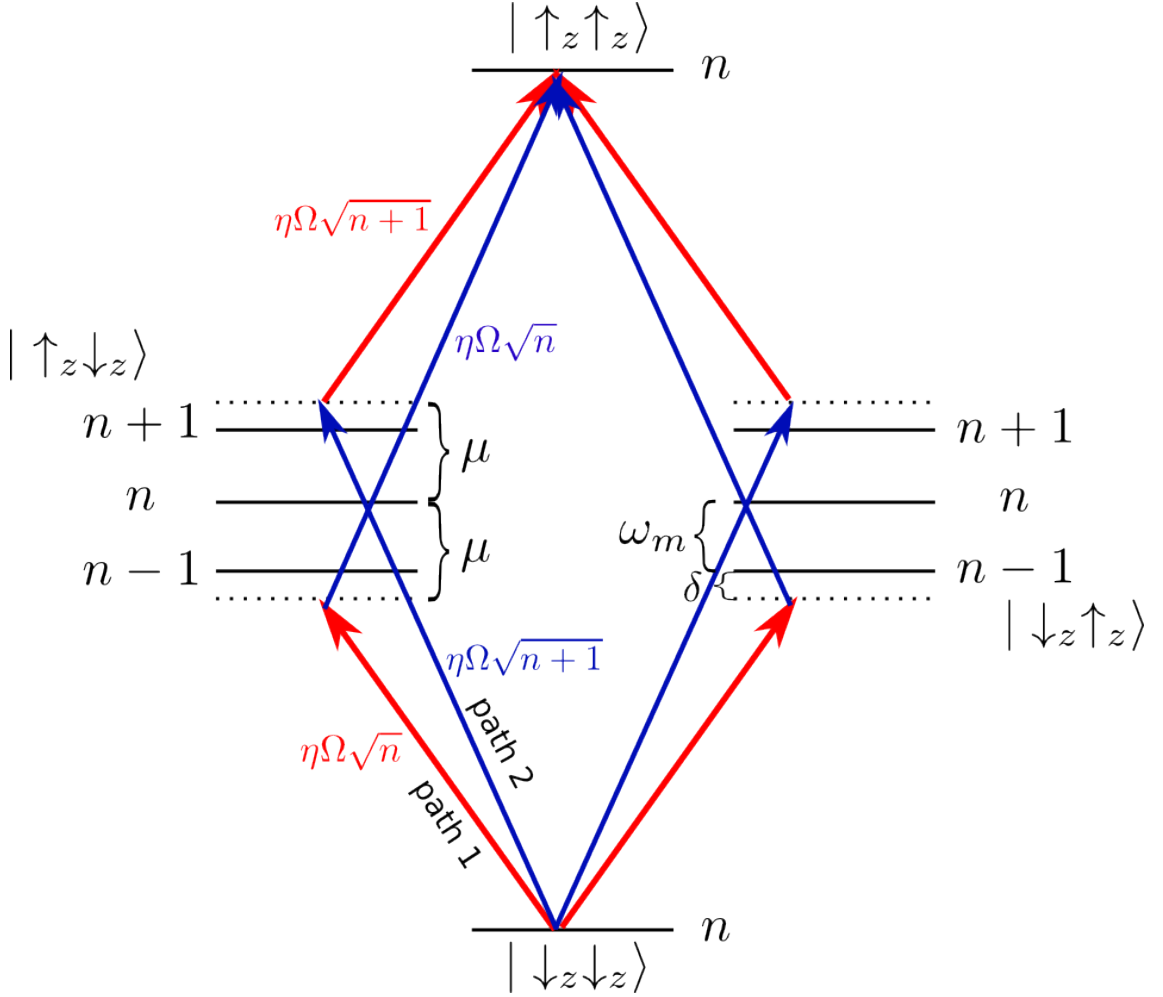


Figure 2.17: **Mølmer-Sørensen transition in a system of two spins:** Off-resonant red and blue sidebands, symmetrically detuned about the carrier transition simulate the two body spin interactions in our experiment [71]. Here we show the spin and the relevant motional states (labeled by the number of phonon n). The red (blue) solid lines show an off-resonant red (blue) sideband transition. The four different pathways connecting $|\downarrow z \downarrow z, n\rangle \rightarrow |\uparrow z \uparrow z, n\rangle$ partially interfere destructively to cancel the dependence on the phonon quantum number n , resulting in a pure spin model in the Lamb-Dicke limit. The Raman beat-note frequency μ controls the nature of the Ising couplings, as discussed in the text.

sideband transition. This amplitude interferes with another path where the spins first absorb a photon from the **bsb** beam, and then from the **rsb** beam, and makes a transition to the $|\uparrow_z\uparrow_z, n\rangle$ state with an amplitude

$$\begin{aligned}\Omega_{|\downarrow_z\downarrow_z, n\rangle \rightarrow |\uparrow_z\uparrow_z, n\rangle, \text{path 2}} &= \frac{\Omega_{|\downarrow_z\downarrow_z, n\rangle \rightarrow |\uparrow_z\downarrow_z, n+1\rangle} \Omega_{|\uparrow_z\downarrow_z, n+1\rangle \rightarrow |\uparrow_z\uparrow_z, n\rangle}}{4\delta} \\ &= \frac{(\eta\Omega\sqrt{n+1})(\eta\Omega\sqrt{n+1})}{-4\delta} \\ &= (n+1) \frac{(\eta\Omega)^2}{4\delta}.\end{aligned}\quad (2.36)$$

Thus the total amplitude from these two paths becomes,

$$\Omega_{\text{path } 1,2} = \frac{(\eta\Omega)^2(n+1)}{4\delta} - \frac{(\eta\Omega)^2n}{4\delta} = \frac{(\eta\Omega)^2}{4\delta}. \quad (2.37)$$

Similarly there are two more paths where the second spin absorbs the **rsb** and the **bsb** photons first, and they add an equal contribution as $\Omega_{\text{path } 1,2}$ to the overall Ising amplitude. From Eq. (2.37) we see that the amplitude of the $|\downarrow_z\downarrow_z, n\rangle \rightarrow |\uparrow_z\uparrow_z, n\rangle$ is independent of the motional state n , as long as the intermediate states with $n-1$ and $n+1$ photons are not populated, resulting in a pure spin Hamiltonian,

$$H_{\text{Ising},\text{eff}} = J_{1,2}\sigma_\phi^1\sigma_\phi^2, \quad (2.38)$$

where $J_{1,2} = (\eta\Omega)^2/2\delta$ is the total amplitude from the interference of all the paths, and is the Ising coupling between the two spins. Here $\sigma_\phi = \cos\phi\sigma_x + \sin\phi\sigma_y$, and hence by properly choosing ϕ by adjusting the beat-note phase of the Raman beams,

we generate a $\sigma_x\sigma_x$ interaction between the spins.

If we include the off-resonant excitation of the blue sideband from the **rsb** beam and the off-resonant excitation of the red sideband from the **bsb** beams, the effective Ising coupling $J_{i,j}$ becomes,

$$\begin{aligned} J_{i,j} &= \frac{(\eta\Omega)^2}{2(\mu - \omega_m)} - \frac{(\eta\Omega)^2}{2(\mu + \omega_m)} \\ &= \frac{(\eta\Omega)^2\omega_m}{\mu^2 - \omega_m^2}. \end{aligned} \quad (2.39)$$

Contribution from off-resonant carrier transitions from the **bsb** and the **rsb** beams cancel between path 1 and path 2.

- **Alternative derivation** - We may get the effective Ising Hamiltonian starting from the effective Hamiltonians for the red sideband and the blue sideband, Eqs. (2.32) and (2.31). We shall get an expression for the effective Hamiltonian for N spins, subject to a red sideband beat-note at a frequency $\omega_{hf} - \mu$ with a phase $\phi = \phi_r$ and a blue sideband beat-note at $\omega_{hf} + \mu$ with a phase $\phi = \phi_b$. Let the normal mode frequencies for the N ions along the transverse direction that couples to the Raman beat-note wave vector $\Delta\mathbf{k}$ be ω_m ($m = 1, 2, \dots, N$). Analogous to the single ion case, we expand the position coordinate of each ion into normal mode coordinate, \hat{a}_m and \hat{a}^\dagger_m . Thus

$$\Delta k \cdot \hat{x}_i = \sum_m \eta_{i,m} \left(\hat{a}_m e^{-i\omega_m t} + \hat{a}^\dagger_m e^{i\omega_m t} \right), \quad (2.40)$$

where the Lamb-Dicke parameters are now defined as,

$$\eta_{i,m} = b_{i,m} \Delta k \sqrt{\frac{\hbar}{2m\omega_m}}. \quad (2.41)$$

Here $b_{i,m}$ are the normal mode eigenvector components between ion i and mode m .

We define Mølmer-Sørensen detunings,

$$\delta_m \equiv \mu - \omega_m. \quad (2.42)$$

Thus the effective Hamiltonian, using Eqs. (2.32) and (2.31), is

$$\begin{aligned} H_{eff} &= H_{bsb} + H_{rsb} \\ &= i \sum_{i=1}^N \sum_{m=1}^N \frac{\eta_{i,m} \Omega_i}{2} \left[a_m \sigma_i^- e^{i(\delta_m t + \phi_b)} - a_m^\dagger \sigma_i^+ e^{-i(\delta_m t + \phi_b)} \right. \\ &\quad \left. + a_m^\dagger \sigma_i^- e^{-i(\delta_m t - \phi_r)} - a_m \sigma_i^+ e^{i(\delta_m t - \phi_r)} \right] \\ &= \sum_{i=1}^N \sum_{m=1}^N \frac{\eta_{i,m} \Omega_i}{2} \left[a_m e^{i\delta_m t} e^{i\phi_M} + a_m^\dagger e^{-i\delta_m t} e^{-i\phi_M} \right] \sigma_{\phi_s}^i, \end{aligned} \quad (2.43)$$

where the motional phase $\phi_M \equiv \frac{\phi_b - \phi_r}{2}$ and the spin phase $\phi_s \equiv \frac{\pi}{2} + \frac{\phi_b + \phi_r}{2}$. The spin operator $\sigma_{\phi_s}^i = \cos \phi_s \sigma_x^i + \sin \phi_s \sigma_y^i$.

We set $\phi_r = 0$, $\phi_b = \pi$, then $\phi_M = \pi/2$ and $\phi_s = \pi$, and the effective Hamiltonian involves $\sigma_{\phi_s}^i = -\sigma_x^i$.

$$H_{eff} = -i \sum_{i=1}^N \sum_{m=1}^N \frac{\eta_{i,m} \Omega_i}{2} \left[a_m e^{i\delta_m t} - a_m^\dagger e^{-i\delta_m t} \right] \sigma_x^i. \quad (2.44)$$

The time evolution operator for this Hamiltonian, using the second-order Magnus

formula, is

$$\begin{aligned}
U(t, 0) &= \hat{T} e^{-i \int_0^t dt_1 H_{eff}(t_1)} \\
&= e^{-i \int_0^t dt_1 H_{eff} - \frac{1}{2} \int_0^t dt_2 \int_0^{t_2} dt_1 [H_{eff}(t_2), H_{eff}(t_1)]} + \dots
\end{aligned} \tag{2.45}$$

$$\begin{aligned}
\int_0^t dt_1 H_{eff} &= -i \int_0^t dt_1 \sum_{i=1}^N \sum_{m=1}^N \frac{\eta_{i,m} \Omega_i}{2} [a_m e^{i\delta_m t_1} - a_m^\dagger e^{-i\delta_m t_1}] \sigma_x^i \\
&= -i \sum_{i=1}^N \sum_{m=1}^N \frac{\eta_{i,m} \Omega_i}{2} \left[\frac{a_m (e^{i\delta_m t} - 1)}{i\delta} + \frac{a_m^\dagger (e^{-i\delta_m t} - 1)}{i\delta} \right] \sigma_x^i \\
&= -i \sum_{i=1}^N \sum_{m=1}^N \frac{\eta_{i,m} \Omega_i}{\delta_m} \sin \left[\frac{\delta_m t}{2} \right] [a_m e^{i\delta_m t/2} - a_m^\dagger e^{-i\delta_m t/2}] \sigma_x^i.
\end{aligned} \tag{2.46}$$

And,

$$\begin{aligned}
&\int_0^t dt_2 \int_0^{t_2} dt_1 [H_{eff}(t_2), H_{eff}(t_1)] \\
&= \sum_{\substack{i,j \\ j < i}} \sum_{m=1}^N \frac{\eta_{i,m} \eta_{j,m} \Omega_i \Omega_j}{4} \int_0^t dt_2 \int_0^{t_2} dt_1 ([a_m, a_m^\dagger] e^{i\delta_m (t_2 - t_1)} \\
&\quad + [a_m^\dagger, a_m] e^{-i\delta_m (t_2 - t_1)}) (2\sigma_x^i \sigma_x^j) \\
&= \sum_{\substack{i,j \\ j < i}} \sum_{m=1}^N \frac{\eta_{i,m} \eta_{j,m} \Omega_i \Omega_j}{2} \\
&\quad \int_0^t dt_2 \int_0^{t_2} dt_1 (e^{i\delta_m (t_2 - t_1)} - e^{-i\delta_m (t_2 - t_1)}) \sigma_x^i \sigma_x^j \\
&= i \sum_{\substack{i,j \\ j < i}} \sum_{m=1}^N \frac{\eta_{i,m} \eta_{j,m}}{\delta_m} \Omega_i \Omega_j \left[t - \frac{\sin \delta_m t}{\delta_m} \right] \sigma_x^i \sigma_x^j.
\end{aligned} \tag{2.47}$$

Here we have ignored the $(\sigma_x^i)^2$ terms in the second line, as they add a constant phase in the unitary evolution operator. Hence, the unitary evolution operator (Eq.

(2.45)) becomes,

$$U(t, 0) = \exp \left[\left(\sum_i \phi_i(t) \sigma_x^i - i \sum_{\substack{i,j \\ j < i}} \chi_{ij}(t) \sigma_x^i \sigma_x^j \right) \right], \quad (2.48)$$

where $\phi_i(t) = \sum_m [\alpha_{i,m}(t) a_m^\dagger - \alpha_{i,m}^*(t) a_m]$ denotes spin-dependent displacements of the m -th motional modes through the phase space by an amount,

$$\alpha_{i,m}(t) = \frac{\eta_{i,m} \Omega_i}{\mu - \omega_m} \sin \frac{(\mu - \omega_m)t}{2} e^{-i(\mu - \omega_m)t/2}. \quad (2.49)$$

In deriving this, we have used the effective Hamiltonians for the red sideband and the blue sidebands (Eq. (2.32) and (2.31)) that use the rotating wave approximation, and ignore the counter-rotating terms at $(\mu + \omega_m)$ in Eq. (2.24). This is a good approximation if the Raman beat-note predominantly excites the high frequency modes, as in the experiments in this thesis, where the Raman beat-note primarily couples to the COM mode (at $\nu_X \approx 2\pi \times 4.8$ MHz, and $\mu - \omega_X < 2\pi \times 150$ KHz). However, if the Raman beat-note is coupling to the low frequency modes, the counter rotating terms may be important. Then, $\alpha_{i,m}(t)$ is modified to [54]

$$\alpha_{i,m}^{full}(t) = \frac{-i\eta_{i,m} \Omega_i}{\mu^2 - \omega_m^2} [\mu - e^{i\omega_m t} (\mu \cos \mu t - i\omega_m \sin \mu t)]. \quad (2.50)$$

The second term in Eq. (2.48) is a spin-spin interaction with coupling,

$$\chi_{i,j}(t) = \sum_{m=1}^N \frac{\eta_{i,m} \eta_{j,m}}{2(\mu - \omega_m)} \Omega_i \Omega_j \left[t - \frac{\sin(\mu - \omega_m)t}{\mu - \omega_m} \right]. \quad (2.51)$$

This phase has a secular term proportional to the time t , and an oscillatory term, which is bounded and can be made small by choosing the detuning $\delta_m = \mu - \omega_m$ to be sufficiently large. Analogous to Eq. (2.50) if we add the contribution from the counter-rotating terms, we get

$$\chi_{i,m}^{full}(t) = -\Omega_i \Omega_j \sum_m \frac{\eta_{i,m} \eta_{j,m}}{\mu^2 - \omega_m^2} \left[\frac{\mu \sin(\mu - \omega_m)t}{\mu - \omega_m} - \frac{\mu \sin(\mu + \omega_m)t}{\mu + \omega_m} + \frac{\omega_m \sin 2\mu t}{2\mu} - \omega_m t \right]. \quad (2.52)$$

The first three terms in the square bracket are bounded, and their amplitudes can be kept under a given value by properly choosing the detuning μ . Similarly the phonon contribution (Eq. (2.50)) can be neglected for sufficiently large $|\mu - \omega_m|$. The last term of Eq. (2.52), however, increases linearly with time. Thus at large time, this will dominate the phase of the time evolution. We identify this term with the time evolution due to an effective Ising Hamiltonian, $H_{Ising} = J_{i,j} \sigma_x^i \sigma_x^j$, with the Ising couplings given by,

$$J_{i,j} = \Omega_i \Omega_j R \sum_m \frac{b_{i,m} b_{j,m}}{\mu^2 - \omega_m^2}, \quad (2.53)$$

as the Lamb-Dicke parameter $\eta_{i,m} = \sqrt{\frac{\hbar \Delta k}{2M\omega_m}} b_{i,m}$, where $b_{i,m}$ is the normal mode eigenvector components between ion i and mode m and M is the mass of a single ion. $R = \frac{\hbar(\Delta k)^2}{2M}$ is the recoil frequency (about $2\pi \times 18.5$ KHz in our system).

Note that Eq. (2.53) is obtained from the coefficient of t in Eq. (2.51) by adding a term containing $\mu + \omega_m$ in the denominator. This is equivalent to off-resonant contribution of the blue sideband transition from the **rsb** beat-note, and the off-

resonant contribution of the red sideband transition from the **bsb** beat-note. The off-resonant contributions from the carrier transition interfere destructively, as the **rsb** and the **bsb** beat-notes are symmetrically detuned from the carrier.

In the experiments, the Raman beat-note frequency μ is the control parameter. Although, this parameter alone does not give full control of the Ising coupling matrix $J_{i,j}$, and not sufficient to simulate an arbitrary fully connected Ising model, it provides us a variety of coupling patterns that are suitable for studying interesting spin physics. Figure 2.18 show the Ising coupling profile for various values of the Raman beat-note detuning in a system of $N = 10$ spins. The COM mode (mode index $m = 1$) makes the interactions uniform, as $b_{i,1} = 1/\sqrt{N}$ for all ion $i = 1, 2, \dots, N$. Other modes add inhomogeneity to the uniform coupling induced by the COM mode. When the beat-note is tuned near the COM mode (Fig. 2.18a), the couplings have same signs and they fall off with distance between the ions. All the couplings are positive or antiferromagnetic when $\mu > \omega_X$. Long range antiferromagnetism introduces frustration in the system, which we study in chapters 4 and 5. On the other hand if we tune the Raman beat-note close to the COM mode with frequency ω_X , but keeping $\mu < \omega_X$, all the Ising couplings are negative or ferromagnetic. We shall study the long range ferromagnetic Ising model in the presence of a transverse field in chapter 3. The range of the interactions can be tuned by varying the Mølmer-Sørensen detuning $\mu - \omega_m$, and also by varying the bandwidth of the vibrational modes. We shall discuss this in chapter 5.

As pointed out earlier, the center ion in a chain with odd number of spins do not couple to the tilt mode, hence $b_{middle\,ion,2} = 0$, and thus $J_{middle\,ion,j} = 0$ for

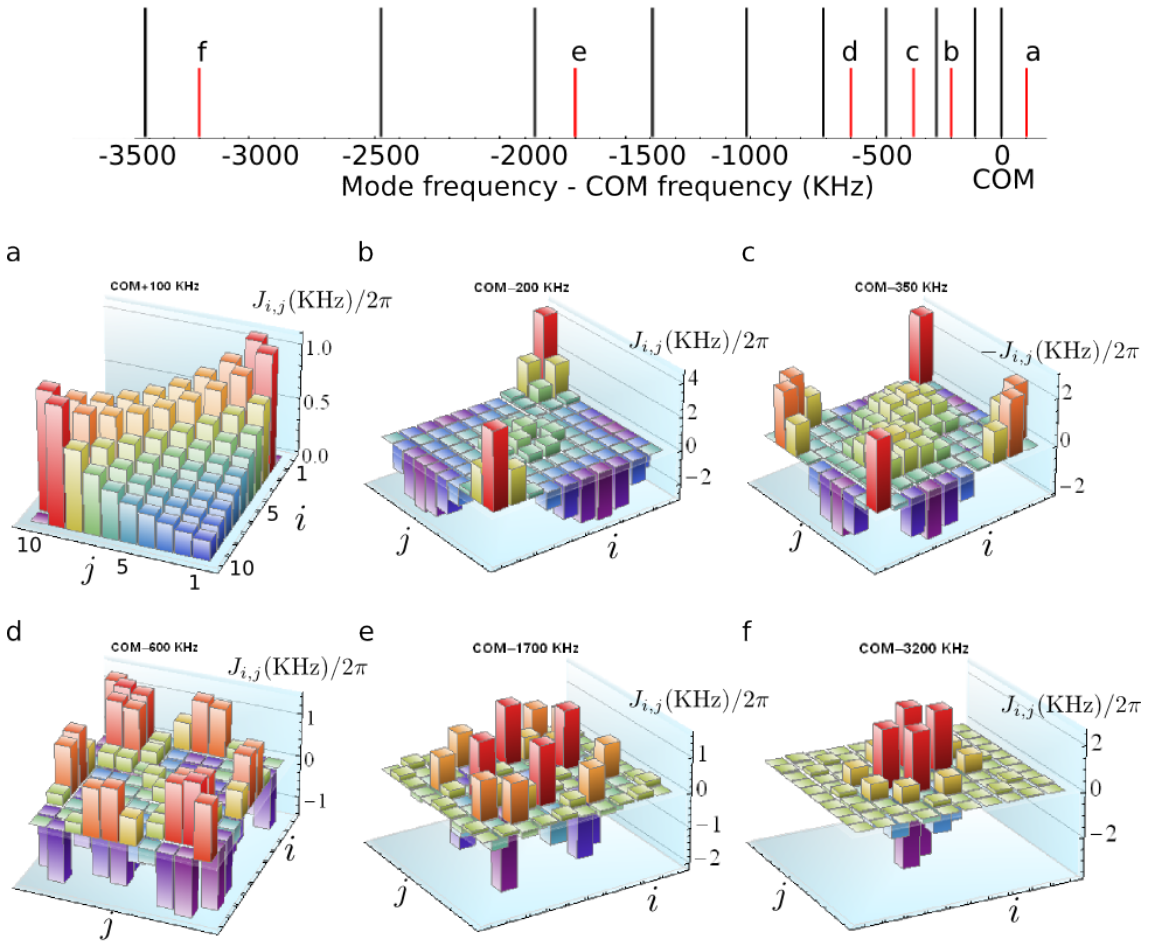


Figure 2.18: Ising couplings for various Mølmer-Sørensen detuning: Top - Transverse normal mode spectrum (black solid lines) for $N = 10$ ions, with axial frequency $\nu_Z = \omega_Z/2\pi = 1$ MHz, and transverse COM frequency $\nu_X = \omega_X/2\pi = 4.8$ MHz. **a-f.** Bar chart of the Ising couplings $J_{i,j}$ (divided by 2π) vs i and j for various detunings (mentioned on top of each figure). The sideband Rabi frequencies are taken to be $\eta\Omega/2\pi = 35$ KHz.

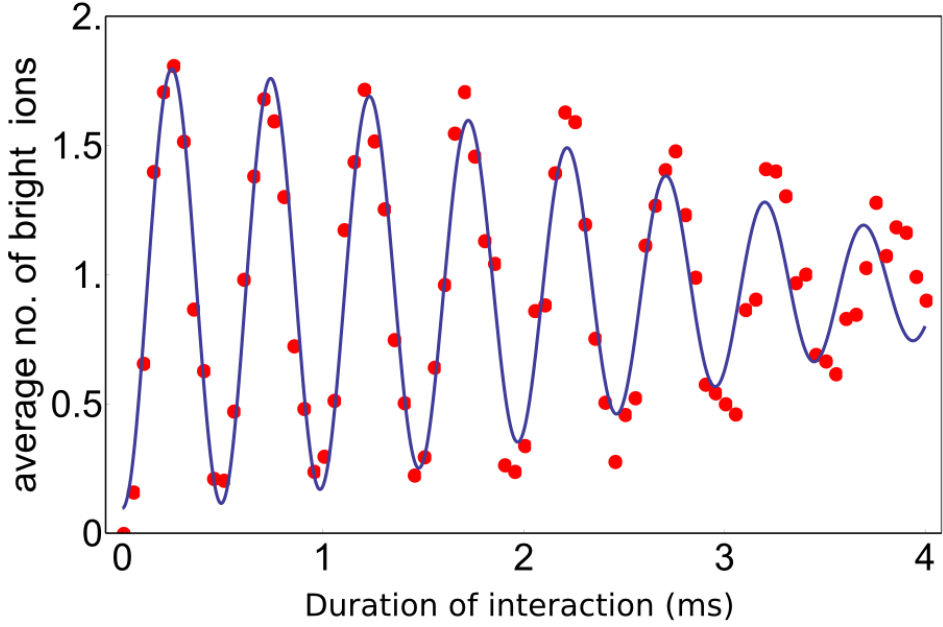


Figure 2.19: **Ising oscillations between spin states:** Two spins are optically pumped to the $|\downarrow_z\downarrow_z\rangle$ state, and made to interact with the Raman beat-notes generating the Ising couplings, according to Eq. (2.53). The sideband Rabi frequency is $\eta_{i,1}\Omega_i/2\pi \approx 35$ KHz for the ion i ($i = 1, 2$) and the COM mode ($m = 1$), and the beat-note $\mu/2\pi \approx \nu_1 + 105$ KHz. The red points are the data and the blue solid line is a fit with an Gaussian decay in the amplitude of oscillations. The contrast of the oscillations decays to $1/e$ in about 3.3 ms, presumably due to decoherence induced by intensity fluctuations in the Raman beams. The Raman beams are generated from the mode-locked tripled Vanadate laser at 355 nm.

all other ion j , from Eq. (2.53). Near the tilt mode long range antiferromagnetic couplings compete with the short range ferromagnetic couplings, and lead to a first order phase transition [100].

- **Measurement of the Ising couplings** - A system with $N = 2$ spins, initialized in the state $|\downarrow_z\downarrow_z\rangle$ (by optical pumping) will undergo Rabi flopping between the states $|\downarrow_z\downarrow_z\rangle$ and $|\uparrow_z\uparrow_z\rangle$, under the unitary evolution operator of the effective

Ising Hamiltonian,

$$\begin{aligned}
U(t)|\downarrow_z\downarrow_z\rangle &= e^{-iH_{Ising}t}|\downarrow_z\downarrow_z\rangle \\
&= e^{-iJt}|\downarrow_z\downarrow_z\rangle \\
&= \cos Jt|\downarrow_z\downarrow_z\rangle - i \sin Jt|\uparrow_z\uparrow_z\rangle,
\end{aligned} \tag{2.54}$$

where $J \equiv J_{1,2}$ is the Ising coupling between the spins. Since the spin state $|\uparrow_z\rangle$ appears as the bright state in our detection scheme (section 2.3.3), average number of bright ions $n_{bright}(t) = 2 \cos^2 Jt$ would oscillate with a frequency $2J$ under the Ising interactions. Thus the strength of the Ising interaction is found from the observed oscillation in the average number of bright ions interacting with the Raman beat-notes. Figure 2.19 shows the oscillations of the system between the spin states under the Ising evolution operator. The measured Rabi frequency is $2\pi \times 1.9$ KHz, and this corresponds to an Ising coupling of $J = 2\pi \times 0.95$ KHz.

We cannot determine the sign of the coupling from this oscillations. If we prepare the spin states along the y -axis of the Bloch sphere by a $\pi/2$ rotation about the x -axis (*i.e.*, by applying $R(\pi/2, 0)$ on the optically pumped state $|\downarrow_z\downarrow_z\rangle$), and then turn on the Ising couplings, the spins will oscillate with opposite phases for the positive and negative Ising couplings. The absolute sign of the Ising couplings still remain undetermined.

For $N > 2$ the oscillations in the observed average number of bright ions contain all the Ising couplings. We can Fourier transform such a signal to extract the Ising couplings. However, this method is not very efficient beyond a few spins,

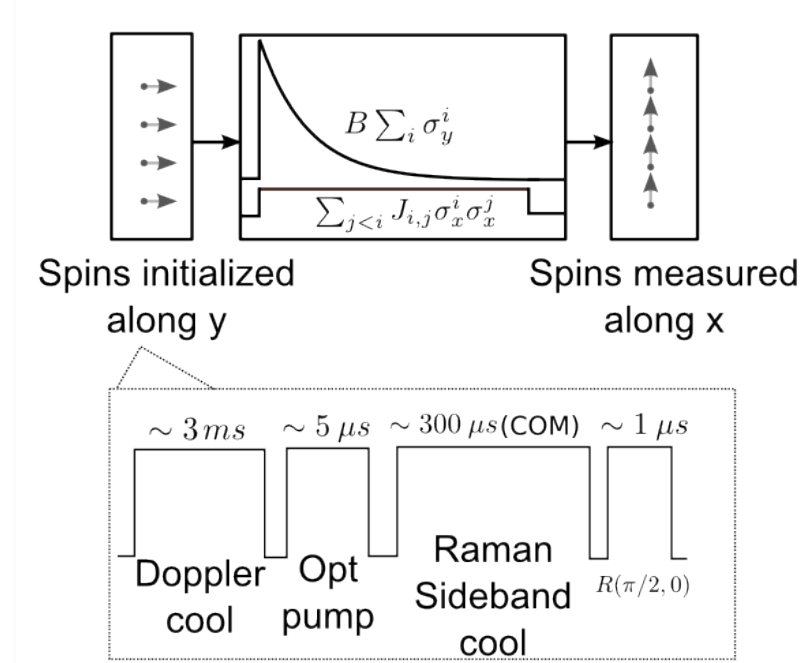


Figure 2.20: **Experimental sequence in a quantum simulation:** Outline of quantum simulation protocol. The spins are initially prepared in the ground state (or the highest excited state) of $B \sum_i \sigma_y^i$, then the Hamiltonian (Eq. (2.34)) is turned on with starting field $B_0 \gg J$ followed by an adiabatic exponential ramping to the final value B , keeping the Ising couplings fixed. Finally the x - component of the spins are detected. Details of the initialization are shown in the dotted box below. Trapped ions are Doppler cooled to an average COM (along the X -direction) phonon occupation number of $\bar{n} \sim 2$, then optically pumped to the spin state $|\downarrow_z \downarrow_z \dots\rangle$. The ions are prepared in their zero-point vibrational energy state by Raman sideband cooling. Finally a coherent $\pi/2$ pulse around the x -axis of the Bloch sphere orients the spins along the magnetic field.

as the Fourier transform contains the sums and differences of all the frequencies and it becomes hard to resolve and identify the Ising couplings.

2.5.2 Adiabatic quantum simulation

In an adiabatic quantum simulation, the simulator is initialized in the ground state of a trivial Hamiltonian. Then, the Hamiltonian is gradually tuned to the more complicated and interesting one. If the ramping is done at a rate slow compared

to the excitation energy scale, the population remains in the ground state. Our experiments are performed in the following steps (fig 2.20):

- The spins are optically pumped to the $|\downarrow_z \downarrow_z \dots\rangle$ state. They are also sideband cooled to get close to the phonon ground states.
- The spins are polarized along the y -direction of the Bloch sphere, by a coherent $\pi/2$ stimulated Raman pulse, about the x -axis of the Bloch sphere.
- The Hamiltonian is turned on with the effective transverse field much larger than the maximum Ising coupling. Thus the spins are in the ground state of the total Hamiltonian, to a very good approximation.
- The effective field B is ramped down exponentially with a time constant τ , keeping the Ising couplings constant, according to,

$$B(t) = B_0 \exp(-t/\tau). \quad (2.55)$$

Here B_0 is the initial effective field.

- Finally, the spins are globally rotated by a $\pi/2$ pulse about the y -axis of the Bloch sphere. This maps the x -components of the spins to the z -components (our measurement basis). Thus, by performing the final spin rotation, we are effectively measuring the spin order along the Ising direction, *i.e.*, the x -axis of the Bloch sphere.

The transverse field couples the instantaneous eigenstates of the Hamiltonian. The minimum energy gap, Δ_c between the ground and the first excited state that couples to the ground state sets the adiabaticity criteria [101, 42],

$$\frac{\dot{B}(t)\epsilon}{\Delta_c^2} \ll 1, \quad (2.56)$$

where $\epsilon \equiv |\langle g(t) | \frac{dH(t)}{dB} | e(t) \rangle|$ characterizes coupling between the instantaneous ground state $|g(t)\rangle$ and the relevant excited state $|e(t)\rangle$.

Exponential ramping is experimentally more convenient than a linear ramping, as this keeps the total duration of the experiment under the time scale set by decoherence processes. Instead of following the ground state, the highest excited state of the Hamiltonian may as well be followed. Following the highest excited state of H is equivalent to following the ground state of the sign inverted Hamiltonian, $-H$. This is an experimental way to flip the effective signs of all the Ising couplings from antiferromagnetic ($J_{i,j} > 0$) to ferromagnetic ($J_{i,j} < 0$), a trick that we follow to simulate the ferromagnetic quantum Ising model, discussed in chapter 3.

2.6 Experimental Apparatus

2.6.1 Ti:Sapphire laser

The Titanium:sapphire laser (MBR-110, developed by Coherent Inc) is pumped by an 18 Watt green laser (Verdi V-18, Coherent Inc) at 532 nm. Figure 2.21 shows a schematic of the MBR-110, and Fig. 2.23 shows a photograph of MBR-110 with

important parts labeled. The rod shaped Titanium:Sapphire crystal is placed inside a bow-tie ring cavity made from a single Aluminum block (The acronym MBR stands for a Monolithic Block Resonator), that stabilizes the cavity against the vibrations of its constituents. The flat faces of the crystal are Brewster cut to minimize reflection. The brass unit holding the crystal is water cooled.

Mirrors M1 and M2 have a radius of curvature of 10 cm each, and coated to be highly reflecting across a large wavelength range. M1 also focuses the 532 nm pump beam onto the Ti:Sapphire crystal. Mirror M3 is a piezo-mounted highly reflecting square-shaped small planar mirror (called a *tweeter mirror*). Mirror M4 is a planar mirror, and also the output coupler.

In between the mirrors M2 and M3, there is an optical diode, consisting of a Faraday rotator crystal placed in a strong permanent magnetic field, and a less than 0.5 mm thick Brewster angled retardation plate. The optical diodes ensure that the light is circulating in one direction only, namely $M1 \rightarrow M2 \rightarrow M3 \rightarrow M4 \rightarrow M1$. The Faraday rotator rotates the polarization by a few degrees in a direction independent of the travel direction of the beam. The retardation plate rotates the polarization in the opposite direction by almost the same amount (undoing the polarization change by the Faraday rotator) for light traveling through it in the ‘right’ direction, and in the same direction for any light traveling in the ‘wrong’ direction. Thus after a few passes through the ring cavity, lights circulating in the wrong direction is blocked by the Brewster angled retardation plate, and the cavity supports p -polarization light circulating in one direction.

The desired single-frequency operation (Fig. 2.22) of MBR-110 is chosen in

**Optical Schematic of the
MBR-110 Ti:Sapphire Laser**

Verdi 532 nm input

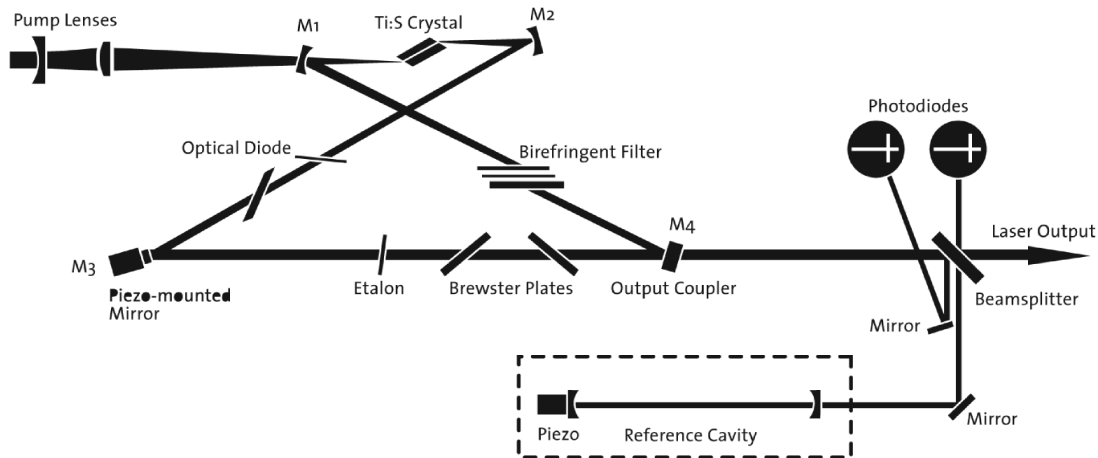


Figure 2.21: Schematics of the MBR-110 Ti:Sapphire laser: The MBR-110 (Coherent Inc) is pumped by an 18 Watt green continuous-wave laser at 532 nm (Verdi-18, Coherent Inc.). MBR-110 houses a bow-tie ring cavity made of the four mirrors M1-M4, and a cylindrical Titanium:Sapphire crystal rod with Brewster cut flat faces is placed in between the curved mirrors M1 and M2 (both with 10 cm radius of curvature). Mirror M1 also serves as the input coupler, and mirror M2 reflects the infrared radiation only, blocking the majority of the pump beam, which is then blocked behind M2. Mirror M3 is a piezo-mounted highly reflecting square-shaped small planar mirror, and the planar mirror M4 also acts as the output coupler. The optical diode, consisting of a Faraday rotator and a retardation plate (a wave plate) positioned at the Brewster angle selects a particular polarization to circulate in the cavity. The birefringent filter, the etalon, the two galvanometer mounter fused silica Brewster plates and the piezo-mounted mirror M3 select the mode of radiation. The cavity mode can also be locked to the piezo controlled external reference cavity, using the error signal generated by the photodiodes shown here, as explained in the text. The electronics is operated from a separate control box. (*Image Credit: Coherent Inc.*)

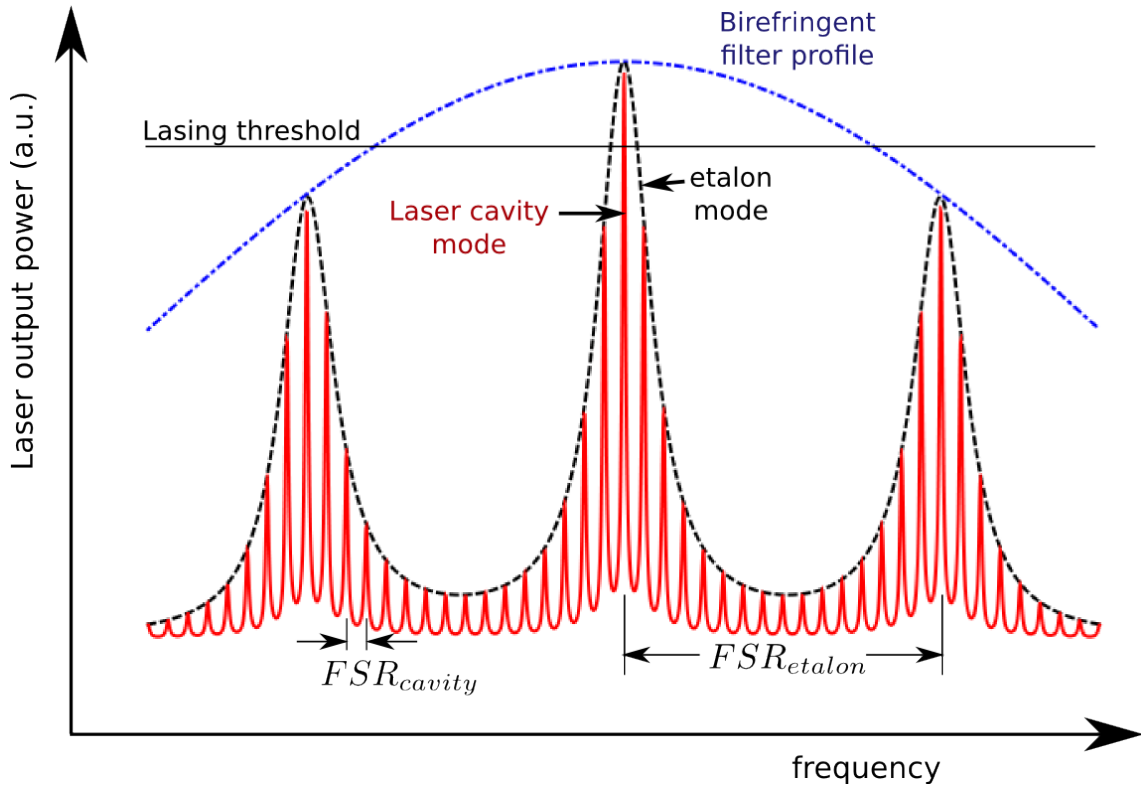


Figure 2.22: MBR modes: The radiation mode that builds up in the laser cavity is determined by the gain profile of the Ti:Sapphire crystal (not shown here), the frequency response of the birefringent filter (blue dashed-dot curve), the etalon modes (black dashed curve) and the cavity modes (red solid curve). The black solid curve shows the lasing threshold where the gain from the Ti:Sapphire crystal equals the loss in the cavity. The birefringent filter has a very broad frequency response (30-40 nm), and the laser output frequency hops between the etalon modes as the filter micrometer is rotated. The etalon has a free spectral range (FSR_{etalon}) of about 225 GHz. The cavity free spectral range (FSR_{cavity}) is about 300 MHz. As the etalon is rotated the laser output hops between the cavity modes. This is a schematic, and not to scale.

the following steps:

- The Ti:Sapphire crystal has a broad gain profile (few hundred nanometers), that offers tunability over a large wavelength range [102]. The optics used in the laser limits the width of the gain profile to under 100 nm. The polarization change through a birefringent material is frequency dependent and thus the *birefringent filter* further narrows down the bandwidth of the radiation circulating in the cavity to about 30-40 nm. The filter rotates the polarization of light with frequencies outside this band appreciably every time the light passes through it, and in a few passes the polarization is blocked by the Brewster angled optics in the cavity. Thus the birefringent filter acts as a coarse wavelength knob.
- *The intracavity etalon* - MBR-110 has a less than 0.5 mm thick etalon placed in between the mirrors M3 and M4, with a finesse of about 25, and a free spectral range of about 225 GHz. As we turn the birefringent filter, it hops between the etalon modes. Rotating the knob clockwise selects a higher frequency etalon mode, and rotating it counter-clockwise selects a lower frequency mode. The etalon is mounted onto a piezo which is mounted onto a galvanometer using an aluminum mount (Fig. 2.23). The galvanometer is mounted onto a rotation stage, with all three translational degrees of freedom. The galvanometer (and hence the etalon) can be rotated from the MBR control box.

The etalon should not be oriented such that the normal to its surface is parallel to the incident light. This orientation is known as the ‘flash’ position, and the power output from the laser will fall to half its normal value (when the etalon is not in the ‘flash’ position), as the cavity lases in both directions.

In the flash position of the etalon, a large fraction of the incident power is reflected back to the exact same direction, and the isolation provided by the optical diode is not sufficient to prevent lasing in the wrong direction.

- *The laser cavity modes*- the ring cavity is about $L = 1$ meter long, and the corresponding free spectral range is $c/L = 300$ MHz. We select a particular cavity mode by turning the angle of the etalon. As we rotate the etalon by turning the ‘etalon tune’ knob from the control box, the laser output hops between the cavity modes.

- *The etalon lock* - The reflected light from the etalon is directed and focused onto a photodiode by a 45° prism mirror and a fast biconvex lens. The intensity of this reflected light can be monitored from a test point in the laser box (‘etalon photodiode signal’ in fig 2.23) using a mini-BNC cable. As the etalon is rotated by turning the etalon knob from the electronic control box this signal increases, from zero, when the knob is fully counter-clockwise, to about 6-8 volts when it is fully clockwise. This signal may also be monitored at the test point TP6 on the analog board in the electronics control box.

If the maximum signal is at the fully clockwise position of the etalon knob is low, make sure that the reflected beam is properly hitting the photodiode by aligning the lens. The trim-pot next to the monitor point in the laser box can also be adjusted to increase the voltage.

The etalon is modulated at a piezo driving frequency of ≈ 82.3 KHz, generated from the electronics control box. This driving signal may be monitored at the test point TP5, and a 90° phase shifted signal may be monitored at test point TP7. The cylindrical piezo has two halves, which are driven with opposite phases. This

sets up a standing wave on the etalon, and the light reflected from the etalon is intensity modulated at this frequency as the reflectivity depends on the angle of the incidence. The amplitude of the intensity modulation is the largest when the beam hits a node of the displacement standing wave, which has the largest change in the angle w.r.t. the incident direction of the beam. This modulated signal may be monitored at the test point TP6 on an AC coupled oscilloscope, triggered by the signal from test point TP5, or TP7. As the etalon knob is turned, the signal on the oscilloscope should show a ‘breathing mode’ with an amplitude of about 100 mV.

An error signal is generated in the electronic control box by demodulating this modulated etalon signal at the driving frequency. The error signal can be monitored from the back panel of the control box. When the etalon knob on the control box is turned clockwise, the error signal hops between the cavity modes, and generates a sawtooth signal on an oscilloscope, with a steeper rise and a slower fall. To lock the etalon to a cavity mode, the error signal should be centered around zero volts, by adjusting the etalon offset from the control box. The etalon error signal is approximatey 300 mV in our system. We center the error signal at a desired cavity mode, by turning the etalon knob on the control box, and press the etalon lock button.

The etalon lock will not be robust, or it may not even lock if the error signal amplitude is below 100 mV. The amplitude may be reduced due to a drift in the driving frequency, or a drift in the mechanical resonance frequency of the piezo. Adjust the trim-pots PR14 (fine) and PR15 (coarse, usually not required) to bring the driving frequency back on the piezo resonance. This is achieved by observing the sawtooth etalon error signal on an oscilloscope while turning the etalon knob, and maximizing the amplitude of the signal.

In some unfortunate cases, the best error signal may be obtained when the incident light hits a spot on the etalon that does not optically transmit well without a significant loss in intensity. Then we may have to compromise between a good error signal and output power. We tested a couple of etalons, and picked the best.

- *The external reference cavity* - MBR-110 has an external reference Fabry-Perot cavity with finesse in the range of 25-50. When the etalon is locked to the laser cavity, the laser frequency does not hop between different etalon modes, but slow thermal drifts in the laser cavity length changes the frequency. The laser cavity can be locked to the reference cavity by feeding back to the tweeter mirror. This is done by superposing an offset signal to the reference cavity signal, such that the fringes are centered about zero volts, and locking the tweeter mirror (M3) to a side of a reference cavity fringe. The reference cavity fringes, as measured by the ‘photodiode A’ in Fig. 2.23 may be monitored at the test point in the laser box (‘Reference cavity signal’), after setting the reference cavity toggle switch on the back of the electronics control box to the ‘dither’ position. The offset static voltage, as measured by the ‘photodiode B’ may be observed at the ‘normalization signal’ port in the laser box, and adjusted by turning the trim-pot next to it. When the offset is properly adjusted, the reference cavity error signal peaks, observed at the back of the electronics control box, should be about 6-8 V high, and centered around zero volt.

For Raman transitions with a two photon detuning of a few THz used in the experiments, the slow drifts in the frequency due to thermal drifts in the reference cavity length is not crucial. However, in order to use the Ti:Sapphire laser for the

near resonant operations (Doppler cooling, detection etc), the reference cavity is locked to an absolute frequency reference, provided by a Doppler free saturation absorption line (at about 405.644321 THz) of Iodine molecules, see Ref. [103] for details. The saturation absorption error signal from the Iodine set up is sent to a PID controller, the output of which is fed into the *Ext Lock* port at the back of the MBR control box. Our MBR-110 generates about 2 Watts of optical power around 740 nm.

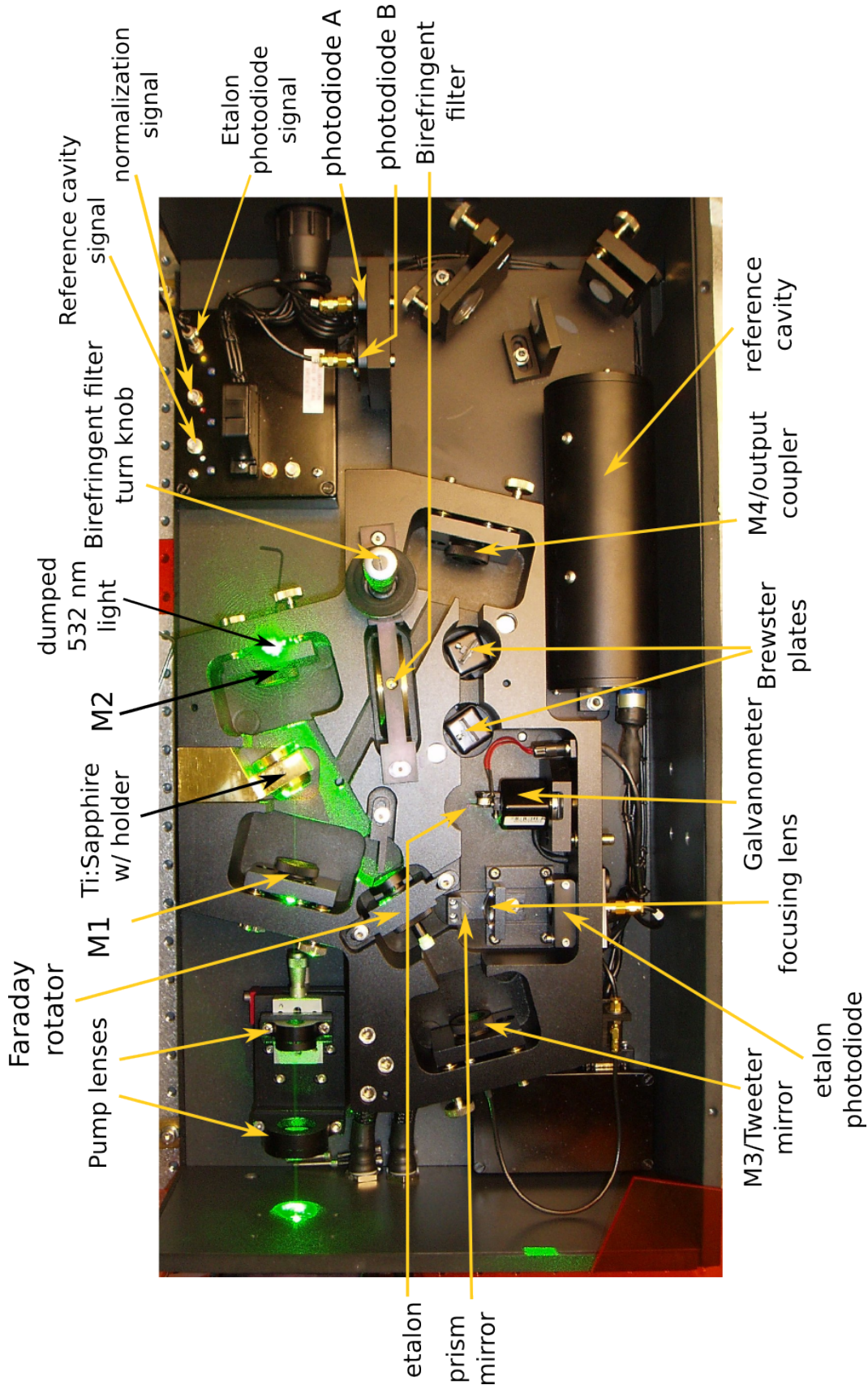


Figure 2.23: MBR-110 Ti:Sapphire laser.

for a

2.6.2 Generating 369.5 nm light by frequency doubling

We frequency double the infrared Ti:Sapphire output to the ultraviolet using a Lithium Triborate (LBO) non-linear crystal in a frequency doubling cavity (WaveTrain, Spectra-Physics). The frequency doubling efficiency is about 10% per Watt, and we get approximately 490 mW of 370 nm light to be used for Raman transitions from an input light of 2.2 W.

We use another WaveTrain frequency doubler to generate 369.5 nm light for Doppler cooling, detection, protection, ionization and optical pumping. The doubling efficiency of this doubler is about 6% per Watt, and we get approximately 20 mW of ultraviolet light, with an input of about 600 mW.

2.6.3 369.5 nm optics schematics

We use the frequency doubled light at 369.5 nm to generate the Doppler cooling, detection, optical pumping and protection beams. Fig 2.24 shows a schematic of the optics set up. The output of the frequency doubler is about 430 MHz red detuned from the $^2S_{1/2} - ^2P_{1/2}$ resonance. A portion of this light is sent to a 7.37 GHz EOM (Model 4851 from New Focus, driven by a Lab Brick Signal generator from Vaunix Corporation, 34 dBm rf power) that generates sidebands required for Doppler cooling the $|\downarrow_z\rangle$ state. An AOM (made by Brimrose Corp.) driven at 400 MHz up-shifts the frequency to about 30 MHz (red detuned) from the resonance.

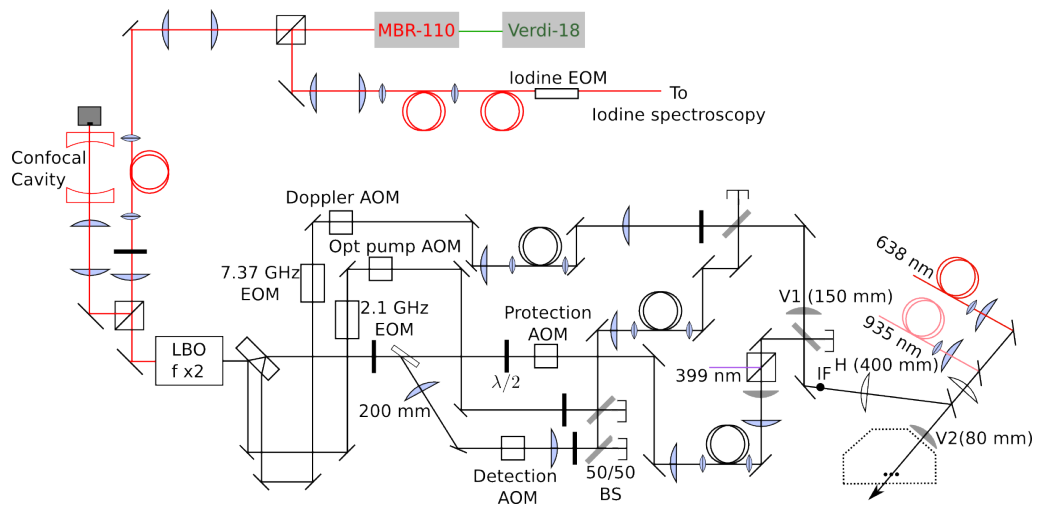


Figure 2.24: Schematics of the 369.5 nm beams: A Ti:Sapphire output at 740 nm is frequency doubled by an LBO crystal inside a triangular cavity is split into the Doppler cooling, detection, optical pumping and the protection beams. 50/50 beam splitters are used to combine multiple beams. Vertical cylindrical lens V2 images the intermediate focus IF at the ion position, with a magnification of 1/5. Spherical lenses are shown in blue, horizontal cylindrical lenses are shown in white and the vertical cylindrical lenses are shown in gray. 399 nm beam is combined with the protection beam on a PBS, 935 nm and 638 nm beams are combined with the 369.5 nm and 399 nm beams on mirrors with appropriate coatings.

Another part of the beam is sent through an AOM driven at about 424 MHz, and this is used as the detection beam. The optical pumping beam is also derived from the same parent beam, and sent through a 2.105 GHz EOM (Model 4431 Visible Phase Modulator from New Focus Inc.) followed by a 424 MHz AOM. The detection and the optical pumping beams are combined on a 50-50 non-polarizing beam splitter (Model BSW20 from Thorlabs), and then coupled to an optical fiber (single mode at 320 nm from Coastal Connections), the output of which is then combined with the Doppler cooling beam on a 50-50 non-polarizing beam splitter (Edmund Optics NT 48-213). The protection (the additional cooling) beam is 200 MHz further red detuned by an AOM (from Intra-Action Corp.), and is mixed with 399 nm light on a polarization beam splitter. The protection and the 399 nm beams are then combined with the Doppler cooling, optical pumping and the detection beams on a 50-50 beam splitter (Edmund Optics NT 48-213). All the beams are focused in the vertical direction at an intermediate focus (labeled IF), which is then imaged at the ion position by an imaging lens (V2) of focal length 80 mm. The magnification in this imaging is 1/5. The final lens V2 is mounted tightly on a fixed cylindrical lens mount which is attached to a pedestal. The beam is vertically shifted by moving the vertical lens V1. The beam at the ion position moves by a factor of 5 less than the vertical translation in the lens V1, making the beam stable against vibrations in the mount holding the lens V1. The cooling, detection and optical pumping beams are approximately $8 \mu\text{m}$ wide in the vertical direction and about $100 \mu\text{m}$ along the horizontal direction ($1/e^2$ radius in intensity) transverse to the beam propagation. Since this beam enters the vacuum chamber at an angle of 45

degrees w.r.t. the axis of the ion chain, the effective beam waist in the horizontal direction is $100 \mu\text{m} / \cos 45^\circ \approx 140 \mu\text{m}$.

A portion of the Ti:Sapphire (MBR-110) output (about 40 mW) is used for the Doppler free saturation absorption spectroscopy. This light is coupled to a fiber EOM (from EO Space Inc., driven at 13.315 GHz), and the output (about 9 mW) is sent to the saturation spectroscopy set up [103]. We also monitor the MBR modes on a home-made 20 cm confocal cavity. Details of the confocal cavity may be found in Appendix C of Ref. [70].

On a historical note, we used a semiconductor diode laser with a tapered amplifier system (Toptica TA 100) to generate the 739.5 nm light (and the Ti:Sapphire laser to generate the Raman beams) for the experiments in chapter 3 (with $N = 2$ to $N = 9$ spins) and chapter 4.

2.6.4 Mode-locked 355 nm laser

We use a mode-locked laser with center wavelength at 355 nm (Vanguard, Spectra-Physics) to drive two photon Raman transitions [104]. The lasing medium is a Neodymium doped Vanadate (Nd:YVO_4). This is an industrial laser used primarily for semiconductor fabrication, and comes in a closed box with no direct access to the laser cavity.

Some parameters of interest are:

- Average optical power ≈ 4 Watt.
- Repetition rate, $\nu_{rep} \approx 80.6$ MHz, delay between the pulses ≈ 12 ns.

- Optical bandwidth ≈ 100 GHz (estimated).

This laser has sufficient optical bandwidth to drive the two photon Raman transitions.

We drive the stimulated Raman transitions by shining two non-co-propagating beams derived from this laser on the ions, as shown in fig 2.25a. Each beam generates an optical frequency comb, with comb-teeth spaced regularly by the repetition rate, ν_{rep} , as shown in Fig. 2.25c. We shift the optical frequency of the first comb (shown in red) relative to the second (blue) by AOM's used in the beam path. The AOM frequency difference $|\Delta\nu_{AOM}|$ is tuned such that the beatnote between m^{th} comb-tooth of the red comb and $(m + n)^{\text{th}}$ comb-tooth of the blue comb (m and n are positive integers) equals the atomic transition frequency, ν_{ab} between states $|a\rangle$ and $|b\rangle$ (Fig. 2.25b), for all m and a particular n . The atom then absorbs a photon from the $(m + n)^{\text{th}}$ tooth of the blue comb and emits to the m^{th} tooth of the red comb to undergo a stimulated Raman transition between the states $|a\rangle$ and $|b\rangle$, via the excited state $|e\rangle$. For example, to drive the hyperfine transition (at the frequency ν_{hf}) between the clock states of $^{171}\text{Yb}^+ \ ^2S_{1/2}$ ground state hyperfine manifold, $\nu_{ab} = \nu_{hf}$, and since the repetition rate of our 355 nm mode-locked laser is approximately 80.6 MHz, we use the $n = 157^{\text{th}}$ comb-tooth. The beatnote is generated by all pairs of comb-teeth separated by $157\nu_{rep}$ in frequency.

The mechanism behind exciting an atomic transition with a frequency comb may also be understood by looking at the frequency spectrum of the light using a radio-frequency photodiode that has a response time fast enough to resolve between

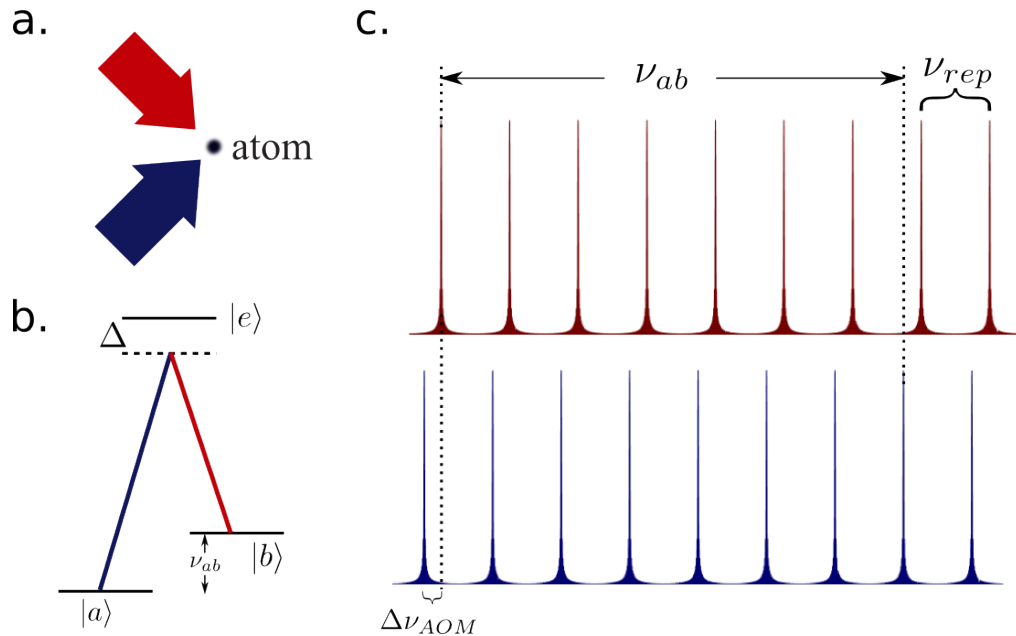


Figure 2.25: Schematics of a two photon Raman transition using a mode-locked laser: **a.** Two non-co-propagating beams generated from the same mode-locked laser drive stimulated Raman transition in an atom. **b.** Level diagram of a three level Λ -system. Individual laser beams off-resonantly couple the states $|a\rangle$ and $|b\rangle$ to the excited state $|e\rangle$. The beams are detuned from the excited state $|e\rangle$ by Δ . In our experiments with $^{171}\text{Yb}^+$ states $|a\rangle$ and $|b\rangle$ are the hyperfine (and motional) ‘clock’ states in the electronic ground state of the $^2S_{1/2}$ manifold, and the excited states used are the $^2P_{1/2}$ and the $^2P_{3/2}$ fine structure states. The beams are detuned by $\Delta \approx 33$ THz blue of the $^2P_{1/2}$ states for our 355 nm mode-locked laser. **c.** Each beam generates an optical frequency comb, shown in red and blue. The frequencies of the beams are shifted by AOMs, and at some difference frequency $|\Delta\nu_{AOM}|$ between the shifts, the beatnote between m^{th} comb-tooth of red first comb and $(m + n)^{\text{th}}$ comb-tooth of the blue comb (m and n are positive integers) equals the atomic transition frequency, ν_{ab} , for all m and a particular n . The atom absorbs a photon from the $(m + n)^{\text{th}}$ tooth of the blue comb and emits a photon to the m^{th} tooth of the red comb to make a transition from state $|a\rangle$ to $|b\rangle$.

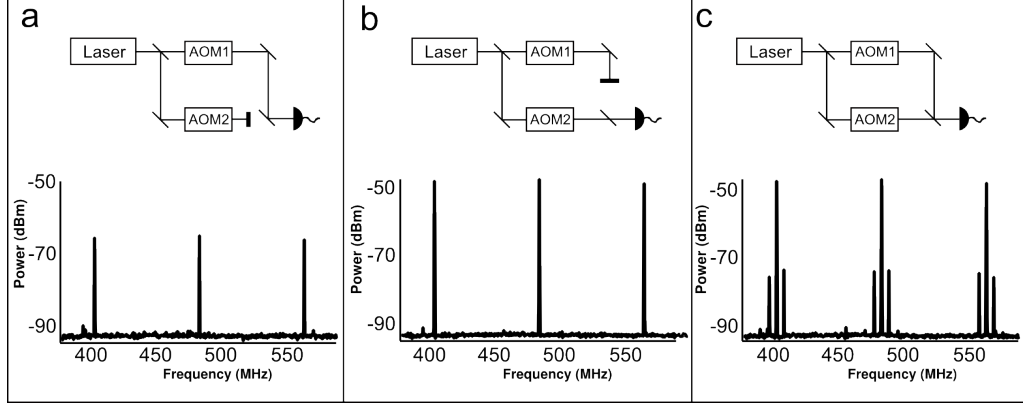


Figure 2.26: Radio frequency comb-teeth used in the two photon Raman transitions: We use a radio-frequency photodiode to look at the radio-frequency spectrum of the mode-locked laser ($\nu_{rep} \approx 80$ MHz) and the beatnote. The light is split into two arms using a beam-splitter, with individual frequency control by the AOMs, and recombined at the second beam-splitter. The radio-frequency photodiode averages over the optical cycles. **(a)** measured spectrum with the beam from AOM2 blocked. **(b)** measured spectrum with the beam from AOM1 blocked, and **(c)** measured spectrum with both the beams. Sidebands at frequencies $\pm|\Delta\nu_{AOM}|$ appear due to interference of the beams. In the two photon STR, atoms take the place of the final beam-splitter.

the pulses, but slow compared to an optical cycle. We illustrate this in Fig. 2.26*. Here the beam from the mode-locked laser is split into two paths, with the AOMs shifting the frequencies of the individual paths. The two arms constitute a Mach-Zehnder interferometer, with the ion replacing the final beam splitter. The radio-frequency photodiode averages out the intensity over the optical cycles but shows the radio frequency comb-teeth at frequencies $m \times \nu_{rep}$ ($m = 0, 1, 2, \dots$) in the measured frequency spectrum of a single beam (Fig 2.26a-b). The effective time constant of the photodiode circuit (and the speed of the amplifier used) limits the overall bandwidth of the radio-frequency beatnote comb detected electronically. Since the two arms of the Mach-Zehnder interferometer are shifted in frequencies by $\pm\nu_{AOM1}$ and $\pm\nu_{AOM2}$

*The data were taken with another mode-locked laser with a repetition rate of 80 MHz.

respectively by the acousto optic modulators (AOMs), the beatnote generated by the final beam-splitter is amplitude modulated at $|\Delta\nu_{AOM}| = |\nu_{AOM1} - \nu_{AOM2}|$ ^{*}. This puts sidebands[†] on the radio frequency comb-teeth at frequencies $m \times \nu_{rep} \pm |\Delta\nu_{AOM}|$. We can control the position of the sidebands by controlling the frequency $|\Delta\nu_{AOM}|$, and bring one of the sidebands on resonance with an atomic transition. An atomic transition, at frequency ν_{ab} is excited when the AOM frequencies are tuned such that ν_{ab} equals a particular sideband frequency $\nu_{sb} = n \times \nu_{rep} - |\Delta\nu_{AOM}|$, where n refers to some comb-tooth in the radio-frequency comb. Hence, we want to stabilize this particular amplitude modulation sideband at the transition frequency.

Repetition rate stabilization

The repetition rate drifts and fluctuates (Fig. 2.27) due to the thermal drift and fluctuations. Since we do not have an easy access to the laser cavity of this laser, we cannot stabilize the repetition rate directly. However, as described in the previous section, our two photon Raman transition is dependent on the beat-note between two beams generated from this laser, and hence we need to stabilize the beat-note only.

One intuitive way to stabilize the beat-note is to measure the repetition rate at time t , $\nu_{rep}(t)$ by a frequency counter, and directly change the driving frequency of one (or both) of the AOMs accordingly using a software locking scheme, to keep the sideband frequency $\nu_{sb} = n \times \nu_{rep}(t) - |\Delta\nu_{AOM}|$ at a constant value. This requires

^{*}without loss of generality, we have chosen the AOM shifts to both be positive.

[†]The carrier is not depleted completely in Fig. 2.26, since the interfering beams are not perfectly mode-matched, and have unequal optical power.

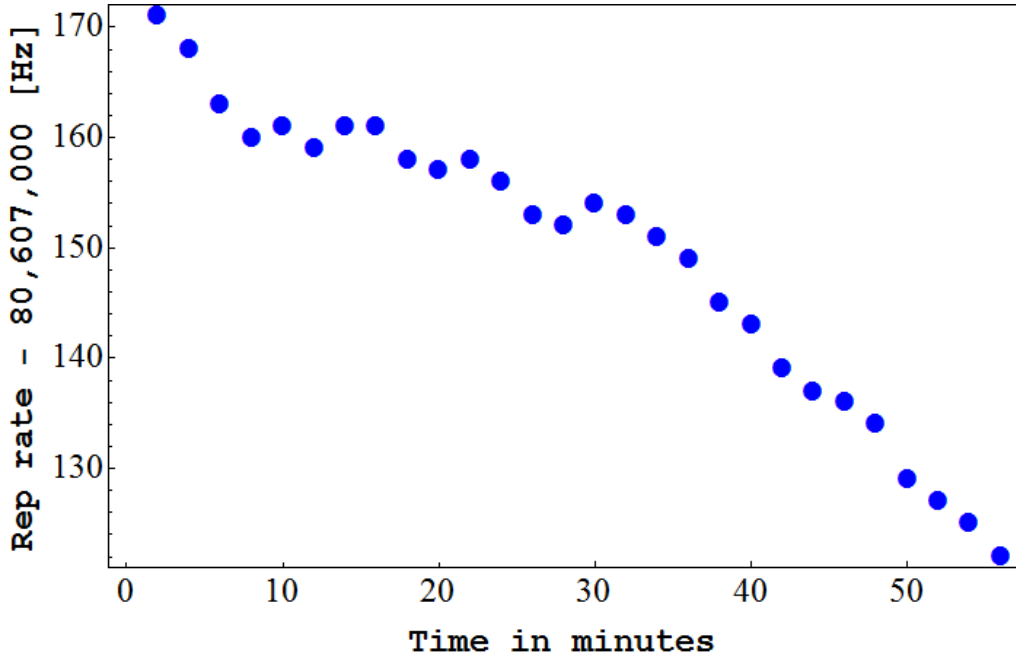


Figure 2.27: Drift in the repetition rate of the 355 nm mode-locked laser: The repetition rate of the mode-locked Vanguard laser at 355 nm is measured with a digital frequency counter in regular two minutes intervals. The repetition rate shows a long term drift of about 1 Hz/minute in this case. The fluctuations are correlated with the ambient temperature fluctuations. Typically the repetition rate approaches a steady state value after about a couple of hours of turning on the laser, provided that the ambient temperature is stable. The two photon Raman transition in $^{171}\text{Yb}^+$ hyperfine states uses the 157th comb-tooth, which drifts by about 157 Hz/minute. We stabilize the fluctuations and the long term drift in the repetition rate by feeding forward to an external acousto optic modulator, as described in the text.

stabilizing ν_{rep} to ϵ/n , in order to stabilize the sideband frequency to ϵ . The software lock would be slow for large n ($n = 157$ in our experiment) as the integration time of the frequency counter could be comparable or larger than the time scale at which the repetition rate fluctuates. In our experiments, to stabilize the sideband within a fraction of 1 KHz, we need to measure $\nu_{rep}(t)$ within a few Hz, which corresponds to an integration time of about a second. We have experimentally found that a software-based lock of this type is insufficient for achieving high-fidelity transitions.

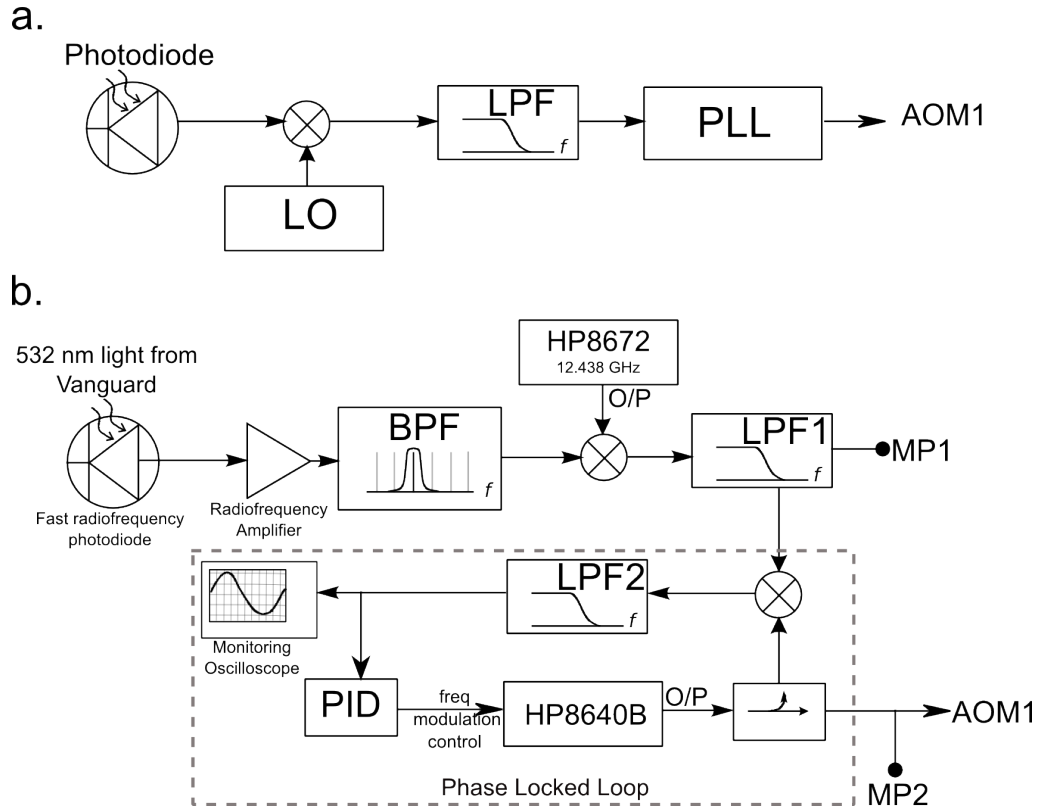


Figure 2.28: Schematics of the repetition rate lock: **a.** The output of a fast photodiode is mixed with a local oscillator (LO) signal, which is sent to a Phase Locked Loop (PLL) after rejecting the high frequency beatnote by using a low pass filter (LPF). The output of the PLL drives the AOM. **b.** Details of the repetition rate lock circuit used in our experimental set up. The second harmonic light (at 532 nm) from a mode-locked tripled Vanadate laser (Vanguard, Spectra Physics, repetition rate $\nu_{rep} \approx 80.6$ MHz) is incident on a radio-frequency photodiode, which generates a radio-frequency comb with comb-teeth at frequencies $m \times \nu_{rep}$ (m is a positive integer). This signal is amplified and passed though a bandpass filter (BPF), which transmits the $n = 157^{\text{th}}$ comb-tooth at $n \times \nu_{rep} \sim 12.655$ GHz. This is then mixed with a radio-frequency signal at $\nu_{LO} = 12.438$ MHz generated by an HP8672A synthesizer, and the lower frequency beatnote (at ≈ 217 MHz) is sent to the PLL, where an HP8640B is frequency modulated to output a signal that is phase locked with the beatnote. The bandwidth of the output signal depends on the bandwidth ν_{BW} of the low pass filter LPF2 used in the PLL. Frequency spectrum of the signals at monitoring points MP1 and MP2 are shown in Fig. 2.29.

To stabilize the beatnote, we monitor the repetition rate continuously by measuring the intensity of the 532 nm light generated in the laser cavity (which has the same repetition rate, and the same fluctuations in the repetition rate) by a fast photodiode (a GaAs PIN Detector, ET-4000, made by Electro-Optics Technology, Inc.), and correct for the fluctuations by feeding forward to the AOMs. We filter the $n (= 157)^{\text{th}}$ comb-tooth by a microwaves mechanical filter, and beat the signal at $n \times \nu_{\text{rep}}(t)$ with a frequency stabilized local oscillator at frequency ν_{LO} , as shown in fig. 2.28(a). Here $\nu_{\text{rep}}(t)$ is the repetition rate at time t (we care about the fluctuation time scale, which is slow compared to the delay between the laser pulses, and hence a repetition rate can be defined at time t). The beatnote is sent through a low pass filter, which allows the lower frequency component of the beat signal at $n \times \nu_{\text{rep}} - \nu_{\text{LO}}$ to pass through (we assume that $n \times \nu_{\text{rep}} > \nu_{\text{LO}}$). In principle, we may use this signal directly to drive one of the AOMs, AOM1 for example. Thus at time t ,

$$\begin{aligned} n \times \nu_{\text{rep}}(t) - \nu_{\text{LO}} &= \nu_{\text{AOM1}}(t) \\ \Rightarrow n \times \nu_{\text{rep}}(t) - \nu_{\text{AOM1}}(t) &= \nu_{\text{LO}} \end{aligned} \quad (2.57)$$

The right hand side of Eq. (2.57) is independent of time, which shows that the time dependence, or the fluctuations in the repetition rate is canceled by a time dependent AOM1 driving frequency. Hence the sideband frequency is at $\nu_{\text{sb}} = n \times \nu_{\text{rep}}(t) - |\Delta\nu_{\text{AOM}}| = n \times \nu_{\text{rep}}(t) - \nu_{\text{AOM1}}(t) + \nu_{\text{AOM2}} = \nu_{\text{LO}} + \nu_{\text{AOM2}}$, independent of time. Note that the fluctuations do not cancel for the other sideband (at $n \times \nu_{\text{rep}} +$

$|\Delta\nu_{AOM}|$) of the n^{th} comb-tooth, or for any other comb-tooth and their sidebands in general.

From a practical point of view, this beat-note may not be used to drive the AOM1 for the following reasons. First, the amplitude of this radio frequency signal is dependent on the photodiode output, and hence on the laser power. Second, the thermal and white noise from the amplifiers used makes the signal very noisy, and the noise may drive unwanted transition. This problem is overcome by feeding the beatnote signal into a phase locked loop (PLL), and using its output to drive the AOM1.

Beyond the bandwidth of the low-pass filter used in the PLL, the noise profile is characteristic of the oscillator used, and the amplitude of the beatnote is independent of the laser power. Fig. 2.29a shows the spectrum of the signals that may be used to drive AOM1, with and without the PLL. The noise floor is ~ 30 dB lower when a PLL is used. In fig. 2.29b we show the observed Raman spectrum of a single trapped $^{171}\text{Yb}^+$ ion as a function of the AOM2 frequency, for a pulse duration of $40\ \mu\text{s}$. The white noise present in the AOM1 signal may drive unwanted Raman transitions for a range of frequencies of AOM2, thus providing a non-zero background in the observed spectrum, as shown in the red trace. When we drive the AOM1 with the output of the PLL, this background goes away, as seen in the black trace.

If the signal to white noise ratio in the AOM driving signal generated from the repetition lock circuit is α , the strength of the stimulated transition by the noise field, $\Omega_{\text{noise}} = \Omega/\sqrt{\alpha}$, as the two photon Rabi frequency is proportional to the electric field of each beam. Here Ω is the Rabi frequency of the stimulated transition

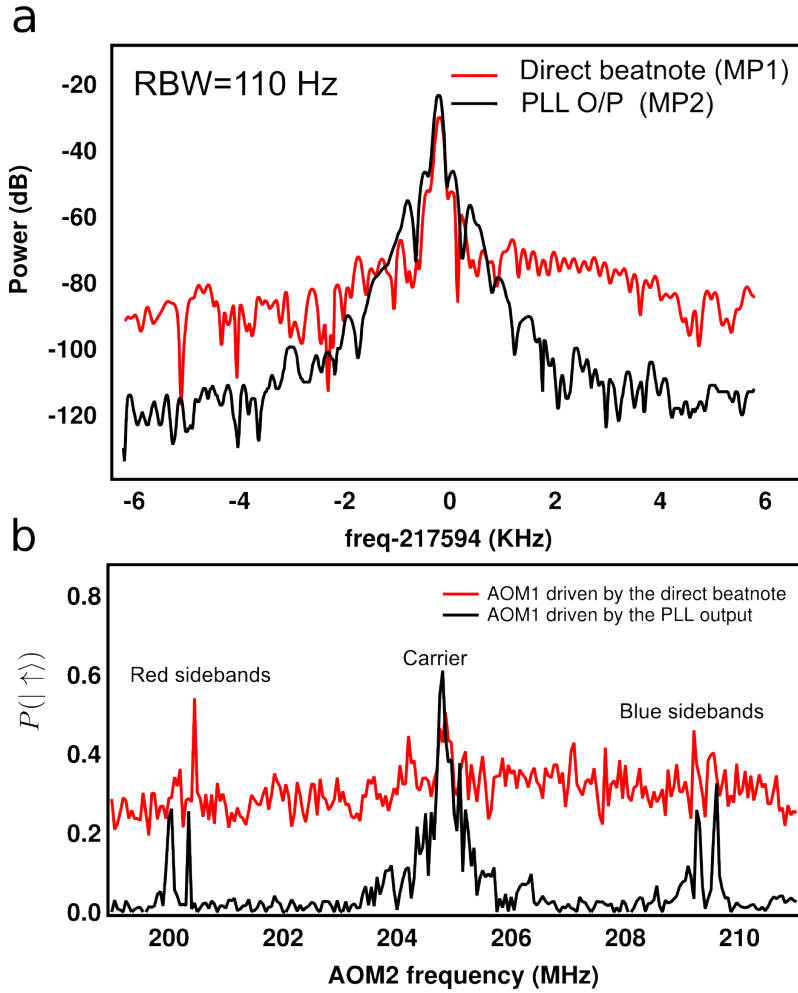


Figure 2.29: The role of the Phase locked loop in the repetition rate stabilization scheme: **a.** Frequency spectra of the beatnote (that may be used to drive the AOM1) at points MP1 and MP2 in Fig. 2.28 respectively. The PLL gets rid of the (white) noise outside the bandwidth of the low pass filter used. **b.** Probability of two photon Raman excitation of a single trapped $^{171}\text{Yb}^+$ ion vs AOM2 frequency with and without the PLL. Here the system is initialized in the state $|\downarrow\rangle$. If the signal at point MP1 is used to drive the AOM1, the noise excites unwanted transitions at all AOM2 frequencies, as seen in the constant background in the Raman spectrum. The output of the PLL does not have this noise beyond the bandwidth of the low pass filter used, and hence the Raman frequency spectrum is cleaner. Here we show the ‘carrier’ transition between the hyperfine $^{171}\text{Yb}^+$ ‘clock’ states at 205 MHz and the vibrational sidebands around 200 MHz and 210 MHz.

by the signal at the transition frequency. In order to keep this unwanted transition probability to under κ in a total experimental time of T , $\Omega_{noise}T \sim \kappa$, which implies that minimum signal to noise ratio $\alpha \sim (\Omega T/\kappa)^2$. Thus for a transition frequency of $\Omega = 1$ MHz, and an experimental duration of 1 ms, we need a signal of noise ratio $\alpha > 10^{10}$, or 100 dB to keep $\kappa \sim 1\%$.

To characterize the stability of the beatnote frequency, we compared it to the $^{171}\text{Yb}^+$ ‘clock’ hyperfine qubit by Ramsey interferometric measurements. With the lock engaged we measured a coherence time of ≈ 800 ms. This coherence time is limited by the presence of noise affecting the qubit frequency, such as magnetic field noise, and not by the noise in the repetition rate. With the repetition rate lock disengaged, the coherence drops to ~ 3 ms, showing the usefulness of this lock to achieve high fidelity quantum operations.

2.6.5 Optical set up for the Raman transitions

Stimulated two photon Raman transitions generate the quantum Ising model in our experiments, as discussed previously. We also use stimulated Raman transitions for single qubit manipulation through the Bloch sphere. The two photon Raman transitions require an optical beatnote at the hyperfine transition (12.64 GHz) for simulating the effective magnetic field. We use two different ways to generate this optical beatnote,

- Frequency modulate the output of a CW laser beam (a Ti:Sapphire laser, frequency doubled in a second harmonic generation process) using an electro

optic modulator (custom made by New Focus Inc.) [105] at $\omega_{EOM}/2\pi = \nu_{EOM} \approx \nu_{hf}/2 \approx 6.32$ GHz.

- Use the suitable comb-teeth pair from an optical frequency comb generated by a mode-locked tripled Vanadate laser with center wavelength at 355 nm. Our mode-locked laser has a repetition rate of $\omega_{rep}/2\pi = \nu_{rep} \approx 80.6$ MHz, and hence we use the comb-teeth pair separated by a frequency of $157 \times \nu_{rep} \approx 12.655$ GHz, which is the closest beatnote to the hyperfine splitting.

A finer control of the frequency of the Raman beatnote is achieved by using AOMs.

The electric field of a CW laser beam at a frequency of ω_L is frequency modulated by the EOM at ω_{EOM} as

$$E_1 = \frac{E_0}{2} \exp [i(kx - \omega_L t)] \sum_{n=-\infty}^{n=\infty} J_n(\phi) \times \exp [in [(\delta k)x - \omega_{EOM}t]] + c.c. \quad (2.58)$$

where E_0 and nu_0 are the incoming (unmodulated) electric field amplitude and frequency respectively. $J_n(\phi)$ is the n^{th} order Bessel function with modulation index ϕ , and $\delta k = \omega_{EOM}/c$, c is the speed of light. The modulation index ϕ depends on the radio-frequency power used to drive the EOM, and increases with higher driving power. Thus the EOM puts on equispaced sidebands around the carrier at ω_L , separated by the modulation frequency ω_{EOM} .

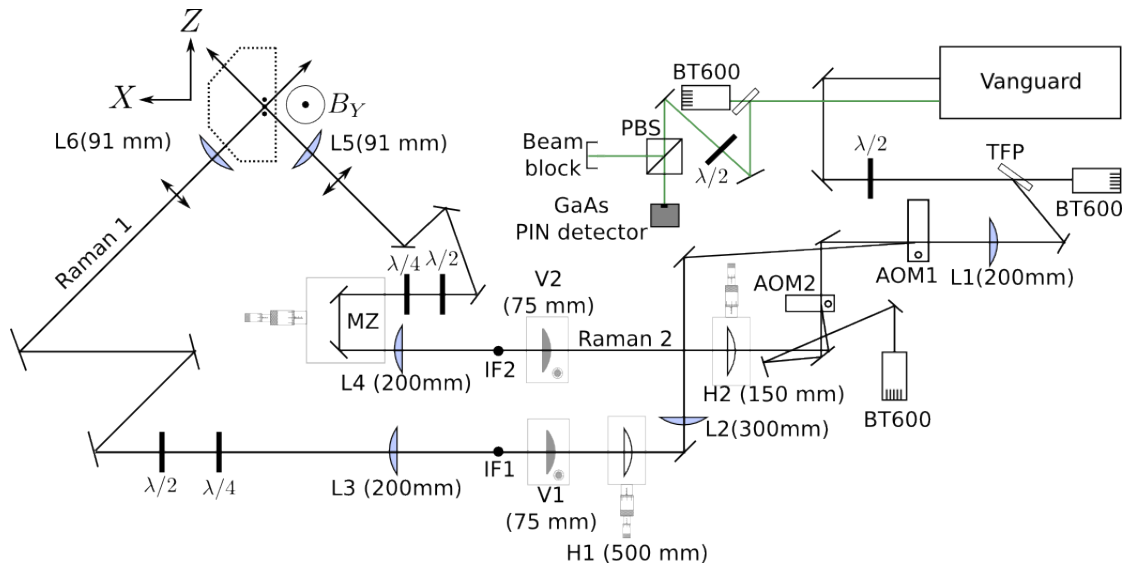


Figure 2.30: Raman transition set up: The schematics of the Raman set up optics with the mode-locked tripled Vanadate laser. AOM1 and AOM2 generate the frequency shifts necessary to address various stimulated Raman transitions. The 532 nm light (shown in green) is used to monitor the repetition rate, and correct for the fluctuations in the repetition rate, as described in the text. The horizontal cylindrical lenses are shown in white, vertical cylindrical lenses are shown in gray and the spherical lenses are shown in blue.

The two photon hyperfine transition Rabi frequency, Ω depends on the product of the electric field amplitudes of the two beams. Thus

$$\Omega \propto \sum_{n=-\infty}^{\infty} J_n(\phi) J_{n+2}(\phi) e^{i2(\delta k)x}, \quad (2.59)$$

as the pair of sidebands separated by $2\omega_{EOM} \approx \omega_{hf}$ contribute to the hyperfine transition.

Unfortunately,

$$\sum_{n=-\infty}^{\infty} J_n(\phi) J_{n+2}(\phi) = 0, \quad (2.60)$$

as $J_{-n}(\phi) = (-1)^n J_n(\phi)$, and hence the Rabi frequency vanishes from destructive interference of sidebands with opposite phases. This problem can be overcome by making the phase in the right hand side of Eq. (2.59) dependent on n , as discussed in Ref. [106]. This is achieved by splitting the frequency modulated beam into two arms of a Mach-Zehnder interferometer and recombining them at the ion position. The delay in the Mach-Zehnder interferometer is adjusted to maximize the Rabi frequency. Even with the properly adjusted interferometer, more than half of the optical power is wasted due to the destructive interference.

We simulated the ferromagnetic quantum Ising model for $N = 2$ to $N = 9$ spins (Chapter 3), and the frustrated spin network with $N = 3$ spins (Chapter 4) with this set up.

A mode-locked laser provides the desired frequency comb without any phase problem as in the EOM. Figure 2.30 shows the optics schematics of our Raman

set up using the mode locked laser. (The set up with the Ti:Sapphire CW laser was almost identical to this one, with the vanguard laser replaced by the frequency doubled Ti:sapphire light sent through the EOM). The two Raman beams, referred to as Raman 1 and Raman 2 in the diagram, intersect perpendicular to each other at the ion position. Thus the wave-vector difference $\Delta k = \sqrt{2}k$, where k is the magnitude of the wave-vector of each beam. Raman 1 is generated by the negative first order deflection of AOM1 (from Brimrose Corp), which is driven by the output MP2 in Fig. 2.28b at approximately 217.7 MHz to stabilize the repetition rate, as described in section 2.6.4. We image an intermediate focus IF1 at the ion position (relay imaging), by first collimating the beam in both the horizontal and the vertical directions using a 200 mm spherical lens, followed by focusing down using a 91 mm spherical lens.

AOM2 is driven by radio frequencies generated by an arbitrary waveform generator (AWG, Model no. DA-12000 made by Chase Scientific Company, 12 bit, 1 Gs/sec, 4 MB memory). The carrier transition is excited at an AOM2 driving frequency $\nu_{AOM2} \approx 204.819$ MHz, while the red and blue sidebands are excited at ≈ 199.97 and ≈ 209.66 MHz respectively. AOM2 is imaged at the ion position by relay imaging method as follows. A horizontal cylindrical lens H2 ($f=150$ mm) images the AOM2 aperture at the intermediate focus IF2. This is also approximately the vertical focus of V2. A 200 mm focal length spherical lens is about 200 mm away from the intermediate focus, and hence it collimates the beam in both the horizontal and the vertical directions. The beam is approximately $220 \mu\text{m}$ ($1/e^2$ radius in intensity) in the horizontal direction and $20 \mu\text{m}$ in the vertical direction

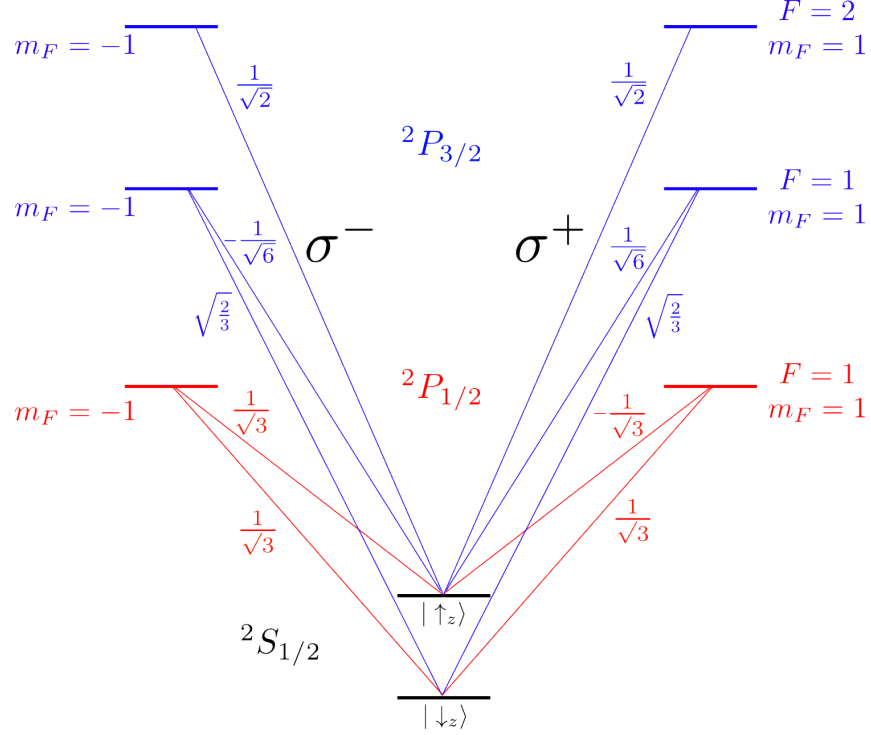


Figure 2.31: **The Clebsh-Gordan coefficients relevant for the two photon hyperfine Raman transition:** We show the Clebsh-Gordan (CG) coefficients for relevant states coupled by the σ^+ and the σ^- polarizations. A linearly polarized light cannot drive the hyperfine transition, as various paths interfere destructively. The transitions $|\uparrow_z\rangle \leftrightarrow ^2P_{3/2}|F = 2, m_F = \pm 1\rangle$ contributes to the Stark shift only.

at the intermediate focus. This collimated beam is then focused by a spherical 91 mm focal length lens at the ions. The Mach-Zehnder delay stage (MZ) is used to equalize the length of the Raman 1 and Raman 2 arms, to overlap the arrival times of the laser pulses at the ion position through these two paths.

The $\lambda/4$ and the $\lambda/2$ wave-plates are used to gain full control of the polarization of the Raman beams. The polarizations are shown in double headed arrows. The magnetic field points upwards in this figure. The choice of our beam polarizations are dictated by the Clebsh-Gordan coefficients of the relevant transitions (Fig. 2.31). We avoid driving the Zeeman transitions between the

$|\downarrow_z\rangle \rightarrow |F = 1, m_F = \pm 1\rangle$ states by minimizing the π polarization component in our Raman beams. The Raman beams are linearly polarized perpendicular to each other and perpendicular to the magnetic field B_Y . A linear polarization is an equal superposition of σ^+ and σ^- light (in the atomic basis, w.r.t. to the externally applied magnetic field B_Y), and cannot drive the hyperfine transition alone, since the transition paths interfere destructively due to a relative negative sign of the Clebsh-Gordan coefficients between the paths, as seen from Fig. 2.31. In our set up each beam is linearly polarized and hence the beams do not interfere at the ion position, and the total intensity is constant at all times. However the two photon Rabi frequency is proportional to the excess electric field in the σ^+ polarization over the σ^- polarization, which creates a beatnote at the frequency difference of the two beams.

The two photon Rabi frequency Ω is proportional to the product of the electric fields of the two Raman beams. Thus, $\Omega \propto \sqrt{\alpha_1 \alpha_2 (1 - \alpha_1)}$ in our set up, where α_1 and α_2 are the deflection efficiencies of AOM1 and AOM2 respectively. The two photon Rabi frequency is maximized for $\alpha_1 = 0.5$.

2.7 Quantum simulation recipe for experimentalists

This section describes the detailed steps of the quantum simulation experiments done in our laboratory. Some of the most important instruments required are:

- **Lasers** - Ti:Sapphire laser (with 532 nm Verdi-18 pump) and frequency dou-

bler for generating the Doppler cooling, detection, optical pumping, and protection/additional cooling light at 369.5 nm, 355 nm mode-locked laser for stimulated Raman transitions, 935 nm and 638 nm (semiconductor diode) repump lasers, 399 nm (semiconductor diode) ionization laser.

- **Imaging** - Photomultiplier tube, and ICCD camera.
- **Frequency modulators** - 7.37 GHz (Doppler cooling), 2.105 GHz (optical pumping) and 3.1 GHz (935 nm repump) EOM; AOMs for Doppler cooling, detection, protection, Raman beams, Iodine saturation absorption spectroscopy. Their supply radio-frequency oscillators, and amplifiers.
- Trap electrode voltage supplies (DC and radio frequency), and
- The FPGA (and the control program) running the experimental sequence, and the data acquisition.

Here are the steps to be followed.

1. Lock all the laser frequencies. This involves locking the Ti:Sapphire laser (etalon lock, reference cavity lock, iodine saturation spectroscopy lock), locks for the diode lasers (935 nm, 399 nm, any 739 nm laser), repetition rate lock of the 355 nm mode-locked laser.
2. **Load a single $^{171}\text{Yb}^+$ ion in the trap** (section 2.2.1).
3. Check the alignment and power of the near resonant beams (detection, Doppler cooling, optical pumping, protection/additional cooling), by maximizing the scatter

from the detection and the cooling beams, and minimizing the scatter from the optical pumping beam by the ion. Block the 935 nm repump to make sure that the scattering is caused due to the ion, and not by scattering off the electrodes, trap parts or the imaging system. Work on the alignment, and the polarizations of all the beams, if necessary. In our set up, the FPGA detection counters are tied to the **Detect** window in the experimental sequence. Hence we use the following experimental sequences to check the optimal settings for the near resonant beams. The experimental chapters are shown in different colors. We use a PMT to monitor the fluorescence from the ion.

- *To check the detection* - **Doppler Cool** → **Detect**. We get approximately ten photon counts on average from the detection beam in $800 \mu s$.
- *To check the Doppler cooling* - same as above, except now block the detection beam with a beam-block, or turn the detection AOM *OFF* from the radio-frequency switch box, and turn the Doppler cooling AOM *ON* all the time. The Doppler cooling time in our experiment is usually 3 ms, but we shall detect the scatter from the ions only during the **Detect** chapter ($800 \mu s$) in this diagnostic test. The PMT detects about ten photons on an average from the cooling beam. Don't forget to put the Doppler AOM back to the computer control, and unblock or turn the detection beam back *ON*.
- *To check the optical pumping* - **Doppler Cool** → **Optical pump** → **Detect**. The PMT counts should be close to zero (less than one count on an average in our experiment).

4. Drive carrier Rabi oscillations with the Raman beams, maximize the Rabi frequency by working on the Raman beam alignments. If the frequency of the carrier transition is unknown, a frequency scan of one of the Raman beam AOMs may be necessary. The experimental sequence is [Doppler Cool](#) → [Optical pump](#) → [Raman](#) → [Detect](#). Scan the [Raman](#) pulse duration to find the $\pi/2$ time, and then maximize the scattering by the ion, keeping the [Raman](#) pulse duration fixed at the $\pi/2$ time. To get a finer response in the alignment, a longer pulse duration ($5\pi/2$, or $9\pi/2$) may be used.

5. Check the spin/qubit coherence. A Ramsey experiment would give us an idea of any decoherence due to magnetic field and other noises, that affect the frequency splitting of the qubit state. If we use the 355 nm mode locked laser for the $\pi/2$ pulses in the Ramsey interferometry, the results would also indicate the efficacy of the beat-note lock. The Ramsey experimental sequence is [Doppler Cool](#) → [Optical pump](#) → [Raman \(\$\pi/2\$ \)](#) → [Delay](#) → [Raman \(\$\pi/2\$ \)](#) → [Detect](#).

The intensity noise on the Raman beams due to beam pointing instability or power fluctuations can be estimated from the decay in the amplitude of the carrier Rabi oscillation signal.

6. Take a frequency scan to observe all the important features of the system, such as the Zeeman states, and the motional sidebands (the Raman pulse duration should be long enough and adjusted to see the features). Make sure that the Zeeman and the motional transition are at the expected frequencies. Any peak due to the micromotion must be removed by tweaking the static voltages on the trap electrodes.

The Zeeman transitions may be suppressed by tweaking the polarizations of the Raman beams, and the direction of the magnetic field by varying the currents flowing through the magnetic coils.

7. *Differential A.C. Stark shift* from each of the Raman beams may be measured by turning on that beam in the [Delay](#) chapter of the Ramsey experimental sequence. The difference in the frequencies of the Ramsey fringes with and without the Raman beam present in the [Delay](#) chapter is the differential A.C. Stark shift from the Raman beam. A typical differential A.C. Stark shift in the qubit states of $^{171}\text{Yb}^+$ with about 1 Watt 355 nm beam focused to a $150\ \mu\text{m} \times 7\ \mu\text{m}$ waists (cylindrical beam) is about 400 Hz. This measurement can be used to center the Raman beams horizontally on the ion. Move the ion horizontally by changing the static voltages on the trap electrodes, and make the A.C. Stark shift from each beam symmetric about the ion position with normal static voltage settings.
8. *Raman sideband cooling* - Turn on the sideband cooling sequence ([SBCool](#)), at the sideband frequencies (estimated from the frequency scan). The red sideband peak in a Raman frequency scan should be depleted in the presence of the sideband cooling. In our experimental geometry, the Raman beams predominantly couple to the X -transverse modes, and hence it is hard to cool the Y -modes appreciably.
9. *Measure the sideband frequencies precisely*. The experimental sequence is: [Doppler Cool](#) → [Optical pump](#) → [SBCool](#) → [Raman](#) → [Detect](#). Turn the power in one of the Raman beams (we call it Raman 2) to a very low value, and find the position of the sidebands carefully. The sideband frequencies in the limit of zero optical power

do not contain the differential A.C. Stark shifts, thus measure the ‘true’ sideband frequencies at this trap configuration. Note that the differential Stark shift from the other beam (Raman 1) is still present. However, the contribution from Raman 1 in this experiment is primarily to add the two photon differential A.C. Stark shift, which is typically negligible compared to the four photon differential A.C. Stark shift, arising due to off-resonant coupling of the Raman beatnote (at the sideband frequency) to the carrier transition. Typical numbers in our set up are 600 Hz for the two photon Stark shift (from the two beams), versus about 30 KHz for the four photon Stark shift (when driving a sideband at about 5 MHz).

Once we find the sideband frequencies, we set the frequency of the carrier transition (that will drive the effective external magnetic field in our quantum Ising Hamiltonian),

$$\nu_{carr} = \frac{\nu_{rsb} + \nu_{bsb}}{2}. \quad (2.61)$$

Our next task is to balance the power in the two Raman beat-notes (referred to as the rsb and the bsb beat-notes), so that the four photon differential A.C. Stark shift from the off-resonant carrier is canceled, when symmetrically detuned about the carrier (to drive the Mølmer-Sørensen transition in multiple spins later). We increase the optical power in the beat-notes by increasing the power in the radio-frequency signal driving the AOM 2. As the differential A.C. Stark shift from the AOM 2 will shift all the three frequencies {carrier, rsb, bsb}, first we add/subtract the pre-calibrated differential A.C. Stark shift from all the frequencies. Next, we detune both the rsb and the bsb beat-notes symmetrically from the carrier by a few

sideband line widths (which can be estimated from the width of the sideband peaks in the frequency scan, or by driving a sideband on resonance).

If the power in the rsb and the bsb beat-notes are balanced, the four photon differential A.C. Stark shift should cancel, as the beat-notes are detuned symmetrically about the carrier. We check this by a Ramsey experiment, with the following sequence, **Doppler Cool** → **Optical pump** → **SBCool** → **Raman ($\pi/2, 0$)** → ***Off-resonant Raman rsb with rf power P_1*** + ***Off-resonant Raman bsb with rf power P_2*** → **Raman ($\pi/2, \pi/2$)** → **Detect**. The duration of the chapter in *italics* is scanned.

Here Raman ($\pi/2, \phi$) is a $\pi/2$ pulse with a phase ϕ . Thus we initialize the spin along the y -axis (by rotating about the x -axis of the Bloch sphere, $\phi = 0$ refers to the x -axis.) Then we turn on the detuned rsb and bsb beat-notes. If the A.C. Stark shift is nulled, these beat-notes do not rotate the spin state in the Bloch sphere, and hence the final rotation about the y -axis ($\phi = \pi/2$) from the Raman transition leave the spin in the same state. So, we'll detect a brightness of 0.5, as the detection basis is along the z -axis of the Bloch sphere. If, however, there is an uncompensated Stark shift due to unbalanced power in the two beams, we shall observe a Ramsey fringe as the duration of the '***Off-resonant Raman rsb with rf power P_1*** + ***Off-resonant Raman bsb with rf power P_2*** ' chapter is scanned. Tweak the power P_1 , and P_2 to null this fringe over the maximum duration of the desired quantum simulation experiment.

10. Drive the red sideband on resonance to measure the sideband Rabi frequency more precisely. For this, set the Raman rsb beat-note on resonance with the motional

red sideband transition, and detune the bsb beat-note from the blue sideband resonance by 4-5 times the estimated sideband Rabi frequency. Since the red sideband transition for the optically pumped spin state $|\uparrow_z\rangle$ is suppressed due to the Raman sideband cooling, we apply a π pulse to flip the spin state to $|\uparrow_z\rangle$. We observe the $|\uparrow_z, n\rangle \leftrightarrow |\downarrow_z, n+1\rangle$ Rabi oscillation, with $n \approx 0$, and measure the frequency of the oscillation. This should be equal to $\eta\Omega$, where η is the Lamb-Dicke parameter, and Ω is the carrier Rabi frequency consistent with the optical intensity applied to drive the sideband. The experimental sequence is: [Doppler Cool](#) → [Optical pump](#) → [SBCool](#) → [Raman \(\$\pi\$ \)](#) → [*Raman rsb on resonance + off-resonant Raman bsb*](#) → [*Detect*](#).

Similarly, measure the blue sideband Rabi frequency precisely by bringing the Raman bsb beat-note on resonance with the motional blue sideband transition, and detuning the rsb beat-note away from the transition. The experimental sequence is, [Doppler Cool](#) → [Optical pump](#) → [SBCool](#) → [*Off-resonant Raman rsb + Raman bsb on resonance*](#) → [*Detect*](#).

Now that we have found the appropriate frequency and power settings for the Mølmer-Sørensen transitions, we shall calibrate the effective transverse magnetic field, B before moving on to multiple ions.

11. The strength of the B field is given by,

$$B = \frac{\Omega_B}{2}, \quad (2.62)$$

where Ω_B is the carrier Rabi frequency. We change the power of the radio frequency signal driving the Raman AOM P to vary Ω_B , and hence B . We calibrate the B field for a given radio-frequency power P , by measuring the B field strength for a few P values, and following the trend.

12. **Load another $^{171}\text{Yb}^+$ ion in the trap.** Now we have two ions, and we are ready to observe Ising coupling induced oscillations between spin states.
13. Detune the Raman rsb and bsb beat-notes symmetrically about the carrier, at frequencies $\nu_{HF} \pm \mu$, where μ is the beat-note frequency, $\mu = \nu_x + \delta$. Choose δ to be larger than a few times the sideband Rabi frequencies ($\eta\Omega$) in order to avoid populating the phonon modes. Now prepare the spins in the $|\downarrow_z\downarrow_z\rangle$ states, and apply the Raman beat-notes. The Ising interaction, $J\sigma_x^1\sigma_x^2$ will make the spins oscillate between the $|\downarrow_z\downarrow_z\rangle$ and $|\uparrow_z\uparrow_z\rangle$ states. The frequency of the oscillations is the Ising coupling (multiplied by two) between the spins. The experimental sequence is:
Doppler Cool → Optical pump → SBCool → Raman rsb and bsb symmetrically detuned from the carrier → Detect.

The probability of $|\uparrow_z\uparrow_z\rangle$ state, $P(|\uparrow_z\uparrow_z\rangle)$ should reach unity (the average number of spins in the $|\uparrow_z\rangle$ state should reach 2) in the course of time evolution. At this point, we may also maximize the contrast of this oscillation by fine adjustments of the rsb and bsb beat-note frequencies. For this, set the pulse duration to the time when $P(|\uparrow_z\uparrow_z\rangle)$ is at its maximum, and frequency scan the rsb beat-note around $\mu = \omega_x + \delta$, keeping the bsb beat-note fixed in the previous experimental sequence. Find the frequency of the rsb beat-note that maximizes $P(|\uparrow_z\uparrow_z\rangle)$. This

should almost be identical to the frequency that we set earlier to observe the Ising coupling induced oscillations. If the new frequency is slightly shifted, reset the carrier according to eq 2.61.

14. **Load the desired number of ions in the trap.**
15. If we are going to use a CCD imager to detect the spatial resolved spin states, at this point we should find the Region of Interests (ROIs), and discriminator counts of the ions [91] on the CCD.
16. [Optional] Take a Raman frequency scan, and identify the motional transitions. Include other modes in the sideband cooling sequence. The transverse modes used for generating the Ising couplings are tightly packed together in frequency, and hence the modes need not be addressed separately for Raman cooling. Empirically, three Raman beat-notes are sufficient to cool down almost all the X -modes for a system of 10 spins in our experiment.
17. Now we are ready to run a quantum simulation experiment. Have the parameters ready for the quantum simulation experiment, such as the Mølmer-Sørensen detuning (δ), phases of the carrier $\pi/2$ pulses for single qubit rotation, the initial B -field, time constant τ of ramping the B field down. Table 2.1 lists the phases of various pulses used in our quantum simulation experiment.

Field/pulse	phase	comments
First $\pi/2$ pulse	180°	for polarizing the spins along the y -direction
B (carrier)	270°	for simulating FM quantum Ising model
B (carrier)	90°	for simulating AFM quantum Ising model
rsb	0°	
bsb	180°	
Final $\pi/2$ pulse	270°	for rotating the measurement basis

Table 2.1: Phases of various pulses used in quantum simulation.

2.8 Troubleshooting with $^{174}\text{Yb}^+$

$^{174}\text{Yb}^+$ has a zero nuclear spin and hence the hyperfine structure is absent in the electronic ground state. Thus the Doppler cooling beam does not need any sideband to cool the atom, unlike $^{171}\text{Yb}^+$ which requires a 14.74 GHz sideband. The lack of hyperfine Zeeman sub-levels also eliminates the coherent population trapping in the dark states [89], and results in an increased fluorescence.

$^{174}\text{Yb}^+$ can be used to troubleshoot optics alignment problems. To load $^{174}\text{Yb}^+$ we need only one 369.5 nm beam, the 935 nm beam and of course the loading beams. We switch all the lasers to $^{174}\text{Yb}^+$ frequencies (Table C.1), and try to capture $^{174}\text{Yb}^+$ ions by making sure that all the beams are approximately passing through the trapping region. Once we load $^{174}\text{Yb}^+$ ions (either in a crystal or in a cloud), we verify of the alignment of individual 369.5 nm beams (detection, Doppler cooling, optical pumping, and the protection beams), and the 935 nm beam.

The EOMs should be turned off to observe maximum fluorescence from

the $^{174}\text{Yb}^+$ ions.

If the alignment was the only problem, we should now be all set to load $^{171}\text{Yb}^+$ in our trap, after switching the current supply to the isotopically enriched oven. If we still cannot load $^{171}\text{Yb}^+$ in the trap, we should verify that the Doppler cooling and 935 nm EOMs are generating appropriate sidebands, and check that the magnetic field coils are not shorted.

Chapter 3

Simulation of the ferromagnetic quantum Ising model

3.1 Overview

The ferromagnetic quantum Ising model is one of the simplest models that admit a quantum phase transition (QPT). For N interacting spin-1/2 objects, the Hamiltonian is given by

$$H = - \sum_{\substack{i,j \\ j < i}} J_{i,j} \sigma_x^i \sigma_x^j - B \sum_i \sigma_y^i \quad (3.1)$$

where σ_α^i ($\alpha = x, y, z$) are the Pauli matrices for the i^{th} spin ($i = 1, 2, \dots, N$), $J_{i,j} (> 0)$ is the Ising coupling between spins i and j , and B is an effective transverse magnetic field. Here the Ising couplings are not limited to the nearest neighbors only, and the range of the interactions can be tuned, as we have discussed in the previous chapter. This Hamiltonian (Eq. (3.1)) shows quantum properties as the Ising interactions and the effective transverse field couple to non-commuting spin components.

In this chapter*, we discuss the simulation of the ferromagnetic quantum Ising Hamiltonian (Eq. (3.1)) in a chain of up to 16 trapped $^{171}\text{Yb}^+$ ions. We tune the effective transverse magnetic field while keeping the Ising couplings fixed, following

*Most of the results presented in this chapter are published in Ref. [41].

the adiabatic quantum simulation protocol [73], and directly measure the spin order along the Ising (x) direction. For an effective transverse magnetic field much stronger than the Ising interactions, the spins are polarized along the y -direction, resulting in a paramagnetic state along the x -direction. As the magnitude of the transverse field is lowered, the spins start to align themselves according to the ferromagnetic Ising couplings, and we observe a crossover between paramagnetic and ferromagnetic spin order. Since a QPT is expected to emerge for a sufficiently large system with a system Hamiltonian given by Eq. (3.1), the observed finite system crossover curves should sharpen as we scale the system up. In this chapter we compare the results of quantum simulation with $N = 2$ to $N = 9$ spins, and observe that the crossover curves between the phases indeed get sharper with increasing system size, prefacing the expected quantum phase transition in the thermodynamic limit. This experiment serves as a benchmark for simulation of arbitrary fully connected quantum spin models, for which the theory becomes intractable for more than a few dozen spins.

As described previously, we use stimulated Raman transitions to engineer Hamiltonian (Eq. (3.1)). The experiments with $N = 2$ to $N = 9$ spins are performed using Raman beams from a Ti:Sapphire laser, which is ≈ 2.7 THz detuned from the $^2S_{1/2}$ to $^2P_{1/2}$ resonance in $^{171}\text{Yb}^+$ at 369.5 nm, resulting in a small but non-negligible probability of spontaneous emission, which introduces decoherence in the coherent time evolution. We compare the experimental results with numerical calculations using a quantum trajectory method, which becomes inefficient beyond a few dozen spins. We use a far detuned pulsed laser at 355 nm to reduce the

decoherence error due to spontaneous emission, and $N = 16$ ion experiments are performed with this laser.

3.2 Symmetries of the Hamiltonian

The quantum Ising Hamiltonian (Eq. (3.1)) has a global spin rotation symmetry by a Bloch vector angle of π about the B field axis, or the y -axis. The single spin unitary rotation operator $U_r = \exp(-i\frac{\pi}{2}\sigma_y) = -i\sigma_y$ is a symmetry operation, under which the x -spin states* transform in the following way,

$$U_r|\uparrow\rangle = -|\downarrow\rangle \quad (3.2a)$$

$$U_r|\downarrow\rangle = |\uparrow\rangle. \quad (3.2b)$$

In our experiments we simulate the quantum Ising model by shining laser beams with nearly uniform intensities on all the ions. Thus the effective transverse magnetic field is near uniform across the spin chain, and the Ising couplings have a spatial reflection symmetry about the center of the spin chain. The Hamiltonian inherits this reflection symmetry.

In the absence of any external biasing field, a finite system does not spontaneously break the symmetry of the Hamiltonian. Thus as we tune the dimensionless parameter of the effective transverse field to the Ising couplings in the Hamiltonian, the symmetries are preserved. We shall elucidate this for a system of $N = 2$ spins in the next section.

*We omit the subscript x from the eigenstates of σ_x throughout this thesis.

3.3 Low energy eigenstates at T=0

We define the effective average Ising coupling as $J = \langle \sum_{j \neq i} J_{i,j} \rangle_i$, where $\langle \dots \rangle_i$ indicates averaging over the index i . With this definition, $J \approx 2J_0$ ($N > 2$) when the Ising couplings are limited to the nearest neighbors only ($J_{i,j} = J_0$ for $j = i \pm 1$, and 0 otherwise), and $J = (N-1)J_0 \approx NJ_0$ for ‘infinite range’ interactions ($J_{i,j} = J_0$ for any i and j). For $B/J \rightarrow 0$ the Hamiltonian is dominated by the Ising interactions, and the spins show ferromagnetic order along the x -direction. In the other limit of $B/J \rightarrow \infty$ the effective transverse field dominates over the Ising interactions, and the spins are polarized along the y -directions, or paramagnetic along the x -direction (we assume that $B > 0$). In between these two extremes, the system undergoes a crossover between these two phases, which approaches a quantum phase transition in the large system limit of $N \rightarrow \infty$.

3.3.1 States near $B/J = 0$

At $B/J = 0$, the ferromagnetic (FM) states $|\uparrow\uparrow\dots\uparrow\rangle$ and $|\downarrow\downarrow\dots\downarrow\rangle$ form a doubly degenerate ground state manifold, where $|\uparrow\rangle$ and $|\downarrow\rangle$ are the eigenstates of σ_x . Any quantum superposition of these two states is also a ground state. To find the ground states for small B/J , we treat the transverse field part of Hamiltonian (Eq. (3.1)), $H_B = -B \sum_i \sigma_y^i$ as a perturbation over the Ising Hamiltonian, $H_I = -\sum_{i<j} J_{i,j} \sigma_x^i \sigma_x^j$. H_B mixes the FM spin states and lifts the degeneracy in the ground state manifold.

As an example, let’s consider the case of $N = 2$ spins. Figure 3.1 shows the

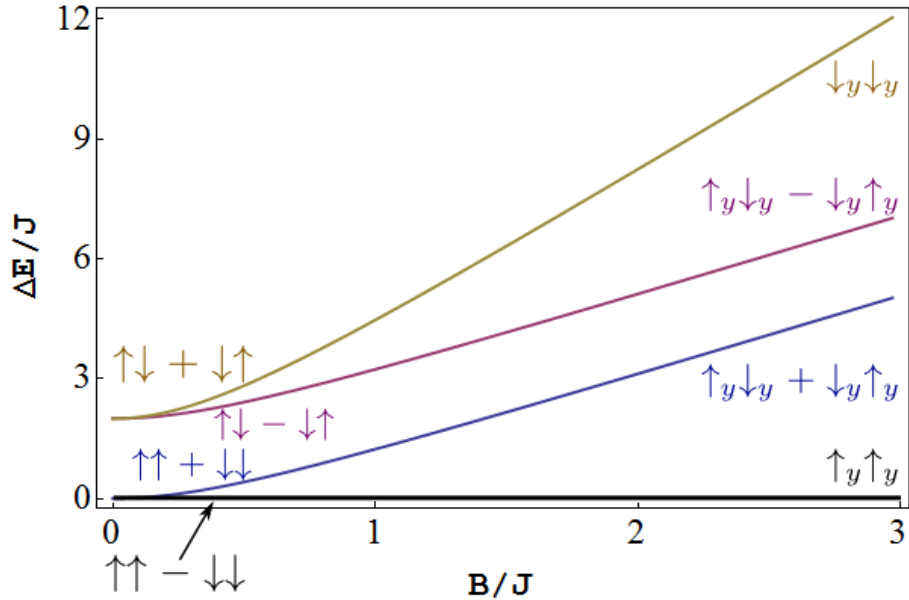


Figure 3.1: Energy spectrum of the ferromagnetic transverse Ising model for $N = 2$ spins: We plot the four eigenstates of Eq. (3.1) for $N = 2$ as a function of the dimensionless parameter B/J . The eigenstates are connected by the symmetries of the Hamiltonian- a global spin rotation symmetry about the y -axis by a Bloch vector angle of ‘ π ’, and the spatial reflection symmetry owing to the symmetric nature of the Ising couplings and the effective transverse field, as explained in section 3.2. The ground state is antisymmetric w.r.t. spin flip, but symmetric w.r.t. reflection. When we ramp the Hamiltonian at a finite rate in our experiment, non-adiabatic effects may lead to spin excitations to levels with the same symmetry as the ground state. The third excited state, which is the highest excited state in the case of $N = 2$ spins has the same symmetries as the ground state.

energy eigenstates of Eq. (3.1) for various values of B/J . At $B/J = 0$, the ground state manifold contains the eigenstates of H_I , namely $|\uparrow\uparrow\rangle$ and $|\downarrow\downarrow\rangle$ with energy $-J$. The other two states $|\downarrow\uparrow\rangle$ and $|\uparrow\downarrow\rangle$ with energies J belong to the excited state manifold. As $\sigma_y|\uparrow\rangle = -i|\downarrow\rangle$ and $\sigma_y|\downarrow\rangle = i|\uparrow\rangle$,

$$H_B|\uparrow\uparrow\rangle = iB(|\uparrow\downarrow\rangle + |\downarrow\uparrow\rangle) \quad (3.3a)$$

$$H_B|\downarrow\downarrow\rangle = -iB(|\uparrow\downarrow\rangle + |\downarrow\uparrow\rangle) \quad (3.3b)$$

$$H_B|\uparrow\downarrow\rangle = -iB(|\uparrow\uparrow\rangle - |\downarrow\downarrow\rangle) \quad (3.3c)$$

$$H_B|\downarrow\uparrow\rangle = -iB(|\uparrow\uparrow\rangle - |\downarrow\downarrow\rangle) \quad (3.3d)$$

Clearly, the first order perturbation matrix element between the two FM states $\langle\uparrow\uparrow|H_B|\downarrow\downarrow\rangle = 0$. The second order matrix elements between $|\uparrow\uparrow\rangle$ and $|\downarrow\downarrow\rangle$ are

$$E_{\uparrow\uparrow,\uparrow\uparrow} = \sum_{\gamma} \frac{\langle\uparrow\uparrow|H_B|\gamma\rangle\langle\gamma|H_B|\uparrow\uparrow\rangle}{E_0 - E_{\gamma}} = -\frac{B^2}{J} \quad (3.4a)$$

$$E_{\uparrow\uparrow,\downarrow\downarrow} = \sum_{\gamma} \frac{\langle\uparrow\uparrow|H_B|\gamma\rangle\langle\gamma|H_B|\downarrow\downarrow\rangle}{E_0 - E_{\gamma}} = \frac{B^2}{J} \quad (3.4b)$$

$$E_{\downarrow\downarrow,\uparrow\uparrow} = \sum_{\gamma} \frac{\langle\downarrow\downarrow|H_B|\gamma\rangle\langle\gamma|H_B|\uparrow\uparrow\rangle}{E_0 - E_{\gamma}} = \frac{B^2}{J} \quad (3.4c)$$

$$E_{\downarrow\downarrow,\downarrow\downarrow} = \sum_{\gamma} \frac{\langle\downarrow\downarrow|H_B|\gamma\rangle\langle\gamma|H_B|\downarrow\downarrow\rangle}{E_0 - E_{\gamma}} = -\frac{B^2}{J} \quad (3.4d)$$

Here states $|\gamma\rangle$ denote all states outside the ground state manifold, *i.e.*, the states $|\uparrow\downarrow\rangle$ and $|\downarrow\uparrow\rangle$, and we have used Eqs. (3.3). Thus the effective Hamiltonian

in the ground state manifold up to the second order in perturbations, in the basis formed by the FM states is,

$$\begin{pmatrix} -J - \frac{B^2}{J} & \frac{B^2}{J} \\ \frac{B^2}{J} & -J - \frac{B^2}{J} \end{pmatrix} = \left(-J - \frac{B^2}{J} \right) \mathbb{I}_2 + \frac{B^2}{J} \begin{pmatrix} 0 & 1 \\ 1 & 0 \end{pmatrix}. \quad (3.5)$$

Thus the new eigenstates are $(|\uparrow\uparrow\rangle - |\downarrow\downarrow\rangle)/\sqrt{2}$ and $(|\uparrow\uparrow\rangle + |\downarrow\downarrow\rangle)/\sqrt{2}$, with energies of $-J - 2B^2/J$ and $-J$ respectively. Since $J > 0$, the antisymmetric superposition is the new ground state, separated from the symmetric state (first excited state) by an energy of $2B^2/J = 2J(B/J)^2$. The ground state is *antisymmetric* w.r.t. the spin flip symmetry (Eqs. (3.2)), and *symmetric* w.r.t. the spatial reflection symmetry.

For a system size of up to a dozen spins, the ground state can be exactly calculated by diagonalizing the Hamiltonian (Eq. (3.1)), but the perturbation treatment presented here gives us some insight on how the degeneracy in the ground state splits in the presence of a small transverse field. We may generalize our discussion to larger spin chains, and note that for a system of N spins, the degeneracy in the ground state is generically broken at the N^{th} order in perturbation, and hence the energy splittings between the perturbed ground states is $\mathcal{O}((B/J)^N)$. We illustrate this for $N = 2$ and $N = 3$ spins in figure 3.2. The ground state is always entangled for small but finite B/J . For very large N , the ground state and the first excited states are nearly degenerate for $B/J < 1$ ($B > 0$). The perturbation theory breaks down when B/J approaches unity.

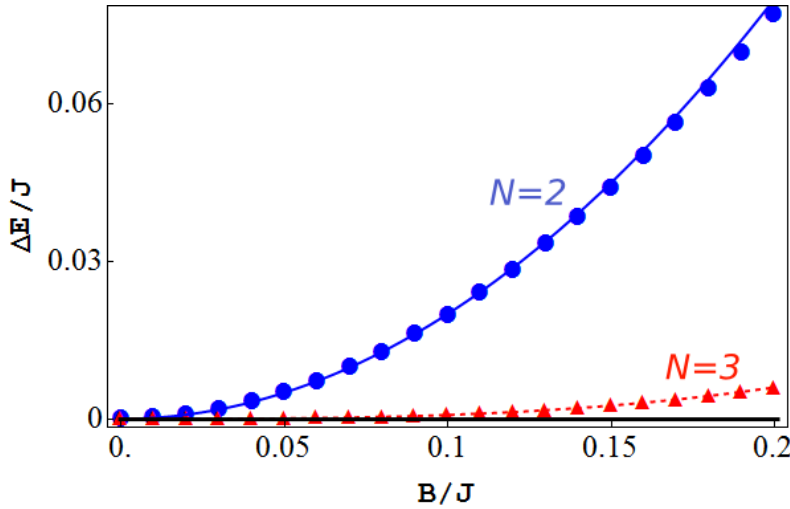


Figure 3.2: **Ground state degeneracy splitting by the transverse field:** A non-zero transverse field B breaks the degeneracy in the ground state manifold of Eq. (3.1) at $B = 0$. Since the FM ground states in the absence of a transverse field are connected by a global spin flip only, the degeneracy is broken in the N^{th} order in perturbation for a system of N spins, as explained in the text. Here we plot the energy of the first excited state (measured from the ground state) as a function of B/J for $N = 2$ and $N = 3$ spins. The disks and the triangles are the results from an exact diagonalization of Eq. (3.1), and the solid lines are quadratic ($N = 2$) and cubic ($N = 3$) polynomials in B/J . For a system of N spins, the energy splitting is $\mathcal{O}(B/J)^N$. When the Ising interactions are antiferromagnetic, the competition between the interactions may lead to increased degeneracy in the ground state manifold, and the transverse field may break the degeneracy more easily, as discussed in chapter 4.

Note that in the presence of long range ferromagnetic interactions the thermodynamic limit of H_I may not exist, as the energy density may become unbounded from below, unless the Ising couplings themselves implicitly depend on the system size N appropriately.

3.3.2 States near $B/J \rightarrow \infty$

At $B/J \rightarrow \infty$ ($J = 0$), the ground state of Hamiltonian (Eq. (3.1)) is non-degenerate, with all spins pointing along the y -direction, namely $|\uparrow_y \uparrow_y \dots\rangle$. The ground state transforms to $(-i\sigma_y)(-i\sigma_y)|\uparrow_y \uparrow_y\rangle = -|\uparrow_y \uparrow_y\rangle$ under the spin flip operation *i.e.*, it is *antisymmetric* w.r.t. the spin flip symmetry. This state is *symmetric* under the reflection symmetry of the Hamiltonian. The first excited states are the single spin flipped states, $|\downarrow_y \uparrow_y \uparrow_y \dots\rangle$, $|\uparrow_y \downarrow_y \uparrow_y \dots\rangle$, \dots . The second excited states are the double spin flipped states and so on.

For $B/J \rightarrow \infty$, we may treat H_I as a perturbation over H_B in the Hamiltonian. H_I lifts the degeneracy between the states in the first excited state manifold, as $-J_{ij}\sigma_x^i\sigma_x^j$ directly couples (first order in perturbation) the excited state with the i -th spin flipped and the excited state with the j -th spin flipped. So the degeneracy in the first excited state manifold is generically broken with a finite Ising interaction between the spins.

As an example, the first excited states with $N = 2$ spins are $|\uparrow_y \downarrow_y\rangle$ and $|\downarrow_y \uparrow_y\rangle$

at $B/J \rightarrow \infty$. As $\sigma_x|\uparrow_y\rangle = i|\downarrow_y\rangle$ and $\sigma_x|\downarrow_y\rangle = -i|\uparrow_y\rangle$,

$$H_I|\uparrow_y\downarrow_y\rangle = -J|\downarrow_y\uparrow_y\rangle \quad (3.6a)$$

$$H_I|\downarrow_y\uparrow_y\rangle = -J|\uparrow_y\downarrow_y\rangle \quad (3.6b)$$

Thus the effective Hamiltonian up to the first order in perturbation in the basis formed by the unperturbed states in first excited state manifold, *i.e.*, $|\uparrow_y\downarrow_y\rangle$ and $|\downarrow_y\uparrow_y\rangle$ is,

$$\begin{pmatrix} 0 & -J \\ -J & 0 \end{pmatrix} \quad (3.7)$$

Hence the new eigenstates are $(|\downarrow_y\uparrow_y\rangle + |\uparrow_y\downarrow_y\rangle)/\sqrt{2}$ with energy $-J$ and $(|\uparrow_y\downarrow_y\rangle - |\downarrow_y\uparrow_y\rangle)/\sqrt{2}$ with energy J . The energy splitting between these states is $2J$, independent of B to the first order in perturbation. Note that the ground state energy is $-2B$, and hence the energy splittings of these two perturbed states from the ground state $|\downarrow_y\downarrow_y\rangle$ are $2B - J$ and $2B + J$ respectively. We tabulate the symmetries of these and the other eigenstates of Eq. (3.1) for $N = 2$ spins in table 3.1. Similarly, for a system of N spins, the unperturbed first excited state manifold contains N single spin flipped states (along y) at $B/J \rightarrow \infty$, that are mixed and entangled by the Ising interactions H_I .

3.3.3 Quantum phase transition at $B = J$

In between the two extreme limits of $B/J \rightarrow 0$ and $B/J \rightarrow \infty$, the Ising interactions and the transverse field compete to align the spins accordingly. As B/J

Parameters	Eigenstates	Spin flip	Spatial Reflection
$B/J \rightarrow 0$	$\frac{1}{\sqrt{2}}(\uparrow\uparrow\rangle - \downarrow\downarrow\rangle)$	antisymmetric	symmetric
	$\frac{1}{\sqrt{2}}(\uparrow\uparrow\rangle + \downarrow\downarrow\rangle)$	symmetric	symmetric
	$\frac{1}{\sqrt{2}}(\uparrow\downarrow\rangle - \downarrow\uparrow\rangle)$	symmetric	antisymmetric
	$\frac{1}{\sqrt{2}}(\uparrow\downarrow\rangle + \downarrow\uparrow\rangle)$	antisymmetric	symmetric
$B/J \rightarrow \infty$	$ \uparrow_y\uparrow_y\rangle$	antisymmetric	symmetric
	$\frac{1}{\sqrt{2}}(\uparrow_y\downarrow_y\rangle + \downarrow_y\uparrow_y\rangle)$	symmetric	symmetric
	$\frac{1}{\sqrt{2}}(\uparrow_y\downarrow_y\rangle - \downarrow_y\uparrow_y\rangle)$	symmetric	antisymmetric
	$ \downarrow_y\downarrow_y\rangle$	antisymmetric	symmetric

Table 3.1: **Symmetries of the eigenstates:** The eigenstates of Eq. (3.1) are either symmetric or antisymmetric w.r.t. the two symmetries of the Hamiltonian—the spin flip symmetry and the reflection symmetry, as described in section 3.2. Here we tabulate the symmetries of the eigenstates of the Hamiltonian (Eq. (3.1)) for $N = 2$ spins in the two extreme limits of $B/J \rightarrow 0$ and $B/J \rightarrow \infty$.

is reduced from its infinite value, the system crosses over from the polarized or the paramagnetic state to the ferromagnetic state in a finite system. As the system size increases, a second order phase transition point emerges.

The ground state of Eq. (3.1) smoothly connects the ground states in these two limits of $B/J \rightarrow 0$ and $B/J \rightarrow \infty$ for all intermediate values of B/J . The first excited state in the limit of $B/J \rightarrow \infty$ remains the first excited state for all $B/J \neq 0$, and becomes a ground state at $B/J = 0$. The second excited state undergoes an avoided level crossing with the ground state.

As we vary the dimensionless parameter B/J , the instantaneous eigenstates of the Hamiltonian change preserving the symmetries (though in the infinite system size limit, the system may break the symmetries spontaneously). If the Hamiltonian is changed faster than the adiabatic limit, the system may be excited from one eigenstate to another, but states with opposite symmetries do not mix. As an

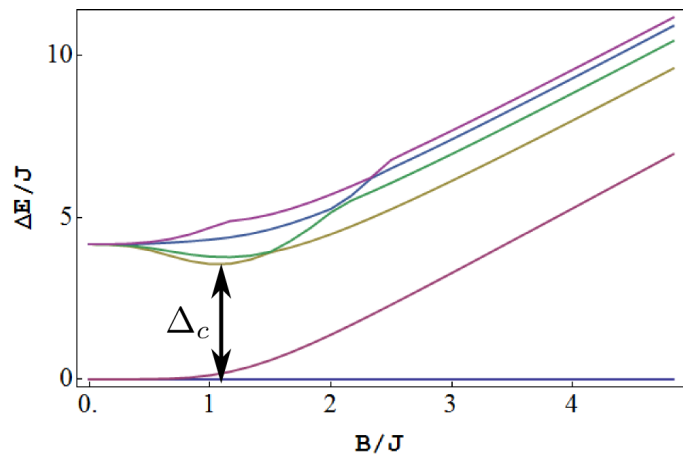


Figure 3.3: A few low energy eigenstates of Eq. (3.1) for $N = 5$ spins: Here we plot the energy spectra of six low energy eigenstates of Eq. (3.1) for $N = 5$. The Ising couplings fall-off with distance as $J_{ij} = J/|i - j|$ in this example. ΔE refers to the energy of the eigenstates relative to the ground state. The minimum energy between the ground and the first excited state having the same symmetry as the ground state is the critical gap, Δ_c that sets the relevant energy scale for an adiabatic quantum simulation, as discussed in the text. The cusps on the highest energy states shown here due to level crossings from other states not included in this diagram.

example, the ground state for $N = 2$ couples to the third (the highest) excited state as they are both antisymmetric w.r.t. spin flip and symmetric w.r.t. reflection. This result holds for $N > 2$ spins, and the minimum gap between the ground and the third excited state is the critical gap, Δ_c , which occurs at $B \approx J$, that sets the time scale of ramping the Hamiltonian in order to be adiabatic. We show a few low energy states of the Hamiltonian (Eq. (3.1)) and the critical gap for a system of $N = 5$ spins, with ferromagnetic coupling in Fig. 3.3. The critical gap depends on the system size, and vanishes in the limit of an infinite system. This also depends on the range of the interactions. For nearest neighbor interactions, this scales as $\approx 1/N$ with system size, while in the other extreme of perfectly uniform interactions between all the spins it scales more favorably, $\Delta_c \approx N^{-1/3}$ [107].

3.4 Experiment: onset of a quantum phase transition

3.4.1 Engineering the ferromagnetic Ising couplings

We simulate the Ising interactions by off-resonant stimulated Raman transitions on the transverse vibrational modes of the ion chain, following the Mølmer-Sørensen scheme [71], as described previously. The Ising coupling J_{ij} between spins i and j is given by

$$J_{i,j} = \Omega_i \Omega_j R \sum_{m=1}^N \frac{b_{i,m} b_{j,m}}{\mu^2 - \omega_m^2}. \quad (3.8)$$

where $b_{i,m}$ is the component of the normal mode eigenvector between ion i and mode m at frequency $\omega_m = 2\pi\nu_m$ (with $\nu_1 = \nu_X$ denoting the COM mode), and

$\Omega_i = g_i^2/\Delta$ is the carrier Rabi frequency on the i th ion. Here g_i is the single photon Rabi frequency of the i^{th} ion and Δ is the detuning of the Raman beams from the ${}^2S_{1/2} \leftrightarrow {}^2P_{1/2}$ transition. $R = \hbar\Delta k^2/(2M)$ is the recoil frequency of a single ion (of mass M) in the stimulated Raman transition process. The Mølmer-Sørensen beatnote μ controls the sign and range of the interactions, as different normal modes are virtually excited. We tune μ close to the COM mode, to make all the couplings of the same sign.

The COM mode ($m = 1$) makes all the couplings uniform across the chain, as the eigenvectors $b_{i,1} = 1/\sqrt{N}$ for all i , and hence J_{ij} is the same for any pair (i,j) . The system exhibits infinite range interactions, and the geometry of the spin chain (and the dimensionality) becomes irrelevant. For a sufficiently large system, each spin feels a ‘mean field’ created by all the other spins. We note that the Ising coupling $J_{ij} \propto 1/N$, thus the thermodynamic limit of Eq. (3.1) exists, and the phase transition point $B = J = \langle \sum_{j \neq i} J_{i,j} \rangle_i$ becomes independent of the system size. Other modes off-resonantly excited by the Raman beatnote suppress the range of the interactions.

We use up to $N = 9$ spins to observe the sharpening of the crossover from the paramagnetic to the ferromagnetic phase. In the experiment $\Delta \approx 2\pi \times 2.7$ THz, $\Omega_i \approx 2\pi \times 370$ KHz and we expect $J/N \approx 2\pi \times 1$ KHz for the beatnote detuning μ such that $\mu - \omega_1 \approx 4\eta_{i,1}\Omega_i$, ^{*}, as shown in Fig. 3.4a . This beatnote corresponds to

^{*}The Lamb-Dicke parameter for COM scales with the system size as $1/\sqrt{N}$. However, as pointed out in Ref. [53], a more stringent condition to avoid phonon excitations would be to keep the detuning constant for all system size. This is due to the fact that, even if the Lamb-Dicke parameter goes down with increasing system size, there are more spin configurations that lead to phonon excitations.

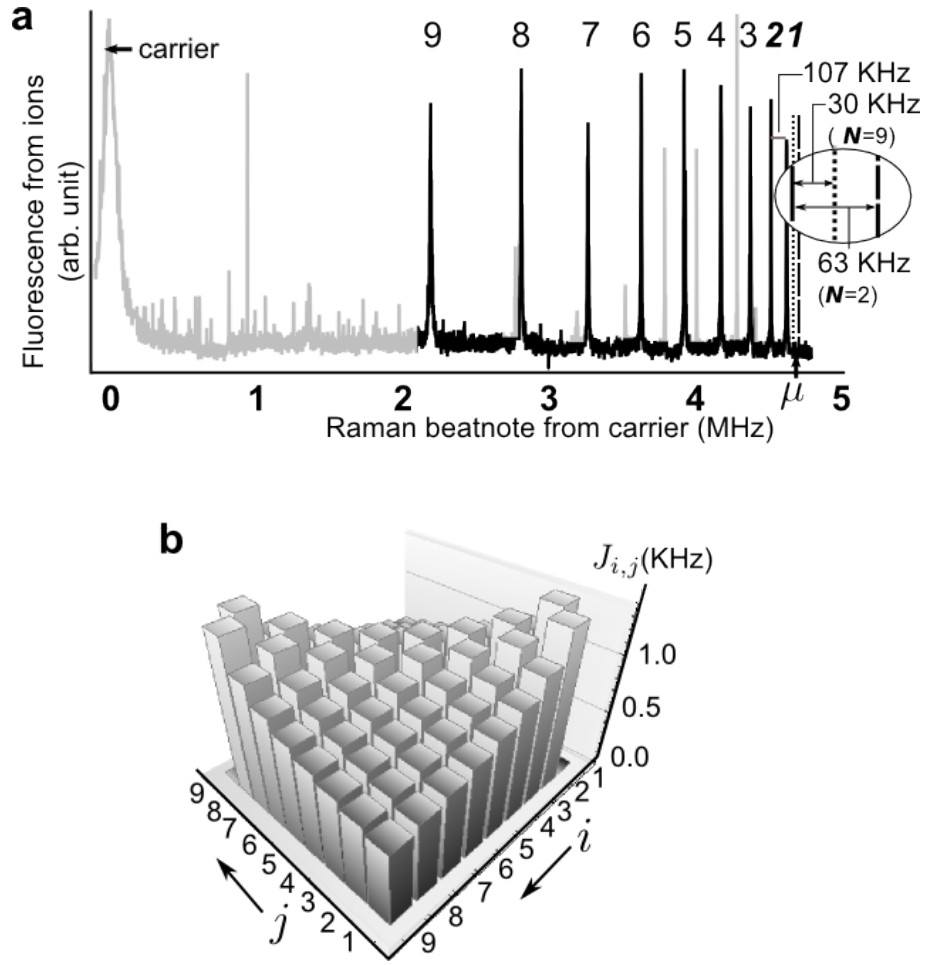


Figure 3.4: Raman spectrum of vibrational modes and Ising coupling profile for $N = 9$ spins: Transverse [108] vibrational modes are used in the experiment to generate Ising couplings according to Eq. (3.8). **a.** Raman sideband spectrum of vibrational normal modes along transverse X –direction for nine ions, labeled by their index m . The two highest frequency modes at ν_1 (CM mode) and $\nu_2 = \sqrt{\nu_1^2 - \nu_z^2}$ (“tilt” mode) occur at the same position independent of the number of ions. The dotted and the dashed lines show beatnote detunings of $\mu \approx \nu_1 + 30$ kHz and $\mu \approx \nu_1 + 63$ kHz used in the experiment for $N = 9$ and $N = 2$ ions respectively. Carrier transition, weak excitation of transverse– Y and axial– Z normal modes and higher order modes are faded (light grey) for clarity. **b.** Theoretical Ising coupling pattern (Eq. (3.8)) for $N = 9$ ions and uniform Raman beams. The main contribution follows from the uniform COM mode, with inhomogeneities given by excitation through the other nearby modes (particularly the tilt mode). Here, $J_{1,1+r} \propto 1/r^{0.35}$ ($r \geq 1$), as found out empirically. For larger detunings, the range of the interaction falls off even faster with distance, approaching the limit $J_{i,j} \propto 1/|i - j|^3$ for $\mu \gg \omega_1$ [109].

$2\pi \times 63$ KHz blue of the COM mode frequency for 2 ions and $2\pi \times 30$ KHz for 9 ions.

The expected Ising coupling pattern for a uniformly illuminated ion chain is shown in Fig. 3.4b for $N = 9$ ions and the couplings are dominated by uniform contribution of the COM mode. The non-uniformity in the Ising couplings arises from other vibrational modes and variation in Ω_i across the ion chain (gaussian Raman beams with a waist of $\approx 70 \mu\text{m}$ along the ion chain and $\approx 7 \mu\text{m}$ perpendicular to the ion chain were used in the experiment). For $N = 9$ ions the chain is $\approx 14 \mu\text{m}$ long, and the variation in Ω_i is $\approx 2\%$.

3.4.2 Experimental protocol and order parameters of the transition

In the experiment, we follow the highest excited state of the Hamiltonian $-H$ [39, 54], which is formally equivalent to the ground state of Hamiltonian H (Eq. (3.1)). This reduces direct excitation of the tilt mode phonons. The quantum simulation experiment proceeds as follows (Fig. 2.20). We cool all the X –transverse modes of vibration to near their ground states, and deep within the Lamb-Dicke regime by standard Doppler and Raman sideband cooling procedures. We initialize the spins to be aligned to the y – direction of the Bloch sphere by optically pumping to $|\downarrow_z \downarrow_z \dots \downarrow_z\rangle$ and then coherently rotating the spins through $\pi/2$ about the Bloch x –axis with a carrier Raman transition. Next we switch on the Hamiltonian H with an effective magnetic field $B_0 \approx 5J$ so that the spins are prepared predominantly in the ground state. Then we exponentially ramp down the effective magnetic field with a time constant of $\tau = 80 \mu\text{s}$ to a final value B , keeping the Ising couplings fixed.

We finally measure the spins along the Ising (x) direction by coherently rotating the spins through $\pi/2$ about the Bloch y -axis before fluorescence detection on a photomultiplier tube (PMT).

We repeat the experiment $\approx 1000 \times N$ times for a system of N spins and generate a histogram of fluorescence counts and fit to a weighted sum of basis functions to obtain the probability distribution $P(s)$ of the number of spins in state ($| \uparrow \rangle$), where $s = 0, 1, \dots, N$. We can generate several magnetic order parameters of interest from the distribution $P(s)$, showing transitions between different spin orders.

One order parameter is the average absolute magnetization (per site) along the Ising direction, $m_x = \frac{1}{N} \sum_{s=0}^N |N - 2s| P(s)$. Eq. (3.1) has a global time reversal symmetry of $\{\sigma_x^i \rightarrow -\sigma_x^i, \sigma_z^i \rightarrow -\sigma_z^i, \sigma_y^i \rightarrow \sigma_y^i\}$ as discussed previously and this does not spontaneously break for a finite system, necessitating the use of average *absolute* value of the magnetization per site along the Ising direction as the relevant order parameter. For a large system, this parameter shows a second order phase transition, or a discontinuity in its derivative with respect to B/J . On the other hand, the fourth-order moment of the magnetization or Binder cumulant $g = \sum_{s=0}^N (N - 2s)^4 P(s) / \left(\sum_{s=0}^N (N - 2s)^2 P(s) \right)^2$ [110, 111] becomes a step function at the QPT and should therefore be more sensitive to the phase transition. We illustrate this point by plotting the exact ground state order in the simple case of uniform Ising couplings for a moderately large system ($N = 100$) in Fig. 3.5.

When the spins are polarized along the y -direction of the Bloch sphere, the distribution of total spin along the x -direction is binomial and approaches a Gaus-

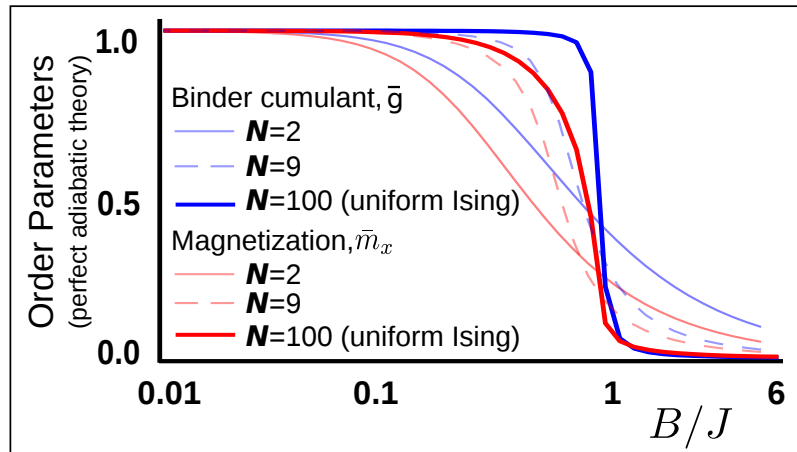


Figure 3.5: **Binder cumulant and magnetization for the adiabatic theory:** Theoretical values of order parameters \bar{m}_x and \bar{g} are plotted vs B/J for $N = 2$ and $N = 9$ spins with non-uniform Ising couplings as used in the experiment in the case of a perfectly adiabatic time evolution. The order parameters are calculated by directly diagonalizing Hamiltonian (3.1). Order parameters are also calculated for a moderately large system ($N = 100$) with uniform Ising couplings, to show the difference between the behaviors of \bar{m}_x and \bar{g} . In case of uniform Ising couplings the effective ground state manifold reduces to $N + 1$ dimensions in the total spin basis. The scaled Binder cumulant \bar{g} , unlike the scaled magnetization \bar{m}_x , approaches a step function near the transition point $B/J \approx 1$, making it experimentally suitable to probe the transition point for relatively small systems.

sian (with zero mean) in the limit of $N \rightarrow \infty$. For system size of N , m_x takes on theoretical value of $m_{x,N}^0 = \frac{1}{N^{2N}} \sum_{n=0}^N {}^N C_n |N - 2n|$ in the perfect paramagnetic phase ($B/|J| \rightarrow \infty$) and unity in the other limit of $B/J = 0$. We rescale m_x to $\bar{m}_x = (m_{x,N}^0 - m_x) / (m_{x,N}^0 - 1)$ which should ideally be zero in perfect paramagnetic phase and unity in perfect ferromagnetic phase for any N . This accounts for the ‘trivial’ finite size effect due to the difference between Binomial and Gaussian distribution. Similarly the Binder Cumulant g is scaled to $\bar{g} = (g_N^0 - g) / (g_N^0 - 1)$, where $g_N^0 = 3 - 2/N$ is the theoretical value of g for $B/J \rightarrow \infty$.

3.4.3 Results

In Fig 3.6a-b we present data for the scaled magnetization \bar{m}_x and the scaled Binder cumulant \bar{g} as B/J is varied in the adiabatic quantum simulation for $N = 2$ and $N = 9$ spins. The data shows the increased steepness for the larger system size. The scaled magnetization \bar{m}_x is suppressed by $\approx 25\%$ (Fig. 3.6a) and the scaled Binder cumulant \bar{g} is suppressed by $\approx 10\%$ (Fig. 3.6b) from unity at $B/J = 0$, predominantly due to decoherence from off-resonant spontaneous emission and additional dephasing due to intensity fluctuations in Raman beams during the simulation. Figure 3.7 shows the scaled magnetization, \bar{m}_x for $N = 2$ to $N = 9$ spins depicting the sharpening of the crossover curves from paramagnetic to ferromagnetic spin order with increasing system size. The linear time scale indicates the exponential ramping profile of the (logarithmic) B/J scale. The three dimensional background is unphysical, and is used just to help us visualize this sharpening.

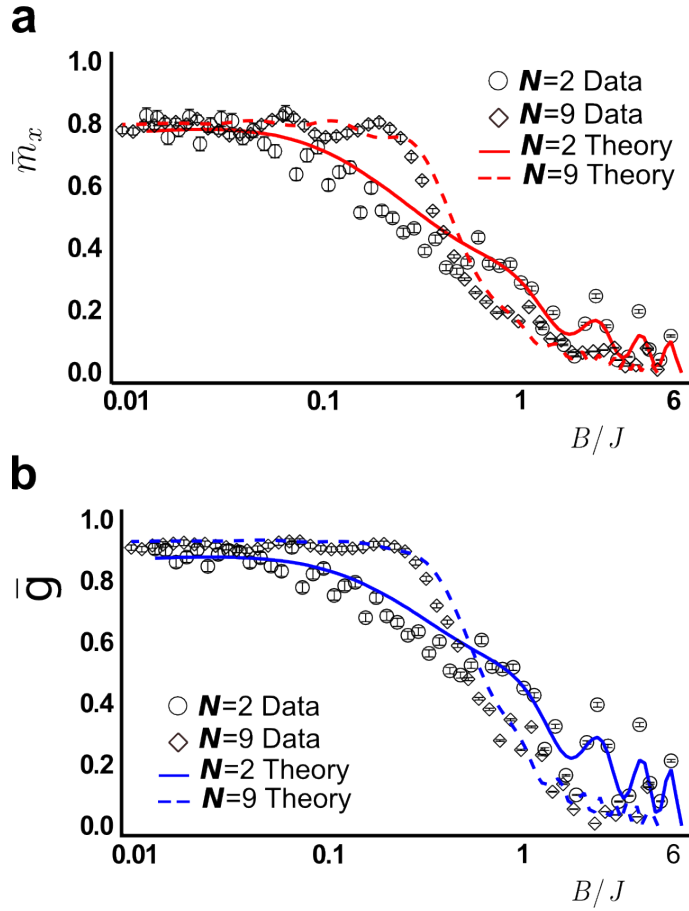


Figure 3.6: Emergence of the ferromagnetic spin order: **a.** Magnetization data for $N = 2$ spins (circles) is contrasted with $N = 9$ spins (diamonds) with representative detection error bars. The data deviate from unity at $B/J = 0$ by $\approx 20\%$, predominantly due to decoherence from spontaneous emission in Raman transitions and additional dephasing from Raman beam intensity fluctuation, as discussed in the text. The theoretical time evolution curves (solid line for $N = 2$ and dashed line for $N = 9$ spins) are calculated by averaging over 10,000 quantum trajectories. **b.** Scaled Binder cumulant (\bar{g}) data and time evolution theory curves are plotted for $N = 2$ and $N = 9$ spins. At $B/|J| = 0$ the data deviate by $\approx 10\%$ from unity, due to decoherence as mentioned before.

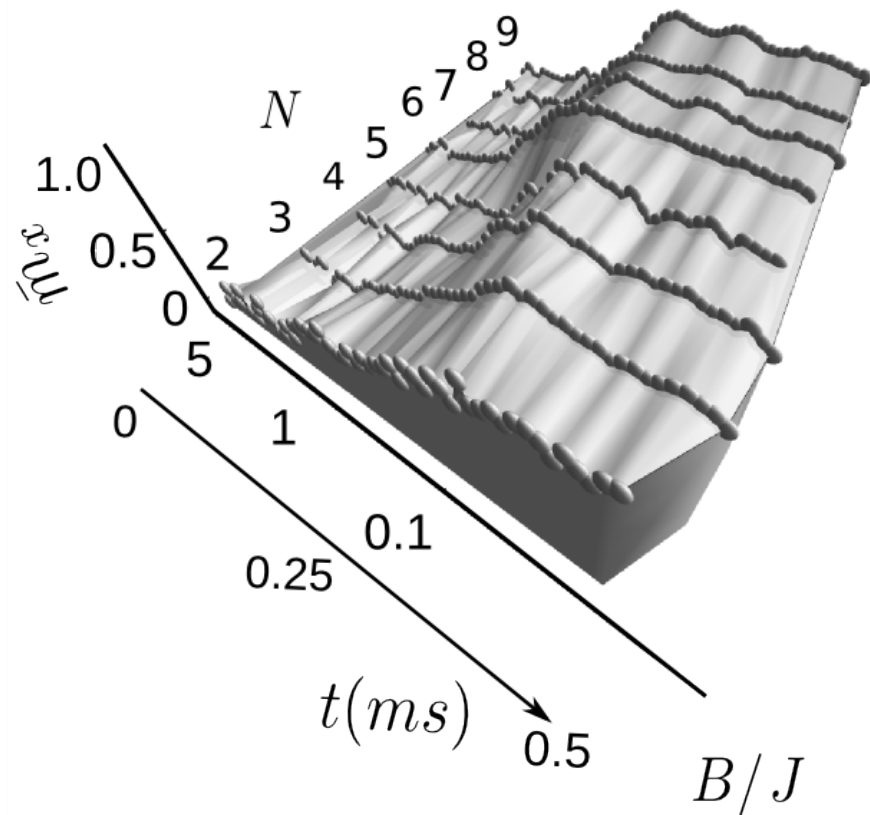


Figure 3.7: **Onset of a quantum phase transition- sharpening of the crossover curves with increasing system size.:** Scaled magnetization, \bar{m}_x vs B/J (and simulation time) is plotted for $N = 2$ to $N = 9$ spins. As B/J is lowered, the spins undergo a crossover from a paramagnetic to ferromagnetic phase. The crossover curves sharpen as the system size is increased from $N = 2$ to $N = 9$, pre-facing a QPT in the limit of infinite system size. The oscillations in the data arise due to imperfect initial state preparation and non-adiabaticity due to finite ramping time. The (unphysical) 3D background is shown to guide eyes.

We compare the data shown in Fig. 3.6 to the theoretical evolution taking into account experimental imperfections and errors discussed below, including spontaneous emission to the spin states and states outside the Hilbert space, and additional decoherence. The evolution is calculated by averaging 10,000 quantum trajectories. This takes only one minute on a single computing node for $N = 2$ spins and approximately 7 hours, on a single node, for $N = 9$ spins. Extrapolating from this calculation suggests that averaging 10,000 trajectories for $N = 15$ spins would require 24 hours on a 40 node cluster, indicating the inefficiency of classical computers to simulate even a small quantum system.

3.4.4 Sources of error in the quantum simulation

In this section we discuss some of the primary sources of errors in our quantum simulation. We characterize errors in the current simulation by plotting the observed parameter $P(FM) = P(0) + P(N)$ for $N = 2$ to $N = 9$ spins in Fig. 3.8. Theoretically $P(FM) = 2/2^N$ when the spins are transversely polarized *i.e.*, $P(FM) = 0.5$ for $N = 2$ spins and exponentially goes down to 0.004 for $N = 9$ spins, and unity when there is perfect ferromagnetic order. Since $P(FM)$ involves only two of the 2^N basis states, it is more sensitive to errors compared with the order parameters \bar{m}_x and \bar{g} . For instance, at $B/J = 0$ in Fig. 3.6a-b and Fig. 3.8a-d we find that \bar{m}_x and \bar{g} do not change appreciably with the system size, but $P(FM)$ degrades to ≈ 0.55 for $N = 9$ spins from ≈ 0.9 for $N = 2$. In Fig. 3.8 we compare the data with theory results that include experimental sources of diabatic errors.

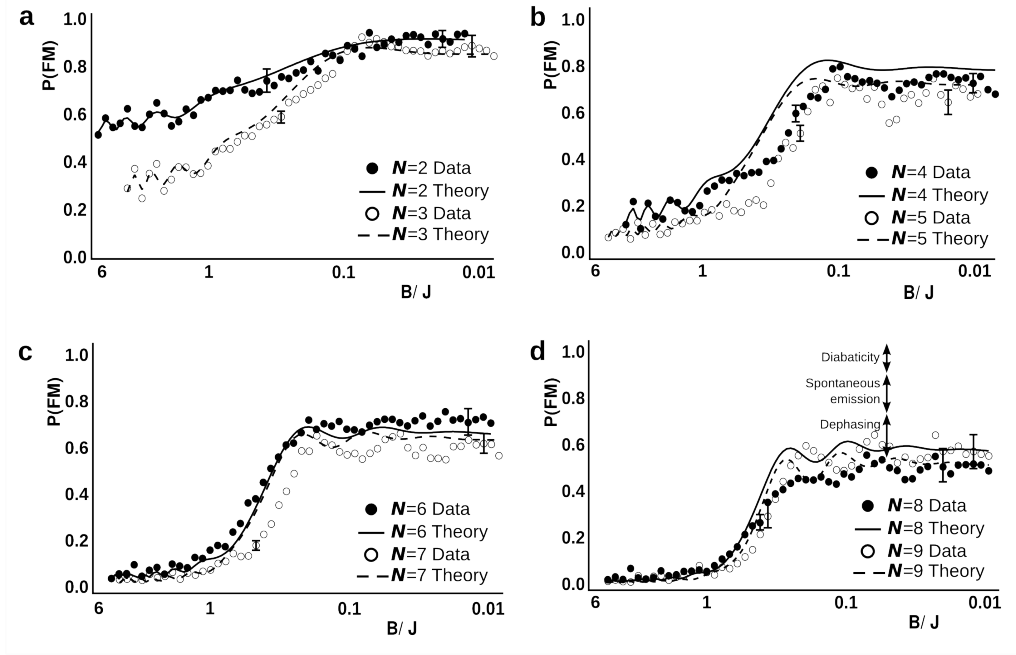


Figure 3.8: Suppression in the ferromagnetic fidelity with increasing system size: **a-d.** Ferromagnetic order $P(\text{FM}) = P(0) + P(N)$ is plotted vs B/J for $N = 2$ to $N = 9$ spins. The circles are experimental data and the lines are theoretical results including decoherence and imperfect initialization. As this quantity includes only two of 2^N basis states random spin-flips and other errors degrade it much faster than the magnetization and Binder cumulant. The representative detection error bars are shown on a few points for each N . The $P(\text{FM})$ reduces from ≈ 0.9 to ≈ 0.55 as the system size is increased from two to nine. The principle contribution to this degradation is decoherence, predominantly due to spontaneous emission from intermediate ${}^2P_{1/2}$ states in the Raman transition and additional dephasing primarily due to intensity fluctuations in Raman beams. Shown in **d** is an estimated breakdown of the suppression of $P(\text{FM})$ from various effects for $N = 9$ spins. Non-adiabaticity due to finite ramping speed, spontaneous emission and additional dephasing due to fluctuating Raman beams suppress $P(\text{FM})$ by $\approx 8\%$, $\approx 18\%$ and $\approx 24\%$ respectively from unity ($B/J \rightarrow 0$).

Some of the primary sources of experimental error are discussed below:

Diabaticity

Since we are ramping the Hamiltonian at a finite speed, there is a non-zero probability of population transfer to the excited states. As discussed in the previous chapter, the diabaticity is related to the critical gap (Δ_c) between the ground and the relevant excited state. Diabaticity due to finite ramping speed and error in initialization is estimated (by direct numerical integration of the Schrödinger's equation) to suppress P(FM) by $\approx 3\%$ for $N = 2$ to $\approx 8\%$ for $N = 9$. This also gives rise to the oscillations seen in the data (Fig. 3.6a-b and Fig. 3.8a-d).

Spontaneous Emission

The experiments with $N = 2$ to $N = 9$ are done with Raman beams detuned by 2.7 THz from the $^2S_{1/2} - ^2P_{1/2}$ transitions, which corresponds to a $\approx 10\%$ spontaneous emission probability per spin in 1 ms.

Spontaneous emission during the otherwise coherent time evolutions leads to the following errors (figure 3.9):

- *Spin flip* – When one of the $^2P_{1/2}|F = 1, m_F = \pm 1\rangle$ states are populated, spontaneous emission from them may lead to spin flip with probability 1/3.
- *Throwing the system out of the Hilbert space* – Spontaneous emission may populate the Zeeman states with a probability of 1/3, which are not included in the Hilbert space of the effective spin-1/2 system. The Zeeman states,

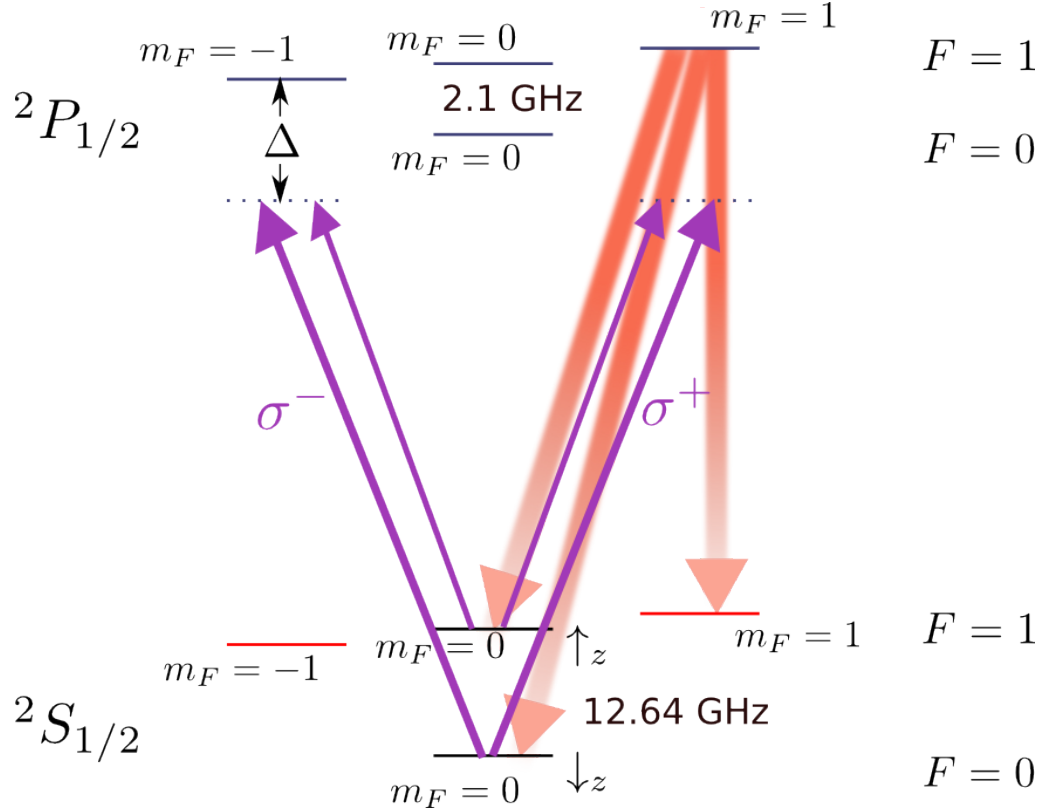


Figure 3.9: Spontaneous emission from the Raman beams: Off-resonant excitations from the Raman beams populate the $^2P_{1/2}$ states, which then spontaneously decay to the $^2S_{1/2}$ states. Spontaneous emission introduces entropy in the coherent quantum evolution, by flipping the spin states randomly and resetting the phase of the evolution. Spontaneous emission may also populate the Zeeman states $|F = 1, m_F = 1\rangle$ and $|F = 1, m_F = -1\rangle$ (shown in red), and thus throws the system out of the Hilbert space. Here the violet arrows denote the σ^+ and σ^- polarization components of a Raman beam, and the red fuzzy arrows are the spontaneous emission channels. For clarity, we show spontaneous emission channels from one of the hyperfine states in the $^2P_{1/2}$ manifold only. Similarly $^2P_{1/2}|F = 1, m_F = -1\rangle$ can decay to the states $|F = 1, m_F = -1, 0\rangle$ and $|F = 0, m_F = 0\rangle$ of the $^2S_{1/2}$ manifold. All the Clebsch-Gordan coefficients have equal magnitudes of $1/\sqrt{3}$ for these transitions. The Raman beams are detuned by Δ from the $^2P_{1/2}$ states. For the frequency doubled CW Ti:sapphire laser used in some of the experiments, $\Delta = 2.7 \text{ THz}$ (red detuned from the $^2P_{1/2}$ states); and for the mode-locked 355 nm laser, $\Delta = 33 \text{ THz}$ (blue detuned from the $^2P_{1/2}$ states).

however, are detected as bright states *i.e.*, as $|\uparrow\rangle$ states.

- *Dephasing* – The $|\uparrow\rangle$ ($|\downarrow\rangle$) state may return to itself, with a probability of $1/3$, after a spontaneous emission event. However, the entanglement between spins may be lost, as the phase of the coherent time evolution is reset.

Spontaneous emission loosely leads to a finite ‘spin temperature’ in this system, though the spins do not fully equilibrate with the ‘bath’ and the total probability of spontaneous emission increases linearly during the quantum simulation. Another physical way to think about the effects of spontaneous emission is that it introduces entropy into the quantum evolution. Spontaneous emission errors grow with increasing system size, which also suppresses P(FM) order with increasing N , as seen in Fig. 3.8a-d. We theoretically estimate the suppression of P(FM) due to diabaticity and spontaneous emission together by averaging over quantum trajectories to be $\approx 7\%$ for $N = 2$ spins and $\approx 26\%$ for $N = 9$ spins.

Intensity fluctuations on the Raman beams

Intensity fluctuations on the Raman beams during the simulation modulate the AC Stark shift on the spins and dephase the spin states, which causes additional diabaticity and degrades the final ferromagnetic order. When we introduce a theoretical dephasing rate of 0.3 per ms per ion (see Appendix A) in the quantum trajectory computation the predicted suppression of P(FM) increases to $\approx 9\%$ for $N = 2$ and $\approx 50\%$ for $N = 9$.

Finite detection efficiency

Imperfect spin detection efficiency contributes $\approx 5 - 10\%$ error in $P(\text{FM})$.

Fluorescence histograms for $P(0)$ and $P(1)$ have a $\approx 1\%$ overlap (in detection time of $800 \mu\text{s}$) due to off-resonant coupling of the spin states to the $^2P_{1/2}$ level [90]. This off-resonant coupling prevents us from increasing detection beam power or photon collection time to separate the histograms. Detection error in the data include uncertainty in fitting the observed fluorescence histograms to determine $P(s)$, intensity fluctuations and finite width of the detection beam.

A problem with detecting the spin states with a PMT is that the bright state histograms for s bright ions overlap strongly with $s + 1$ bright ions for large s . This is illustrated in Fig. 3.10, where we show the photon count histograms for $s = 1$ to $s = 9$ bright ions. The increased overlap between the histograms with increasing system size results in detection error in the measured magnetization. We define the overlap between the histograms as,

$$\mathcal{P}_{m,n} = \frac{\sum_{k=0}^{\infty} \mathcal{P}_m(k) \mathcal{P}_n(k)}{[\sum_{k=0}^{\infty} \mathcal{P}_m(k)^2 \sum_{k=0}^{\infty} \mathcal{P}_n(k)^2]^{1/2}}, \quad (3.9)$$

where $\mathcal{P}_s(k)$ is the probability of observing n photons in the detection time window from s bright ions. With this definition, the overlap increases from $\mathcal{P}_{1,2} = 2\%$ between $s = 1$ and $s = 2$ bright ions, to $\mathcal{P}_{8,9} = 80\%$ between $s = 8$ and $s = 9$ bright ions.

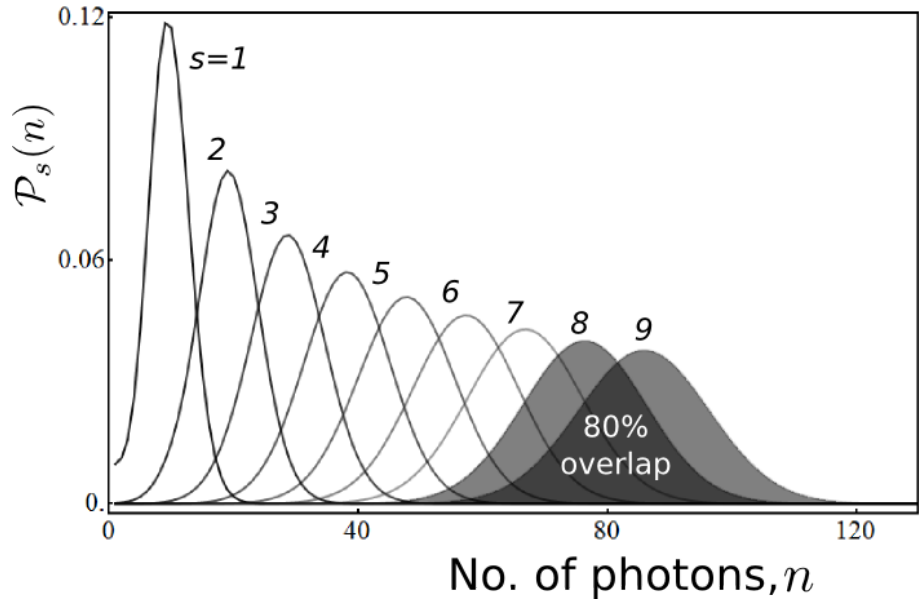


Figure 3.10: Detection with a PMT – overlapping photon count histograms: We use state dependent fluorescence to detect the spin state of the ions. If an ion is in the $|\uparrow_z\rangle$ state, it fluoresces when hit by a laser beam resonant with the $^2S_{1/2}|F = 1, m_F = 0\rangle - ^2P_{1/2}|F = 0, m_F = 0\rangle$ transition, which we collect using $f/2.1$ optics (numerical aperture, $NA=0.24$) on a PMT for about $800 \mu s$. Over repeated measurements, the emitted photons from a $|\uparrow_z\rangle$ spin form a modified Poisson distribution, as discussed in the text. A $|\downarrow_z\rangle$ spin, on the other hand, does not fluoresce as the exciting laser is off-resonant (by ≈ 14.7 GHz compared to the natural linewidth of ≈ 20 MHz) to the $^2S_{1/2}|F = 0, m_F = 0\rangle - ^2P_{1/2}|F = 1, m_F = 1, 0, -1\rangle$ transitions. Thus we identify $|\uparrow_z\rangle$ as the observed ‘bright’ state, and $|\downarrow_z\rangle$ as the ‘dark’ state. Here we show typical fluorescence histograms for $s = 1$ to $s = 9$ bright spins. n denotes the number of photons collected by the PMT in the detection time, and $\mathcal{P}_s(n)$ denotes the probability of observing n photons for s bright ions. The overlap between the photon distributions for s and $s \pm 1$ bright ions increases with increasing s . Thus the detection error increases as the system size grows. As an example, the overlap between the histograms for $s = 8$ and $s = 9$ bright spins is $\approx 80\%$.

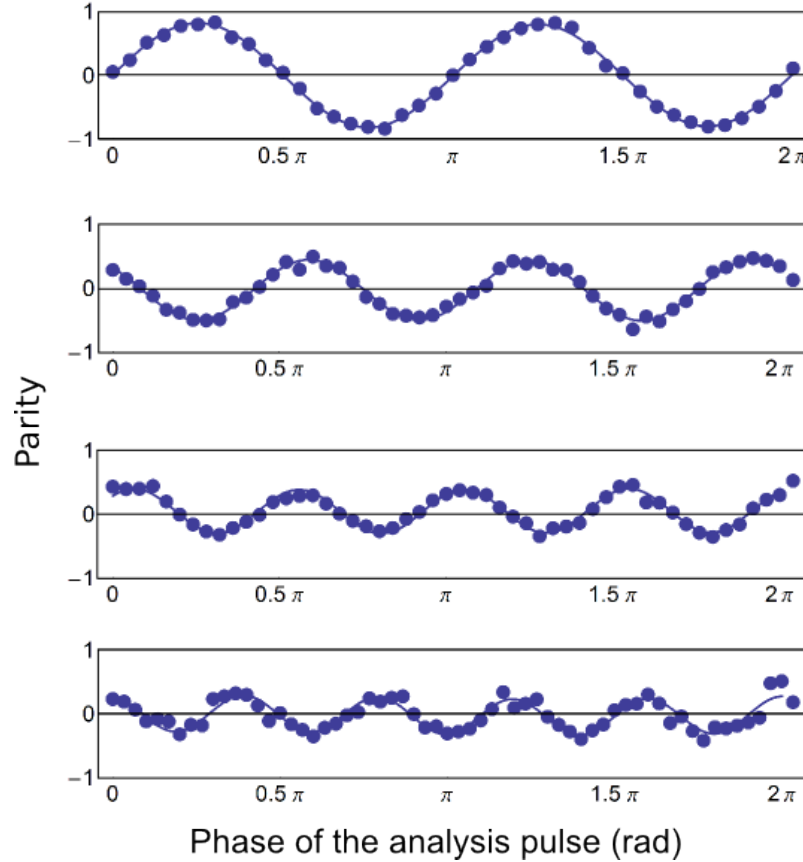


Figure 3.11: Suppression in the GHZ coherence with increasing system size: GHZ coherence or parity of the observed spin state is shown for $N = 2$ to $N = 5$ spins. Here we apply an analysis $\pi/2$ pulse after ramping the transverse field B to near zero, and scan the phase of the pulse. The decreasing contrast of the parity oscillation curves denote the decaying GHZ entanglement in the simulation as the system size grows. Phonons play an important role in reducing the GHZ entanglement, as phonon states mix symmetric and antisymmetric FM spin combinations, and the GHZ entanglement is partly destroyed when we trace over the phonon states during measurement. The amplitude of the parity oscillation is 0.8, 0.47, 0.35 and 0.27 for $N = 2, 3, 4$ and 5 spins respectively. Other primary sources of decoherence include spontaneous emission from the Raman beams, and dephasing from intensity fluctuations on the Raman beams, as discussed in the text. Here the blue circles are the experimental data, and the solid curves are sinusoidal fit to the data.

Phonons

The role of phonons in the results of the quantum simulation is investigated both experimentally and numerically. Phonons destroy the spin flip symmetry of the pure spin Hamiltonian (Eq. (3.1)), as the term in the unitary evolution operator that contains the phonon operators (a and a^\dagger), also includes the spin operator σ_x . Thus states with symmetries different from the ground state are excited in the adiabatic quantum simulation, and the pure spin entanglement is partly destroyed when we trace over the phonon states during the measurement. The final FM state achieved in the quantum simulation with the phonon effects included is of the form $(|\uparrow\uparrow\dots\rangle|\alpha\rangle \pm |\downarrow\downarrow\dots\rangle|-\alpha\rangle)$ [112], where $|\alpha\rangle$ is a coherent state, with average phonon occupation $\langle n \rangle = |\alpha|^2$. The phonon occupation for $N = 9$ spins was numerically found to be under $\langle n \rangle = 1.5$, and lower for $N < 9$ spins. However, these phonons do not alter the ground state spin ordering and hence preserve spin-spin correlation.

In Fig. 3.11 we show the loss of entanglement in the simulation with increasing system size for $N = 2$ to $N = 5$ spins. We apply an analysis $\pi/2$ pulse with phase ϕ after the quantum simulation, and observe the parity as the phase ϕ is scanned from 0 to 2π . The fidelity of the GHZ state, defined to be the overlap of the ideal GHZ state with the actual experimentally observed FM state, $|\Psi_{FM}\rangle$ is given by, $F_{GHZ} = |\langle\Psi_{FM}|GHZ\rangle|^2 = \frac{1}{2}(P_{\downarrow\downarrow\dots\downarrow} + P_{\uparrow\uparrow\dots\uparrow}) + |C_{\downarrow\downarrow\dots\downarrow,\uparrow\uparrow\dots\uparrow}|$. Here, $P(FM) = P_{\downarrow\downarrow\dots\downarrow} + P_{\uparrow\uparrow\dots\uparrow}$ and $|C_{\downarrow\downarrow\dots\downarrow,\uparrow\uparrow\dots\uparrow}|$ denotes the GHZ coherence, *i.e.*, the coefficient of $|\downarrow\downarrow\dots\downarrow\rangle\langle\uparrow\uparrow\dots\uparrow|$ in the density matrix [113]. We measure the GHZ coherence by observing the contrast of the oscillating parity signal, $(P(0) + P(2) + \dots) - (P(1) + P(3) + \dots)$.

As shown in Fig. 3.11, the observed amplitude of the parity oscillations is ≈ 0.8 for $N = 2$ spins, and decreases to ≈ 0.27 for $N = 5$ spins. This corresponds to a GHZ fidelity, F_{GHZ} of ≈ 0.95 for $N = 2$ spins to ≈ 0.52 for $N = 5$ spins. For $N > 5$ spins, the fidelity drops below 0.5, indicating the loss of GHZ entanglement, possibly from phonon occupation, along with other sources of decoherence like spontaneous emission discussed in this section.

3.5 Scaling up the simulation to $N = 16$ with 355 nm mode locked laser

Two of the primary sources of decoherence in our experiments with $N = 2$ to $N = 9$ spins, spontaneous emission and fluctuating differential AC Stark shift, can be reduced by using a laser detuned farther from the ${}^2P_{1/2}$ energy level for the stimulated Raman transitions. The Rabi frequency of the transition Ω and the decoherence effects (spontaneous emission and the differential Stark shift) depend on the detuning, Δ as,

$$\Omega \propto \frac{1}{\Delta} \quad (3.10a)$$

$$\Gamma_{spont} \propto \frac{1}{\Delta^2} \quad (3.10b)$$

$$\Omega_{AC} \propto \frac{1}{\Delta^2}, \quad (3.10c)$$

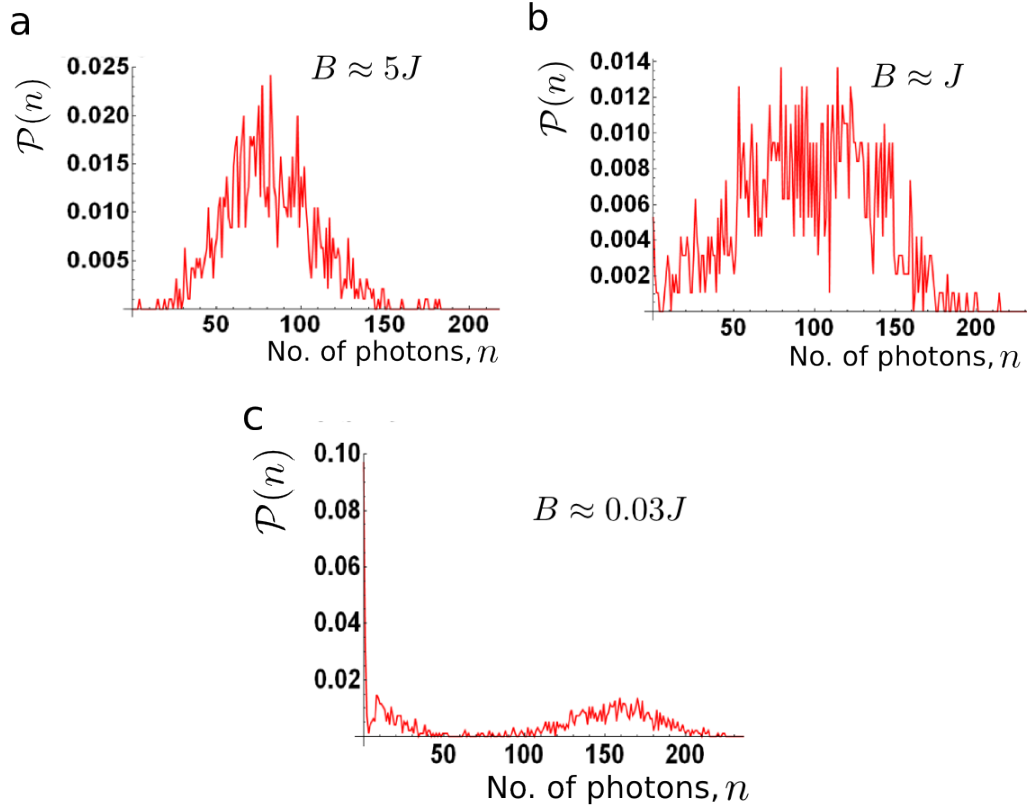


Figure 3.12: Quantum simulation of the ferromagnetic Ising model with $N = 16$ spins: We simulate Eq. (3.1) in a system of $N = 16$ spins. The Hamiltonian is simulated using a tripled Vanadate mode-locked laser at 355 nm, which virtually eliminates spontaneous emission error in the experiment. We use a PMT to detect the fluorescence from the ions, and repeat the experiments about 2000 times to make a histogram of the collected photons. Each spin in the $|\uparrow\rangle$ state emits ≈ 10 photons on average in the detection time of 800 μs . **a.** At $B \gg J$, the spins are polarized along the effective field B (paramagnetic phase) and hence half of the total number of spins are in state $|\uparrow\rangle$. We observe a histogram centered at ≈ 80 photons, as expected. **b.** As the transverse field is reduced, the FM correlations start to build up, thus the fluorescence distribution broadens. **c.** At a very low field ($B \ll J$), the spins order ferromagnetically, as seen in the bifurcation of the histogram.

where Γ_{spont} and Ω_{AC} are the rate of spontaneous emission and the AC Stark shift respectively. Thus increasing the detuning Δ helps reducing the decoherence effects compared to the Rabi strength in the Raman transitions. We use a mode locked tripled Vanadate laser with the center wavelength at 355 nm and an average optical power of 4 W to alleviate laser-induced decoherence. With this laser, $\Gamma_{spont}/\Omega < 10^{-5}$ and $\Omega_{AC}/\Omega < 10^{-5}$ [114], thus practically eliminating these issues.

We ran a quantum simulation experiment with $N = 16$ spins with this laser. As we tune the effective external field B compared to the ferromagnetic Ising couplings, we observe the emergence of FM order. In Fig. 3.12 we show the total fluorescence counts for this experiment, at three different values of the effective external field. When the spins are polarized along the y -axis of the Bloch sphere, we observe a mean fluorescence count of about 80. This denotes that roughly half of the spins are in the state $|\uparrow\rangle$ (a spin $|\uparrow\rangle$ would fluorescence with about 10 mean photons in our detection time of 800 μ s). As B is reduced keeping the Ising couplings constant, the fluorescence histogram broadens, and finally bifurcates at $B/J \rightarrow 0$, characteristic of the FM phase in absence of any biasing field, and any spontaneous symmetry breaking.

Chapter 4

Three frustrated Ising spins on a triangle

4.1 Overview

A network is said to be frustrated when it is impossible to satisfy all the interactions ('bonds') individually. Frustrated magnetic systems [72, 115] may lead to non-trivial many body properties, such as massive degeneracy in the ground state, and entanglement [43] in a quantum system. Frustration is believed to be a key ingredient to understand properties of exotic spin systems like quantum spin liquids and spin glasses [116, 47, 117, 118]. Other complex systems and phenomena such as social [119] and neural [120] networks, and protein folding [121] owe their complexity to frustration.

Three Ising spins interacting antiferromagnetically with each other on the corners of an equilateral triangle constitute one of the simplest examples of spin frustration. As shown in Fig. 4.1a, for antiferromagnetically oriented spins 1 and 2, spin 3 cannot satisfy both the (antiferromagnetic) interactions with the other spins simultaneously, and hence the ground state is frustrated. Out of $2^3 = 8$ possible basis spin states, six belong to the ground state manifold. Since any quantum superposition of the basis ground states is also a ground state, it is possible to prepare a massive entangled ground state while experimentally simulating this spin model.

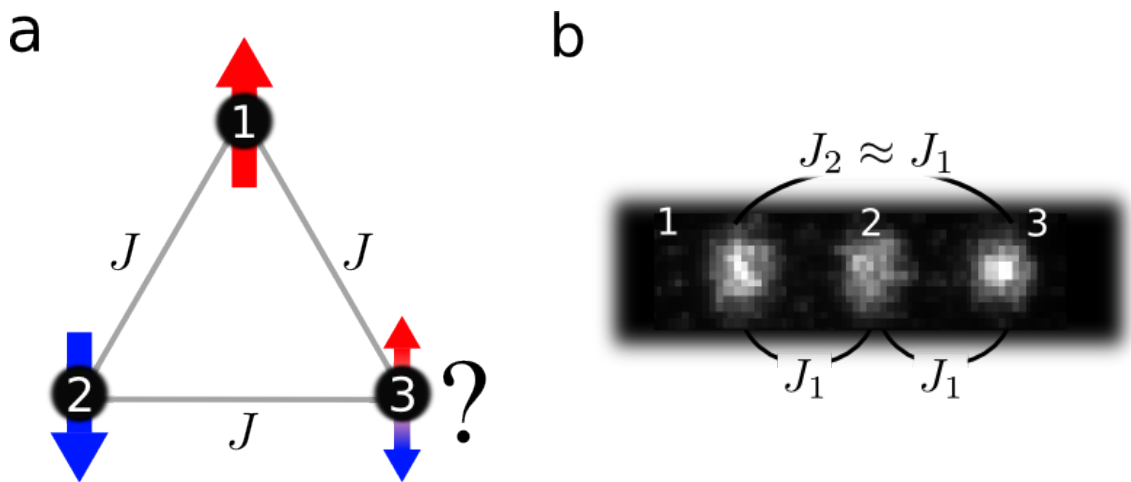


Figure 4.1: Three frustrated Ising spins on a triangle: **a.** Three spins interacting antiferromagnetically on the corners of a triangular lattice cannot satisfy all the interactions simultaneously, a phenomenon known as the geometric frustration. Here spin 3 cannot simultaneously anti-align to both the spins 1 and 2. For a classical spin system, spin 3 chooses one of the spin configurations (\uparrow or \downarrow) at random. A quantum system may be in both the configurations at the same time, owing to the quantum superposition principle. Frustration in a magnetic system usually leads to an exponentially large number (in the system size) of degenerate ground states, leading to a non-zero entropy at the lowest temperature. **b.** For a fully connected spin network, the geometry of the lattice is irrelevant. Here we simulate the frustrated spin network with three spins given by the hyperfine states of trapped $^{171}\text{Yb}^+$ ions in a linear configuration. Spins 1 and 3 interact with Ising coupling J_2 , which is almost equal to the nearest neighbor interactions J_1 , effectively generating the triangular network geometry. Here the bright spots (enumerated as 1, 2 and 3) are the CCD images of three trapped and laser-cooled $^{171}\text{Yb}^+$ ions.

In this chapter* we describe the simulation of frustrated Ising spins on a triangle. We probe the ground state of the transverse field Ising model by adiabatically ramping the transverse magnetic field. The ground state reached using this method is an entangled state. Note that the Hamiltonian has a global spin rotation symmetry by a Bloch vector angle of π about the y -axis (section 3.2), which may lead to entanglement even when the system is not frustrated. This symmetry is, however, broken easily by applying an axial magnetic field. Since the degeneracy in the ground state in the case of antiferromagnetic interactions arises from the interactions, rather than the symmetry in the Hamiltonian, the entanglement does not go away completely when the axial field is turned on.

This chapter is organized in the following sections:

- Section 4.2 - we describe the theoretical ground state of the transverse field antiferromagnetic Ising model with $N = 3$ spins.
- Section 4.3 - a brief introduction to the entanglement and entanglement witness that is used to characterize the ground state entanglement.
- Section 4.4 - we describe the choice of the experimental parameters, and describe the experimental sequence to simulate the frustrated spin model.
- Section 4.5 - we present data showing the frustrated ground state, and entanglement. We compare this case with results from the simulation of a ferromagnetic model that does not show frustration.

*The results presented in this chapter are published in Ref. [43].

4.2 Frustrated quantum Ising model

We simulate [43] the frustrated Ising model in presence of an effective transverse magnetic field, in a system of $N = 3$ Ising spins. The Hamiltonian is given by,

$$H = J_1(\sigma_x^1\sigma_x^2 + \sigma_x^2\sigma_x^3) + J_2\sigma_x^1\sigma_x^3 - B(\sigma_y^1 + \sigma_y^2 + \sigma_y^3). \quad (4.1)$$

Here the Ising couplings J_1 and J_2 are antiferromagnetic (> 0), σ_x^i and σ_y^i are the x and y spin-1/2 Pauli matrices for the i^{th} spin ($i = 1, 2, 3$), and B is the effective transverse magnetic field.

Note that the exact geometry of the spin chain is irrelevant in this example, as the network is fully-connected. In fact, we simulate Eq. (4.1) with a linear chain of three spins. For $J_1 = J_2 = J$ this system is equivalent to the system shown in Fig. 4.1b, and the ground state is highly frustrated.

4.2.1 States near $B/J = 0$

At $B/J = 0$, the ground state of Eq. (4.1) lies in the six dimensional Hilbert space formed by the basis states $|\uparrow\uparrow\downarrow\rangle, |\uparrow\downarrow\uparrow\rangle, |\uparrow\downarrow\downarrow\rangle, |\downarrow\downarrow\uparrow\rangle, |\downarrow\uparrow\downarrow\rangle, |\downarrow\uparrow\uparrow\rangle$. The two ferromagnetic states $|\uparrow\uparrow\uparrow\rangle$ and $|\downarrow\downarrow\downarrow\rangle$ and all their quantum superpositions belong to the excited state manifold.

A finite transverse field induces couplings between the members of the ground state manifold and hence splits the degeneracy. For $B/J \rightarrow 0$ we treat the coupling to the transverse field as a perturbation over the Ising spin couplings. Using perturbation theory, analogous to our treatment in section 3.3.1, we find that a unique

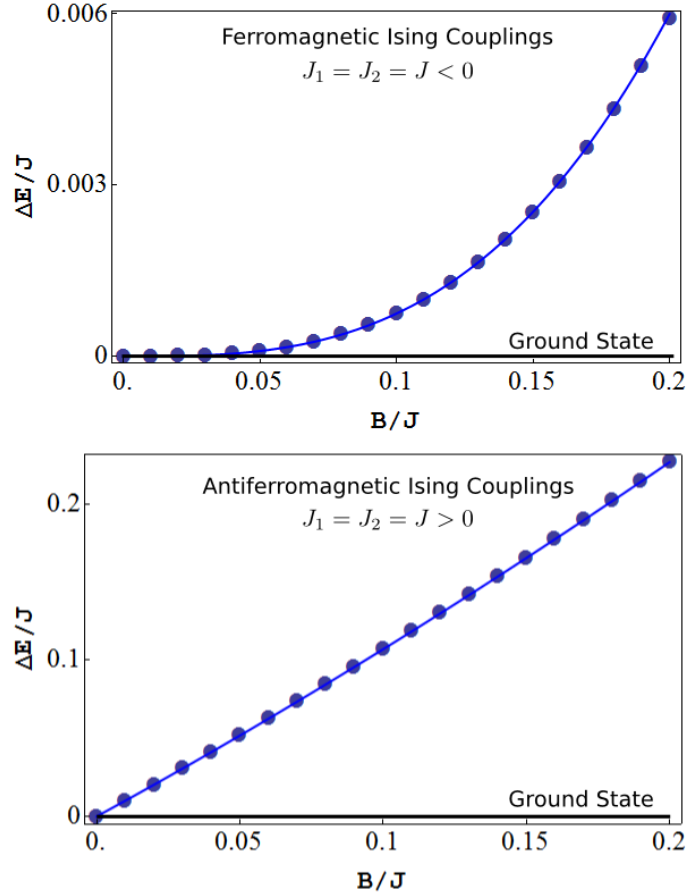


Figure 4.2: Increased sensitivity to quantum fluctuations in presence of frustration: In the absence of the effective transverse magnetic field B in Eq. (4.1), the ground state manifold contains two fold degenerate FM states ($|\uparrow\uparrow\uparrow\rangle$ and $|\downarrow\downarrow\downarrow\rangle$) when the Ising couplings are negative ($J_1 < 0$, $J_2 < 0$), and six fold degenerate AFM states ($|\uparrow\uparrow\downarrow\rangle$, $|\uparrow\downarrow\uparrow\rangle$, $|\downarrow\uparrow\uparrow\rangle$, $|\downarrow\downarrow\uparrow\rangle$, $|\downarrow\uparrow\downarrow\rangle$, $|\uparrow\downarrow\downarrow\rangle$) when the couplings are equal and positive ($J_1 = J_2 = J > 0$). A small transverse field induces quantum fluctuations between the spin states and lifts the degeneracy. **a.** In case of ferromagnetic couplings, the energy splitting between the ground and the first excited state is $\mathcal{O}(B/|J|)^3$, as explained in the text. Here the blue circles are exact energy calculated from the direct diagonalization of Eq. (4.1). The blue solid line is a cubic polynomial of the form $\Delta E/J = 0.75(B/J)^3$. (Here ΔE is the energy measured from the ground state). **b.** In case of antiferromagnetic couplings (frustration), the degeneracy is split in the first order in B/J . The blue circles are the exact results from the diagonalization, and the blue solid line is a polynomial of the form $\Delta E/J = B + 0.75B^2 - 0.35B^3$.

ground state emerges for non-zero field, namely $|\uparrow\uparrow\downarrow\rangle + |\uparrow\downarrow\uparrow\rangle + |\downarrow\uparrow\uparrow\rangle - |\uparrow\downarrow\downarrow\rangle - |\downarrow\downarrow\uparrow\rangle - |\downarrow\uparrow\downarrow\rangle$. This is a superposition of two W states [122].

This can be contrasted with the case where all the interactions are ferromagnetic (*i.e.*, for $J_1 < 0$, $J_2 < 0$ in Eq. (4.1)). At $B/J = 0$ ($J_1 = J_2 = J$) the ground state manifold is two dimensional, and spanned by the ferromagnetic (FM) states $|\uparrow\uparrow\uparrow\rangle$ and $|\downarrow\downarrow\downarrow\rangle$. For a finite $B/|J|$, the ground state is $(|\uparrow\uparrow\uparrow\rangle + |\downarrow\downarrow\downarrow\rangle)/\sqrt{2}$, and the energy splitting between the ground state and the first excited state is $\mathcal{O}((B/J)^3)$. This is due to the fact that the FM states are only related by the global spin flip symmetry (along x) for the ferromagnetic Ising model, and to break the degeneracy between the states, we need to go to $N = 3^{\text{rd}}$ order in perturbation, as illustrated previously in section 3.3.1. In the case of antiferromagnetic Ising model, the frustration present in the system leads to extra degeneracy in the ground state manifold, and a small quantum fluctuation may break the symmetry of the ground state, and lead to non-trivial phases.

4.2.2 Preparing the entangled state in adiabatic quantum simulation

As in the case of the ferromagnetic quantum Ising model, we follow the ground state of Eq. (4.1) (nearly) adiabatically in the experiment. For large B/J , the ground state is the spin polarized state $|\uparrow_y\uparrow_y\uparrow_y\rangle$. As we change the dimensionless ratio B/J , the ground state evolves, maintaining the symmetry of the Hamiltonian, as discussed in section 3.3.3. Thus we reach the ground state $|\uparrow\uparrow\downarrow\rangle + |\uparrow\downarrow\uparrow\rangle + |\downarrow\uparrow\uparrow\rangle - |\uparrow\downarrow\downarrow\rangle - |\downarrow\downarrow\uparrow\rangle - |\downarrow\uparrow\downarrow\rangle$ when the effective transverse field is ramped down to

zero. Clearly this state is entangled, as it cannot be written as a product state of the three spins.

The entanglement present in the system can be characterized by measuring the ‘entanglement witness operators’. In the next section, we describe the witness operators in brief.

4.3 Frustration and entanglement

A genuine tripartite entanglement in a system of three qubits belongs to one of the following two classes:

- Greenberger-Horne-Zeilinger (GHZ) entangled state, $|GHZ\rangle = |\uparrow\uparrow\uparrow\rangle + |\downarrow\downarrow\downarrow\rangle$, also referred to as a ‘Schrödinger’s cat state’, and
- W-states- Superposition of states with k number of spins flipped from the state $|\downarrow\downarrow\downarrow\rangle$. For $N = 3$ spin system, there are two W-states, corresponding to $k = 1, 2$; namely, $|W_1\rangle = |\uparrow\downarrow\downarrow\rangle + |\downarrow\uparrow\downarrow\rangle + |\downarrow\downarrow\uparrow\rangle$ and $|W_2\rangle = |\downarrow\uparrow\uparrow\rangle + |\uparrow\downarrow\uparrow\rangle + |\uparrow\uparrow\downarrow\rangle$

The constituent basis spin states may have arbitrary phases in both the GHZ and W-states. Note that W_1 and W_2 are connected by a global spin flip symmetry in the case of a system with three spins. Any tripartite entangled state of the three spins can be transformed to either a GHZ or a W-state by local (single qubit) unitary operations.

A general way to characterize entanglement is to experimentally measure the density matrix ρ of the system, also known as quantum tomography [66]. The

off-diagonal terms in the density matrix quantify the quantum coherence in the system. However, measuring the density matrix involves exponentially many measurements (in system size) and hence is not always practical or efficient. Measuring the expectation value of an entanglement witness operator provide a practical alternative to detect and characterize entanglement. The witness operators are defined to detect entanglement of a particular kind, and it may be non-trivial to construct a witness operator.

In general a witness operator W_ψ with respect to some entangled state ψ is constructed as,

$$W_\psi = \alpha \mathbb{I} - |\psi\rangle\langle\psi|, \quad (4.2)$$

where the constant α is chosen such that

$$\text{Trace } \rho W_\psi \leq 0 \quad (4.3)$$

if the system shows this particular (ψ type) entanglement. If Eq. (4.3) is not satisfied, we cannot rule out entanglement in the system, but we may conclude that the system does not exhibit entanglement of the type ψ . In case of three spins, $\psi = \text{GHZ}$ or W .

In this chapter we prepare the frustrated ground state of the three spin Ising network. The ground state is a superposition of the two W -states. We compare it to the case of ferromagnetic couplings, where there is no frustration present in the system, and the expected ground state is a GHZ state. We use the following witness

operators to detect the tripartite entanglement (GHZ or W-state) present in our system [122, 43, 113],

$$W_{GHZ} = 9/4 - \hat{\mathcal{J}}_x^2 - \sigma_\phi^{(1)}\sigma_\phi^{(2)}\sigma_\phi^{(3)} \quad (4.4a)$$

$$W_W = 4 + \sqrt{5} - 2(\hat{\mathcal{J}}_y^2 + \hat{\mathcal{J}}_z^2), \quad (4.4b)$$

where $\hat{\mathcal{J}}_\alpha \equiv \frac{1}{2} \sum_i \sigma_\alpha^{(i)}$ is proportional to the projection of the total effective angular momentum of the three spins along the α -direction, and ϕ is a direction in the yz -plane of the Bloch sphere.

The degeneracy in the ground state due to competing antiferromagnetic interactions leads to entanglement, which we detect and quantify using the witness W_W . By switching all the interactions to ferromagnetic, we observe a GHZ entanglement, characterized by W_{GHZ} . In presence of an axial magnetic field, the GHZ entanglement is destroyed, as the magnetic field destroys the spin flip symmetry in Eq. (4.1) and a non-degenerate ground state emerges ($|\uparrow\uparrow\uparrow\rangle$ or $|\downarrow\downarrow\downarrow\rangle$, depending on the sign of the axial field). This is in sharp contrast with the frustrated ground state, which retains some entanglement even after the symmetry is broken. This establishes a connection between frustration and an extra degree of entanglement. We use the bipartite spin-squeezing witness operator, W_{SS} [43, 122] to characterize entanglement of the symmetry broken frustrated antiferromagnetic ground state. The witness is given by,

$$W_{SS} = (\hat{\mathcal{J}}_x^2 + \frac{3}{4})^2 - 4\langle\hat{\mathcal{J}}_x\rangle^2 - (\hat{\mathcal{J}}_y^2 + \hat{\mathcal{J}}_z^2 - \frac{3}{2})^2, \quad (4.5)$$

which is less susceptible to experimental errors than the W-state witness operator [43].

4.4 Experimental methods

We work with three $^{171}\text{Yb}^+$ ions forming a linear chain along the Z direction of our Paul trap, with a center of mass (COM) trap frequency of $\nu_Z = 1.49$ MHz. The three normal modes of transverse vibrational motion, along the X -direction occur at,

- COM mode: $\omega_1/2\pi = \nu_1 = 4.334$ MHz
- Tilt mode : $\omega_2/2\pi = \nu_2 = 4.074$ MHz
- Zig-zag mode : $\omega_3/2\pi = \nu_3 = 3.674$ MHz.

Like the simulation of the ferromagnetic Ising model, discussed in the previous chapter, the effective spin-1/2 system is represented by the $^2S_{1/2}$ $|F = 1, m_F = 0\rangle$ and $|F = 0, m_F = 0\rangle$ hyperfine “clock” states in each ion, depicted by $|\uparrow_z\rangle$ and $|\downarrow_z\rangle$, respectively [123], and separated in frequency by $\nu_{HF} = 12.642819$ GHz (This corresponds to ≈ 5 G magnetic field to define the quantization axis). To simulate Eq. (4.1), we shine Raman beams on the ions that drive the motional modes off-resonantly, as explained previously, and obtain an effective spin-spin Ising type interaction, following the Mølmer-Sørensen scheme [71]. A carrier Raman transition with suitably defined phase simulates the effective transverse magnetic field.

To simulate the frustrated spins on the corners of an equilateral triangle, we tune the Mølmer-Sørensen Raman beatnote (μ) near the X -COM mode ($\mu > \omega_1$). From Eq. (3.8), we see that the Ising couplings are all positive, and hence anti-ferromagnetic. The nearest neighbor and the next nearest neighbor Ising couplings are almost equal, and hence the interaction graph resembles an equilateral triangle. The far off-resonant tilt mode makes the nearest neighbor slightly stronger than the next nearest neighbor. We use a scaled Mølmer-Sørensen detuning $\tilde{\mu}$ in this chapter, defined as

$$\tilde{\mu} \equiv \frac{\mu^2 - \omega_1^2}{\omega_Z^2}. \quad (4.6)$$

With this definition, the COM, tilt and the zigzag modes correspond to $\tilde{\mu} = 0, -1$ and -2.4 respectively.

We cool all transverse x modes to near their zero point of motion and deep within the Lamb-Dicke regime, then we initialize the electronic states of each $^{171}\text{Yb}^+$ ion along the y -axis of the Bloch sphere through optical pumping and rotation operations [123]. Next we apply the Ising coupling along with a strong transverse field and adiabatically ramp down the field.

An ideal triangle geometry would mean $J_1 = J_2$, which is obtained by coupling to the COM mode only. Here J_1 and J_2 are the nearest and the next nearest neighbor Ising couplings respectively. The far off-resonant tilt mode breaks this symmetry and makes $J_1 > J_2$. The energy spectrum in presence of unequal couplings is shown in Fig. 4.3. The nearest neighbor antiferromagnetic states $|\uparrow\downarrow\uparrow\rangle$ and $|\downarrow\uparrow\downarrow\rangle$ are lower in energy than the next nearest antiferromagnetic states, $|\uparrow\uparrow\downarrow\rangle$, $|\uparrow\downarrow\downarrow\rangle$, $|\downarrow\downarrow\uparrow\rangle$

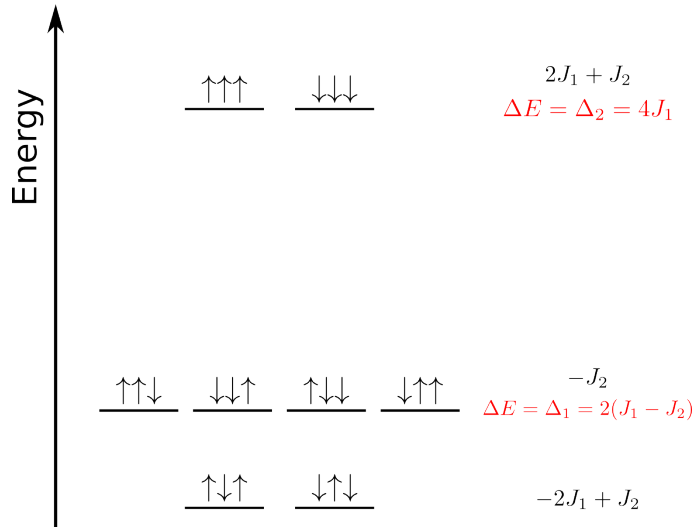


Figure 4.3: **Energy diagram for $J_1 \neq J_2$:** Weak couplings to the tilt and the zigzag vibrational modes make the Ising interactions slightly non-uniform. Here we show the energy diagram of $2^3 = 8$ spin configurations according to the quantum Ising Hamiltonian (Eq. (4.1)), at $B = 0$. The nearest neighbor AFM states ($|\uparrow\downarrow\uparrow\rangle$ and $|\downarrow\uparrow\downarrow\rangle$) are the degenerate ground states, the next nearest neighbor AFM states ($|\uparrow\uparrow\downarrow\rangle$, $|\downarrow\downarrow\uparrow\rangle$, $|\uparrow\downarrow\downarrow\rangle$, and $|\downarrow\uparrow\uparrow\rangle$) are the first excited states, and the FM states ($|\uparrow\uparrow\uparrow\rangle$ and $|\downarrow\downarrow\downarrow\rangle$) are the third and highest excited states. The energy of each state and the difference from the ground state energy (ΔE) is shown next to the levels. In our experiment, $J_2 \approx 0.85J_1$. To simulate the triangle geometry with equal couplings, we ramp the Hamiltonian in our experiment faster than the energy splitting between the ground and the first excited states, but keep the ramping slow enough to avoid exciting the system to the FM states.

and $|\downarrow\uparrow\uparrow\rangle$ by energy $\Delta_1 = 2(J_1 - J_2)$. The ferromagnetic states, $|\uparrow\uparrow\uparrow\rangle$ and $|\downarrow\downarrow\downarrow\rangle$ are $\Delta_2 = 2(J_1 + J_2)$ above the ground states. We mimic the triangular coupling by ramping the effective transverse magnetic field in Eq. (4.1) faster compared to Δ_1 , but slower compared to the splitting between the ground and the ferromagnetic states, Δ_2 (Fig. 4.3).

We finally measure the spins along the x -axis of the Bloch sphere by rotating the spins from the x -basis to the z -basis and measuring the spin state ($|\downarrow_z\rangle$ or $|\uparrow_z\rangle$) through standard spin-dependent fluorescence techniques [123], using a charge-coupled device (CCD) imager (detection efficiency $\approx 95\%$ per spin including initialization and rotation errors). We determine the probability of each spin configuration by repeating the above procedure ≈ 1000 times. We also measure the number of spins in state $|\uparrow\rangle$ by using a photomultiplier tube (PMT), which is useful for higher efficiency measurements of certain symmetric observables such as entanglement fidelities and witness operators.

4.5 Experimental Results

In Fig. 4.4 we show the observed spin order in the quantum simulation for the ferromagnetic and the frustrated cases, for various magnetic field end points B . The theoretical curves show both the exact ground-state populations as well as the expected population evolution from the actual applied time-dependent Hamiltonian [108], using the Trotter formula and including the contribution from phonons to lowest order in the Lamb-Dicke expansion [124]. Fig. 4.4a corresponds to nearly

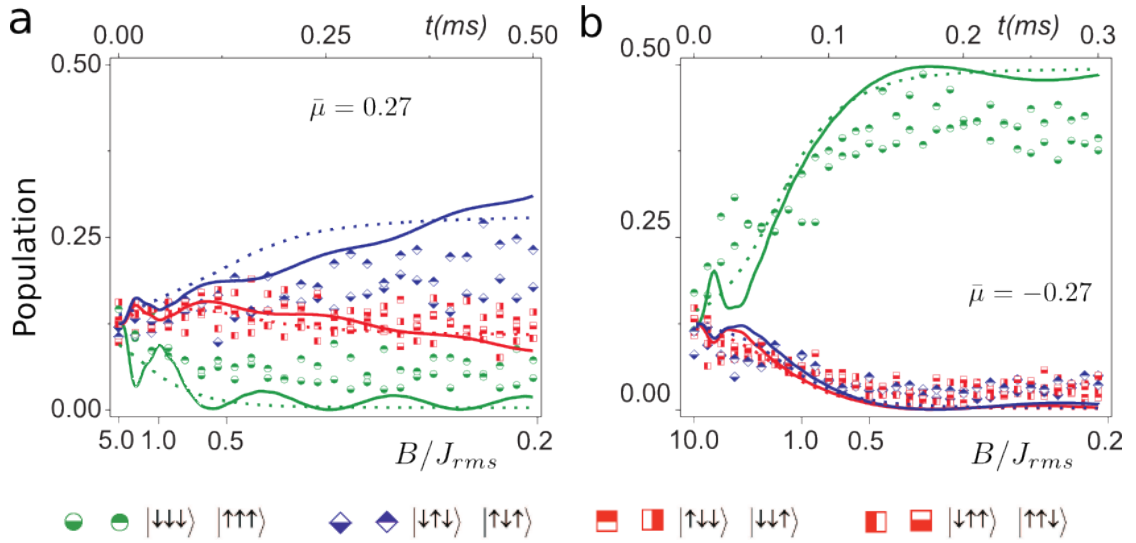


Figure 4.4: Population of spin states with ferromagnetic and antiferromagnetic Ising couplings: Here we show the results from quantum simulation of the ferromagnetic and the antiferromagnetic Ising models as a function of the ratio of the effective transverse magnetic field B to the average Ising coupling $J_{rms} = \sqrt{(2J_1^2 + J_2^2)/3}$. The green circles are the two FM states, the blue diamonds are the two symmetric AFM states, and the red squares are the remaining four asymmetric AFM states. The dashed lines correspond to the populations in the exact ground state and the solid lines represent the expected theoretical evolution from the actual ramp, including non-adiabaticity from the initial sudden turn on of the Ising Hamiltonian. The probability of inelastic spontaneous scattering is not included in the theory curves. **(a)** All AFM interactions (scaled Mølmer-Sørensen detuning $\bar{\mu} = 0.27$). The FM-ordered states vanish and the six AFM states are all populated as $B/J_{rms} \rightarrow 0$. Because $J_2 \approx 0.8J_1$ for this data, a population imbalance also develops between symmetric and asymmetric AFM states. **(b)** All FM interactions (scaled Mølmer-Sørensen detuning $\bar{\mu} = -0.27$), with evolution to the two FM states as $B/J_{rms} \rightarrow 0$.

uniform AFM couplings and gives roughly equal probabilities for all six AFM states (3/4 of all possible spin states). The slight inequality of the Ising couplings J_1 and J_2 are reflected in the higher probability of the symmetric AFM states, $|\uparrow\downarrow\uparrow\rangle$ and $|\downarrow\uparrow\downarrow\rangle$. Fig. 4.4b corresponds to FM couplings, and the two FM states are clearly predominant.

In order to compare these two cases, we characterize the entanglement in the system at each point in the adiabatic evolution by measuring particular entanglement witness operators, with negative expectation values indicating the corresponding form of entanglement [122]. For the FM case, we measure the GHZ witness operator [113, 122] W_{GHZ} (Eq. (4.4a)). For the AFM (frustrated) case, we measure the symmetric W-state witness [122], W_W (Eq. (4.4b)). In both cases, as shown in Fig. 4.5, we find that entanglement of the corresponding form develops during the adiabatic evolution. In this AFM/FM comparison, we operate with $\tilde{\mu} \approx 0.22$ for both cases ($J_2 \approx 0.8J_1 > 0$), but for the FM case we reverse the sign of B and follow the highest excited state [39], which is formally equivalent to measuring the ground state of the sign-inverted Hamiltonian. Thus all the antiferromagnetic couplings are effectively turned into ferromagnetic couplings. We may also simulate the ferromagnetic couplings by tuning the beat-note μ between the COM and the tilt mode ($-1 < \tilde{\mu} < 0$). But the enhanced contribution of the tilt mode phonons due to the proximity of the mode (compared to the case of $\mu > \omega_1$, or $\tilde{\mu} > 0$) degrades the GHZ entanglement fidelity.

In macroscopic systems, the global symmetry in the Ising Hamiltonian of Eq. 3.1 is spontaneously broken, and ground-state entanglement originating from this

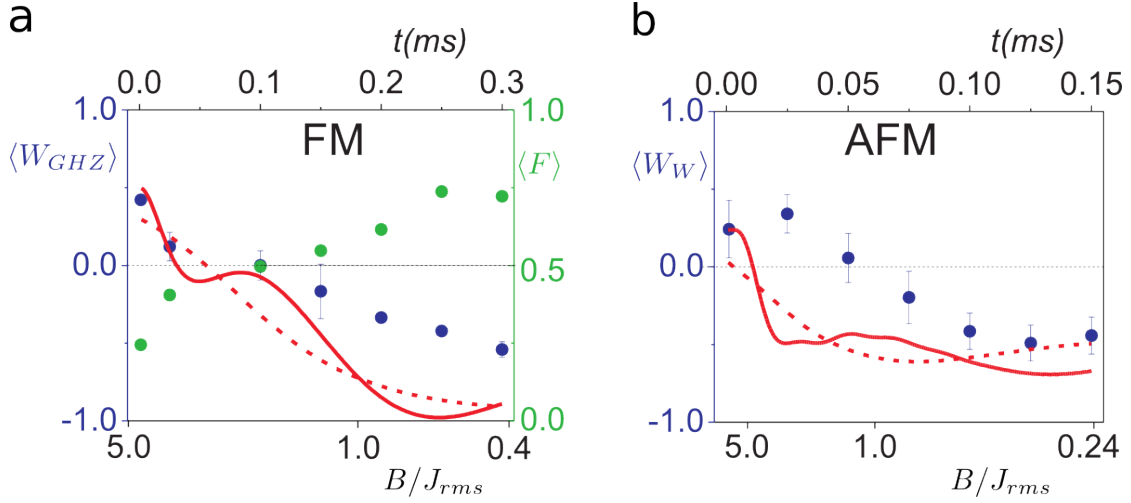


Figure 4.5: Entanglement generation through the quantum simulation: We showed the entanglements through entanglement witness measurements, using a PMT for detection. For (a) FM and (b) AFM situations as B/J_{rms} is ramped down, with a negative value of the witness operator indicating entanglement. For this data, $|J_2/J_1| \approx 0.85$. (a) For the FM regime we measure a GHZ witness operator with $\phi = y$ (blue circles) and find that entanglement occurs for $B/J_{\text{rms}} < 1.25$. The GHZ fidelity F (green circles), or the overlap probability with the ideal GHZ state, is also extracted from this measurement, where $F > 0.5$ indicates entanglement [113]. (b) For the frustrated AFM case we measure a W-state witness operator (blue circles) and find that entanglement emerges for $B/J_{\text{rms}} < 1.1$. In both plots, the dashed lines are theoretical witness values for the exact ground states, while the solid lines theoretically describe the expected witness values given the actual ramps, not including errors due to spontaneous scattering, fluctuations in control parameters, and detection errors. The error bars represent the spread over the observed witness expectations following various absolute global rotation directions, and indicate the uncertainty from parasitic effective magnetic fields not appearing in Eq. (4.1) as well as possible drifts in the control parameters.

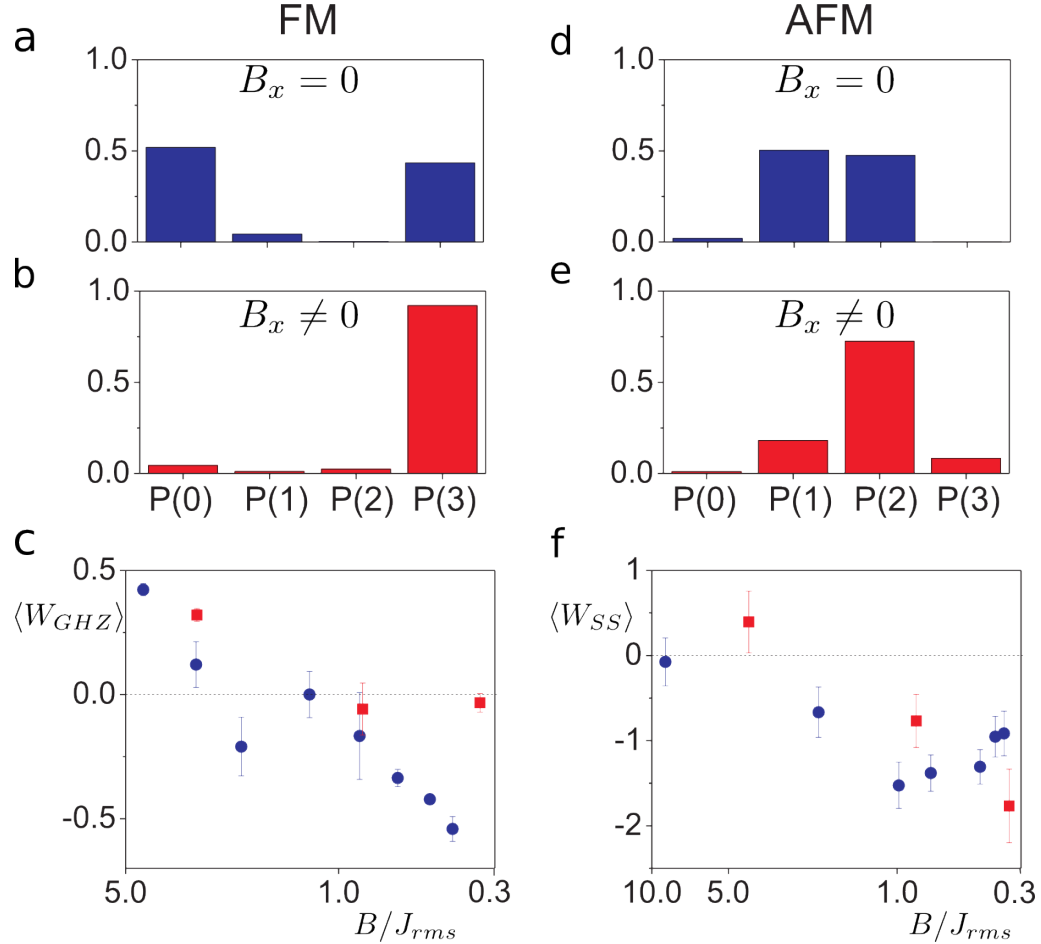


Figure 4.6: Entanglement from the frustration: The effect of symmetry-breaking on the FM and AFM cases of the Ising model, using a PMT for detection. (a) Measured x -basis populations with FM Ising model ($J_1, J_2 < 0, B/J_{rms} = 0.42$), labeled by the probability $P(N)$ of N spins in state $|\uparrow\rangle$. (b) Measured populations of FM Ising model with $B/J_{rms} = 0.34$, where a symmetry-breaking field is added during the ramp, increasing linearly to $B_x/J_{rms} = 0.87$, showing the emergence of the single state $|\uparrow\uparrow\uparrow\rangle$. (c) Measurement of GHZ witness operator without (blue circles) and with (red squares) symmetry-breaking field, showing a quenching of entanglement. In the latter case, the direction ϕ in the GHZ witness operator is coordinated with the time-dependent phase of the GHZ state. (d) Measured x -basis populations of AFM Ising model ($J_1, J_2 > 0, B/J_{rms} = 0.36$). (e) Measured populations of AFM Ising model with $B/J_{rms} = 0.34$, where a symmetry-breaking field is added during the ramp, increasing linearly to $B_x/J_{rms} = 1.19$, showing the emergence of the three states $|\uparrow\uparrow\downarrow\rangle, |\uparrow\downarrow\uparrow\rangle$, and $|\downarrow\uparrow\uparrow\rangle$ (f) Measurement of bipartite spin-squeezing entanglement witness operator applied to the AFM case, showing that entanglement remains even after symmetry is broken. As in Fig. 4.5, the error bars in (c) and (f) represent the uncertainty from parasitic effective magnetic fields and drifts not appearing in Eq. (4.1).

symmetry is expected to vanish for the non-frustrated FM case [47]. However, for the frustrated AFM case, the resultant ground state after symmetry-breaking (e.g., $|\uparrow\uparrow\downarrow\rangle + |\uparrow\downarrow\uparrow\rangle + |\downarrow\uparrow\uparrow\rangle$) is still entangled. While spontaneous symmetry-breaking does not occur in a small system of three spins, we can mimic its effect by adding a weak effective magnetic field $-B_x \sum_i \sigma_x^{(i)}$ during the adiabatic evolution [125]. Figure 4.6a shows the measured final populations after adiabatic evolution to the Ising Hamiltonian ($B \ll J_{\text{rms}}$) in the FM case without symmetry-breaking. Figure 4.6b shows the same with a symmetry-breaking field $B_x \approx J_{\text{rms}}$ that breaks the degeneracy of the two components of the FM ground state and leaves a dominant $|\uparrow\uparrow\uparrow\rangle$ product state. Figure 4.6c shows a measurement of the corresponding GHZ witness operator, displaying a clear quenching of GHZ-type entanglement when symmetry is broken.

For the frustrated AFM case, Fig. 4.6d shows the measured final populations of the evolution of the Ising Hamiltonian, with the six AFM states dominating. But when symmetry is broken (Fig. 4.6e), the AFM system primarily evolves to the three states $|\uparrow\uparrow\downarrow\rangle$, $|\uparrow\downarrow\uparrow\rangle$, and $|\downarrow\uparrow\uparrow\rangle$, consistent with the expected W-state. The residual population in the other states is attributed to nonadiabatic evolution and a finite value of B at the end of the ramp. We characterize entanglement of the symmetry-broken frustrated AFM case by measuring the bipartite spin-squeezing witness operator [122] W_{SS} (Eq. (4.5)). We choose this witness operator because it is less sensitive to experimental errors than the W-state witness operator W_W [122]. The observation of negative values of W_{SS} presented in Fig. 4.6f shows directly that the frustrated ground state carries entanglement even after global symmetry is

broken in the Ising model, and thereby establishes a link between frustration and an extra degree of entanglement.

4.6 Summary and outlook

We have simulated a frustrated spin network with three spins, interacting antiferromagnetically on a triangle. The antiferromagnetic couplings induce competition between spin states, resulting in a massive degeneracy in the ground state. By introducing an effective transverse magnetic field and following the adiabatic quantum simulation protocol, we prepare an entangled state of the degenerate spin states. This entanglement is fundamentally different, in its origin and nature, from the case where all the couplings are ferromagnetic. Unlike the GHZ entanglement achieved in the ferromagnetic model, the W-state entanglement in the frustrated model is robust against a small biasing field.

In the next chapter we shall simulate an antiferromagnetic quantum Ising model with tunable range of interactions in a system of $N > 3$ spins, and observe frustration in spin ordering. It is possible to simulate an arbitrary lattice geometry in this chain of trapped ions by appropriately tailoring the interactions between each pair of spins. We shall conjecture on how to realize this in the Outlook chapter of this thesis.

Chapter 5

Frustrated magnetic ordering with tunable range antiferromagnetic couplings

5.1 Overview

Long range antiferromagnetic interactions lead to frustration, as the individual interactions cannot be satisfied simultaneously. This may lead to massive degeneracy in the ground state and entanglement, as discussed in the previous chapter in the context of three Ising spins on a triangle. Ising models with beyond nearest neighbor interactions, the so called ANNNI models, have been studied in great detail, and a plethora of interesting phases have been theoretically uncovered [126, 127].

Here we simulate a transverse field long range antiferromagnetism Ising model using a chain of up to $N = 16$ spins. The Hamiltonian is given by

$$H = \sum_{\substack{i,j \\ j < i}} J_{i,j} \sigma_x^i \sigma_x^j - B \sum_i \sigma_y^i, \quad (5.1)$$

where σ_α^i ($\alpha = x, y, z$) are the Pauli matrices for the i^{th} spin ($i = 1, 2, \dots, N$), $J_{i,j} (> 0)$ is the antiferromagnetic (AFM) Ising coupling between spins i and j , and B is an effective transverse magnetic field. The Ising coupling between spins i and

j approximately fall off with the separation between them as,

$$J_{i,j} = \frac{J_0}{|i-j|^\alpha}. \quad (5.2)$$

We observe * the onset of antiferromagnetic spin ordering as the transverse field is made weaker than the Ising couplings. We also tune the range of the interactions for a system of $N = 10$ spins, by controlling the transverse vibrational mode spectrum, and thereby control the frustration in the system. By directly measuring the spin correlations, we observe the role of frustration in the spin ordering.

The Ising couplings are simulated by imparting off-resonant spin dependent forces from a mode-locked laser (at a center wavelength of 355 nm, see section 2.6.4) to the $^{171}\text{Yb}^+$ ions, following the Mølmer-Sørensen scheme [71] as explained in the previous chapters.

This chapter is organized as follows:

- Section 5.2- we discuss some features of the long range antiferromagnetic quantum Ising model, in particular the ground and a few low lying energy states.

The critical energy gap between the ground and excited states in presence of the effective transverse magnetic field depends on the range of the interactions, which we explain in this section.

- Section 5.3- we describe the simulation of the AFM quantum Ising Hamiltonian

*Most of the results presented here are from the following manuscript in preparation. “Frustrated magnetic ordering with variable range interactions in a trapped ion quantum simulator”, R. Islam, C. Senko, W. C. Campbell, S. Korenblit, J. Smith, A. Lee, E. E. Edwards, J. C.-C. Wang, J. Freericks and C. Monroe.

(Eq. (5.1)), and the mechanism of tuning the range of interactions by changing the trapping parameters. We discuss the experimental protocol and some order parameters used to detect the spin order.

- Section 5.4- we compare the spin ordering in quantum simulation with various ranges of interactions, and present data that show suppression of the AFM or Neel order as the frustration increases in the system.

5.2 Some features of the long range antiferromagnetic quantum Ising model

5.2.1 Ground and low energy eigenstates

For $\underline{\alpha} \neq 0$: In the absence of the transverse field ($B = 0$ in Eq. (5.1)) the two fold degenerate antiferromagnetic (AFM) states $|\uparrow\downarrow\uparrow\dots\rangle$ and $|\downarrow\uparrow\downarrow\dots\rangle$ are the ground states for $\alpha \neq 0$ in Eq. (5.1). The first excited states contain two adjacent spins flipped from the AFM states on one end, and hence has a domain wall between the second and the third spins from one of the edges. Here a domain wall consists of two neighboring spins aligned in the same direction. Due to the left-right symmetry of the couplings, and the global spin flip symmetry of the Hamiltonian, the first excited state is four fold degenerate, namely $|\downarrow\uparrow\uparrow\downarrow\uparrow\dots\rangle$, $|\dots\downarrow\uparrow\downarrow\downarrow\uparrow\rangle$, $|\uparrow\downarrow\downarrow\uparrow\downarrow\dots\rangle$ and $|\dots\uparrow\downarrow\uparrow\uparrow\downarrow\rangle$. Here we have shown the spins that are flipped from the AFM ground states in red. The energy (measured from the ground state energy) of the

first excited states is,

$$\Delta E_{double,end} = 2J_0 \left[1 - 2 \sum_{n=2}^{N-2} (-1)^n \frac{1}{n^\alpha} + \frac{1}{(N-1)^\alpha} \right]. \quad (5.3)$$

This energy ($\Delta E_{double,end}$) is lower than the energy of the states with two adjacent spins flipped from the ground state in the bulk of the chain, as such states have two domain walls.

The states with one of the end spins flipped (from the AFM states) have an energy of

$$\Delta E_{single,end} = 2J_0 \left[\sum_{n=1}^{N-1} (-1)^{n-1} \frac{1}{n^\alpha} \right], \quad (5.4)$$

which is lower than the energy of the states with a bulk spin flipped, as they have two domain walls. Figure 5.1 shows a few excited state energies for various range of the interactions, $0 < \alpha < 3$. Eqs. (5.3) and (5.4) hold for $\alpha = 0$ as well, but the position of the excitation becomes irrelevant in calculating the excitation energy.

For $\underline{\alpha = 0}$: In case of a uniform antiferromagnetic Ising model ($\alpha = 0$), the Hamiltonian can be written in terms of the total spin operator $S_\gamma = \sum_i \sigma_\gamma^i$ ($\gamma = x, y, z$) as,

$$H = J_0 S_x^2 - B S_y. \quad (5.5)$$

Here we have subtracted a constant term of $J_0 N/2$ from the Hamiltonian. For $B = 0$, states with minimum S_x belong to the ground state. For an even system size N , $S_x = 0$ states form the ground state manifold. The number of such states is ${}^N C_{N/2}$, which is exponential in the system size N .

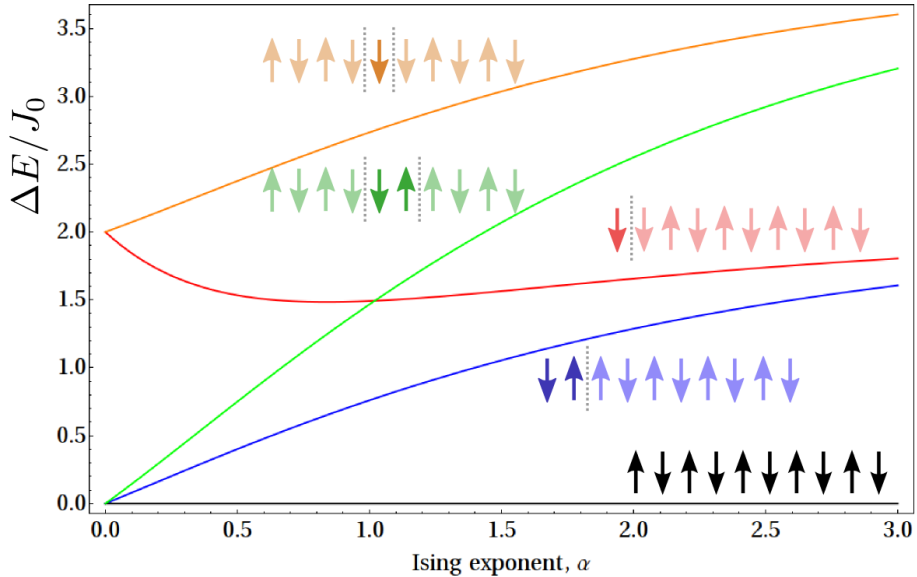


Figure 5.1: Energy of creating spin excitations in the long range antiferromagnetic Ising model: The ground states of the long range antiferromagnetic Ising model (Eq. (5.1) at $B = 0$) are the AFM states, $|\uparrow\downarrow\uparrow\dots\rangle$ and its globally spin flipped state $|\downarrow\uparrow\downarrow\dots\rangle$ for the exponent $\alpha \neq 0$ (in Eq. (5.2)). Any spin flip from this state creates domain walls, and costs some excitation energy. Here we plot the energies of creating a few types of excitations in a system of $N = 10$ spins, relative to the ground state energy (black line, black arrows denote one of the AFM states). The first excited states have two adjacent spins on the end flipped (blue), which contain a single domain wall (gray dotted line) between spins 2 and 3. Only one of the four degenerate first excited states are shown in terms of the blue arrows. It costs more energy to flip two adjacent spins in the bulk of the chain (green), as that involves creating two domain walls. The states with an end spin flipped (red) has more energy than the double spin flipped (on the end of the chain) states. States with a single bulk spin flipped (orange) have two domain walls, and hence are more energetic compared to the end spin flipped states. They are also higher in energy than the double adjacent spins flipped in the bulk states. The energies of the domain walls created depend on the range of the interactions, α . For the uniform Ising model ($\alpha = 0$) the position of the excitation does not matter.

In presence of the transverse field, S_x does not commute with the Hamiltonian (Eq. (5.5)), but $S^2 = S_x^2 + S_y^2 + S_z^2$ does. We probe the magnetic ordering by initializing the system in the ground state of $-BS_y$, which has a total $S_y = N$, and hence belongs to the $S^2 = N$ manifold, and then tune the effective transverse field B in Eq. (5.5). Thus the system can only access the ground states that belong to the total spin N manifold.

In presence of the transverse field B the ground state passes through a quantum phase transition from the paramagnetic phase (all spins polarized along the transverse field) to the AFM phase (for $\alpha \neq 0$). The critical gap and the critical field depend on the range of the interactions.

5.2.2 Frustration and the range of the interactions

In Fig. 5.2a, we plot a few of the low energy excited states of Eq. (5.1) for the case of $N=10$ spins, and $\alpha = 1.0$. In our quantum simulation experiment, we initialize the spins in the ground state of a ‘trivial’ Hamiltonian, which is just the part of the Hamiltonian (Eq. (5.1)) that couples to the magnetic field only. Then the Hamiltonian is ramped at a finite rate, and the dimensionless ratio of the effective transverse field to the Ising couplings is reduced. The system follows the ground state if the ramping is perfectly adiabatic. For a finite rate of ramping, some population is excited to excited states that have the same symmetry (w.r.t. the spin flip and spatial reflection, as discussed in section 3.2) as the ground state. The gap between the ground state and the lowest excited state with the same symmetry is

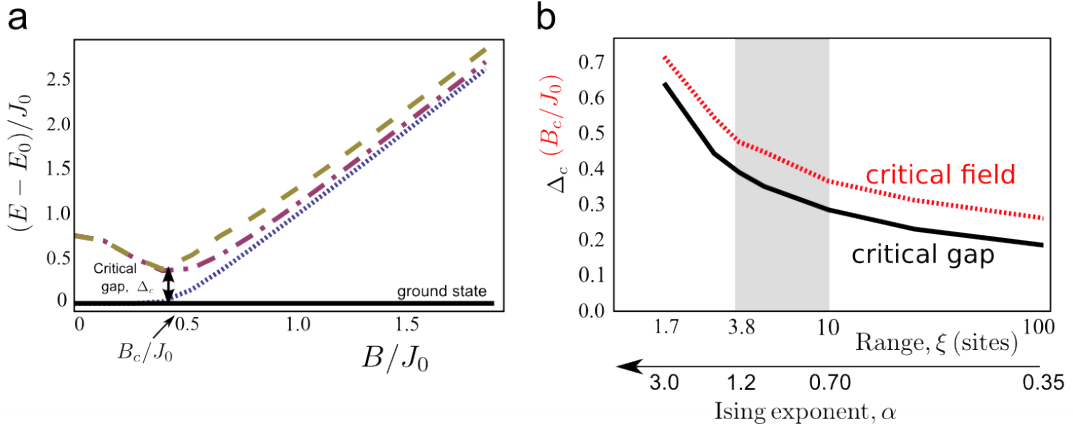


Figure 5.2: Dependence of the spectrum of Hamiltonian (5.1) on frustration: The energy spectrum of the long range antiferromagnetic quantum Ising model (Eq. (5.1)) with Ising coupling J_{ij} between spins i and j falling off with distance as $J_{ij} = J_0/|i - j|^\alpha$ depends on the amount of frustration in the system or the range of the interaction, ξ . **(a)** Few low lying energy states of the frustrated Hamiltonian (5.1) as a function of the dimensionless parameter B/J_0 for $\alpha = 1$ or $\xi = 5$. The spacing between the ground state and the second excited state reaches a bottleneck at a critical value B_c/J_0 . Here Δ_c is the critical energy gap of the Hamiltonian. **(b)** Dependence of B_c/J_0 (red dotted line) and Δ_c (black solid line) on the range of the interaction. As the interaction becomes long ranged (ξ increases, or α decreases) the competing long range couplings make it easy to create excitations in the system, the gap is reduced, and a relatively small effective transverse field can break the spin ordering. Both these parameters approach zero as $\alpha \rightarrow 0$ or $\xi \rightarrow \infty$. Our current experiments are performed with parameters in the shaded region. The apparent kinks on the curves are due to connecting a finite number of points by straight lines in the plot.

known as the critical gap, Δ_c , and the value of the effective magnetic field (the Ising couplings are fixed in our problem) at which the system passes through the critical gap is known as the critical field, B_c . Both the critical field B_c and the critical gap Δ_c depend on the range α , as shown in Fig. 5.2b. Both the quantities decrease monotonically as the range of the interactions, and hence the amount of frustration, increases.

To visualize the range of the interactions more intuitively, we define an effective range ξ as the distance between the spins at which the Ising coupling falls off to 20% of the nearest neighbor value. The choice of 20% as the cut-off is arbitrary, and motivated by our system size of $N = 10$ in some of the following experiments. With this definition, $\xi = 5^{1/\alpha}$, and varies between $\xi \approx 4$ and $\xi \approx 8$ sites for our experimentally accessible range of $\alpha \approx 0.76$ to $\alpha \approx 1.12$.

As the nearest neighbor interaction always wins over the long range couplings for this chain of spins (except at $\alpha = 0$), the ground state shows the nearest neighbor AFM ordering, regardless of the range of the interactions. Frustration in this model brings the excited states closer to the ground state in energy. Hence to observe the effects of frustration we ramp the effective transverse magnetic field B in the Hamiltonian (Eq. (5.1)) faster than the critical gap (Δ_c) to populate the excited states. The observed spin order depends on the amount of excitations created, and hence on the frustration. The system should exhibit less ground state character for the more frustrated (longer range) couplings for the same rate of ramping, and the same nearest neighbor energy scale.

5.3 Experimental simulation of the model

We simulate the quantum Ising model (Eq. (5.1)) by off-resonant excitations of transverse phonon modes, following the Mølmer-Sørensen scheme as explained in the previous chapters. The Raman beat-note detuning (μ in Eq. (3.8), Fig. 5.3a) is chosen to be bigger than the COM frequency, and thus all the Ising couplings are positive, or antiferromagnetic. The effective transverse magnetic field is simulated by a resonant carrier transition, with phase shifted by $\pi/2$ from the Raman beat-notes generating the Ising interactions. In our experiment we use global Raman beams (approximately 1 Watt each, with the 355 nm mode-locked laser) with horizontal and vertical waists of $\approx 150 \mu\text{m}$ and $\approx 7 \mu\text{m}$ respectively to address the ions. This produces a carrier Rabi frequency $\Omega \approx 2\pi \times 600 \text{ KHz}$, which is more than 98% homogeneous across a chain of $N = 16$ spins. We set the beatnote detuning μ to $\approx \omega_X + 3\eta\Omega$, where η is the single ion Lamb-Dicke parameter, and ω_X is the transverse COM frequency. We fit a power law profile (Eq. (5.2)) to the calculated Ising couplings, and extract the exponent α . The Ising coupling, $J_{i,j}$ between the spins i and j depend on the site i (in addition to the separation between the spins $|i - j|$), due to the finite size effects. This results in a site i dependent exponent, which varies by $\approx 10\%$ across the chain. Figure 5.3b shows the Ising couplings $J_{1,1+r}$ ($r = 1, 2, \dots, 9$) for typical experimental parameters (listed in the plot), in a system of $N = 10$ spins. The Ising coupling falls off as $J_{1,1+r} \propto 1/r^{1.0}$ ($\alpha = 1.0$) in this example. The nearest neighbor Ising couplings are stronger near the end of the spin chain compared to the center (Fig. 5.3c), and they vary by $\approx 20\%$ across the

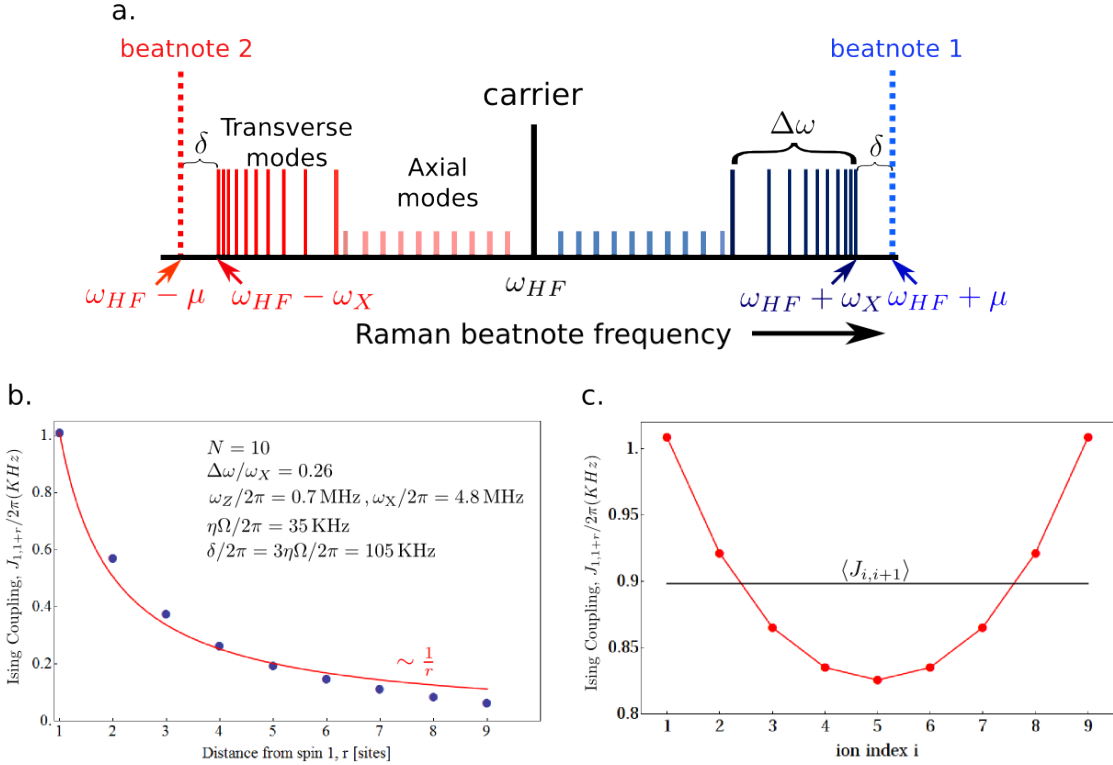


Figure 5.3: Ising coupling profile and fit to a power law: **a.** The Ising interactions between the spins are mediated by virtual phonon excitations. We show the red and the blue sidebands of the axial (light blue for the blue sidebands, and light red for the red sidebands) and the transverse (dark blue for the blue sidebands, and dark red for the red sidebands) vibrational normal modes of $N = 10$ trapped ions. To simulate the Ising interactions, we shine non-co-propagating laser beams with two beatnotes (beatnote 1 and 2 in this figure), symmetrically detuned from the carrier transition. The beatnotes are detuned from the transverse COM mode by a frequency δ . **b.** Ising couplings in KHz (blue circles) between spin 1 and the others, $J_{1,1+r}$ ($r = 1, 2, \dots, 9$) for a system of $N = 10$ spins, calculated from Eq. (3.8). The single ion sideband Rabi frequency, $\eta\Omega = 2\pi \times 35 \text{ KHz}$ and the Mølmer-Sørensen detuning, $\delta = 3\eta\Omega = 2\pi \times 105 \text{ KHz}$. The red curve is a power law fit to the Ising couplings ($J_{1,1+r} \propto 1/r^{1.0}$). **c.** Calculated nearest neighbor Ising couplings between spins i and $i + 1$, $J_{i,i+1}$ vs site i , according to Eq. (3.8). The interaction is the strongest at the ends of the chain, and varies by $\approx 20\%$ across the chain. The solid black line shows the average nearest neighbor interaction.

chain. This is primarily due to the contribution of the ‘tilt’ mode, which is the next lower energy vibrational mode after the COM. The ions near the center have smaller amplitudes of motion for this mode, and hence the ‘tilt’ mode does not contribute (Eq. (3.8)) to the nearest neighbor couplings near the center of the chain.

5.3.1 Tuning the range of Ising interactions

The range of the Ising interactions can be tuned by the following two methods:

- By changing the Raman beat-note frequency μ (or the Mølmer-Sørensen detuning δ), keeping the vibrational spectrum fixed.
- By changing the bandwidth of the vibrational spectrum, keeping the Mølmer-Sørensen detuning, $\delta = \mu - \omega_{COM}$ fixed.

We follow the second method, as this keeps the COM phonon occupation probability approximately at the same level for various ranges. The bandwidth of the transverse vibrational modes is controlled by tuning the trap anisotropy. A higher trap anisotropy (defined to be the ratio of the transverse COM freq to the axial COM frequency) moves the ions farther from each other, and reduce the bandwidth of the modes. On the other hand, a more isotropic trapping potential brings the ions closer together, until they cannot sustain a linear configuration and break into a zig-zag shape. We change the anisotropy of the trapping potential, and hence the bandwidth of the transverse vibrational modes, by changing the DC voltages applied on the trap electrodes, keeping the radio frequency power generating the ponderomotive potential at a constant value. Figure 5.4a shows the dependence

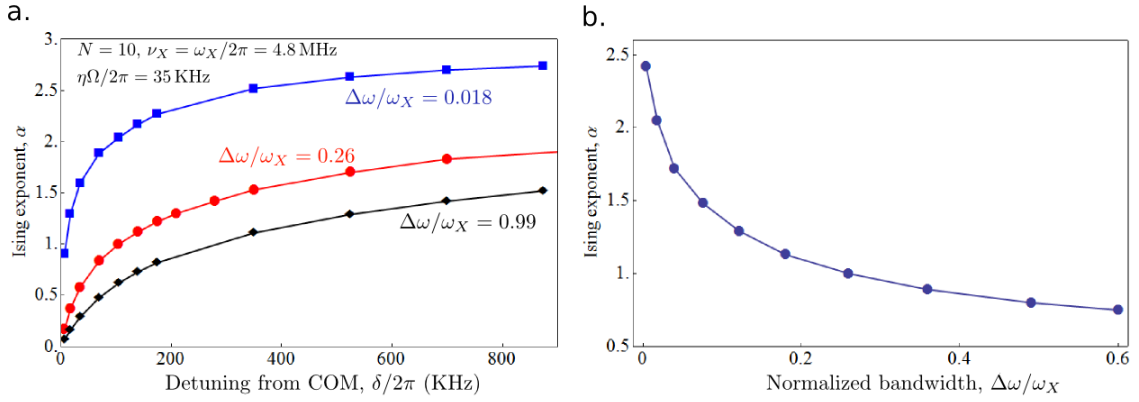


Figure 5.4: Dependence of the range of Ising interactions on the Mølmer-Sørensen detuning and the bandwidth of vibrational modes: **a.** We can tune the range of the Ising interactions by varying the Raman beatnote's detuning δ from the COM mode. Here we show theoretical calculations of the dependence of the Ising exponent, α (Eq. (5.2)) as a function of the detuning δ for normalized bandwidth $\Delta\omega/\omega_X = 0.018$, (blue squares), $\Delta\omega/\omega_X = 0.26$ (red circles), and $\Delta\omega/\omega_X = 0.99$ (black rhombuses). For comparison, a typical COM sideband Rabi frequency is $\eta\Omega/2\pi = 35$ KHz. The solid lines are interpolated in between the calculated points. **b.** Dependence of α on the bandwidth of the transverse modes, $\Delta\omega$ (Fig. 5.3) for a fixed detuning ($\delta/2\pi = 105$ KHz) from the COM mode. The bandwidth is controlled by changing the trap anisotropy. The coupling is more uniform when the normalized bandwidth is higher, and approaches a dipole interaction, *i.e.*, $\alpha = 3$, in the limit of $\Delta\omega/\omega_X \rightarrow 0$.

on the Ising coupling profile exponent α on the Mølmer-Sørensen detuning for two different sets of trapping parameters. A weaker trap along the axial direction leads to a larger bandwidth (red circles and line), $\Delta\omega$ (Fig. 5.3a) of the transverse vibrational modes, and thus it is easier to excite the COM modes exclusively without coupling to the other modes. This induces long range couplings, and the Ising exponent α is smaller than when the bandwidth is smaller (blue squares and line). It is relatively easier to access shorter range interactions (larger α) with higher bandwidth. In the limit of very large Mølmer-Sørensen detuning compared to the bandwidth, $\delta \gg \Delta\omega$ the Ising couplings take the form of a dipolar decay, or $J_{i,j} = J_0/|i - j|^3$, *i.e.*, $\alpha = 3$. In Fig. 5.4b we set a fixed Mølmer-Sørensen detuning $\delta/2\pi = 3\eta\Omega/2\pi = 105$ KHz, and show the dependence of the Ising exponent α on the bandwidth of the transverse modes. In the limit of $\Delta\omega/\omega_X \rightarrow 0$ the exponent $\alpha \rightarrow 3$, and in the other limit of $\Delta\omega/\omega_X = 1$, the interaction range is the longest at the specific Mølmer-Sørensen detuning, for the given system size, before the mechanical instability breaks the linear configuration of the ion chain. For the current experiments, we choose four trap settings, corresponding to four different ranges of interactions, as shown in Table 5.1.

For the range of axial frequencies used in the current experiment (between $\omega_Z = 2\pi \times 0.62$ MHz and $2\pi \times 0.95$ MHz), the Ising profile exponent α varies between 0.76 to 1.12, which corresponds to the variation of the range of interactions between $\xi = 4$ to $\xi = 8$ sites, the latter indicating that the range approaches the system size.

Settings	End avg DC (V_{end})	Central average ($V_{central}$)	Axial COM freq, $\omega_Z/2\pi$ (MHz)	Transverse COM freq, $\omega_X/2\pi$ (MHz)	Normalized mode bandwidth ($\Delta\omega/\omega_X$)	Ising exponent, α
I	25	1.1	0.952	4.87	0.56	0.76
II	20	0.9	0.857	4.75	0.44	0.9
III	13	0.6	0.691	4.80	0.25	1.0
IV	10	0.4	0.62	4.80	0.19	1.12

Table 5.1: **Experimental parameters used to generate long range Ising model with variable range:** The bandwidth of the transverse vibrational modes ($\Delta\omega$) is varied by changing the axial confinement of the ions to tune the range of the Ising couplings. We tabulate the average static voltages applied on the electrodes, axial and transverse COM trap frequency, the bandwidth of the modes normalized to the transverse COM frequency, and the Ising coupling exponent α for experiments with $N = 10$ ions reported here.

5.3.2 Experimental protocol and the order parameters

We initialize all the spins along the direction of the effective transverse magnetic field, *i.e.*, along the y -direction of the Bloch sphere by applying a resonant Raman pulse of appropriate duration and phase (a $\pi/2$ pulse about the x -axis of the Bloch sphere). Then we turn on Hamiltonian 5.1 with an initial field $B_0 \approx 5J_0$, where J_0 is the average nearest neighbor Ising coupling, such that our prepared spin state approximates the ground state of the initial Hamiltonian. (The overlap between the exact ground state of the initial Hamiltonian and the prepared polarized state is about 99%). The effective magnetic field is then ramped exponentially with a time constant of τ up to a final value B of the transverse field. We then measure the x -component of each spin by rotating our measurement axes, and using state dependent fluorescence signal on an intensified CCD imager. The experiments are

repeated $\sim 2000 - 4000$ times to collect statistics.

From the measured spin states, we construct the order parameters appropriate for observing the antiferromagnetic order and excitations. Various moments constructed from a distribution of staggered magnetization, defined as $m_s = \frac{1}{N} |\sum_{odd} \sigma_x - \sum_{even} \sigma_x|$, would differentiate between a paramagnetic and an antiferromagnetic state, and also quantify spin flip excitations. Here $\sum_{odd(even)}$ refers to summation over all the odd (even) sites of the lattice. In particular, we use the fourth moment, the staggered Binder cumulant,

$$g_s = \frac{\langle (m_s - \langle m_s \rangle)^4 \rangle}{\langle (m_s - \langle m_s \rangle)^2 \rangle^2}. \quad (5.6)$$

Here $\langle \dots \rangle$ denotes averaging over experimental realizations. In the paramagnetic phase the staggered magnetization, m_s is distributed according to a Binomial distribution, which approaches a Gaussian in a very large system. The Binder cumulant is, $g_s^0 = 3 - 2/N$ in the paramagnetic phase for a system of N spins. In the AFM phase, the distribution of the staggered magnetization consists of two Kronecker Delta functions, at $m_s = N$, and $m_s = -N$. The corresponding staggered Binder cumulant is unity in the AFM phase. Here we scale the Binder cumulant to take the finite size effect into account to

$$\bar{g}_s \equiv \frac{g_s^0 - g}{g_s^0 - 1}, \quad (5.7)$$

where g is the measured staggered Binder cumulant, according to Eq. (5.6).

We also construct two point correlation functions between the spins i and j , $C_{i,j}$ from the measured spin states, according to the following formula.

$$C_{i,j} = \langle \sigma_x^i \sigma_x^j \rangle - \langle \sigma_x^i \rangle \langle \sigma_x^j \rangle. \quad (5.8)$$

The two point correlation function allows us to directly probe the spin order at each experimental realization.

The Fourier transform of the correlation function, also known as the structure function $S(k)$, provides valuable information about the spin order. The structure function is defined as

$$S(k) = \frac{1}{N} \sum_{|i-j|} C_{i,j} \cos(k|i-j|) \quad (5.9)$$

For a finite system size of N spins, we calculate the structure function at distinct points, $k = 0, \frac{\pi}{N}, \frac{2\pi}{N}, \dots, \pi$. Since the two point correlation function $C_{i,j}$ depends on the site i itself for the finite size of the system, we use the averaged correlation of all the pairs of spins separated by $|i-j|$ sites. The structure function at $k = \pi$ is then

$$\begin{aligned} S(k = \pi) &= \frac{1}{N} \sum_{|i-j|} (-1)^{|i-j|} C_{i,j} \\ &= 1, \text{ for AFM state,} \end{aligned}$$

as $C_{i,j} = (-1)^N$ for a perfect AFM order. Thus a signature of spin frustration in our experiment would be the decay of the structure function at $k = \pi$.

5.4 Results of the quantum simulation

5.4.1 Onset of antiferromagnetic correlations in quantum simulation

for $N = 10$ and $N = 16$ spins

In Fig. 5.5 we plot the two point correlation between an end spin and the rest, $C_{1,1+r}$ ($r = 1, 2, \dots, N - 1$) for various values of the dimensionless parameter B/J_0 , for a range of $\xi = 4$ or $\alpha = 1.12$ (Eq. (5.2)) in a system of $N = 10$ spins. For our chosen experimental parameters, $J_0 \approx 800 Hz$. For $B/J_0 = 5$ we do not observe any appreciable correlation between the spins, consistent with a paramagnetic phase. As the ratio B/J_0 is lowered, the correlation with the nearest neighbor spin starts going negative at $B/J_0 \approx 1.5$. For lower values of B/J_0 , AFM correlations build up and the spins separated by even number of sites start to align themselves along the same direction, as seen by the alternating signs of the correlation coefficients with distance. The excitations created by non-adiabatic effects reduce the correlations from the perfect AFM state value of unity, and the best (anti)correlation achieved is $\approx 60\%$ for $B/J_0 \leq 0.01$.

Figure 5.7 shows the averaged CCD image of the $N = 10$ ions, all in the bright ($|\uparrow_z\rangle$), all in the dark ($|\downarrow_z\rangle$) and in the AFM states. The spins order in the two AFM states about 3% of the times (842 events out of 28,000 realizations). The spin flip symmetry is preserved in the simulation, as seen by the approximately equal number of experiments leading to either of the two AFM states (442 and 440 corresponding to spin $|\uparrow\rangle$ on the odd and even sites respectively). The probability of obtaining the

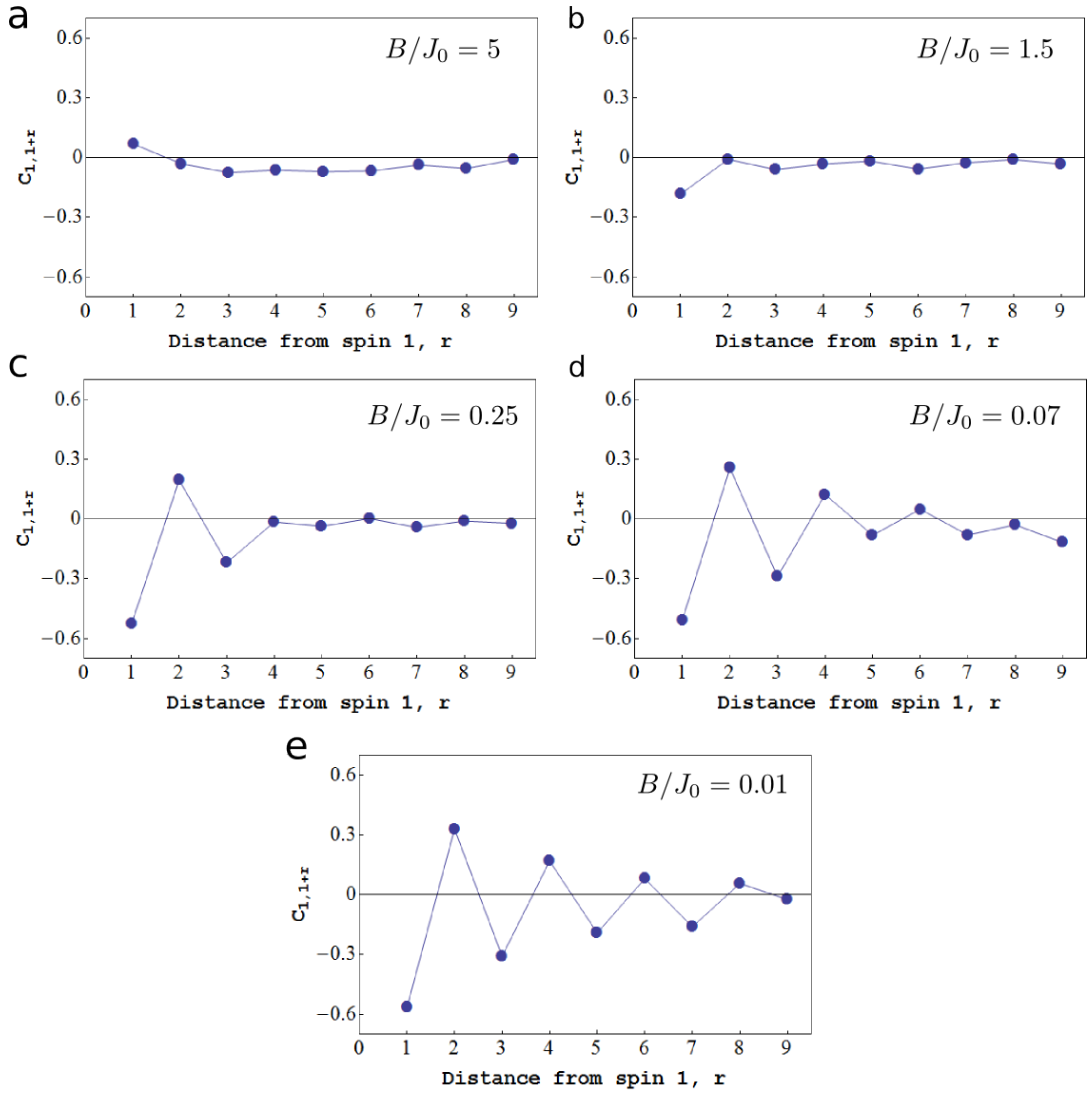


Figure 5.5: Onset of the antiferromagnetic ordering with 10 spins: As we tune the ratio of the effective transverse magnetic field to the antiferromagnetic Ising couplings, the spins undergo a crossover from the paramagnetic phase to the antiferromagnetic phase. **a-e.** Here we show the two point correlations between an edge spin, labeled as spin 1 and the others. By imaging the spin state dependent fluorescence of the trapped ions with single site resolution optics on an intensified CCD imager (model PIMax3: 1024i, made by Princeton Instruments), we directly measure the two point correlation functions. In this example, the Ising couplings approximately fall off with distance as $J_{i,j} = J_0/|i - j|^{1.2}$. The correlations do not reach unity, as expected from a perfect AFM ordering at zero temperature, primarily due to the finite speed of ramping in the quantum simulation (we ramped the external field exponentially down from $B = 5J_0$ with a time constant of $2\pi \times (0.4/J_0)$).

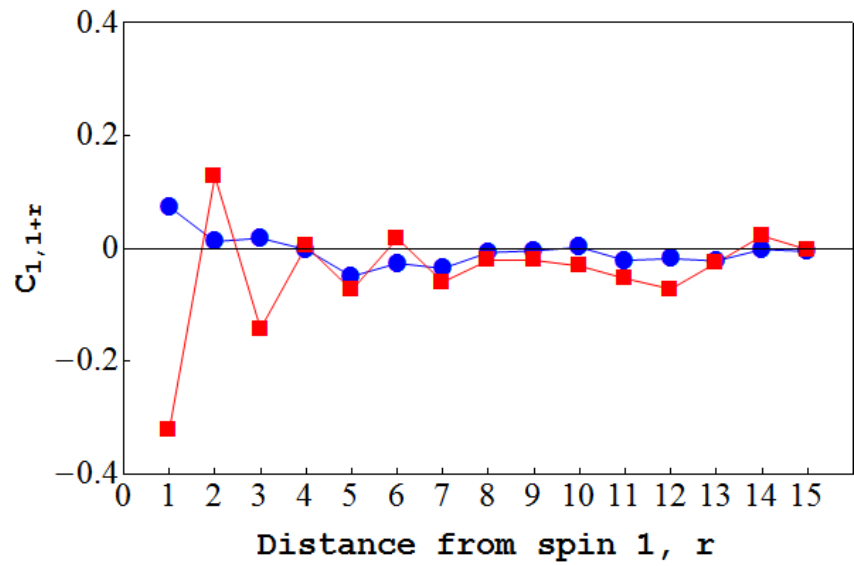


Figure 5.6: **Antiferromagnetic spin ordering with 16 spins:** We scale our quantum simulator up to $N = 16$ spins, and observe the onset of antiferromagnetic spin correlations. The Ising exponent is $\alpha = 1.0$ in this case. For the frustrated Ising model, the critical gap closes sharply with the system size. Thus maintaining the adiabaticity in simulation is harder compared to the ferromagnetic model. The blue circles are the two point correlations for $B/J_0 \sim 5$, and the red squares are for $B/J_0 \sim 0.01$.

AFM states is $2/2^{10} \approx 0.2\%$ in the paramagnetic phase.

In Fig. 5.6 we compare the correlations between an end spin and others, $C_{1,1+r}$ ($r = 1, 2, \dots, 15$) at $B/J_0 \approx 5$ (blue) and $B/J_0 \approx 0.01$ (red) for a system of $N = 16$ spins. At lower values of the ratio of the effective external field to the Ising couplings ratio, the system shows some antiferromagnetic spin ordering. The nearest neighbor correlation builds up to about -0.35 , and the correlation length (defined as the distance at which the correlation drops to $1/e$ of the nearest neighbor) is limited to about 5 sites. The lack of a very good ground state (AFM) order is primarily due to the vanishing critical gap Δ_c in presence of frustration when the system size grows, making our ramping of the ratio B/J_0 (we ramped the effective field exponentially with a time constant of $450 \mu s$, keeping the Ising couplings constant) too fast to be adiabatic.

5.4.2 Frustration of the AFM order with increasing range of interactions

We observe the spin order achieved in a quantum simulation experiment, for each of the four ranges of interactions described in table 5.1. The spins are initialized along the effective transverse field, B (in the y -direction of the Bloch sphere), then the Hamiltonian (Eq. (5.1)) is turned on with $B \approx 5J_0$, where J_0 is the average nearest neighbor Ising coupling. The effective field B is then exponentially turned down with a time constant $\tau/2\pi = 0.4/J_0$, and the spin order is detected at time $t = 6\tau$, where $B/J_0 \approx 0.01$. Figure 5.8a shows the scaled staggered Binder cumulant,

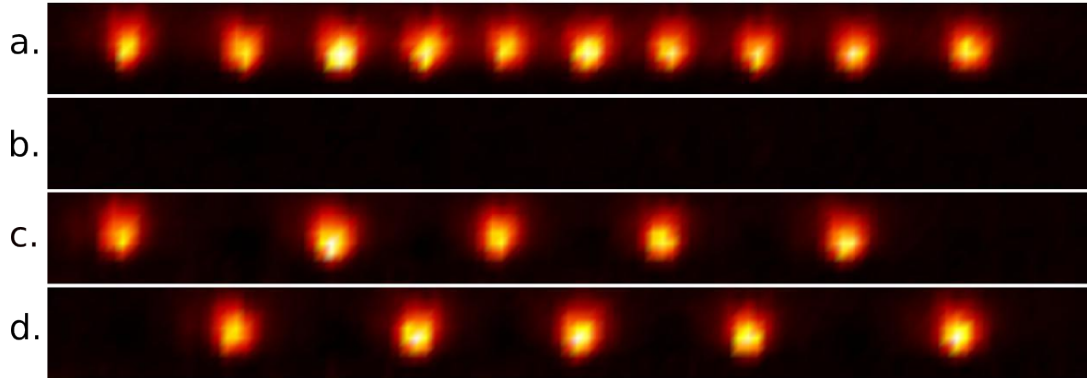


Figure 5.7: CCD image of $N = 10$ antiferromagnetically ordered spins: **a.** CCD image of 10 ions in spin $|\uparrow_z\rangle$ states. The image is obtained by averaging 440 experiments where each ion are prepared in the $|\uparrow_z\rangle$ state by applying a carrier Raman π pulse and then detected for 3 ms. **b.** Averaged CCD image (over 440 experiments) of the same 10 ions in $|\downarrow_z\rangle$ state, prepared by optical pumping. **c-d.** Averaged CCD image of the two AFM states. We post-select the AFM states from 28,000 quantum simulation experiments with long range AFM couplings, at a ratio of the effective transverse magnetic field to the nearest neighbor Ising coupling $B/J_0 \approx 0.03$. The CCD raw images of all such states with the same spin ordering (as detected by discriminating the fluorescence counts from the ions) are averaged to obtain the AFM states. 440 experiments resulted in an AFM state with $|\uparrow\rangle$ spins on the odd sites and 442 experiments with the $|\uparrow\rangle$ spins on the even sites. The measurement axes are rotated before the spin state detection such as a bright ion corresponds to the state $|\uparrow\rangle$ (in the x -basis).

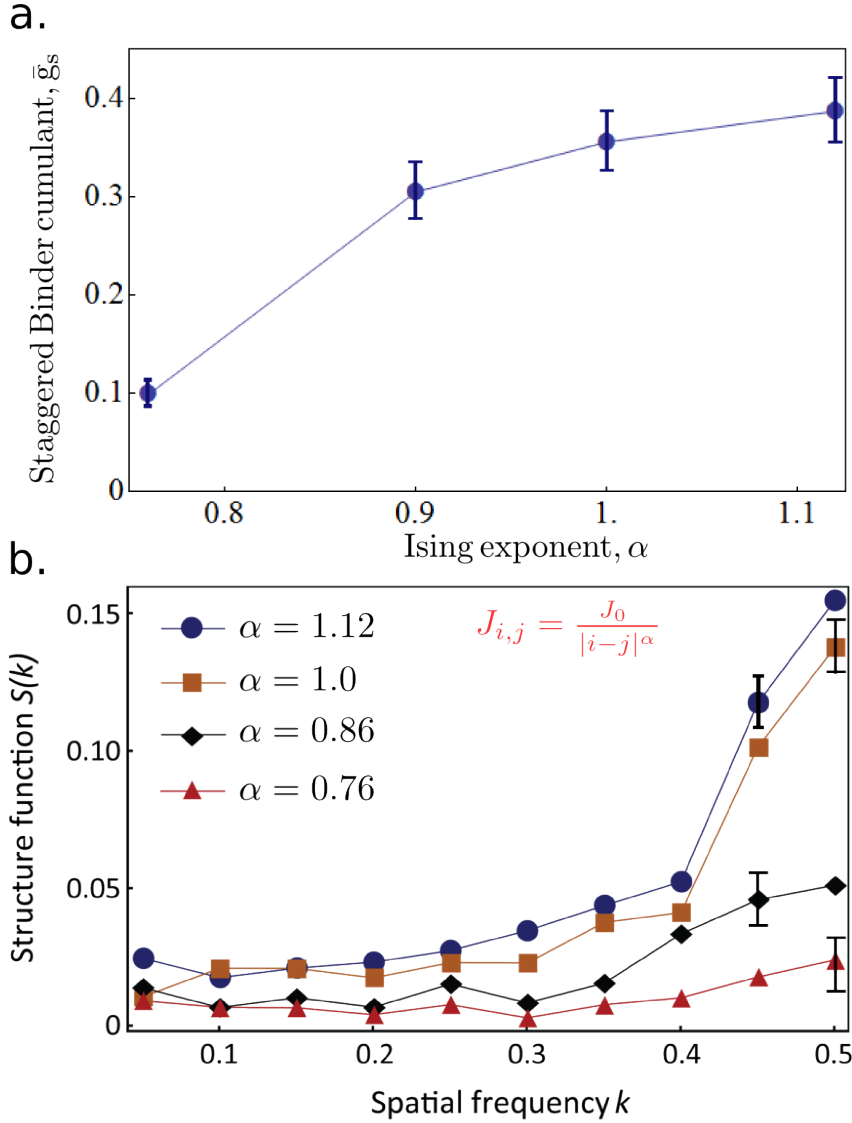


Figure 5.8: Frustration of antiferromagnetic spin ordering with increasing range of interactions: We compare the experimental data for four different ranges of Ising couplings, quantified by the exponent, α (Eq. (5.2)), which lies between 0.76 and 1.12 in our experiments. Frustration increases as the interaction range grows, and the excited states come closer to the ground state leading to a reduction in the value of the critical gap (Fig. 5.2). Thus for a given rate of ramping, the system is more excited from the ground state (non-adiabaticity) for longer range of interactions. **a.** The staggered Binder cumulant (Eq. (5.7)) at $B/J_0 \approx 0.01$ vs the exponent α . The order parameter goes down with increasing range, or decreasing α . The error bars are from a conservative estimate of the uncertainty in detecting the spin states. **b.** The structure function $S(k)$ (Eq. (5.9)) at $B/J_0 \approx 0.01$ for various ranges of interactions. The ground state ordering is denoted by $k = \pi$, which goes down with the increasing range of interactions. Characteristic error bars are conservative estimates of the uncertainty in detecting spin states. The solid lines are presented just to guide our eyes.

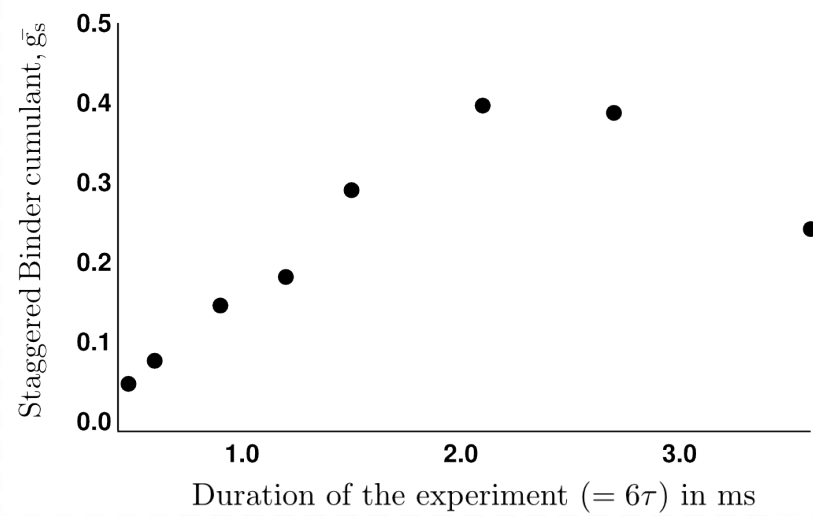


Figure 5.9: **Plausible decoherence in our quantum simulation:** We probe the spin order in the quantum simulation experiment as a function of the ramping speed of the Hamiltonian (Eq. (5.1)), with the Ising exponent $\alpha = 1.12$. The spins are polarized along the effective external magnetic field. The Hamiltonian is turned on with $B \approx 5J_0$, so that the initial spin state is an approximate ground state. Next the field is ramped down exponentially with a time constant τ for a time $t = 6\tau$, keeping the Ising couplings fixed, and the x -components of the spins are detected. The final value of the $B/J_0 \approx 0.01$. The experiment should be more adiabatic for a slower ramping, and hence a longer experimental duration, consistent with our observation up to $t = 6\tau \approx 2.5$ ms. The spin order goes down for slower ramping, which indicates the presence of some form of decoherence in the system. The intensity fluctuations in the Raman beams is one of the primary sources of decoherence in the system.

\bar{g}_s (Eq. (5.7)) vs the range of the interactions, quantified by the Ising exponent α . The staggered Binder cumulant monotonically decreases with increasing range (decreasing α) or frustration. Figure 5.8b shows the structure function, $S(k)$ (Eq. (5.9)) vs the spatial frequency, k for various range of interactions. The ground state AFM order is shown by the spatial frequency, $k = \pi$, which steadily goes down with the increasing range or frustration.

5.5 Discussions and conclusion

In this experiment, we have qualitatively observed the effect of frustration in the observed spin order. Our current experiment is not limited by decoherence due to spontaneous emission from the Raman beams, as the 355 nm Raman beams are far detuned from the $^2S_{1/2} - ^2P_{1/2}$ and $^2S_{1/2} - ^2P_{3/2}$ lines, and the spontaneous emission per Rabi cycle is suppressed to $\sim 10^{-5}$. The time scale for the spontaneous emission is then ~ 100 ms, which is more than an order of magnitude slower than the experimental time scales (< 5 ms).

In order to probe any decoherence effects, we repeat the simulation experiment with various ramping speed of the effective magnetic field. In Fig. 5.9 we plot the antiferromagnetic order parameter \bar{g}_s vs the total duration for the experiment for $\alpha = 1.12$. Here each data point represents the spin order achieved after ramping the B field down exponentially from $B \approx 5J_0$ for a total duration of $t = 6\tau$, where τ is the time constant with which the effective field is ramped down. The spin ordering into the antiferromagnetic state grows with slower ramping, as expected, for up to $t \approx 2.5$ ms. Then we observe a decay in the spin order, which might indicate the presence of decoherence effects in the system. A principal source of decoherence might be the intensity fluctuations in the Raman beams, due to beam pointing instabilities, and fluctuations in the optical power.

Chapter 6

Outlook

In this thesis, I presented some proof-of-principle experiments that benchmark a quantum simulator. We can further explore the long range nature of the interactions in the trapped ion system to study new many body physics. From a quantum computation point of view, the simulator must be scaled to a large number of qubits, that can outperform a classical computer. While there is no road-block in principle [128], several technological challenges need to be overcome in order to build a quantum computer or a universal quantum simulator. Here we discuss a few directions towards that goal.

6.1 Scaling up the system - large numbers of equally spaced ions in a Paul trap

To scale the ion trap system up to a size where the quantum simulator outperforms a classical computer, a stable large chain of ions is needed. While our current trap can handle a couple of dozens of spins without any technical upgrade, new trap architectures should help us scale the system further.

A shortcoming of using harmonic confining potential in a linear ion trap is that the ions near the center of the chain are closely packed together, compared to the outermost ones. This is less preferable to a chain of uniformly spaced ion crystal

for the following reasons.

- At a given ratio of the axial to the radial confinement, a linear ion chain undergoes a structural phase transition to a zig-zag configuration. This is unwanted in quantum information processing, as the ions in the zigzag configuration experience micromotion from the driving radio-frequency field. In a harmonic trap, this instability depends only on a few ions at the center that are very close to each other.
- Relatively larger spacings near the edge of the ion crystal limit the number of ions that can be trapped in a given length of the confining zone.
- As we shall discuss in this section, simulation of an arbitrary fully connected spin network requires individual addressing of the ions by well focused Raman beams. A uniform chain of ions would be ideal for this, as we can image a regularly spaced grid for this purpose. Also, switching a single beam between the ions by an AOM will be easier with a uniformly spaced ions.
- A uniformly spaced ion crystal makes the imaging easier, such as it would allow the use of a uniformly spaced PMT array, or a regularly spaced region of interest (ROI) on a CCD.

The problem of non-uniform ion spacing can be solved by adding anharmonic terms in the confining potential, such that the ions near the center are pushed out, and the outermost ions are pushed towards the center. A potential which is flatter than the harmonic potential near the center of the chain, and steeper at the edge is useful for

this purpose. Hence, to make a uniform chain of ions, at least a quartic potential is required to the lowest order [129]. An electrode with five or more segments is needed to generate a quartic potential in a linear trap.

6.2 Creating an arbitrary lattice geometry

It is possible to tailor the long range interactions in the trapped ion system properly to simulate a spin model on an arbitrary lattice geometry. The ultimate goal would be control every pairwise interaction in a fully connected spin network. In a system of N spins, there are ${}^N C_2 = N(N-1)/2 \approx N^2/2$ two body interactions, and thus we need at least $N^2/2$ control knobs to generate an arbitrary spin network. This is feasible by addressing the ions with individual Raman beams, each of which will contain several beat-notes to drive multiple normal modes selectively. Thus, extending Eq. 2.53 to the general case [130], the Ising coupling between spins i and j becomes,

$$J_{i,j} = \sum_{n=1}^N \Omega_{i,n} \Omega_{j,n} R \sum_{m=1}^N \frac{b_{i,m} b_{j,m}}{\mu_n^2 - \omega_m^2}. \quad (6.1)$$

Here R is the recoil frequency, $\Omega_{i,n}$ is the single spin carrier Rabi frequency consistent with the optical power on the i^{th} ion, and n^{th} beat-note at frequency μ_n . Thus we have N amplitude knobs $\Omega_{i,n}$ ($i = 1, 2, \dots, N$ for a fixed beat-note index n) corresponding to each beat-note μ_n ($n = 1, 2, \dots, N$) - a total of N^2 controls. Thus in principle, it should be possible to solve for the $N \times N$ Rabi frequency matrix $\Omega_{i,n}$ for any arbitrary $J_{i,j}$.

6.3 Other interesting spin physics

In the experiments presented in this thesis, we have tuned the Raman beat-note close to the COM mode, for which all the interactions have equal sign. Tuning the Raman beat-note in between the normal modes will give more versatility in the Ising couplings, allowing us to observe new spin phases. As an example, if the beat-note is tuned in between the second (tilt) and the third mode in the order of decreasing frequency, short range ferromagnetic couplings compete with the long range antiferromagnetic couplings. The resulting spin order is predicted to undergo a first order, or ‘sharp’ phase transition between a ferromagnetic and a ‘kink’ phase [100]. In the ferromagnetic phase all spins point in the same direction, and in the kink phase, a domain wall appears near the center of the spin chain. This prediction opens up an interesting avenue to explore, as this is an example of a truly sharp transition in a very small spin system.

While the quantum Ising model with arbitrary long range interactions admits many aspects of non-trivial many body physics, an access to several other spin models, such as the xy and the Heisenberg models, will enhance the versatility of the ion trap quantum simulator. The anisotropic Heisenberg model, xxz model can also be mapped to a Bose-Hubbard Hamiltonian in the context of ultracold atoms in optical lattices [131]. The xy model can be engineered by adding another pair of Raman beams coupling to the vibrational modes along the other transverse direction (y), and off-setting the phase of the Mølmer-Sørensen couplings induced by the additional laser beams by $\pi/2$ from the original beams. However, error terms

due to the cross-talk between the normal modes generating the $\sigma_x\sigma_x$ and the $\sigma_y\sigma_y$ interactions must be kept under control by properly shaping the mode excitations. In principle, we can add yet another beam to simulate the $\sigma_z\sigma_z$ couplings, in order to simulate the anisotropic Heisenberg interactions. However, due to our choice of the $^{171}\text{Yb}^+$ ‘clock’ hyperfine states as the spin states, the Ising couplings along the z direction may be smaller than the other two directions. This issue can be overcome by choosing one of the Zeeman states as the $|\uparrow_z\rangle$ state. The new spin-1/2 states are now more sensitive to any magnetic field fluctuations, and hence the magnetic field must be stabilized and the stray fields have to be shielded to maintain a long coherence time between the spin states.

Appendix A

Quantum trajectory calculations

Quantum trajectories (chapter 3) are generated* by numerically integrating the Schrödinger equation, with Hamiltonian 3.1, while simultaneously executing quantum jumps to account for spontaneous emission and decoherence. The probability of spontaneous emission used is consistent with the experimental parameters. The rate of dephasing (primarily due to the fluctuations in the intensities of the Raman beams) is treated as a fitting parameter. Spontaneous emission from ion i either localizes the spin of the ion, projecting it into $2S_{1/2}|F = 0, m_F = 0\rangle$ (spin state $|\downarrow_z\rangle$) or $2S_{1/2}|F = 1, m_F = 0\rangle$ (spin state $|\uparrow_z\rangle$), or it projects the ion into $2S_{1/2}|F = 1, m_F = 1\rangle$, in which case ion i is factored out of the Schrödinger evolution, though it is counted as spin up at the time of measurement. Decoherence (dephasing) is modeled by the quantum jump operator σ_x ; thus a jump for ion i , $|\psi\rangle \rightarrow \sigma_x^i |\psi\rangle$, introduces a π phase shift between the spin states $|\uparrow\rangle$ and $|\downarrow\rangle$ (in x -basis). Jump rates are taken to be fixed and equal for all ions. Note that a decoherence jump rate of Γ_{decoh} leads to decay of the spin coherence at rate $2\Gamma_{\text{decoh}}$. To determine the entangled state of the spin ensemble after a spontaneous emission,

*The calculations are performed by Changsuk Noh and Prof. Howard Carmichael, Auckland University, NZ.

e.g. from ion i , we assume that the ground state configuration prior to emission,

$$|\uparrow_z\rangle_i \prod_{j \neq i} (\alpha_{i,j} |\uparrow_z\rangle_j + \beta_{i,j} |\downarrow_z\rangle_j) + |\downarrow_z\rangle_i \prod_{j \neq i} (\gamma_{i,j} |\uparrow_z\rangle_j + \delta_{i,j} |\downarrow_z\rangle_j),$$

is mapped, by the far detuned Raman beams, into a very small excited-state contribution to the overall system entangled state,

$$\lambda |2P_{1/2}\rangle_i \prod_{j \neq i} [(\alpha_{i,j} + \gamma_{i,j}) |\uparrow_z\rangle_j + (\beta_{i,j} + \delta_{i,j}) |\downarrow_z\rangle_j],$$

with $\lambda \ll 1$ proportional to the amplitude of the Raman beams and inversely proportional to their detuning. The (unnormalized) state after the emission is

$$|?\rangle_i \prod_{j \neq i} [(\alpha_{i,j} + \gamma_{i,j}) |\uparrow_z\rangle_j + (\beta_{i,j} + \delta_{i,j}) |\downarrow_z\rangle_j],$$

where $|?\rangle_i$ is $|\uparrow_z\rangle_i$, $|\downarrow_z\rangle_i$, or the factored state $2S_{1/2}|F=1, m_F=1\rangle$.

Appendix B

Detection of spin states

This appendix describes the methods used to detect the spin ordering in the quantum simulation of the ferromagnetic Ising model with $N = 2$ to $N = 9$ spins, described in chapter 3.

The spin states are detected by spin-dependent fluorescence signals collected through $f/2.1$ optics by a photomultiplier tube. Spin state $|\uparrow_z\rangle$ is resonantly excited by the 369.5 nm detection beam and fluoresces from $^2P_{1/2}$ states, emitting Poisson distributed photons with mean ~ 12 in 0.8 ms. This state appears as ‘bright’ to PMT. The detection light is far off-resonant to spin state $|\downarrow_z\rangle$ and this state appears ‘dark’ to the PMT. However, due to weak off-resonant excitation bright state leaks onto dark state, altering the photon distribution [90]. Unwanted scattered light from optics and trap electrodes also alter the photon distribution. We construct the basis function for s bright ions by convolution techniques, and include a 5% fluctuation in the intensity of detection beam, which is representative of our typical experimental conditions. We then fit the experimental data to these basis functions, and obtain probabilities $P(s)$ at each time step t_i in the experiment. Mean photon counts for dark (m_D) and bright (m_B) states are used as fitting parameters so as to minimize the error residues.

The best fitting at time step t_i is obtained for the parameters $\{m_{D,i}, m_{B,i}\}$.

These parameters fluctuate at different time steps of the quantum simulation, primarily due to fluctuations in the intensity of detection beam and background scatter, and also due to uncertainties in a multivariate fitting. The fitting errors are propagated to the spin state probabilities $P(s)$ using Monte Carlo method of error analysis, as follows. We extract $P(s)$ and compute the order parameters at time step t_i with mean dark and bright state counts chosen randomly from a Gaussian distribution with mean $\{\bar{m}_D, \bar{m}_B\}$ and standard deviations $\{\delta m_D, \delta m_B\}$ respectively. Here \bar{m}_D and \bar{m}_B are averages of $m_{D,i}$ and $m_{B,i}$ respectively over different time steps t_i . Similarly δm_D and δm_B are standard deviations of $m_{D,i}$ and $m_{B,i}$ respectively. By repeating this process ~ 400 times we generate a histogram of each order parameter and fit the histograms to a Gaussian distribution. The standard deviation of the distribution is chosen to represent the random error due to fitting in that order parameter. The uncertainty in amount of fluctuation of the detection beam power during the experiment is conservatively included in the error analysis by repeating the fitting process for a range of fluctuations. The finite width of the detection beam is taken care of by modeling the Gaussian beam having a three step intensity profile with appropriate intensity ratios.

Appendix C

Relevant Frequencies for $^{171}\text{Yb}^+$ and $^{174}\text{Yb}^+$

The following table lists the frequency lock points of various lasers used in our experiments. The 739.5 nm laser (Ti:Sapphire) is locked to a hyperfine transition of Iodine molecules. This light is sent to the Iodine saturation absorption spectroscopy set up through an EOM driven at 13.315 GHz, and the (positive) first order side-band of this light excites the Iodine line. The 739.5 nm laser frequency lock points are about 400 MHz red detuned from the cooling transition resonance, and thus appropriate for using 400 MHz AOMs.

Without changing the lock point of the 739.5 nm laser, we can address the $^{174}\text{Yb}^+$ resonance by shifting the Iodine EOM drive frequency to 12.103 GHz (while locking the laser to 405.644318 THz).

Laser	Frequency for $^{171}\text{Yb}^+$ (THz)	Frequency for $^{174}\text{Yb}^+$ (THz)	Comments
739.5 nm	405.644318	405.645530	Iodine EOM at 13.315 GHz
935 nm	320.56922	320.57190	
399 nm	751.52764	751.52680	
638 nm	469.445, 469.442	469.439	scanned around these two lines

Table C.1: Frequency lock points for various lasers

Bibliography

- [1] P. A. M. Dirac, *The Principles of Quantum Mechanics*, vol. 27 of *International series of monographs on physics (Oxford, England)*. second ed., 1935.
- [2] A. Einstein, B. Podolsky, and N. Rosen, “Can quantum-mechanical description of physical reality be considered complete?,” *Phys. Rev.*, vol. 47, p. 777, 1935.
- [3] R. Feynman, “Simulating physics with computers,” *Int. J. Theor. Phys.*, vol. 21, pp. 467–488, 1982.
- [4] S. Lloyd, “Universal quantum simulators,” *Science*, vol. 273, p. 1073, 1996.
- [5] T. D. Ladd, F. Jelezko, R. Laflamme, Y. Nakamura, C. Monroe, and J. L. O’Brien, “Quantum computers,” *Nature*, vol. 464, p. 45, 2010.
- [6] D. P. DiVincenzo and P. W. Shor, “Fault-tolerant error correction with efficient quantum codes,” *Phys. Rev. Lett.*, vol. 77, pp. 3260–3263, Oct 1996.
- [7] J. I. Cirac and P. Zoller, “Quantum computation with cold trapped ions,” *Phys. Rev. Lett.*, vol. 74, pp. 4091–4094, 1995.
- [8] D. Porras and J. I. Cirac, “Effective quantum spin systems with trapped ions,” *Phys. Rev. Lett.*, vol. 92, p. 207901, May 2004.
- [9] X.-L. Deng, D. Porras, and J. I. Cirac, “Effective spin quantum phases in systems of trapped ions,” *Phys. Rev. A*, vol. 72, p. 063407, Dec 2005.
- [10] R. Blatt and C. F. Roos, “Quantum simulations with trapped ions,” *Nature Physics*, vol. 8, p. 277, 2012.
- [11] I. Bloch, J. Dalibard, and S. Nascimbène, “Quantum simulations with ultracold quantum gases,” *Nature Physics*, vol. 8, pp. 267–276, Apr 2012.
- [12] M. Greiner and S. Fölling, “Q & A Optical lattices,” *Nature*, vol. 453, pp. 736–738, June 2008.
- [13] R. J. Schoelkopf and S. M. Girvin, “Wiring up quantum systems.,” *Nature*, vol. 451, pp. 664–9, Feb. 2008.
- [14] A. A. Houck, H. E. Türeci, and J. Koch, “On-chip quantum simulation with superconducting circuits,” *Nature Physics*, vol. 8, pp. 292–299, Apr. 2012.
- [15] D. B. Othman, J. A. Barrat, F. Albareda, A. Halliday, D. Lee, S. Levasseur, N. Teutsch, Y. Guo, E. D. Young, H. D. Ash, N. Dauphas, R. T. Helz, D. A. Ionov, C. M. Johnson, M. Wadhwa, R. T. Helz, F. Tera, R. T. Helz, R. J. Walker, E. D. Young, and C. E. Manning, “Diamond for Quantum Computing,” *Science*, vol. 320, p. 1601, 2008.

- [16] J. L. O'Brien, "Optical quantum computing," *Science*, vol. 318, no. 5856, pp. 1567–1570, 2007.
- [17] B. P. Lanyon, J. D. Whitfield, G. G. Gillett, M. E. Goggin, M. P. Almeida, I. Kassal, J. D. Biamonte, M. Mohseni, B. J. Powell, M. Barbieri, A. Aspuru-Guzik, and A. G. White, "Towards quantum chemistry on a quantum computer.," *Nature Chemistry*, vol. 2, pp. 106–11, Feb 2010.
- [18] X.-s. Ma, B. Dakic, W. Naylor, A. Zeilinger, and P. Walther, "Quantum simulation of the wavefunction to probe frustrated Heisenberg spin systems," *Nature Physics*, vol. 7, pp. 399–405, Feb. 2011.
- [19] A. Aspuru-Guzik and P. Walther, "Photonic quantum simulators," *Nature Physics*, vol. 8, pp. 285–291, Apr. 2012.
- [20] B. Lanyon, C. Hempel, D. Nigg, M. Mueller, R. Gerritsma, F. Zaehringer, P. Schindler, J. T. Barreiro, M. Rambach, G. Kirchmair, M. Hennrich, P. Zoller, R. Blatt, and C. F. Roos, "Universal digital quantum simulation with trapped ions," *Science*, vol. 334, no. 6052, p. 57, 2011.
- [21] I. Buluta and F. Nori, "Quantum simulators," *Science*, vol. 326, no. 5949, pp. 108–111, 2009.
- [22] J. Hubbard, "Electron correlations in narrow energy bands.," *Series A. Mathematical and Physical Sciences*, vol. 276(1365), p. 238257, 1963.
- [23] K. A. Chao, J. Spałek, and A. M. Oleś, "Canonical perturbation expansion of the hubbard model," *Phys. Rev. B*, vol. 18, pp. 3453–3464, Oct 1978.
- [24] P. W. Anderson, "Localized magnetic states in metals," *Phys. Rev.*, vol. 124, pp. 41–53, Oct 1961.
- [25] K. Yamada, *Electron correlation in metals*. Cambridge University Press, 2004.
- [26] V. Anisimov and Y. Izyumov., *Electronic structure of strongly correlated materials*. Springer-Verlag, 2010.
- [27] P. A. Lee, N. Nagaosa, and X.-G. Wen, "Doping a Mott insulator: Physics of high-temperature superconductivity," *Rev. Mod. Phys.*, vol. 78, pp. 17–85, Jan 2006.
- [28] A. Hewson., *The Kondo problem to heavy fermions*. Cambridge University Press, 1993.
- [29] A. Ramirez., "Colossal magnetoresistance.," *J. Phys: Condens. Matter*, vol. 9, p. 8171, 1997.
- [30] L. Balents, "Spin liquids in frustrated magnets.," *Nature*, vol. 464, pp. 199–208, Mar. 2010.

- [31] H. L. Stormer, D. C. Tsui, and A. C. Gossard, “The fractional quantum Hall effect,” *Rev. Mod. Phys.*, vol. 71, pp. S298–S305, Mar 1999.
- [32] M. P. Nightingale and C. J. Umrigar, *Quantum Monte Carlo Methods in Physics and Chemistry*. NATO Science Series, 1998.
- [33] U. Schollwöck, “The density-matrix renormalization group,” *Rev. Mod. Phys.*, vol. 77, pp. 259–315, Apr 2005.
- [34] P. Henelius and A. W. Sandvik, “Sign problem in monte carlo simulations of frustrated quantum spin systems,” *Phys. Rev. B*, vol. 62, pp. 1102–1113, Jul 2000.
- [35] A. W. Sandvik, “Ground states of a frustrated quantum spin chain with long-range interactions,” *Phys. Rev. Lett.*, vol. 104, p. 137204, Mar 2010.
- [36] M. P. A. Fisher, P. B. Weichman, G. Grinstein, and D. S. Fisher, “Boson localization and the superfluid-insulator transition,” *Phys. Rev. B*, vol. 40, pp. 546–570, Jul 1989.
- [37] M. Greiner, O. Mandel, T. Esslinger, T. W. Hänsch, and I. Bloch, “Quantum phase transition from a superfluid to a Mott insulator in a gas of ultracold atoms,” *Nature*, vol. 405, pp. 39–44, 2002.
- [38] W. S. Bakr, A. Peng, M. E. Tai, R. Ma, J. Simon, J. I. Gillen, S. Flung, L. Pollet, and M. Greiner, “Probing the superfluid to Mott insulator transition at the single-atom level,” *Science*, vol. 329, no. 5991, pp. 547–550, 2010.
- [39] A. Friedenauer, H. Schmitz, J. T. Glueckert, D. Porras, and T. Schaetz, “Simulating a quantum magnet with trapped ions,” *Nature Physics*, vol. 4, pp. 757–761, 2008.
- [40] J. Simon, W. S. Bakr, R. Ma, M. E. Tai, P. M. Preiss, and M. Greiner, “Quantum simulation of an antiferromagnetic spin chains in an optical lattice.,” *Nature*, vol. 472, pp. 307–312, Apr 2011.
- [41] R. Islam, E. E. Edwards, K. Kim, S. Korenblit, C. Noh, H. Carmichael, G.-D. Lin, L.-M. Duan, C.-C. J. Wang, J. K. Freericks, and C. Monroe, “Onset of a quantum phase transition with a trapped ion quantum simulator,” *Nature Communications*, vol. 2, p. 377, 2011.
- [42] E. E. Edwards, S. Korenblit, K. Kim, R. Islam, M.-S. Chang, J. K. Freericks, G.-D. Lin, L.-M. Duan, and C. Monroe, “Quantum simulation and phase diagram of the transverse-field ising model with three atomic spins,” *Phys. Rev. B*, vol. 82, p. 060412, Aug 2010.
- [43] K. Kim, M.-S. Chang, S. Korenblit, R. Islam, E. E. Edwards, J. K. Freericks, G.-D. Lin, L.-M. Duan, and C. Monroe, “Quantum simulation of frustrated ising spins with trapped ions,” *Nature*, vol. 465, pp. 590–593, 2010.

- [44] G.-B. Jo, Y.-R. Lee, J.-H. Choi, C. A. Christensen, T. H. Kim, J. H. Thywissen, D. E. Pritchard, and W. Ketterle, “Itinerant ferromagnetism in a Fermi gas of ultracold atoms,” *Science*, vol. 325, no. 5947, pp. 1521–1524, 2009.
- [45] J. Bardeen, L. N. Cooper, and J. R. Schrieffer, “Theory of superconductivity,” *Phys. Rev.*, vol. 108, pp. 1175–1204, Dec 1957.
- [46] C. A. Regal and D. S. Jin, “Experimental Realization of BCS-BEC Crossover with a Fermi Gas of Atoms,” *Advances in Atomic, Molecular and Optical Physics*, vol. 54, no. 06, 2007.
- [47] S. Sachdev, *Quantum Phase Transitions*. Cambridge, UK: Cambridge University Press, 1999.
- [48] S. Sachdev, “Quantum magnetism and criticality,” *Nature Physics*, vol. 4, pp. 173–185, 2008.
- [49] X. Zhang, C.-L. Hung, S.-K. Tung, and C. Chin, “Observation of quantum criticality with ultracold atoms in optical lattices,” *Science*, vol. 335, no. 6072, pp. 1070–1072, 2012.
- [50] G.-D. Lin, S.-L. Zhu, R. Islam, K. Kim, M.-S. Chang, S. Korenblit, C. Monroe, and L.-M. Duan, “Large-scale quantum computation in an anharmonic linear ion trap,” *Europhysics Letters*, vol. 86, p. 60004, 2009.
- [51] R. Gerritsma, G. Kirchmair, F. Zaehringer, E. Solano, R. Blatt, and C. F. Roos, “Quantum simulation of the Dirac equation,” *Nature*, vol. 462, p. 68, 2010.
- [52] R. Gerritsma, B. P. Lanyon, G. Kirchmair, F. Zaehringer, C. Hempel, J. Casanova, J. J. Garcia-Ripoll, E. Solano, R. Blatt, and C. F. Roos, “Quantum simulation of the Klein paradox,” *Phys. Rev. Lett.*, vol. 106, p. 060503, 2011.
- [53] J. Britton, B. Sawyer, A. Keith, C.-C. J. Wang, J. Freericks, H. Uys, M. Beireruk, and J. Bollinger, “Engineered two-dimensional ising interactions in a trapped-ion quantum simulator with hundreds of spins,” *Nature*, vol. 484, pp. 489–492, Apr 2012.
- [54] K. Kim, M.-S. Chang, R. Islam, S. Korenblit, L.-M. Duan, and C. Monroe, “Entanglement and tunable spin-spin couplings between trapped ions using multiple transverse modes,” *Phys. Rev. Lett.*, vol. 103, p. 120502, Sep 2009.
- [55] S. Haravifard, A. Banerjee, J. C. Lang, G. Srivastava, D. M. Silevitch, B. D. Gaulin, H. A. Dabkowska, and T. F. Rosenbaum, “Continuous and discontinuous quantum phase transitions in a model two-dimensional magnet.,” *Proceedings of the National Academy of Sciences of the United States of America*, vol. 109, no. 7, pp. 2286–9, 2012.

- [56] H. Feshbach, “Unified theory of nuclear reactions,” *Annals of Physics*, vol. 5, pp. 357–390, 1958.
- [57] S. Inouye, M. R. Andrews, J. Stenger, H.-J. Miesner, D. M. Stamper-Kurn, and W. Ketterle, “Observation of Feshbach resonances in a Bose-Einstein condensate,” *Nature*, vol. 392, pp. 151–154, 1998.
- [58] J. E. Lye, L. Fallani, M. Modugno, D. S. Wiersma, C. Fort, and M. Inguscio, “Bose-Einstein condensate in a random potential,” *Phys. Rev. Lett.*, vol. 95, p. 070401, Aug 2005.
- [59] T. Schulte, S. Drenkelforth, J. Kruse, W. Ertmer, J. Arlt, K. Sacha, J. Zdziarski, and M. Lewenstein, “Routes towards Anderson-like localization of Bose-Einstein condensates in disordered optical lattices,” *Phys. Rev. Lett.*, vol. 95, p. 170411, Oct 2005.
- [60] M. Pasienski, D. McKay, M. White, and B. DeMarco, “A disordered insulator in an optical lattice,” *Nature Physics*, vol. 6, pp. 677–680, July 2010.
- [61] W. S. Bakr, J. I. Gillen, A. Peng, S. Flung, and M. Greiner, “A quantum gas microscope for detecting single atoms in a Hubbard-regime optical lattice,” *Nature*, vol. 462, no. 7269, pp. 74–7, 2009.
- [62] R. Blatt and D. Wineland, “Entangled states of trapped atomic ions,” *Nature*, vol. 453, p. 1008, 2008.
- [63] C. Monroe, D. M. Meekhof, B. E. King, W. M. Itano, and D. J. Wineland, “Demonstration of a fundamental quantum logic gate,” *Phys. Rev. Lett.*, vol. 75, p. 4714, 1995.
- [64] F. Schmidt-Kaler, H. Haeffner, M. Riebe, S. Guld, G. P. T. Lancaster, T. Deuschle, C. Becher, C. F. Roos, J. Eschner, and R. Blatt, “Realization of the Cirac-Zoller controlled-not quantum gate,” *Nature*, vol. 422, p. 408, 2003.
- [65] F. Schmidt-Kaler, H. Haeffner, S. Gulde, M. Riebe, G. P. T. Lancaster, T. Deuschle, C. Becher, W. Haensel, J. Eschner, C. F. Roos, and R. Blatt, “How to realize a universal quantum gate with trapped ions,” *Applied Physics B*, vol. 77, p. 789, 2003.
- [66] M. Riebe, K. Kim, P. Schindler, T. Monz, P. O. Schmidt, T. K. Körber, W. Hänsel, H. Häffner, C. F. Roos, and R. Blatt, “Process tomography of ion trap quantum gates,” *Phys. Rev. Lett.*, vol. 97, p. 220407, Dec 2006.
- [67] M. Riebe, H. Haeffner, C. F. Roos, W. Haensel, J. Benhelm, G. P. T. Lancaster, T. W. Koerber, C. Becher, F. Schmidt-Kaler, D. F. V. James, and R. Blatt, “Deterministic quantum teleportation with atoms,” *Nature*, vol. 429, p. 734, 2004.

- [68] M. D. Barrett, J. Chiaverini, T. Schaetz, J. Britton, W. M. Itano, J. D. Jost, E. Knill, C. Langer, D. Leibfried, R. Ozeri, and D. J. Wineland, “Deterministic quantum teleportation of atomic qubits,” *Nature*, vol. 429, p. 737, 2004.
- [69] S. Olmschenk, D. N. Matsukevich, P. Maunz, D. Hayes, L.-M. Duan, and C. Monroe, “Quantum teleportation between distant matter qubits,” *Science*, vol. 323, p. 486, 2009.
- [70] S. M. Olmschenk, *Quantum Teleportation between Distant Matter Qubits*. PhD thesis, University of Michigan, Ann Arbor, 2009.
- [71] K. Mølmer and A. Sørensen, “Multiparticle entanglement of hot trapped ions,” *Phys. Rev. Lett.*, vol. 82, p. 1835, 1999.
- [72] H. T. Diep, *Frustrated Spin Systems*. World Scientific Publishing Company, 2005.
- [73] E. Farhi, J. Goldstone, S. Gutmann, J. Lapan, A. Lundgren, and D. Preda, “A quantum adiabatic evolution algorithm applied to random instances of an np-complete problem,” *Science*, vol. 292, p. 472, 2001.
- [74] S. Earnshaw, “On the nature of the molecular forces which regulate the constitution of the luminiferous ether,” *Trans. Camb. Phil. Soc.*, vol. 7, pp. 97–112, 1842.
- [75] W. Paul, “Electromagnetic traps for charged and neutral particles,” *Rev. Mod. Phys.*, vol. 62, pp. 531–540, Jul 1990.
- [76] L. S. Brown and G. Gabrielse, “Geonium theory: Physics of a single electron or ion in a Penning trap,” *Rev. Mod. Phys.*, vol. 58, pp. 233–311, Jan 1986.
- [77] H. G. Dehmelt, “Radiofrequency spectroscopy of stored ions I: Storage,” *Advances in Atomic, Molecular and Optical Physics*, vol. 3, p. 53, 1967.
- [78] D. J. Berkeland, J. D. Miller, J. C. Bergquist, W. M. Itano, and D. J. Wineland, “Minimization of ion micromotion in a Paul trap,” *Journal of Applied Physics*, vol. 83, pp. 5025–5033, 1998.
- [79] J. Siversen, L. Simkins, S. Weidt, and W. Hensinger, “On the application of radio frequency voltages to ion traps via helical resonators,” *Applied Physics B*, doi:10.1007/s00340-011-4837-0, 2012.
- [80] D. Das, S. Barthwal, A. Banerjee, and V. Natarajan, “Absolute frequency measurements in Yb with 0.08 ppb uncertainty: Isotope shifts and hyperfine structure in the 399-nm $^1s_0 \rightarrow ^1p_1$ line,” *Phys. Rev. A*, vol. 72, p. 032506, Sep 2005.

- [81] P. T. H. Fisk, M. J. Sellars, M. A. Lawn, C. Coles, A. G. Mann, and D. G. Blair, "Very high Q microwave spectroscopy on trapped $^{171}\text{Yb}^+$ ions: Application as a frequency standard," *IEEE Transactions on Instrumentation and Measurement*, vol. 44, p. 113, 1995.
- [82] P. T. H. Fisk, M. J. Sellars, M. A. Lawn, and C. Coles, "Accurate measurement of the 12.6 Ghz 'clock' transition in trapped $^{171}\text{Yb}^+$ ions," *IEEE Transactions on Ultrasonics, Ferroelectrics, and Frequency Control*, vol. 44, no. 2, pp. 344–354, 1997.
- [83] A. S. Bell, P. Gill, H. A. Klein, A. P. Levick, C. Tamm, and D. Schnier, "Laser cooling of trapped ytterbium ions using a four-level optical-excitation scheme," *Phys. Rev. A*, vol. 44, pp. R20–R23, Jul 1991.
- [84] E. D. Black, "An introduction to pound-drever-hall laser frequency stabilization," *Am. J. Phys.*, vol. 69, p. 79, 2001.
- [85] H. Lehmitz, J. Hattendorf-Ledwoch, R. Blatt, and H. Harde, "Population trapping in excited Yb ions," *Phys. Rev. Lett.*, vol. 62, pp. 2108–2111, May 1989.
- [86] D. S. A. Bauch and C. Tamm, "Collisional population trapping and optical de-excitation of ytterbium ions in a radiofrequency trap," *J. Mod. Opt.*, vol. 39, p. 389, 1992.
- [87] S. Olmschenk, K. C. Younge, D. L. Moehring, D. N. Matsukevich, P. Maunz, and C. Monroe, "Manipulation and detection of a trapped Yb^+ hyperfine qubit," *Phys. Rev. A*, vol. 76, p. 052314, 2007.
- [88] L. Deslauriers, *Cooling and Heating of the Quantum Motion of Trapped Cd⁺ Ions*. PhD thesis, University of Michigan, Ann Arbor, 2006.
- [89] D. J. Berkeland and M. G. Boshier, "Destabilization of dark states and optical spectroscopy in zeeman-degenerate atomic systems," *Phys. Rev. A*, vol. 65, p. 033413, 2002.
- [90] M. Acton, *Detection and Control of Individual Trapped Ions and Neutral Atoms*. PhD thesis, University of Michigan, Ann Arbor, 2008.
- [91] A. Lee, "Ytterbium ion qubit state detection on an iccd camera," Bachelor's thesis, University of Maryland, College Park, 2012.
- [92] M. O. Scully and M. S. Zubairy, *Quantum Optics*. Cambridge University Press, 1997.
- [93] F. S. Crawford Jr., *Waves*. Berkeley Physics Course, Vol. 3, 1968.
- [94] J. P. Schiffer, "Phase transitions in anisotropically confined ionic crystals," *Phys. Rev. Lett.*, vol. 70, p. 818, 1993.

- [95] D. H. E. Dubin, “Theory of structural phase transitions in a trapped coulomb crystal,” *Phys. Rev. Lett.*, vol. 71, pp. 2753–2756, Oct 1993.
- [96] A. Steane, “The ion trap quantum information processor,” *Applied Physics B*, vol. 64, p. 623, 1997.
- [97] T. W. B. Kibble, “Topology of cosmic domains and strings,” *Journal of Physics A: Mathematical and General*, vol. 9, no. 8, p. 1387, 1976.
- [98] W. H. Zurek, “Cosmological experiments in superfluid helium?,” *Nature*, vol. 317, pp. 505–508, 1985.
- [99] A. Retzker, R. C. Thompson, D. M. Segal, and M. B. Plenio, “Double well potentials and quantum phase transitions in ion traps,” *Phys. Rev. Lett.*, vol. 101, p. 260504, Dec 2008.
- [100] G.-D. Lin, C. Monroe, and L.-M. Duan, “Sharp phase transitions in a small frustrated network of trapped ion spins,” *Phys. Rev. Lett.*, vol. 106, p. 230402, Jun 2011.
- [101] L. I. Schiff, *Quantum Mechanics, 3rd ed.* McGraw-Hill, New York, 1968.
- [102] K. F. Wall and A. Sanchez, “Titanium sapphire lasers,” *The Lincoln Laboratory Journal*, vol. 3, p. 447, 1990.
- [103] A. Chew, “Doppler-free spectroscopy of iodine at 739nm,” Bachelor’s thesis, University of Michigan, Ann Arbor, 2008.
- [104] D. Hayes, D. N. Matsukevich, P. Maunz, D. Hucul, Q. Quraishi, S. Olmschenk, W. Campbell, J. Mizrahi, C. Senko, and C. Monroe, “Entanglement of atomic qubits using an optical frequency comb,” *Phys. Rev. Lett.*, vol. 104, p. 140501, 2010.
- [105] P. J. Lee, B. B. Blinov, K.-A. Brickman, L. Deslauriers, M. Madsen, R. Miller, D. L. Moehring, D. Stick, and C. Monroe, “Atomic qubit operations with an electro-optic modulator,” *Opt. Lett.*, vol. 28, p. 1582, 2003.
- [106] P. J. Lee, *Quantum Information Processing with Two Trapped Cadmium Ions.* PhD thesis, University of Michigan, Ann Arbor, 2006.
- [107] T. Caneva, R. Fazio, and G. E. Santoro, “Adiabatic quantum dynamics of the Lipkin-Meshkov-Glick model,” *Phys. Rev. B*, vol. 78, p. 104426, Sep 2008.
- [108] S.-L. Zhu, C. Monroe, and L.-M. Duan, “Trapped ion quantum computation with transverse phonon modes,” *Phys. Rev. Lett.*, vol. 97, p. 050505, 2006.
- [109] D. Porras and J. I. Cirac, “Effective quantum spin systems with trapped ions,” *Phys. Rev. Lett.*, vol. 92, no. 20, p. 207901, 2004.

- [110] K. Binder, “Finite size scaling analysis of ising model block distribution functions,” *Physik B*, vol. 43, p. 119, 1981.
- [111] K. Binder, “Critical properties from Monte Carlo coarse graining and renormalization,” *Phys. Rev. Lett.*, vol. 47, pp. 693–696, Aug 1981.
- [112] K. Kim, S. Korenblit, R. Islam, E. E. Edwards, M.-S. Chang, C. Noh, H. Carmichael, G.-D. Lin, L.-M. Duan, C. C. Joseph Wang, J. K. Freericks, and C. Monroe, “Quantum simulation of the transverse Ising model with trapped ions,” *New Journal of Physics*, vol. 13, p. 105003, Oct. 2011.
- [113] C. A. Sackett, D. Kielpinski, B. E. King, C. Langer, V. Meyer, C. J. Myatt, M. Rowe, Q. A. Turchette, W. M. Itano, D. J. Wineland, and C. Monroe, “Experimental entanglement of four particles,” *Nature*, vol. 404, p. 256, 2000.
- [114] W. C. Campbell, J. Mizrahi, Q. Quraishi, C. Senko, D. Hayes, D. Hucul, D. N. Matsukevich, P. Maunz, and C. Monroe, “Ultrafast gates for single atomic qubits,” *Phys. Rev. Lett.*, vol. 105, p. 090502, Aug 2010.
- [115] R. Moessner and A. P. Ramirez, “Geometrical frustration,” *Phys. Today*, vol. 59, p. 24, Feb 2006.
- [116] K. Binder and A. P. Young, “Spin glasses: Experimental facts, theoretical concepts, and open questions,” *Rev. Mod. Phys.*, vol. 58, pp. 801–976, Oct 1986.
- [117] C. M. Dawson and M. A. Nielsen, “Frustration, interaction strength, and ground-state entanglement in complex quantum systems,” *Phys. Rev. A*, vol. 69, no. 5, p. 052316, 2004.
- [118] B. Normand and A. M. Oles, “Frustration and entanglement in the t_{2g} spin-orbital model on a triangular lattice: Valence-bond and generalized liquid states,” *Phys. Rev. B*, vol. 78, p. 094427, 2008.
- [119] S. Wasserman and K. Faus, *Social Network Analysis: Methods and Applications*. Cambridge, UK: Cambridge University Press, 1994.
- [120] S. N. Dorogovtsev, A. V. Goltsev, and J. F. F. Mendes, “Critical phenomena in complex networks,” *Reviews of Modern Physics*, vol. 80, p. 1275, 2008.
- [121] J. D. Bryngelson and P. G. Wolynes, “Spin glasses and the statistical mechanics of protein folding,” *Proc. Nat. Acad. Sci.*, vol. 84, p. 7524, 1987.
- [122] O. Gühne and G. Toth, “Entanglement detection,” *Physics Reports*, vol. 474, p. 1, 2009.
- [123] S. Olmschenk, K. C. Younge, D. L. Moehring, D. N. Matsukevich, P. Maunz, and C. Monroe, “Manipulation and detection of a trapped Yb⁺ hyperfine qubit,” *Phys. Rev. A*, vol. 76, no. 5, p. 052314, 2007.

- [124] D. Liebfried, R. Blatt, C. Monroe, and D. Wineland, “Quantum dynamics of single trapped ions,” *Reviews of Modern Physics*, vol. 75, p. 281, 2003.
- [125] H. Schmitz, A. Friedenauer, C. Schneider, R. Matjeschk, M. Enderlein, T. Huber, J. Glueckert, D. Porras, and T. Schaetz, “The “arch” of simulating quantum spin systems with trapped ions,” *Appl. Phys. B*, vol. 95, pp. 195–203, 2009.
- [126] M. E. Fisher and W. Selke, “Infinitely many commensurate phases in a simple Ising model,” *Phys. Rev. Lett.*, vol. 44, pp. 1502–1505, Jun 1980.
- [127] M. E. Fisher and W. Selke, “Low temperature analysis of the axial next-nearest neighbour Ising model near its multiphase point,” *Phil. Trans. R. Soc. Lond. A*, vol. 302, pp. 1–44, 1981.
- [128] P. Zoller, T. Beth, D. Binosi, R. Blatt, H. Briegel, D. Bruss, T. Calarco, J. I. Cirac, D. Deutsch, J. Eisert, A. Ekert, C. Fabre, N. Gisin, P. Grangiere, M. Grassl, S. Haroche, A. Imamoglu, A. Karlson, J. Kempe, L. Kouwenhoven, S. Krell, G. Leuchs, M. Lewenstein, D. Loss, N. Ltkenhaus, S. Massar, J. E. Mooij, M. B. Plenio, E. Polzik, S. Popescu, G. Rempe, A. ergienko, D. Suter, J. Twamley, G. Wendin, R. Werner, A. Winter, J. Wrachtrup, and A. Zeilinger, “Quantum information processing and communication. strategic report on current status, visions and goals for research in Europe..,” *Eur. Phys. J. D*, vol. 36, pp. 203–228, 2005.
- [129] G.-D. Lin, S.-L. Zhu, R. Islam, K. Kim, M.-S. Chang, S. Korenblit, C. Monroe, and L.-M. Duan, “Large-scale quantum computation in an anharmonic linear ion trap,” *Europhys. Lett.*, vol. 86, p. 60004, 2009.
- [130] S. Korenblit, D. Kafri, W. C. Campbell, R. Islam, E. E. Edwards, Z.-X. Gong, G.-D. Lin, L. Duan, J. Kim, K. Kim, and C. Monroe, “Quantum simulation of spin models on an arbitrary lattice with trapped ions.,” *arXiv:1201.0776v1*, 2012.
- [131] L.-M. Duan, E. Demler, and M. D. Lukin, “Controlling spin exchange interactions of ultracold atoms in optical lattices,” *Phys. Rev. Lett.*, vol. 91, p. 090402, Aug 2003.